

ELPH ANNUAL REPORT

2017

Editor

MURAMATSU, Norihito
KIKUNAGA, Hidetoshi
MUTO, Toshiya
TOKIYASU, Atsushi

Research Center for Electron Photon Science
Tohoku University
1-2-1 Mikamine, Taihaku, Sendai 982-0826
Japan

Phone: +81, 22-743-3400

Fax: +81, 22-743-3402

Web site: <http://www.lns.tohoku.ac.jp/>

982-0826 仙台市太白区三神峯1-2-1

東北大学電子光理学研究センター

電話 022-743-3400

Fax 022-743-3402

Preface

We are pleased to issue the ELPH Annual Report 2017 that covers scientific and technical activities carried out at Research Center for Electron Photon Science (ELPH), Tohoku University in FY2017 (April, 2017 to March, 2018).

The ELPH has been a part of Joint Usage / Research Centers since FY2011. The Joint Usage / Research Centers (JURC) system was engaged by the Ministry of Education, Culture, Sports, Science and Technology (MEXT) to encourage and promote collaborative research passing through the border of respective universities.

As one knows framework of joint research activity in Japan had been progressed based on laboratories belonging to national universities before the incorporation in 2004. The framework was refurbished to be a system of JURC officially accredited by the minister of MEXT in order to extract further research performance in 2008. The former “KAKURIKEN (核理研)” (Laboratory for Nuclear Science) became independent of Faculty of Science in the end of 2009, and then ELPH was established in order to be a member of JURC. We, however, suffered from the incredible earthquake and Tsunami occurred March 11, 2011, just before launch of JURC activity. Although the first two years we spent the whole time to be recovered, the ELPH was fortunately re-approved at the 6-year terminal evaluation and is now in the 2nd term of JURC activity.

Since the ELPH has been developing own research and education task based on the basic natural science, it is unlikely to collaborate with industry use and so-called innovative applicability. In order to obtain public comprehension, we have to explore the interest of basic science and post the amount of scientific information. As a first step, “The ELPH Symposium” was held in March, 2018. The symposium is opened for every ELPH users to overcome brick walls among the research fields. In addition, we invited Prof. Eizo Nakamura, director of Institute of Planetary Materials, Okayama University. Although different research filed, we have deeply impressed by his talk regarding outstanding philosophy for education, research and laboratory management. We would like to continue the ELPH symposium annually, and hope to create some fused scientific fields.

We sincerely ask facility users and related scientific field communities for continuous supports and cooperation.

November, 2018

Director

Hiroyuki Hama

ELPH Annual Report 2017

Contents

I. Topics

The First ELPH Symposium as a Joint Usage / Research Center.....1
N. Muramatsu

Winning Prizes in FY2017.....3
T. Ishikawa, K. Nanbu, K. Takahashi, and Y. Honda

II. Papers

Study of dibaryons via $\gamma d \rightarrow \pi^0 \pi^0 d$ at $E_\gamma = 0.75\text{--}1.15$ GeV.....5
T. Ishikawa, H. Fujimura, H. Fukasawa, R. Hashimoto, Q. He, Y. Honda, T. Iwata,
S. Kaida, H. Kanda, J. Kasagi, A. Kawano, S. Kuwasaki, K. Maeda, S. Masumoto,
M. Miyabe, F. Miyahara, K. Mochizuki, N. Muramatsu, A. Nakamura, K. Nawa,
S. Ogushi, Y. Okada, K. Okamura, Y. Onodera, K. Ozawa, Y. Sakamoto, M. Sato,
H. Shimizu, H. Sugai, K. Suzuki, Y. Tajima, S. Takahashi, Y. Taniguchi, Y. Tsuchikawa,
H. Yamazaki, R. Yamazaki, and H.Y. Yoshida

How to measure the $\Delta(1232)$ radius.....9
H. Shimizu, Q. He, Y. Honda, T. Ishikawa, M. Miyabe, Y. Matsumura, N. Muramatsu,
A. Tokiyasu, Y. Tsuchikawa, and H. Yamazaki

Measurement of a photon transmittance at high intensity.....15
Y. Matsumura, T. Ishikawa, Y. Honda, S. Kido, M. Miyabe, I. Nagasawa, K. Nanbu,
H. Shimizu, K. Takahashi, Y. Tsuchikawa, and H. Yamazaki

Current status of the FOREST/BLC experiments at ELPH.....20
T. Ishikawa, K. Aoki, H. Fujioka, Y. Honda, T. Hotta, Y. Inoue, K. Itahashi, H. Kanda,
H. Kawai, K. Maeda, Y. Matsumura, M. Miyabe, S. Miyata, N. Muramatsu, T. Nishi,
H. Ohnishi, K. Ozawa, H. Shimizu, M. Tabata, A.O. Tokiyasu, Y. Tsuchikawa, and
H. Yamazaki

Performance evaluation of Aerogel Cherenkov Counter with a refractive index of 1.10 for the
 Σp scattering experiment at J-PARC.....25
K. Kobayashi, K. Miwa, R. Honda, Y. Akazawa, M. Ikeda, S. Ozawa, N. Fujioka,
A. Sakaguchi, Y. Nakada, H. Kawai, M. Tabata, H. Ito, A. Kobayashi, N. Kaneko,
T. Mizuno, T. Akaishi, K. Shirotori, M. Asano, S. Ashikaga, M. Ichikawa, M. Naruki,
T. Takahashi, K. Ozawa, and M. Sekimoto

Performance Evaluation of Silicon-Tungsten Electromagnetic Calorimeter Detector (ALICE
FoCal) and High Timing Resolution MRPC-TOF for High Energy Heavy Ion Experiment.....47
R. Aoyama, T. Chujo, T. Hachiya, M. Hatakeyama, Y. Hoshi, T. Ichisawa, M. Inaba,
H. Kato, Y. Kawamura, D. Kawana, Y. Miake, T. Nonaka, K. Ozawa, S. Sakai, H. Sako,
T. Sakamoto, M. Shimomura, T. Sugitate, T. Suzuki, K. Tadokoro, M. Takamura, and
S. Takasu

Development of high-rate detectors by using MPPC for the charmed baryon spectroscopy experiment at J-PARC.....	55
K. Shirotori, T. Akaishi, H. Asano, R. Honda, T. Ishikawa, Y. Ma, H. Noumi, A. Sakaguchi, H. Sako, and T. N. Takahashi for the J-PARC E50 collaboration	
Performance of a shower depth measurement method for the KOTO CsI calorimeter.....	68
N. Hara, K. Kotera, T. Mari, H. Nanjo, H. Nishimiya, Y. Sato, N. Shimizu, Y. Tajima, T. Yamanaka	
Search for an η' d bound state by use of the $\gamma d \rightarrow \eta d$ reaction.....	75
H. Fujioka, T. Ishikawa, and T. Sekihara	
Development of an Aerogel Chrenkov Counter with Efficient Light Collection.....	77
H. Yamada, N. Morita, K. Matsuda, M. Okabe, and N. Muramatsu	
Development of Electro-magnetic Sampling Calorimeter with Active Absorbers.....	83
Y. Hasegawa, H. Ishihama, H. Sato, T. Takeshita, R. Terada, Y. Yamashita, and Y. Yoshimura	
Influence of the Coulomb distortion on the measurement of the proton radius.....	86
T. Tamae and T. Suda	
Light meson photoproduction off the proton at the SPring-8 BGOegg experiment.....	97
N. Muramatsu, J.K. Ahn, W.C. Chang, J.Y. Chen, S. Daté, T. Gogami, H. Hamano, T. Hashimoto, Q.H. He, K. Hicks, T. Hiraiwa, Y. Honda, T. Hotta, Y. Inoue, T. Ishikawa, I. Jaegle, J.M. Jo, Y. Kasamatsu., H. Katsuragawa., S. Kido, Y. Kon, S. Masumoto, Y. Matsumura, K. Miki, M. Miyabe, K. Mizutani, T. Nakamura, T. Nakano, M. Niiyama, Y. Nozawa, Y. Ohashi, H. Ohkuma, H. Ohnishi, T. Ohta, M. Oka, K. Ozawa, Y. Sada, M. Sasagawa, T. Shibukawa, H. Shimizu, R. Shirai, K. Shiraishi, Y. Sugaya, M. Sumihama, S. Suzuki, S. Tanaka, A. Tokiyasu, N. Tomida, N. Tran, Y. Tsuchikawa, T. Ueda, H. Yamazaki, R. Yamazaki, Y. Yanai, T. Yorita, C. Yoshida, and M. Yosoi	
A trial to measure a spectral function of η' mesons.....	103
H. Shimizu, Y. Matsumura, J. K. Ahn, W. C. Chang, J. Y. Chen, S. Daté, T. Gogami, H. Hamano, T. Hashimoto, Q. He, T. Hiraiwa, Y. Honda, T. Hotta, T. Ishikawa, J. M. Jo, Y. Kasamatsu, H. Katsuragawa, Y. Kon, S. Masumoto, K. Miki, M. Miyabe, K. Mizutani, N. Muramatsu, T. Nakamura, T. Nakano, M. Niiyama, Y. Nozawa, Y. Ohashi, H. Ohnishi, T. Ohta, M. Oka, K. Ozawa, C. Rangacharyulu, Y. Sada, T. Shibukawa, R. Shirai, Y. Sugaya, M. Sumihama, S. Suzuki, S. Tanaka, Y. Taniguchi, A. Tokiyasu, N. Tomida, N. Tran, Y. Tsuchikawa, T. Ueda, H. Yamazaki, R. Yamazaki, T. Yorita, C. Yoshida, and M. Yosoi	
Radiochemical measurement of photonuclear reaction yields for photon activation analysis.....	111
Y. Oura, H. Terasaki, Y. Yamaguchi, T. Hara, J. Kaneko, N. Kuroiwa, I. Endo, and Y. Miura	
Identification of Elemental Composition and Preparation of Radio-tracer for Recovery of Rare Metals in Household Garbage Incineration Slag by Photon Activation Method.....	117

K. Akiyama, K. Ito, S. Kubuki, and H. Kikunaga

Radioactive phantom productions for PET and β -ray imaging system.....121
T Fukuchi, H. Haba, and H. Kikunaga

III. Status Report

Status of Accelerator Facilities in FY2017.....125
Accelerator group

User Support Office Report in FY2017.....129
M. Miyabe and User Support Office

Radiation Safety Report 2017.....132
Radiation Safety Office

IV. List of Publication135

V. Members of Committees155

VI. Approved Experiments159

I. Topics

The First ELPH Symposium as a Joint Usage / Research Center

Norihito Muramatsu

Research Center for Electron Photon Science, Tohoku University, Sendai 982-0826

After the recovery from the Great East Japan Earthquake, the accelerator facilities at Research Center for Electron Photon Science (ELPH), Tohoku University, have been stably operated and used by many internal and external researchers in wide scientific fields as a Joint Usage / Research Center (JURC). On 2 March 2018, the first symposium was held for the purpose to share the research activities and achieved results of the individual user programs using the ELPH facilities in FY2017. This symposium also aimed to promote the participant's considerations about the JURC operation and the future direction of the facilities.

At the beginning of the symposium, the Director of ELPH, Prof. Hama, gave an opening address with the explanation about the facility status and the activities as a JURC. Scientific reports from several users then followed with open discussions for their activities and results. There were one talk from the field of accelerator development and synchrotron radiation, four from nuclear and high energy physics, and two from the researches using radioisotopes. Two special lectures were also arranged to discuss the facility issues: the near future experiment of proton radius measurement at ELPH, given by Prof. Suda, and the new challenges at the Institute for Planetary Materials, Okayama University, by Director Prof. Nakamura.

The symposium was co-hosted by ELPH and the Users Association. At the final session, a general meeting by the Users Association started from a greeting speech by President Prof. Tamura, and continued the exchange of user's suggestions and requests to the ELPH facilities and the other users. More than 50 people joined in the symposium and shared a productive time. We plan to continue the ELPH symposium once per year from now on.

Table 1 Program of the ELPH symposium for FY2017 (in Japanese).

== 第一部 拠点シンポジウム ==

- 9:30 センター長挨拶およびセンター拠点活動の概要
濱 広幸 東北大学 電子光物理学研究センター
- 9:55 成果報告1 (放射光・加速器)
山本 樹 高エネルギー加速器研究機構 放射光科学研究施設
「極短周期アンジュレータの開発と東北大・試験線形加速器 (t-ACTS) を用いた放射の評価実験」
- 10:20 成果報告2 (原子核・高エネルギー)
大西 宏明 東北大学 電子光物理学研究センター
「ELPH におけるハドロン物理」
- 10:45 休憩
- 10:55 成果報告3 (原子核・高エネルギー)
永尾 翔 東北大学 高度教養教育・学生支援機構
「NKS2 を用いたストレンジネス光生成反応研究の成果と今後の展望」
- 11:20 成果報告4 (原子核・高エネルギー)
本多 良太郎 東北大学 理学研究科
「GeV γ 実験室を利用した Σp 散乱実験 (J-PARC E40) 用の耐高計数 AC 検出器の性能評価」
- 11:45 成果報告5 (原子核・高エネルギー)
西口 創 高エネルギー加速器研究機構 素粒子原子核研究所
「ELPH 電子ビームを利用した高エネルギー物理実験用検出器開発 J-PARC COMET 実験での例」
- 12:10 昼食
- 13:30 成果報告6 (RI 利用)
白崎 謙次 東北大学 金属材料研究所
「電子光センターでの核種製造と溶媒抽出」
- 13:55 成果報告7 (RI 利用)
福地 知則 理化学研究所ライフサイエンス技術基盤研究センター
「次世代イメージング装置を用いた放射化分析」
- 14:20 休憩
- 14:30 特別講演 I
須田 利美 東北大学 電子光物理学研究センター
「ELPH での低エネルギー電子散乱による陽子電荷半径測定 —Proton Radius Puzzle の解明・理解を目指して—」
- 15:20 特別講演 II
中村 栄三 岡山大学 惑星物質研究所
「小規模研究所からの共同利用・共同研究拠点の新しい機能への挑戦」
- 16:10 休憩
- == 第二部 利用者の会 ==
- 16:30 会長挨拶
田村 裕和 東北大学 理学研究科
- 16:35 ユーザーオフィスからの報告
宮部 学 東北大学 電子光物理学研究センター
- 16:45 ユーザー講演
石川 貴嗣 東北大学 電子光物理学研究センター
「FOREST 実験の位置づけと将来の展望」
金田 雅司 東北大学 理学研究科
「NKS2 グループからの要望」
菊永 英寿 東北大学 電子光物理学研究センター
「大強度電子線形加速器を利用する共同利用者・プラットフォーム利用者のマシンタイム希望の現状」
- 17:30 総会 (幹事 須田利美)
- 18:30 意見交換会・懇親会 (研究棟 1 階 多目的室)

Winning Prizes in FY2017

Takatsugu Ishikawa, Ken'ichi Nanbu, Ken Takahashi, Yuki Honda

Research Center for Electron Photon Science, Tohoku University, Sendai 982-0826

In FY2017, four staff members won the prizes at Research Center for Electron Photon Science, Tohoku University.

Morita Memorial Award of the Senshu society (Takatsugu Ishikawa)

The leading role for the following achievements received recognition:

- 1) development of a high-intensity photon beamline including construction of a photon-tagging system and a profile monitor of the photon beam [NIM A622 (2010) 1],
- 2) construction of main detectors consisting of electromagnetic calorimeters, FOREST at ELPH [NIM A832 (2016) 108] and BGOegg at SPring-8/LEPS2 [NIM A837 (2016) 109], for meson photoproduction experiments,
- 3) study of hadrons with baryon number $B=2$ (dibaryon) via double neutral-meson photoproduction on the deuteron [PLB 772 (2017) 398], and
- 4) recovery of the photon beamline and FOREST detector at ELPH from the 2011 earthquake, conducting a new generation experiment for the precise and accurate determination of the scattering length between the eta meson and nucleon utilizing a special kinematics.

Excellent Presentation Award in the Division of Engineering and Technical Staff (Ken'ichi Nanbu)

The electron accelerator complex, including a high intensity 60 MeV linac, a 90 MeV injector linac, a 1.35 GeV BST (booster-storage) ring and a test accelerator, has been operated for education and research works at ELPH. In addition, there are some large dipole electromagnets for discriminating charged particles. Since these accelerators and experimental apparatuses consume a large amount of electricity, the operating cost is getting increased recently because of the increase in electricity charges. It is difficult to reduce the electricity consumption, limiting the beam time due to the allocated operation budget. Shortening the beam time has significant influence on the education and research. In this work, we improved management methods to reduce the cost for operating the utilities such as an air conditioning system and an accelerator cooling system. The operating cost has been reduced successfully to maintain the beam time.

Technology Award in the Faculty of Science (Ken Takahashi)

The systems for RI manufacturing and real-time beam measurement were developed to provide "safe experimental environment" and "qualified electron beam irradiation" to joint users. For the RI manufacturing, the system was improved comprehensively from both aspects of hardware and software. The irradiation system with low exposure was constructed by adding more compact and sufficient radiation shielding performance and improving a sample transporting device. The exposure of the user has been thus reduced when replacing the sample. In addition, the system for real-time beam measurement was developed with a current monitor, a space size monitor using a fluorescent screen and a camera, etc. The measurement programs and the display methods were improved so that users should be able to grasp the status of beam irradiation at all times.

New Face Award of Nuclear Physics Community (Yuki Honda)

Liquid metals were bombarded by a D_3^+ beam, and an unknown d+d reaction peculiar to the molecular beam was discovered. We proposed "Cooperative colliding mechanism" (CCM): one deuteron is elastically scattered toward another deuteron in the same molecule by the target metal nuclei, and causes a d+d reaction. The CCM explains the unknown d+d reaction quantitatively. Screening potentials of the d+d reaction in the metals were estimated to be very small with CCM, and it could be understood by the electron screening effect. In addition, it was found that the CCM should affect past solid metal experiments, and make misidentification of the screening potential of several hundred eV.

Table 1 Awards won by the ELPH staff in FY2017

第 13 回森田記念賞 平成 29 年 11 月 11 日@青葉サイエンスホール
石川貴嗣 「光子ビームによるクォーク・ハドロン物理の探求」
総合技術部職員研修会 優秀発表賞 平成 29 年 11 月 17 日@片平さくらホール
南部健一 「電子光物理学研究センターにおける加速器運転経費削減の取り組み」
理学研究科・理学部技術研究会 理学研究科技術賞 平成 29 年 11 月 28 日@青葉サイエンスホール
高橋健 「低被曝 RI 製造システムの構築とリアルタイム電子ビーム計測システムの開発」
原子核談話会新人賞 平成 30 年 1 月
本多佑記 「Study of the low-energy d+d reaction in liquid Metals」

II. Papers

(ELPH Experiment : #2623, #2640, #2655, #2694, #2710)

Study of dibaryons via $\gamma d \rightarrow \pi^0 \pi^0 d$ at $E_\gamma = 0.75\text{--}1.15$ GeV

T. Ishikawa¹, H. Fujimura^{1*}, H. Fukasawa¹, R. Hashimoto^{1†}, Q. He^{1‡},
 Y. Honda¹, T. Iwata², S. Kaida¹, H. Kanda^{3§}, J. Kasagi¹, A. Kawano⁴,
 S. Kuwasaki¹, K. Maeda³, S. Masumoto⁵, M. Miyabe¹, F. Miyahara^{1¶},
 K. Mochizuki¹, N. Muramatsu¹, A. Nakamura¹, K. Nawa¹, S. Ogushi¹,
 Y. Okada¹, K. Okamura¹, Y. Onodera¹, K. Ozawa⁶, Y. Sakamoto⁴, M. Sato¹,
 H. Shimizu¹, H. Sugai^{1||}, K. Suzuki^{1**}, Y. Tajima², S. Takahashi¹,
 Y. Taniguchi¹, Y. Tsuchikawa^{1††}, H. Yamazaki^{1‡‡}, R. Yamazaki¹,
 and H.Y. Yoshida²

¹*Research Center for Electron Photon Science (ELPH), Tohoku University, Sendai 982-0826, Japan*

²*Department of Physics, Yamagata University, Yamagata 990-8560, Japan*

³*Department of Physics, Tohoku University, Sendai 980-8578, Japan*

⁴*Department of Information Science, Tohoku Gakuin University, Sendai 981-3193, Japan*

⁵*Department of Physics, University of Tokyo, Tokyo 113-0033, Japan*

⁶*Institute of Particle and Nuclear Studies, High Energy Accelerator Research Organization (KEK), Tsukuba 305-0801, Japan*

The total and differential cross sections were measured for the $\gamma d \rightarrow \pi^0 \pi^0 d$ reaction at incident energies ranging from 0.75 to 1.15 GeV by using the FOREST detector at ELPH: the excitation function of the total cross section, angular distributions of d and π^0 s, invariant-mass distributions for $\pi^0 d$ and $\pi^0 \pi^0$. The main objective of investigating this reaction is to study isoscalar dibaryons in the $\pi^0 \pi^0 d$ system and an isovector dibaryon in the $\pi^0 d$ system. The deduced experimentally enable us to give evidence not only for the 2.15-GeV/ c^2 isovector dibaryon but also for 2.47- and 2.63-GeV/ c^2 isoscalar

*Present address: Department of Physics, Wakayama Medical University, Wakayama 641-8509, Japan

†Present address: Institute of Materials Structure Science (IMSS), High Energy Accelerator Research Organization (KEK), Tsukuba 305-0801, Japan

‡Present address: Institute of Fluid Physics, China Academy of Engineering (CAEP), Mianyang 621900, China

§Research Center for Nuclear Physics (RCNP), Osaka University, Ibaraki 567-0047, Japan

¶Present address: Accelerator Laboratory, High Energy Accelerator Research Organization (KEK), Tsukuba 305-0801, Japan

||Present address: Gunma University Initiative for Advanced Research (GIAR), Maebashi 371-8511, Japan

**Present address: The Wakasa Wan Energy Research Center, Tsuruga 914-0192, Japan

††Present address: Department of Physics, Nagoya University, Nagoya 464-8602, Japan

‡‡Present address: Radiation Science Center, High Energy Accelerator Research Organization (KEK), Tokai 319-1195, Japan

dibaryons. The details are described in a preprint [arXiv: 1805.08928 (2018)].

§1. Introduction

The study of the $B = 2$ systems (dibaryons) has a long history [1]. An early work by Dyson and Xuong [2] predicts the sextet of non-strange dibaryons \mathcal{D}_{IJ} with isospin I and spin J (\mathcal{D}_{01} , \mathcal{D}_{10} , \mathcal{D}_{12} , \mathcal{D}_{21} , \mathcal{D}_{03} , and \mathcal{D}_{30}) based on the first known dibaryon, deuteron (\mathcal{D}_{01}), the 1S_0 - NN virtual states (\mathcal{D}_{10}), and a resonance-like structure at $M=2.16$ GeV/ c^2 for the 1D_2 - pp amplitude (\mathcal{D}_{12}) of the partial wave analysis for the $\pi^+d \rightarrow pp$ reaction. The recent observation of the $d^*(2380)$ (\mathcal{D}_{03}) by the CELSIUS/WASA and WASA-at-COSY collaborations [3, 4] has made us pay attention to the classification. It is important to establish the excitation spectrum of dibaryons in order to understand their internal structures and basic building blocks of hadrons. A dibaryon is an interesting object to study its basic configuration from a molecule-like state consisting of two baryons (such as the deuteron) to a hexaquark hadron state, which is expected to appear as a spatially-compact exotic particle.

Although the πd system has a resonance-like structure at approximately 2.15 GeV/ c^2 , the structure can be also understood as a quasi-free (QF) Δ excitation from a nucleon in the deuteron. Currently, any experimental data are not recognized to show evidence for the existence of the 2.15-GeV/ c^2 resonance, $d^*(2150)$ corresponding to \mathcal{D}_{12} . The $d^*(2150)$ is a key state to understand the sextet of dibaryons. In photoinduced reactions, the $\gamma d \rightarrow \pi^0 d$ reaction is a convenient approach to study $d^*(2150)$. Even if it is observed, it can be also understood as a quasi-free (QF) Δ excitation from a nucleon in the deuteron similarly to the $\pi^+d \rightarrow pp$ and $\pi^\pm d \rightarrow \pi^\pm d$ reactions. The $\gamma d \rightarrow \pi^0 \pi^0 d$ reaction is more advantageous to find $d^*(2150)$ in the $\pi^0 d$ subsystem because the QF Δ excitation is kinematically separable as discussed later. Thus, we study the $\gamma d \rightarrow \pi^0 \pi^0 d$ reaction, aiming to observe isovector $d^*(2150)$ in the $\pi^0 d$ system through π^0 decay from a possible higher-mass isoscalar dibaryon in the $\pi^0 \pi^0 d$ system.

§2. Kinematics

Possible mechanisms for the $\gamma d \rightarrow \pi^0 \pi^0 d$ reaction can be classified in the following three:

1. QF $\pi^0 \pi^0$ production on a nucleon followed by deuteron coalescence (QFC),
2. the first π^0 is emitted from the QF nucleon, subsequently the NN (ΔN) reaction occurs with the spectator nucleon to generate a dibaryon resonance, followed by the second π^0 and deuteron emission, and
3. both the two π^0 s are emitted from a dibaryon resonance in a broad sense.

In the mechanisms 1 (2), the second π^0 should be emitted to compensate for the momentum given to the QF participant nucleon by the first emitted π^0 to coalesce into a deuteron (a dibaryon resonance). Thus, the angular distribution of deuteron emission becomes strongly backward (sideway) peaking for the mechanism 1 (2). While the mechanism 3 makes a rather flat distribution. Since the three mechanisms give completely different angular distributions, we can separate (or distinguish) the three mechanisms.

§3. Results

The total and differential cross sections were measured for the $\gamma d \rightarrow \pi^0 \pi^0 d$ reaction at the incident energy ranging from 0.75 to 1.15 GeV [5–9] at the Research Center for Electron Photon Science (ELPH), Tohoku University. The analysis of the $\gamma d \rightarrow \pi^0 \pi^0 d$ reaction was made in the same way as in Ref. [10]. The excitation function of γd center-of-mass system $W_{\gamma d}$ is not monotonically increasing but shows resonance-like behavior peaked at around 2.47 and 2.63 GeV. The angular distribution of deuteron emission is rather flat, and the kinematic condition for the obtained data completely differs from the QFC and semi-QF processes. Thus, we consider the possibility that the resonance-like structure might be due to a manifestation of dibaryons. In the observed reaction, both the two nucleons obviously participate before emitting π^0 s.

The differential cross section $d\sigma/dM_{\pi d}$ as a function of πd invariant mass $M_{\pi d}$ shows two peaks. The centroid of the low-mass peak is ~ 2.15 GeV/ c^2 independently of the incident energy. However, that of the high-mass peak decreases with a decrease of the incident energy, and finally the two peaks are merged into a bump. The high-mass peak reflects the appearance of the 2.15-GeV/ c^2 peak in $d\sigma/dM_{\pi d}$ between the other pion and deuteron (reflection). The resonance-like structure give a mass of 2.15 ± 0.01 GeV/ c^2 with a width of 0.11 ± 0.01 GeV/ c^2 . The angular distributions for the two π^0 s limit J^π of the state to 1^+ , 2^+ , or 3^- . The 2^+ assignment is consistent with the theoretically predicted \mathcal{D}_{12} state, and with the resonance structure of the 3P_2 - πd amplitude.

§4. Summary

The total and differential cross sections have been measured for the $\gamma d \rightarrow \pi^0 \pi^0 d$ reaction at incident energies from 0.75 to 1.15 GeV. The total cross section as a function of $W_{\gamma d}$ shows resonance-like behavior peaked at around 2.47 and 2.63 GeV. The experimental angular distributions of deuteron emission can never be understood in the QFC mechanism. The present work shows evidence for the existence of the 2.15-GeV/ c^2 isovector dibaryon in the $\pi^0 d$ channel, and of the 2.47- and 2.63-GeV/ c^2 isoscalar dibaryons in the $\pi^0 \pi^0 d$ channel. The details including figures can be found in a preprint [arXiv:1805.08928 (2018)].

Acknowledgments

The authors express their gratitude to the ELPH accelerator staff for stable operation of the accelerators in the FOREST experiments. They also acknowledge Mr. K. Matsuda, Mr. K. Nanbu, and Mr. I. Nagasawa for their technical support. This work was supported in part by the Ministry of Education, Culture, Sports, Science and Technology, Japan through Grants-in-Aid for Scientific Research (B) No. 17340063, for Specially Promoted Research No. 19002003, for Scientific Research (A) No. 24244022, for Scientific Research (C) No. 26400287, and for Scientific Research (A) No. 16H02188.

References

- [1] H. Clement: *Prog. Part. Nucl. Phys.* 93 (2017) 195.
- [2] F.J. Dyson, N.-H. Xuong: *Phys. Rev. Lett.* 13 (1964) 815.
- [3] M. Bashkanov *et al.* (CELSIUS/WASA collaboration): *Phys. Rev. Lett.* 102 (2009) 052301.
- [4] P. Adlarson *et al.* (WASA-at-COSY collaboration): *Phys. Rev. Lett.* 106 (2011) 242302.
- [5] T. Ishikawa *et al.*: *JPS Conf. Proc.* 10 (2016) 031001.
- [6] T. Ishikawa *et al.*: *Nucl. Instrum. Meth. A* 622 (2010) 1.
- [7] T. Ishikawa *et al.*: *Nucl. Instrum. Meth. A* 811 (2016) 124.
- [8] T. Ishikawa *et al.*: *Nucl. Instrum. Meth. A* 832 (2016) 108.
- [9] Y. Matsumura, T. Ishikawa *et al.*: *Nucl. Instrum. Meth. A* 902 (2018) 103.
- [10] T. Ishikawa *et al.*: *Phys. Lett. B* 772 (2017) 398.

(ELPH Experiment : #2623, #2640, #2655, #2694, #2710)

How to measure the $\Delta(1232)$ radius

H. Shimizu¹, Q. He², Y. Honda¹, T. Ishikawa¹, M. Miyabe¹, Y. Matsumura¹,
N. Muramatsu¹, A. Tokiyasu¹, Y. Tsuchikawa³, and H. Yamazaki⁴

¹Research Center for Electron Photon Science, Tohoku University, Sendai 982-0826

²Department of Nuclear Science & Engineering, Nanjing University, Nanjing 210016

³Department of Physics, Nagoya University, Nagoya 464-8602

⁴Institute of Particle and Nuclear Studies, KEK, Tsukuba 305-0801

A new method of measuring the $\Delta(1232)$ radius has been developed, detecting Bose-Einstein correlation effects in $\pi^0\Delta \rightarrow \pi^0\pi^0N$ events obtained in GeV- γ experiments at ELPH. A three-dimensional distribution of π^0 emitter sources is employed to extract the mean square radius of the Δ resonance.

§1. Introduction

We have been discussing the application of $\pi^0\pi^0$ Bose-Einstein correlation (BEC) to the measurement of the size of hadrons with a four-dimensional distribution of π^0 emitter sources [1]. It is possible to extract information on the space-time extension of a source from a space-like $2\pi^0$ correlation function, which can be obtained experimentally by measuring a space-like momentum transfer Q [$Q^2 \equiv -(p_1 - p_2)^2 > 0$] of each $\pi^0\pi^0$ event having four-dimensional momenta, p_1 and p_2 [2]. However, the physical meaning of the time component of the distribution is quite unclear. Therefore we return back to a three-dimensional distribution with which we can directly discuss the size of emitter sources.

In general, BEC effects may be expressed with two-particle correlation function $C_{\text{BEC}}(\mathbf{p}_1, \mathbf{p}_2)$ as

$$C_{\text{BEC}}(\mathbf{p}_1, \mathbf{p}_2) = \frac{P_{\text{BEC}}(\mathbf{p}_1, \mathbf{p}_2)}{P_0(\mathbf{p}_1, \mathbf{p}_2)}. \quad (1)$$

Here $P_{\text{BEC}}(\mathbf{p}_1, \mathbf{p}_2)$ denotes the probability density to find two identical bosons, subject to Bose-Einstein symmetry (BES), at r_1 and r_2 with momenta p_1 and p_2 , respectively, in three-dimensional space. The

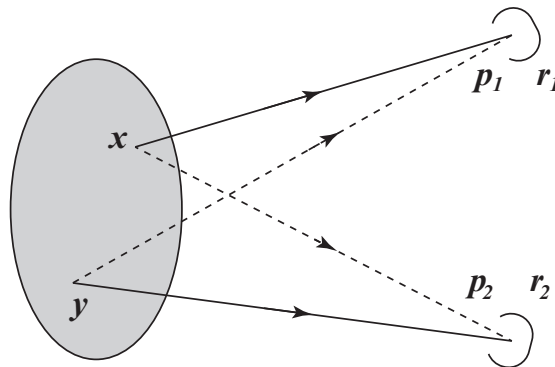


Fig.1. Symmetrization of two identical π^0 's with respect to their originating points x and y .

denominator $P_0(\mathbf{p}_1, \mathbf{p}_2)$ is another probability density of two identical bosons in the absence of BES. The probability density $P_{\text{BEC}}(\mathbf{p}_1, \mathbf{p}_2)$ is expressed as

$$P_{\text{BEC}}(\mathbf{p}_1, \mathbf{p}_2) = \int d^3x d^3y |\psi_2(\mathbf{p}_1, \mathbf{p}_2)|^2 \rho(\mathbf{x}) \rho(\mathbf{y}) \quad (2)$$

where $\psi_2(\mathbf{p}_1, \mathbf{p}_2)$ is a symmetrized two-particle plane wave function written by

$$\psi_2(\mathbf{p}_1, \mathbf{p}_2) = \frac{1}{\sqrt{2}} \left[e^{i\mathbf{p}_1 \cdot (\mathbf{r}_1 - \mathbf{x})} e^{i\mathbf{p}_2 \cdot (\mathbf{r}_2 - \mathbf{y})} + e^{i\mathbf{p}_1 \cdot (\mathbf{r}_1 - \mathbf{y})} e^{i\mathbf{p}_2 \cdot (\mathbf{r}_2 - \mathbf{x})} \right], \quad (3)$$

and $\rho(\mathbf{x})$ represents a normalized emitter source distribution. Here \mathbf{x} and \mathbf{y} are the places where bosons are emitted in the source. We have

$$|\psi_2(\mathbf{p}_1, \mathbf{p}_2)|^2 = 1 + \frac{1}{2} e^{-i\mathbf{q} \cdot (\mathbf{x} - \mathbf{y})} + \frac{1}{2} e^{i\mathbf{q} \cdot (\mathbf{x} - \mathbf{y})}, \quad (4)$$

with $\mathbf{q} = \mathbf{p}_1 - \mathbf{p}_2$. The probability density is then written by

$$\begin{aligned} P_{\text{BEC}}(\mathbf{p}_1, \mathbf{p}_2) &= \int d^3x d^3y \left[1 + \frac{1}{2} e^{-i\mathbf{q} \cdot (\mathbf{x} - \mathbf{y})} + \frac{1}{2} e^{i\mathbf{q} \cdot (\mathbf{x} - \mathbf{y})} \right] \rho(\mathbf{x}) \rho(\mathbf{y}) \\ &= 1 + |f(\mathbf{q})|^2, \end{aligned} \quad (5)$$

by employing $f(\mathbf{q})$, the Fourier transform of $\rho(\mathbf{x})$,

$$f(\mathbf{q}) = \int d^3x e^{i\mathbf{q} \cdot \mathbf{x}} \rho(\mathbf{x}), \quad (6)$$

where $\rho^*(\mathbf{x}) = \rho(\mathbf{x})$ is assumed. In this formulation, $P_0(\mathbf{p}_1, \mathbf{p}_2)$ is normalized to 1,

$$\begin{aligned} P_0(\mathbf{p}_1, \mathbf{p}_2) &= \int d^3x d^3y |\psi_0(\mathbf{p}_1, \mathbf{p}_2)|^2 \rho(\mathbf{x}) \rho(\mathbf{y}) \\ &= \frac{1}{2} \int d^3x d^3y \left[|e^{i\mathbf{p}_1 \cdot (\mathbf{r}_1 - \mathbf{x})} e^{i\mathbf{p}_2 \cdot (\mathbf{r}_2 - \mathbf{y})}|^2 + |e^{i\mathbf{p}_1 \cdot (\mathbf{r}_1 - \mathbf{y})} e^{i\mathbf{p}_2 \cdot (\mathbf{r}_2 - \mathbf{x})}|^2 \right] \rho(\mathbf{x}) \rho(\mathbf{y}) \\ &= \int d^3x d^3y \rho(\mathbf{x}) \rho(\mathbf{y}) \\ &= 1, \end{aligned} \quad (7)$$

and then the two-particle correlation function can be written by

$$C_{\text{BEC}}(\mathbf{p}_1, \mathbf{p}_2) = 1 + |f(\mathbf{q})|^2. \quad (8)$$

We assume 2π emissions take place in random phases at the emission points as indicated in the independent integration over x and y in (5).

It is necessary to show no q dependence of $C_{\text{BEC}}(\mathbf{p}_1, \mathbf{p}_2)$ for the events having no BEC, although it is not easy to find such a reference distribution without BEC. A two pion probability density distribution $P_2(\mathbf{p}_1, \mathbf{p}_2)$ for $\pi^+\pi^-$ events is a good candidate in principle for the reference distribution with no BEC. For $\pi^+\pi^-$ events, we have

$$|\psi_2(\pi^+ : \mathbf{p}_1, \pi^- : \mathbf{p}_2)|^2 = \frac{1}{2} \left[|e^{i\mathbf{p}_1 \cdot (\mathbf{r}_1 - \mathbf{x})} e^{i\mathbf{p}_2 \cdot (\mathbf{r}_2 - \mathbf{y})}|^2 + |e^{i\mathbf{p}_1 \cdot (\mathbf{r}_1 - \mathbf{y})} e^{i\mathbf{p}_2 \cdot (\mathbf{r}_2 - \mathbf{x})}|^2 \right] \quad (9)$$

since there is no BEC between π^+ and π^- , in contrast to $\pi^0\pi^0$ events which have to be symmetrized. However it is difficult in practice to utilize the $\pi^+\pi^-$ events to get the reference since experimental setups and devices are in general rather different for $\pi^+\pi^-$ detections from $\pi^0\pi^0$ measurements. We have been working on the development of a method to get the reference distribution with an event-mixing technique applying for experimentally obtained $\pi^0\pi^0$ events [3].

§2. Gaussian type distribution

We employ a spherically-symmetric three-dimensional Gaussian type distribution $\rho(\mathbf{x})$

$$\rho(\mathbf{x}) = \frac{1}{(\sqrt{2\pi}\alpha)^3} \exp\left(\frac{-\mathbf{x}^2}{2\alpha^2}\right) \quad (10)$$

with a Gaussian parameter α . The Fourier transform of $\rho(\mathbf{x})$ is then given by

$$\begin{aligned} f(\mathbf{q}) &= \int d^3x e^{i\mathbf{q}\cdot\mathbf{x}} \rho(\mathbf{x}) \\ &= \frac{1}{(\sqrt{2\pi}\alpha)^3} \int d^3x e^{i\mathbf{q}\cdot\mathbf{x}} \exp\left(\frac{-\mathbf{x}^2}{2\alpha^2}\right) \\ &= \frac{1}{(\sqrt{2\pi}\alpha)^3} \int d^3x \exp\left(-\frac{(\mathbf{x} - i\alpha^2\mathbf{q})^2}{2\alpha^2} - \frac{\alpha^2\mathbf{q}^2}{2}\right) \\ &= \exp\left(-\frac{\alpha^2\mathbf{q}^2}{2}\right). \end{aligned} \quad (11)$$

The integration over \mathbf{y} can be performed likewise. Thus we have

$$\int d^3x d^3y e^{i\mathbf{q}\cdot(\mathbf{x}-\mathbf{y})} \rho(\mathbf{x})\rho(\mathbf{y}) = |f(\mathbf{q})|^2 = \exp(-\alpha^2\mathbf{q}^2) \quad (12)$$

and

$$C_{\text{BEC}}(q) = 1 + |f(\mathbf{q})|^2 = 1 + e^{-\alpha^2q^2}, \quad (13)$$

where $q = |\mathbf{q}|$ is not a Lorentz invariant quantity but a three-dimensional momentum transfer. We assume that the two-particle correlation function can experimentally be written by

$$C_{\text{BEC}}(q) = 1 + \lambda |f(q)|^2 = 1 + \lambda e^{-\alpha^2q^2}, \quad (14)$$

since all the events do not come from the process under consideration. Here λ ($0 \leq \lambda \leq 1$) is introduced to describe chaoticity that measures the strength of the BEC effects.

§3. Application to $\pi\Delta$ processes

We discuss here an application of $\pi^0\pi^0$ BEC effects to a size measurement of $\Delta(1232)$ using $\pi^0\Delta$ events obtained in $\pi^0\pi^0$ photoproduction at an incident photon energy around 1 GeV. In this process, π^0 and Δ are produced at the same time at first. Then the Δ decays into π^0N . If there is an overlap of the Δ and the first π^0 wave functions, some information on the size of Δ is obtainable through $\pi^0\pi^0$ BEC in the Δ rest frame under the following considerations.

1. $\pi\Delta$ system

We focus on a $\pi\Delta$ system no matter what its origin would be in the $\gamma N \rightarrow \pi^0\Delta \rightarrow \pi^0\pi^0N$ reaction. Experimentally, using a Dalitz plot of $m^2(\pi^0, p)$ versus $m^2(\pi^0, \pi^0)$, for example, we can select $\pi\Delta$ events effectively.

2. Originating places of π^0

We restrict our considerations to quark-antiquark or three quark systems for hadrons. Then the size of a baryon can be understood as the range of existence of quarks in the baryon. We assume an energetic quark inside a hadron gives rise to meson emission as indicated in Fig. 2. It is clear

that the first π^0 and Δ are produced at the same time in the $\gamma N \rightarrow \pi^0 \Delta$ process, whether s -channel resonance N^* takes place or not. It is difficult in general, however, to say the place where the π^0 appears. But the momentum vectors of π^0 and Δ can be traced back to the same space-time point where an energetic quark Q was placed. The $\pi^0 - \Delta$ system has a relative angular momentum of

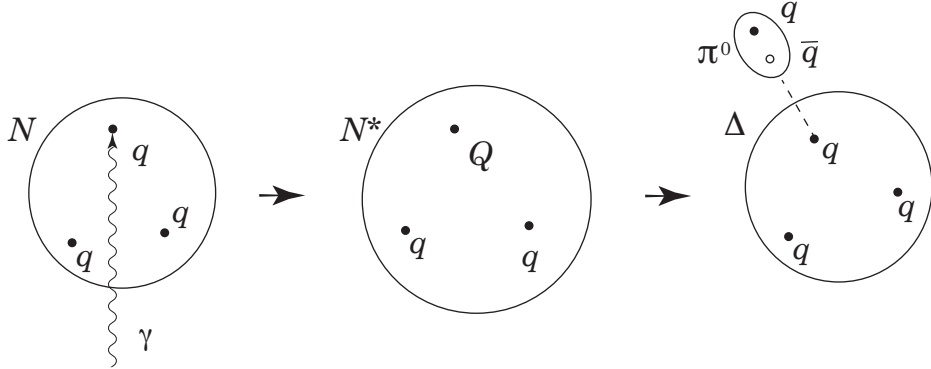


Fig.2. S wave meson emission due to an energetic quark.

0 (S wave) in the $\pi^0 \Delta$ threshold region. It is natural to think that the wave functions of π^0 and Δ overlap each other at the origin of the $\pi^0 \Delta$ system. Thus we assume that the first π^0 appears somewhere within Δ according to the quark distribution and then goes apart from the Δ , which sequentially emits the second π^0 afterward.

3. Space-time coordinates

The space-time coordinates can be defined so that the center of Δ is the origin of the coordinates, O , when the first π^0 and Δ appear simultaneously at $\tau = 0$, where τ denotes the proper time at the rest frame of Δ . In this space-time coordinate frame, the first and second π^0 s appear at $A(0, x)$

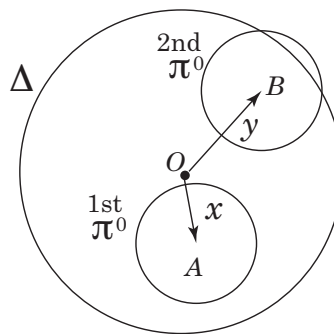


Fig.3. Space-time coordinates of Δ at rest.

and $B(\tau, y)$, respectively. We define the space-time coordinates like this for each $\pi^0 \pi^0$ event. Thus we can get information of the Δ size by measuring the BEC effects of $\pi^0 \pi^0$ events having momenta p_1 and p_2 in the inertial frame of Δ at rest, where the decay time τ does not give any effect in the measurement as far as strong decay is concerned.

4. The definition of the size of Δ

We assume one of the quarks becomes energetic in Δ so as to emit a pion. The energetic quark Q appears at \mathbf{y} according to the quark distribution function $\rho(\mathbf{y})$ in Δ . Once a decay process $Q \rightarrow q\bar{q}+q$ starts to emit a pion, the remaining three quarks form a nucleon so that the relative angular momentum of the πN system becomes 1 (P wave) with the total momentum of zero as illustrated in Fig. 4. The place of the pion traced back to the energetic quark gives a "pion emitter source"

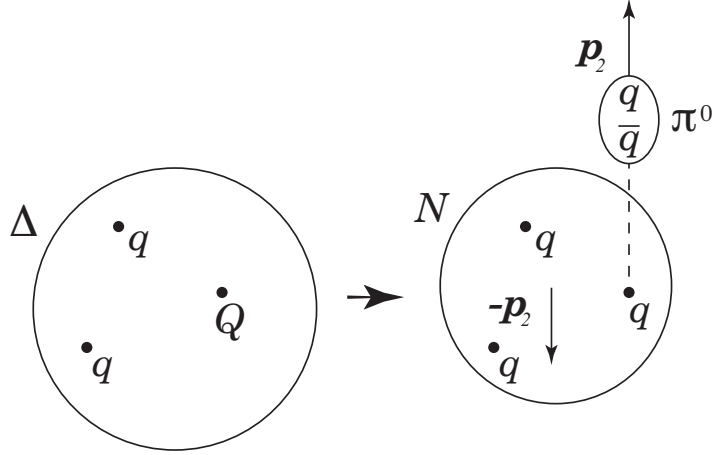


Fig.4. $\Delta \rightarrow \pi^0 N$ decay originated by an energetic quark Q .

distribution corresponding to $\rho(\mathbf{y})$ in the decay process of $\Delta \rightarrow \pi^0 N$, in which the relative angular momentum 1 has to be taken into account. Employing cylindrical coordinates $\mathbf{y} = (r, \theta, z)$ with the z axis taken to be along the momentum vector \mathbf{p}_2 of π^0 decaying from Δ , we have

$$|2\mathbf{y} \times \mathbf{p}_2| = 2rp_2 = 1 \quad (15)$$

in the Δ rest frame, where $p_2 = |\mathbf{p}_2|$.

Under these conditions, the reference distribution corresponding to Eq. (7) may be given by

$$\begin{aligned} P_0(\mathbf{p}_1, \mathbf{p}_2) &= \int d^3x d^3y |\psi_0(\mathbf{p}_1, \mathbf{p}_2)|^2 \rho(\mathbf{x}) \rho(\mathbf{y}) \delta(r - \beta) \quad \left(\beta \equiv \frac{1}{2p_2} \right) \\ &= \frac{1}{(\sqrt{2\pi}\alpha)^6} \int d^3x d^3y \exp\left(\frac{-\mathbf{x}^2}{2\alpha^2}\right) \exp\left(\frac{-\mathbf{y}^2}{2\alpha^2}\right) \delta(r - \beta) \\ &= \frac{1}{(\sqrt{2\pi}\alpha)^3} \int r dr d\theta dz \exp\left(\frac{-\mathbf{y}^2}{2\alpha^2}\right) \delta(r - \beta) \\ &= \frac{1}{(\sqrt{2\pi}\alpha)^3} \int 2\pi\beta dz \exp\left(-\frac{z^2 + \beta^2}{2\alpha^2}\right) \\ &= \frac{\beta}{\alpha^2} \exp\left(-\frac{\beta^2}{2\alpha^2}\right). \end{aligned} \quad (16)$$

And Eq. (2) becomes

$$\begin{aligned}
P_{\text{BEC}}(\mathbf{p}_1, \mathbf{p}_2) &= \int d^3x d^3y |\psi_2(\mathbf{p}_1, \mathbf{p}_2)|^2 \rho(\mathbf{x}) \rho(\mathbf{y}) \delta(r - \beta) \\
&= \frac{1}{(\sqrt{2\pi}\alpha)^6} \int d^3x d^3y \left[1 + \frac{1}{2} e^{-i\mathbf{q} \cdot (\mathbf{x} - \mathbf{y})} + \frac{1}{2} e^{i\mathbf{q} \cdot (\mathbf{x} - \mathbf{y})} \right] \exp\left(\frac{-\mathbf{x}^2}{2\alpha^2}\right) \exp\left(\frac{-\mathbf{y}^2}{2\alpha^2}\right) \delta(r - \beta) \\
&= \frac{1}{(\sqrt{2\pi}\alpha)^3} \int d^3y \left[1 + \exp\left(-\frac{\alpha^2 \mathbf{q}^2}{2}\right) \exp(i\mathbf{q} \cdot \mathbf{y}) \right] \exp\left(\frac{-\mathbf{y}^2}{2\alpha^2}\right) \delta(r - \beta) \\
&= \frac{1}{(\sqrt{2\pi}\alpha)^3} \int r dr d\theta dz \exp\left(\frac{-\mathbf{y}^2}{2\alpha^2}\right) \delta(r - \beta) \left[1 + \exp\left(-\frac{\alpha^2 \mathbf{q}^2}{2}\right) \exp(irq_r \cos \theta + irq_z z) \right] \\
&= P_0(\mathbf{p}_1, \mathbf{p}_2) + \frac{\beta}{(\sqrt{2\pi}\alpha)^3} \exp\left(-\frac{\alpha^2 \mathbf{q}^2}{2}\right) \int d\theta dz \exp\left(-\frac{z^2 + \beta^2}{2\alpha^2}\right) \exp(i\beta q_r \cos \theta + i\beta q_z z) \\
&= \frac{\beta}{\alpha^2} \exp\left(-\frac{\beta^2}{2\alpha^2}\right) + \frac{\beta}{(\sqrt{2\pi}\alpha)^3} \exp\left(-\frac{\alpha^2 \mathbf{q}^2}{2}\right) \\
&\quad \cdot \int_{-\infty}^{\infty} dz \exp\left(-\frac{(z - i\beta q_z)^2 + \beta^2(1 + q_z^2)}{2\alpha^2}\right) \int_0^{2\pi} d\theta \exp(i\beta q_r \cos \theta) \\
&= \frac{\beta}{\alpha^2} \exp\left(-\frac{\beta^2}{2\alpha^2}\right) + \frac{\beta}{\alpha^2} \exp\left(-\frac{\alpha^2 \mathbf{q}^2}{2}\right) \exp\left(-\frac{\beta^2(1 + q_z^2)}{2\alpha^2}\right) J_0(\beta q_r), \tag{17}
\end{aligned}$$

where $\mathbf{q} = (q_r, 0, q_z)$ and $J_0(x)$ denotes the 0th order Bessel function of the first kind. Therefore the correlation function may be written as

$$C_{\text{BEC}}(q, p_2) = 1 + \lambda \exp\left(-\frac{\alpha^2 q^2}{2}\right) \exp\left(-\frac{\beta^2 q_z^2}{2\alpha^2}\right) J_0(\beta q_r) \quad (q^2 = q_r^2 + q_z^2) \tag{18}$$

for $\pi^0\pi^0$ events in the $\gamma N \rightarrow \pi^0 \Delta \rightarrow \pi^0 \pi^0 N$ process. This correlation function depending on q and p_2 ($= 1/(2\beta)$) has to be measured in the frame of Δ at rest to get the proper x distribution. The Gaussian form factor given by (10) yields the BEC function (18), in which the BEC parameter α^2 is experimentally obtainable. Then the mean square radius of Δ can be calculated as

$$\langle \mathbf{x}^2 \rangle = \frac{1}{(\sqrt{2\pi}\alpha)^3} \int \mathbf{x}^2 \exp\left(\frac{-\mathbf{x}^2}{2\alpha^2}\right) d^3x = 3\alpha^2. \tag{19}$$

In this way, once we find the BEC parameter α^2 by applying (18) to experimentally obtained $\pi^0\pi^0$ data, we can get the mean square radius $\langle \mathbf{x}^2 \rangle$ of $\Delta(1232)$ given as $3\alpha^2$.

Acknowledgment

This work was supported in part by MEXT (Grant No. 19002003), and by JSPS (No. 24244022).

References

- [1] Q. He *et al.*, ELPH Annual Report (2011, 2012, 2013) 73.
- [2] H. Shimizu *et al.*, ELPH Annual Report (2014) 22.
- [3] Q. He *et al.*, Chinese Phys. **40** (2016) 114002; Prog. Theor. Exp. Phys. (2017) 033D02.

(ELPH Experiment : #2776)

Measurement of a photon transmittance at high intensity

Y. Matsumura^{1*}, T. Ishikawa¹, Y. Honda¹, S. Kido¹, M. Miyabe¹,
I. Nagasawa¹, K. Nanbu¹, H. Shimizu¹, K. Takahashi¹, Y. Tsuchikawa^{1†},
and H. Yamazaki^{1‡}

¹*Research Center for Electron Photon Science (ELPH), Tohoku University, Sendai 982-0826,
Japan*

A transmittance monitor has been developed for the second tagged-bremsstrahlung-photon beamline at ELPH. The transmittance, which is defined as the probability of finding a photon arrival at the target position when a post-bremsstrahlung electron is detected with a photon-tagging counter, should be determined to deduce cross sections for photoinduced reactions. The developed monitor consists of a telescope of thin plastic scintillators with a positron and electron converter, and a dedicated circuit implemented in a field-programmable gate array chip. The measured transmittance is found to be constant independently of the circulating electron current in the synchrotron. The details are described in a published paper [Y. Matsumura, T. Ishikawa *et al.*, Nucl. Instrum. Meth. A **902**, 103 (2018)].

§1. Introduction

Photoinduced reactions with the incident energy ranging from several hundred MeV to a few GeV are important to study the structure of hadrons in detail. Meson photoproduction experiments have been conducted [1–5] with an electromagnetic-calorimeter (EMC) complex, FOREST [6], on the second photon beamline [7] at ELPH. A bremsstrahlung photon beam is generated by inserting a radiator into circulating electrons [7] in the electron synchrotron called Booster Storage (BST) ring [8]. The energy of each photon is determined by measuring the momentum of its corresponding post-bremsstrahlung electron with a tagging detector system, STB-Tagger II [7]. The tagging signal does not always correspond to a photon arriving at the target for the meson photoproduction experiments. Thus, the photon transmittance (so called the tagging efficiency), which is defined as the probability of finding a photon coming to the target position when an electron is detected with STB-Tagger II, should be determined to deduce cross sections for photoinduced reactions. The transmittance is experimentally measured since it is difficult to incorporate all the conditions of circulating electrons in the calculation.

So far, we have measured the transmittance, T_γ , using a large SF5 lead-glass Cherenkov counter [9] on the photon beamline. The energy of a photon is measured with the counter in response to the tagging

*Present address: Research Center for Nuclear Physics (RCNP), Osaka University, Ibaraki 567-0047, Japan

†Present address: Department of Physics, Nagoya University, Nagoya 464-8602, Japan

‡Present address: Radiation Science Center, High Energy Accelerator Research Organization (KEK), Tokai 319-1195, Japan

signal. The singles rate of the counter should be reduced so that it could work, namely the photon-beam intensity should be much lowered by decreasing the circulating current in the BST ring (faint beam). We have developed a transmittance monitor for high-intensity photon beams at normal operation (circulating current of ~ 20 mA and photon-tagging rate of ~ 20 MHz), and confirmed the transmittance is the same between the faint and high-intensity photon beams.

§2. Developed transmittance monitor

We used the same detector system for the photon-beam profile monitor with scintillating-fiber hodoscopes (BPM) [10]. BPM in this work consisted of a plastic scintillator (PS) for charge veto (Gv), an aluminum-plate converter with a thickness of 0.5 mm, and two trigger PSs (Gt1 and Gt2). The thicknesses of the three PSs measured 1 mm each. Additional two layers of scintillating-fiber hodoscopes to give the intensity map of the photon beam were not used. The condition of finding a photon by this detector system (BPM trigger) was

$$\text{Tr} = \overline{\text{Gv}} \otimes \text{Gt1} \otimes \text{Gt2}, \quad (1)$$

where \otimes stands for coincidence of signals. The Gv signal rejected the events containing a charged particle produced upstream, and the Gt1 and Gt2 signals required the events having an e^+e^- pair. The discriminator thresholds for producing logic signals of Gv, Gt1, and Gt2 were set to $0.5V_{\text{mip}}$, $1.5V_{\text{mip}}$, and $1.5V_{\text{mip}}$, respectively. Here V_{mip} denotes the pulse height in response to the minimum ionizing particle.

A circuit to give R_γ^i for each tagging channel i has been implemented into a developed NIM module called MPLM4. MPLM4 is a prototype of MPLM4X in Ref. [10] containing a field-programmable gate array (FPGA) chip, Xilinx Spartan-6 [11]. MPLM4 (MPLM4X) accepts and produces NIM standard signals through 36 (38) input and 18 output channels. The logical circuit has been designed using edge-aligned signals with an internal 200-MHz clock signal. The R_γ^i is determined by the numbers, N s, of three signals for each tagging channel Tci:

$$R_\gamma^i = \frac{N(\text{Tci} \otimes \text{Tr}) - N(\text{Tci} \otimes \text{Tr}')}{N(\text{Tci})}, \quad (2)$$

where Tr' denotes the 165-ns delayed signal for Tr , and the coincidence widths are the same between $\text{Tci} \otimes \text{Tr}$ and $\text{Tci} \otimes \text{Tr}'$. The harmonic number of the BST ring with an RF frequency of 500.14 MHz is 83 [8]. The 165-ns delay approximately corresponds to the time of a revolution in the BST ring. The logic signals of Gv, Gt1, and Gt2 from the BPM detector, and those of 32 tagging channels out of 116 [7] are delivered to MPLM4.

The BPM detector itself is sensitive only to charged particles (e^+e^- pairs) produced downstream of Gv. This fraction (sampling ratio), η_γ , is proportional to the probability of finding a photon in the BPM detector with respect to a tagging signal (BPM-response probability), R_γ . The actual photon transmittance, T_γ , can be determined from R_γ and η_γ :

$$T_\gamma = \frac{R_\gamma}{\eta_\gamma}. \quad (3)$$

Since T_γ is directly measured for a faint beam with an EMC module on the beamline, η_γ can be determined from the measured T_γ and R_γ values in the same condition. The sampling ratio, η_γ , was

determined using faint beams with tagging rates of 1 and 6 kHz. We describe the rate for all the tagging signals simply as the tagging rate. The η_γ is found to be constant, and average values obtained are 0.00673 ± 0.00033 and 0.00662 ± 0.00020 for the 1- and 6-kHz tagging rates, respectively. These values are consistent with the expected value of $0.00658 \pm 0.00015(\text{thr}) \pm 0.00022(\text{mat})$ for the sampling ratio, which is determined by a Monte-Carlo simulation based on Geant4 [12]. The errors $0.00015(\text{thr})$ and $0.00022(\text{mat})$ are given by the uncertainty of the effective discriminator threshold values ($\pm 20\%$) and that of the material thickness covering each PS (± 0.05 mm), respectively. Since the measured value of η_γ includes the uncertainty of the material thickness, we have adopted the average value 0.00665 ± 0.00017 with a systematic uncertainty of 0.00015 for the measured sampling ratio.

§3. Measurement of a transmittance at high intensities

We measured the BPM-response probabilities for the six circulating currents of 1, 2, 4, 8, 12, and 18 mA. Since the circulating currents given by a DC current transformer (DCCT) did not have enough accuracy, the ratio of the measured tagging rates were employed for that of photon intensities. The ratio of photon intensities for 1, 4, 8, 12, and 18 mA to the intensity at 2 mA were found to be 0.286 ± 0.010 , 1.970 ± 0.022 , 4.445 ± 0.045 , 6.152 ± 0.062 , and 9.535 ± 0.096 , respectively. The actual currents of 1, 4, 8, 12, and 18 mA were approximately 0.6, 3.9, 8.9, 12.3, and 19.1 mA, respectively, if the circulating current of 2 mA was correctly measured. The counting efficiency of the BPM response for each circulating current was estimated from singles rate of signals from BPM by using a Monte Carlo simulation which incorporate finite widths and jitters of them. Since η_γ must be constant, the transmittance as a function of the circulating current can be observed in the measured BPM-response probability. Fig. 1 shows the ratio of BPM-response probability to that obtained in the 1-mA circulating current. The obtained ratios of the BPM-response probabilities have a constant value in a range from 0.95 to 1.05 including the results from the faint beams. Thus, the measured transmittance for each tagging channel is constant independently of the circulating current (photon intensity). The actual transmittance, T_γ^i , can be obtained dividing the BPM-response probability, R_γ^i , by the sampling ratio $\eta_\gamma = 0.00665 \pm 0.00017 \pm 0.00015$ and attenuation factor α_{att} .

§4. Summary

A photon-transmittance monitor has been developed for the second tagged-photon beamline at ELPH. The developed monitor consists of the BPM detector and a dedicated circuit implemented in MPLM4. The transmittance, T_γ , can be obtained from the response probability of the detector, R_γ , and sampling ratio (the probability of e^+e^- production with the converter), η_γ . The η_γ is determined using faint beams by comparing the R_γ and directly measured T_γ . The η_γ is found to be $0.00665 \pm 0.00017(\text{sta.}) \pm 0.00015(\text{sys.})$. The R_γ can be successfully measured with this monitor for high-intensity photon beams corresponding to 20 MHz tagging signals. The measured R_γ is found to be constant with respect to the photon intensity for each photon-tagging channel within the statistical error (approximately $\pm 5\%$). This suggests that T_γ is constant independently of the circulating current. The accuracy

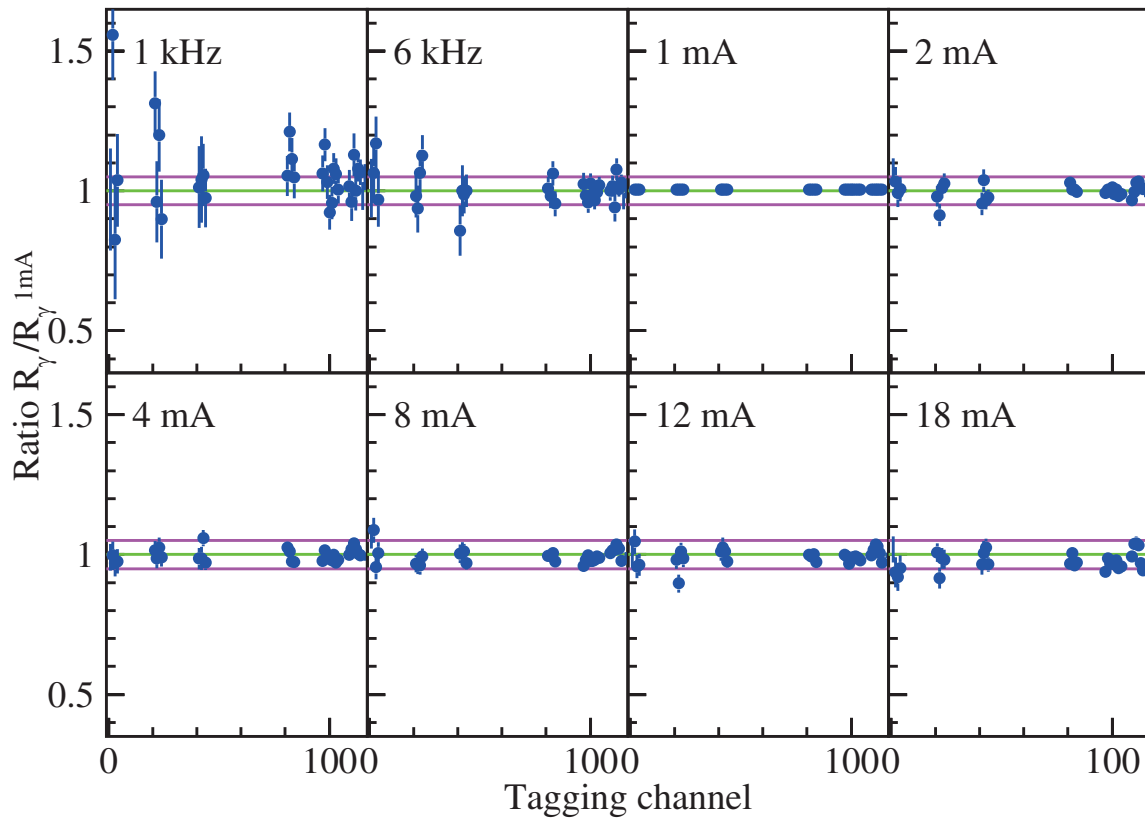


Fig.1. The ratio of response probabilities of BPM. The measured response probability, R_γ , is divided by that for the circulating current of 1 mA. The three horizontal lines correspond to the ratio of 0.95, 1.00, and 1.05. The tagging rate of 1 kHz approximately corresponds to the circulating of 1 μ A.

of the transmittance measured at high intensity is expected to be $\pm 5\%$ owing to the uncertainty of η_γ . The details are described in a published paper [Y. Matsumura, T. Ishikawa *et al.*, Nucl. Instrum. Meth. A **902**, 103 (2018)].

Acknowledgments

The authors express many thanks to the ELPH accelerator staff for providing the primary electron beam in stable condition. This work was supported in part by Grants-in-Aid for Scientific Research (A) No. 24244022, for Scientific Research (C) No. 26400287, and for Scientific Research (A) No. 16H02188.

References

- [1] T. Ishikawa *et al.*: Phys. Lett. B **772**, 398 (2017).
- [2] T. Ishikawa *et al.*: Proceedings of the XV International Conference on Hadron Spectroscopy-Hadron 2013, PoS(Hadron 2013)095;
T. Ishikawa *et al.*: Proceedings of the 10th International Workshop on the Physics of Excited Nucleons (NSTAR2015), JPS Conference Proceedings **10**, 031001 (2016).

- [3] Y. Tsuchikawa *et al.*: Proceedings of the 12th International Conference on Hypernuclear and Strange Particle Physics (HYP2015), JPS Conference Proceedings **17**, 062007 (2017).
- [4] T. Ishikawa *et al.*: Proceedings of the 26th International Nuclear Physics Conference, PoS(INPC2016)267.
- [5] S.X. Nakamura, H. Kamano, T. Ishikawa: Phys. Rev. C **96**, 042201 (R) (2017);
T. Ishikawa *et al.*: Acta Phy. Polon. B **48**, 1801 (2017).
- [6] T. Ishikawa *et al.*: Nucl. Instrum. Meth. A **832**, 108 (2016).
- [7] T. Ishikawa *et al.*: Nucl. Instrum. Meth. A **622**, 1 (2010).
- [8] F. Hinode *et al.*: Proceedings of 11th International Conference on Synchrotron Radiation Instrumentation (SRI2012), Journal of Physics: Conference Series **425**, 072011 (2013);
F. Hinode *et al.*: Proceedings of the 7th International Particle Accelerator Conference (IPAC2016), p. 701.
- [9] A. Ando *et al.*: KEK report, KEK-79-21 (1979).
- [10] T. Ishikawa *et al.*: Nucl. Instrum. Meth. A **811**, 124 (2016).
- [11] Spartan-6 website:
(<http://www.xilinx.com/products/silicon-devices/fpga/spartan-6.html>).
- [12] S. Agostinelli *et al.*: Nucl. Instrum. Meth. A **506**, 250 (2003);
J. Allison *et al.*: IEEE Transactions on Nuclear Science **53**, 270 (2006);
Geant4 website (<http://geant4.cern.ch/>).

(ELPH Experiment : #2803, #2844, #2882)

Current status of the FOREST/BLC experiments at ELPH

T. Ishikawa¹, K. Aoki², H. Fujioka³, Y. Honda¹, T. Hotta⁴, Y. Inoue¹,
 K. Itahashi⁵, H. Kanda⁴, H. Kawai⁶, K. Maeda⁷, Y. Matsumura¹, M. Miyabe¹,
 S. Miyata⁸, N. Muramatsu¹, T. Nishi⁵, H. Ohnishi¹, K. Ozawa², H. Shimizu¹,
 M. Tabata⁶, A.O. Tokiyasu¹, Y. Tsuchikawa⁹, and H. Yamazaki¹

¹*Research Center for Electron Photon Science (ELPH), Tohoku University, Sendai 982-0826, Japan*

²*Institute of Particle and Nuclear Studies, High Energy Accelerator Research Organization (KEK), Tsukuba 305-0801, Japan*

³*Department of Physics, Tokyo Institute of Technology, Tokyo 152-8551, Japan*

⁴*Research Center for Nuclear Physics (RCNP), Osaka University, Ibaraki 567-0047, Japan*

⁵*Nishina Center for Accelerator-Based Science, RIKEN, Wako 351-0198, Japan*

⁶*Department of Physics, Chiba University, Chiba 263-8522, Japan*

⁷*Department of Physics, Tohoku University, Sendai 980-8578, Japan*

⁸*Department of Physics, University of Tokyo, Tokyo 113-0033, Japan*

⁹*Department of Physics, Nagoya University, Nagoya 464-8602, Japan*

The FOREST/BLC experiments are conducted to reveal the non-perturbative QCD phenomena. The main objective at the first stage is to determine low-energy S -wave ηn scattering parameters using the $\gamma d \rightarrow p\eta n$ reaction. The photon beam with energies around 940 MeV can give the recoilless condition of η mesons by detecting the protons at 0° . The effects of the the final-state ηn interaction must be enhanced due to the small relative momentum between the η meson and the residual neutron in this kinematics. In this year, the physics data were collected from October 30 to December 2 in 2017. In this report, a brief summary of the first-stage FOREST/BLC experiment and collected data is described.

§1. Introduction

The nucleon resonance $N(1535)S_{11}$ (simply described N^* below), a candidate for the chiral partner of the nucleon N , is of particular importance. The interaction between an η meson and an N is important to study N^* since it strongly couples to ηN and lies near the ηN threshold. The low-energy ηN interaction is described using the scattering length $a_{\eta N}$ and effective range $r_{\eta N}$ in an effective-range expansion of the S -wave phase shift:

$$k \cot \delta(k) = \frac{1}{a_{\eta N}} + \frac{1}{2} r_{\eta N} k^2 + O(k^4). \quad (1)$$

The $a_{\eta N}$ values have been extracted using many theoretical analyses from the differential and total cross sections for the $\pi N \rightarrow \pi N$, $\pi N \rightarrow \eta N$, $\gamma N \rightarrow \pi N$, and $\gamma N \rightarrow \eta N$ reactions. Although the imaginary part of $a_{\eta N}$ ($\text{Im}[a_{\eta N}]$) concentrates ~ 0.26 fm for different analyses, its real part ($\text{Re}[a_{\eta N}]$) scatters in a wide range from 0.2 to 1.1 fm [1]. This uncertainty comes from the fact that the existing experimental

data do not include ηN scattering directly. We propose the $\gamma d \rightarrow \eta pn$ reaction to determine $a_{\eta N}$ at a certain kinematics, which enhances the ηN scattering effect.

The incident photon bombards the proton in the deuteron and produces a virtual η meson with a very low momentum. Events are selected in which the incident energy is approximately 0.94 GeV and the proton is detected at 0° . The kinematics for these events satisfies the recoilless condition of the produced η mesons. Thus, the ideal low-energy ηn scattering is expected to take place in this condition, where the pn and ηp rescattering effects are suppressed due to their large relative momenta (~ 0.94 GeV/ c). The sensitivity to the $\text{Re}[a_{\eta n}]$ and $\text{Re}[r_{\eta n}]$ values are investigated and summarized in Ref. [2] by using a dynamical coupled-channel model [3, 4].

§2. Experimental setup

The $\gamma d \rightarrow p\eta n$ reaction is measured at ELPH with the FOREST electromagnetic calorimeter system [5, 6] together with an additional forward charged-particle spectrometer [7]. Fig. ?? shows the experimental setup for the precise determination of $a_{\eta n}$. The incident photon energy ranges from 0.82 to 1.26 GeV [8] for the circulating electron energy of 1.32 GeV in the electron synchrotron [9]. The details of the FOREST detector including the liquid deuterium target is described elsewhere [5]. The forward scattered proton is momentum-analyzed with a bending magnet BLC (transported from the low-energy ring of KEKB) behind FOREST. The trajectory of a charged particle is measured with 2 planar drift chambers (DCs), and the time of flight is measured with 14 plastic scintillator (PS) hodoscopes (PSH+). An additional e/π separation is made using 10 SF5 lead-glass Cherenkov counters (LGCs). Fig. 1 shows the current experimental setup for the determination of $a_{\eta n}$ together with the geometry of the forward spectrometer, and the placement of the detectors. The detectors are rotated by 15.7° with respect to the photon beam direction so that ~ 900 -MeV/ c protons are injected perpendicularly on the surface of the two DCs.

In this year, the physics data were collected in the two periods from October 30 to November 20 (2017D) and November 23 to December 2 (2017E) in 2017. After commissioning in May 2017 [10], number of detectors for the forward spectrometer are increased. All the wires in the two DCs can be read out by fixing broken wires and increasing the number of RAINER boards from 6 to 10. The board includes the amplifier-shaper-discriminator and time-to-digital converter functions, and accepts 32-channel input signals. The number of active wires has become 272 from 175. Thanks to the dedicated detector frame, the number of PSs are increased from 9 to 14, and that of LGCs are increased from 6 to 10. In the 2017E period, a small hodoscope consisting of 16 3-mm-width PSs (originally used for STB Tagger [11]) is placed inside the BLC magnet to detect negative particles emitted at 0° . Accordingly, the circuitry is modified slightly.

In commissioning in May 2017, the power supply for BLC, QC1LE, halted many times, indicating the ground fault error, which was caused by the low resistance of cooling water together with the noise from the refrigerator for the cryogenic target. Ion-exchange resins are inserted in the cooling systems at the GeV- γ building. From October 2017, BLC can be excited at normal operation with a coil current

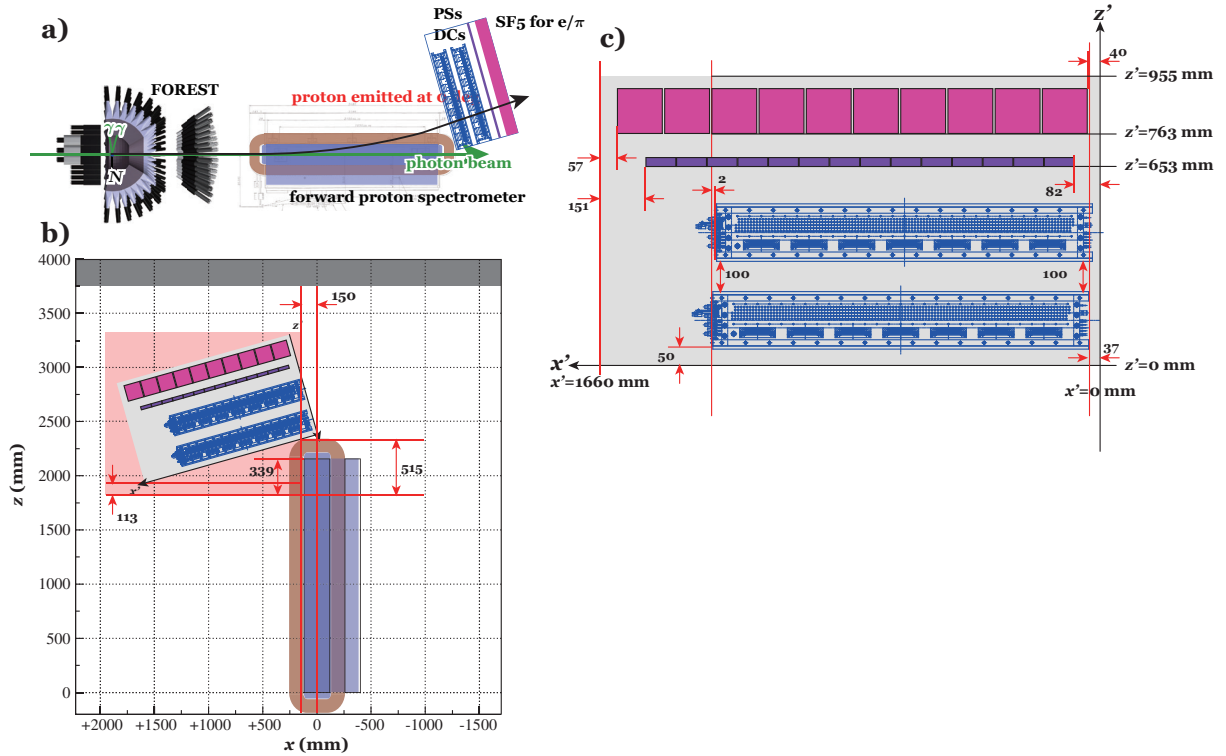


Fig.1. a) Experimental setup at ELPH for the determination of $a_{\eta n}$ (from October in 2017). The momentum and time of flight of the proton scattered at 0° are measured through a bending magnet. The forward emitted proton is momentum-analyzed with a bending magnet behind FOREST. The trajectory of a charged particle emitted at 0° is measured with two planar drift chambers, and the time of flight is measured with plastic scintillator hodoscopes. Additional e/π separation is made using SF5 lead-glass Cherenkov counters. b) Geometry of the forward spectrometer. The z axis is defined along the photon beam direction in this panel. c) Placement of the detectors. The z' axis is rotated by 15.7° with respect to the z axis.

of 1400 A. The magnetic flux B_y at the center was monitored with a nuclear magnetic resonance (NMR) probe during the experiments, and $B_y = 716.0$ mT was adjusted by changing the coil current. Fig. 2 shows the magnetic flux B_y at the center for the 2017D and 2017E periods.

Unfortunately, one of our high-voltage (HV) power supply systems, LeCroy 1440, was out of order. Many HV cables were rearranged within a newly introduced system, iSeg ECH 44A, and the other existing HV systems. Due to this trouble, we have some missing channels in the collected data in this fiscal year.

§3. Collected data

The physics data with the deuterium and hydrogen targets were collected in the 2017D period, and those with the hydrogen target were collected in the 2017E period. The BST ring was operated with a circulating energy of 1.3 GeV, a current of approximately 20 mA, and an RF frequency of 500.14 MHz. It should be noted that the frequency was 500.18 MHz before the 2011 earthquake. Table 1 summarizes the number of spills and events of the collected data in this fiscal year (2017). The statistics for the

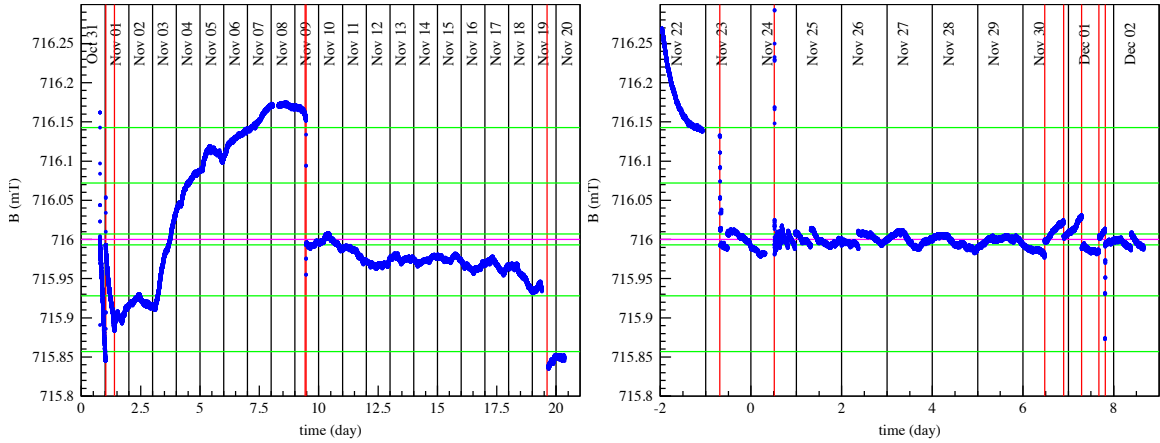


Fig.2. Magnetic flux B_y at the center for the 2017D (left) and 2017E (right) periods measured with an NMR probe. The horizontal solid lines correspond to the magnetic flux values increased by $\pm 0.001\%$, $\pm 0.01\%$, $\pm 0.02\%$ from the central value 716.00 mT.

hydrogen data is similar to that for the 2009D period, and that for the deuterium data is only a third. The data analysis is on-going to select coincidence events between the STB-Tagger II, FOREST, and BLC detectors

Table 1. Numbers of spills and events collected in this fiscal year (2017). The circulating electron energy of the BST ring was 1.3 GeV. The targets used were liquid hydrogen, deuterium, and empty.

period	hydrogen		deuterium		empty	
	#spills	#events	#spills	#events	#spills	#events
2017D	46.26 k	397.30 M	31.95 k	309.83 M	3.91 k	19.84 M
2017E	26.42 k	198.36 M	—	—	10.05 k	49.74 M

§4. Summary

The first-stage FOREST/BLC experiment, aiming at the determination of the low-energy ηN scattering parameters $\text{Re}[a_{\eta N}]$ and $\text{Re}[r_{\eta N}]$, started from October 30 in 2017. The number of collected events for the deuterium target is 0.3 G. We continue to collect data in a few years to determine $\text{Re}[a_{\eta N}]$ with an accuracy of 0.1 fm.

Acknowledgments

The authors give thanks to the ELPH accelerator staff for their great efforts in the stable operation of the electron synchrotron. They deeply acknowledge S.X. Nakamura and H. Kamano for giving us the predictions for the ηn rescattering effect in the proposed $\gamma d \rightarrow p\eta n$ experiment. This work was supported in part by Grants-in-Aid for Scientific Research (A) (24244022), for Scientific Research (C) (26400287), and for Scientific Research (A) (16H02188).

References

- [1] Q. Haider and L.C. Liu: *Int. J. Mod. Phys. E* **24**, 1530009 (2015);
and references therein.
- [2] S.X. Nakamura, H. Kamano, and T. Ishikawa: *Phys. Rev. C* **96**, 042201 (R) (2017).
- [3] A. Matsuyama, T. Sato, T.-S.H. Lee: *Phys. Rep.* **439**, 193 (2007).
- [4] H. Kamano *et al.*: *Phys. Rev. C* **88**, 035209 (2013).
- [5] T. Ishikawa *et al.*: *Nucl. Instrum. and Meth. A* **832**, 108 (2016).
- [6] T. Ishikawa *et al.*: *Phys. Lett. B* **772**, 398 (2017);
T. Ishikawa *et al.*: *PoS (INPC2016)* 267;
T. Ishikawa *et al.*: *PoS (Hadron2013)* 095.
- [7] T. Ishikawa *et al.*: *Acta. Phys. Polon. B* **48**, 1801 (2017);
T. Ishikawa *et al.*: *JPS Conf. Proc.* **13**, 020031 (2017);
T. Ishikawa *et al.*: *JPS Conf. Proc.* **10**, 031001 (2016).
- [8] T. Ishikawa *et al.*: *Nucl. Instrum. and Meth. A* **622**, 1 (2010);
T. Ishikawa *et al.*: *Nucl. Instrum. and Meth. A* **811**, 124 (2016);
Y. Matsumura, T. Ishikawa *et al.*: *Nucl. Instrum. and Meth. A* **902**, 103 (2018).
- [9] F. Hinode *et al.*: *J. Phys. Conf. Ser.* **425**, 072011 (2013).
- [10] T. Ishikawa *et al.*: *ELPH Annual report 2016*, 11 (2017).
- [11] H. Yamazaki *et al.*: *Nucl. Instrum. Meth. A* **536**, 70 (2005).

(ELPH Experiment : #2838 and #2858)

Performance evaluation of Aerogel Cherenkov Counter with a refractive index of 1.10 for the Σp scattering experiment at J-PARC

Kazuya Kobayashi¹, Koji Miwa², Ryotaro Honda^{1*}, Yuya Akazawa²,
 Michihiko Ikeda², Shotaro Ozawa², Norina Fujioka², Atsushi Sakaguchi¹,
 Yoshiyuki Nakada^{1,4}, Hideyuki Kawai³, Makoto Tabata³, Hiroshi Ito³,
 Atsushi Kobayashi³, Naomi Kaneko³, Takayuki Mizuno³, Takaya Akaishi¹,
 Kotaro Shirotori⁵, Mitsuhide Asano⁵, Sakiko Ashikaga⁶, Masaya Ichikawa⁶,
 Megumi Naruki⁶, Tomonori Takahashi⁵, Kyoichiro Ozawa⁸,
 and Michiko Sekimoto⁷

¹*Department of Physics, Osaka University, Toyonaka, 560-0043*

²*Department of Physics, Tohoku University, Sendai, 980-8578*

³*Department of Physics, Chiba University, Chiba, 263-8522*

⁴*Japan Atomic Energy Agency (JAEA), Tokai, 319-1184*

⁵*Research Center for Nuclear Physics (RCNP), Osaka University, Suita, 567-0047*

⁶*Department of Physics, Kyoto University, Kyoto, 606-8502*

⁷*RIKEN, wako, 351-0198*

⁸*High energy Accelerator Research Organization (KEK), Tsukuba, 305-0801*

We developed an Aerogel Cherenkov Counter (AC) with an index of 1.10 for a Σp scattering experiment at J-PARC which was used to veto π particles of momentum range up to 1.4 GeV/c. The size of AC was 480 (H) \times 400 (V) \times 80 (T) mm³ which was determined from a geometrical condition of a magnetic spectrometer (KURAMA spectrometer). In order to obtain detection efficiency more than 98%, we selected radiator index of 1.10 which was rather high index as an Aerogel and totally 12 fine-mesh PMTs were used to collect enough photons. The other requirement is that this AC should keep the efficiency under the high single rate condition up to 300 kHz which is the expected value in the Σp scattering experiment. From the performance test experiment at ELPH, the mean photon electron number was obtained to be 23 for e^+ beam of 400 MeV. The efficiency was obtained to be 98% for 300 kHz beam rate by setting the threshold to be 3 photo electron.

§1. Introduction

One of the most important purposes of strange nuclear physics is to investigate the Baryon Baryon (BB) interaction. This is because the BB interaction is the basic interaction to describe a system including hyperons such as hypernuclei and high density matter in neutron stars. The understanding of the BB interaction also becomes a key to understand the origin of the short range repulsive cores in nuclear

*Present address: Department of Physics, Tohoku University, Sendai, 980-8578

force and the BB interaction. In order to investigate ΣN interaction, we proposed a Σp scattering experiment (J-PARC E40) to measure differential cross sections of the $\Sigma^+ p, \Sigma^- p$ elastic scatterings and the $\Sigma^- p \rightarrow \Lambda n$ inelastic scattering in the momentum range of $400 < p \text{ (MeV/c)} < 700$. The physics motivation is to verify the large repulsive force due to Pauli effect in the quark level in the $\Sigma^+ p$ channel. We also investigate the ΣN interaction systematically by separating isospin channels.

In the experiment, we detect two successive reactions of the Σ production by the $\pi p \rightarrow K^+ \Sigma$ reaction and the Σp scattering with magnetic spectrometers (the KURAMA spectrometer) and recoiled proton detector (CATCH), respectively. Figure 1 shows the experimental setup of the E40 experiment. One of the experimental key points is that we have to accumulate more than 10^7 Σ particles, to determine the differential cross section by detecting more than 10,000 scattering events. The KURAMA spectrometer is a suitable spectrometer because it has large acceptances of 4% and 7% for Σ^- and Σ^+ , respectively, and has a quite short flight length of ~ 3 m to keep a survival rate of K^+ . However, in order to perform experiment within a reasonable beam time of a few weeks, a high intensity π beams of 20 M/spill (1 spill is 2 seconds beam duration with 6 seconds cycle) should be used. In order to accumulate Σ particles effectively with 20 M/spill π beam particles, the trigger system is quite important. Especially, outgoing π particles can make dummy triggers. From the spatial constraint, an AC counter should be placed between the yoke and the end guard of the KURAMA magnet where the fringing magnetic field of 0.4 T is expected with magnetic field excitation of 0.75 T. In order to keep a reasonable trigger rate less than 10 k/spill, the AC counter is required to have an efficiency more than 97%. In order to satisfy such requirements, we developed AC counters with an index of 1.10. In this development process, we take a two-step way. In the first step, we optimized the transparency of the AC radiator and the reflection method, that is, mirror reflection or diffuse reflection with a small prototype detector. After the optimization, we developed the actual AC counter. At each stage, the performances of the detectors were checked with a positron beam in the test beam line at Research Center for Electron Photon Science (ELPH), Tohoku university.

In this annual report, we report the result of the performance check of the AC counters.

§2. Design of AC counter

The basic design of the AC counter was determined from the spatial condition. The AC counter should be installed between DC1 and SCH as shown in Fig. 1. The thickness of the AC counter was limited to be less than 80 cm. The horizontal and vertical sizes were determined to be 480 mm (H) \times 400 mm (V) to cover the hit profile of charged particles at the AC position. Fig. 2 shows the design of the AC counter. The orange ellipse in Fig. 2 shows the rough beam envelope. Because the beam intensity is 20 MHz/spill (10 MHz) and the AC detector can not work under such high intensity, the AC was designed to have a beam hole not to cover the beam region. However, the expected singles rate was still as high as ~ 900 kHz in total. Therefore we divided the AC counter into four rooms which were also shown in Fig. 2. The room1 and room2 are the same structure and these rooms are placed at the upper and lower sides of the beam region. These rooms are read with a single PMT. The room 3 are placed at right side

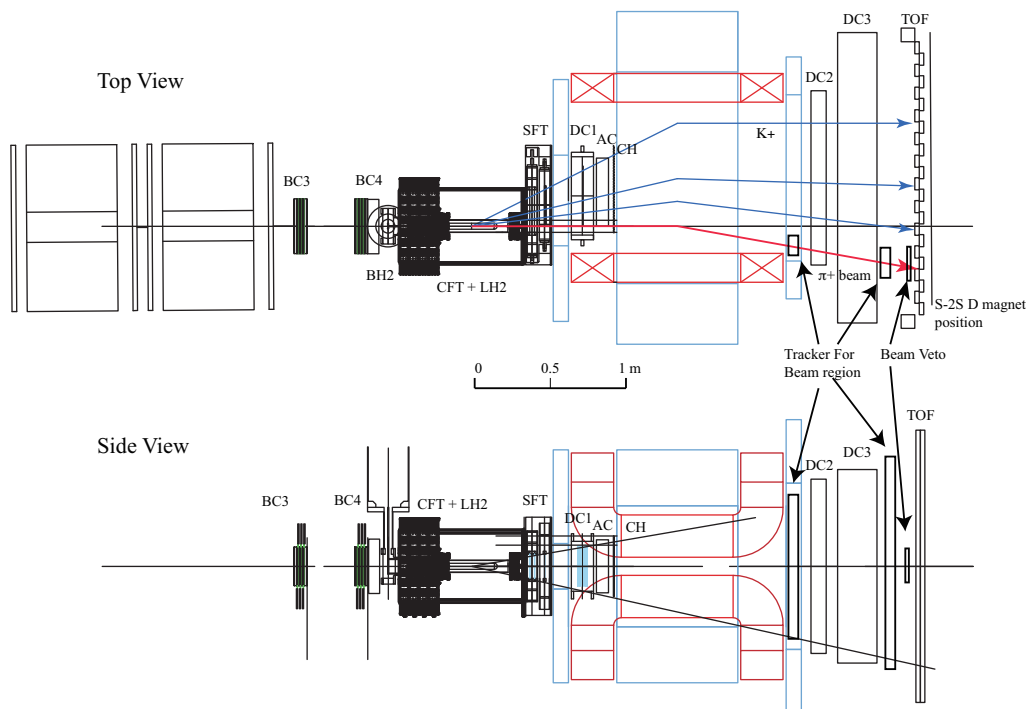


Fig. 1. Experimental setup of the E40 experiment. Both horizontal and vertical views are shown. The AC counter is shown as AC which is sandwiched by DC1 and CH. The size of AC is determined to have enough acceptance for the charged particle at this position

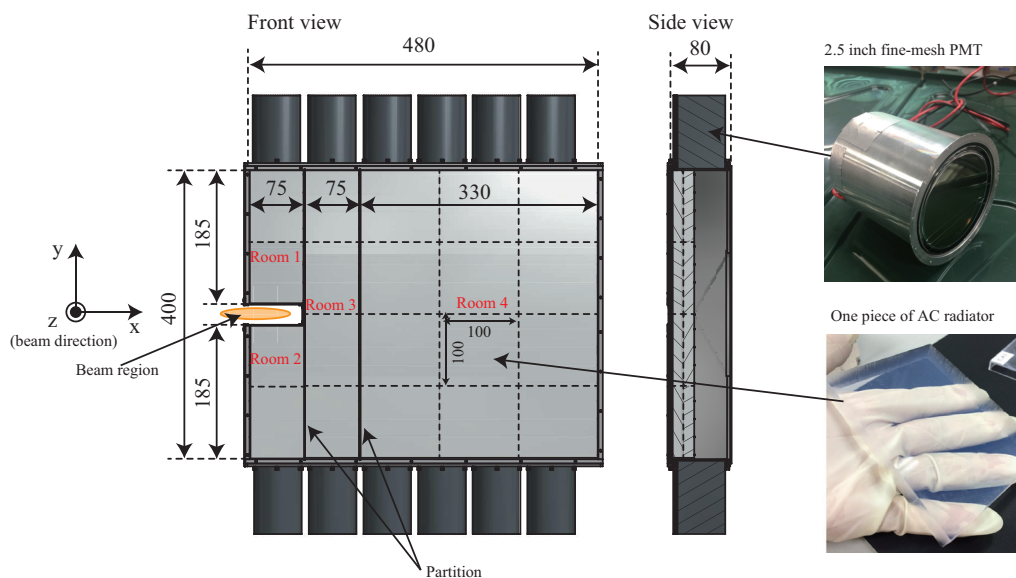


Fig. 2. Realistic drawing of the AC counter. The orange ellipse shows the rough beam envelope. The AC counter is divided to 4 rooms to reduce the single rate for each room. The index of the aerogel is 1.10 and 12 fine-mesh PMTs are used to readout photons from the aerogel radiators.

of the beam region and two PMTs are attached at top and bottom side of the room. The room 4 is the farthest from the beam region and has a large region because the singles rate is much lower. The singles rates for each room are 300 kHz for room 1, 2 and 250 kHz and 40 kHz for room 3 and 4, respectively.

Photons from radiator are collected by 12 fine-mesh PMTs with a diameter of 2.5 inch which were used in the Belle experiment.

We ask Chiba university group to make an aerogel radiator. They have a skill to make aerogels with a large refraction index more than 1.05 which is the largest index commercially available. They can also make a high transparency type of radiator in addition to a normal transparency type [1] [2]. In order to maximize the photon number, we performed a simulation study with GEANT4 by changing the index of radiator and its transparency type. We also studied by changing the thickness of the radiator to optimize the ratio between the radiator thickness and the air region. For example, if the radiator thickness is 30 mm, the air region thickness is 50 mm, because the total length is 80 mm. We also compared the photon numbers for two reflection types, that is, mirror reflection and diffuse reflection. In this simulation, we took into account the scattering length of the radiator, the quantum efficiency of PMT and reflectivity of the reflector and so on. On the other hand, we could not measure the absorption length of the aerogel which was necessary in the simulation. In this simulation, we used a scaled value of the scattering length with a factor of 10 conservatively. Figure 3 shows the dependence of the obtained mean photon number by changing the refraction index ($n=1.06\sim 1.10$), the transparency type and the thickness of the air region, that is, thickness of the radiator. As expected, the larger photon numbers were obtained for the high transparency type compared to the normal transparency type. As for the dependence of the radiator and air thickness, there were two trends. For the lower index such as $n=1.06$, the dependence for the radiator and air thicknesses was small and the maximum photon number was obtained for the air thickness of 30 mm and the radiator thickness of 50 mm. In the lower index radiator, the photon number emitted in unit length was smaller. Therefore the long thickness of the radiator was necessary. The scattering length and the absorption length were relatively longer and the effect of the absorption or scattering of the photon in the radiator was relatively small. From these two factors, the maximum photon was obtained in this condition for $n=1.06$. On the other hand, for the higher index such as $n=1.10$, the maximum photon number was obtained for the air thickness of 50 mm and the radiator thickness of 30 mm. In this index, the photon number emitted in unit length was larger and the scattering and absorption lengths were relatively short. The effect of the absorption or scattering of the photon in the radiator was relatively large. Therefore, the maximum photon number was obtained in this condition, that is, smaller radiator thickness of 30 mm and the larger air thickness of 50 mm. In the middle index such as $n=1.08$, the obtained photon number was minimum. This reason could be also understood from these two factors. The photon number was still relatively small and the scattering length was also relatively short. Therefore the obtained photon number was small. From these studies, we decided to use the radiator of $n=1.10$ and the configuration of the radiator and air thicknesses was determined to be 30 mm and 50 mm, respectively. As for the transparency type, the clear type is expected to be much better. However, the uncertainty of the absorption length is large. Therefore this should be checked with a beam. We also studied the reflection type between the mirror reflection and the diffuse reflection with a teflon. The maximum photon was obtained for the mirror reflection with the mirror plate at the center region of the AC counter. The mirror plate angle was optimized to maximize the photon yield and was

determined to be 60 degrees where the emitted photon could arrive at PMT with the single reflection at this mirror. Finally, we determined the design of the AC counter as shown in Figure 2. Cotton strings are placed at the back side of the radiators to prevent the radiators from falling down to the air region.

In order to finalize the AC counter, at first, we constructed two prototype counters corresponding to room 1, 2 with a mirror reflection and diffused reflection to compare these performances. Then we performed a test experiment using a positron beam at ELPH.

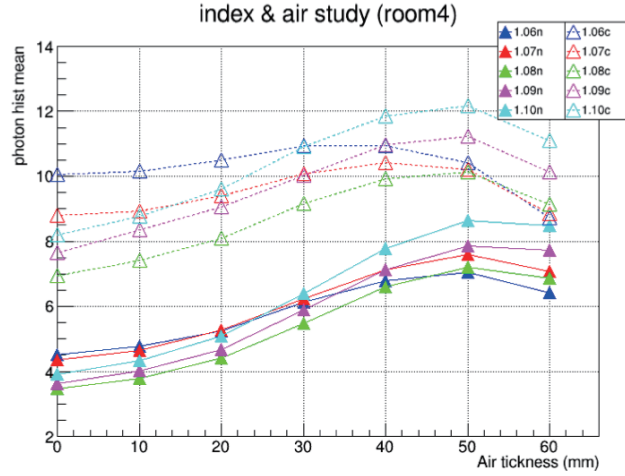


Fig.3. Air thickness (aerogel thickness) dependence for photo-electron yield from a Geant4 simulation. The aerogel thickness is expressed as "80 mm – (Air thickness)". The open triangle points show the results for the high transparency type.

§3. Performance test of the prototype counters

3.1 Prototype counters

We constructed the prototype counters with the same structure with room1, 2 which size of the prototype counter was $75 \text{ (H)} \times 185 \text{ (V)} \times 80 \text{ (T)} \text{ mm}^3$. One PMT was attached at the top of the counter. In order to compare the performance for different reflection method, we fabricated one AC counter with the mirror reflection (AC1) and one AC counter with the diffused reflection (AC2).

- AC1 (mirror reflection)

AC1 has a mirror reflection. As for the reflector we selected the MetalumyTM sheet which was measured to have a larger reflectance with a thin sheet from previous research [3]. A reflection mirror with a tilt angle of 60 degrees was set to guide the Cherenkov radiated photon to PMT with a single reflection. The tilt angle was optimized for 1.3 GeV/c π^- beam. The two MetalumyTM sheets with 25 μm were pasted on the inner surface of the detector frame and the inserted reflection mirror. The aerogel radiator was supported with cotton strings at the downstream side. In order to calibrate the PMT's gain, one optical fiber was inserted into the detector frame though a hole. The optical fiber was connected to LED and could provide photons inside the detector.

- AC2 (diffused reflection)

The structure of AC2 is the almost same with AC1. In AC2, the reflection mirror is not mounted because AC2 has a diffused reflector. The three sheets of Teflon with $80 \mu\text{m}$ thickness were pasted inner surface of the counter frame. Because AC2 has no additional structure such as the reflection mirror in AC1, it is suitable to check the radiator's thickness dependence on the photon yield. We originally prepared the support cotton string's holes corresponding to 15, 30, 45 and 60 mm, respectively, on the side frame. The optical fiber for the PMT's calibration is also mounted to the frame.



Fig.4. Photograph showing the insides of the detector frames of AC1 (right, mirror reflection) and AC2 (left, diffused reflection)

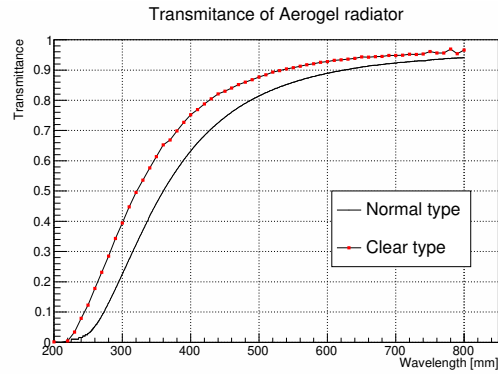


Fig.5. Transmittance of the aerogel radiator of $n = 1.10$. The black and red points represent the transmittances for the normal and high transparency types, respectively.

Fig. 4 shows a photograph of the insides of the detector frames for AC1 and AC2.

3.2 Aerogel radiator of $n = 1.10$

In this prototype, we checked the effect of the transparency type. Fig. 5 shows the measured transmittance of the aerogel radiator with $n = 1.10$ for both normal and clear types. The typical transmission lengths are 20 mm and 40 mm at the wavelength of 400 nm for the normal and clear types, respectively. The advantage of the clear type is that much larger photon yield is expected to minimize the absorption of the radiated photon in the aerogel radiator thanks to its longer transmission length. However, the extraction rate of the clear type is lower than that of the normal type due to the difficulties at the production process. Therefore, we decided to finalize the transparency type after checking performance for both types in the beam experiment. The maximum available size of the aerogel radiator was $100 \times 100 \times 15 \text{ mm}^3$. For this prototype counter, we prepared two sets of radiator tile of $75 \times 100 \times 15 \text{ mm}^3$ and $75 \times 85 \times 15 \text{ mm}^3$. In order to minimize the ineffective area at the gap between two tiles, the tiles were placed with a staggered manner to the beam direction as shown in Fig. 6 in the next subsection.

3.3 Performance test experiment with a positron beam

We performed a test experiment of this prototype detector using a positron beam in the GeV- γ test beam line at ELPH in June 2016. The momentum of the positron beam was set to be 580 MeV/c. The purpose of this experiment was to determine the optimal condition for AC counter by changing some

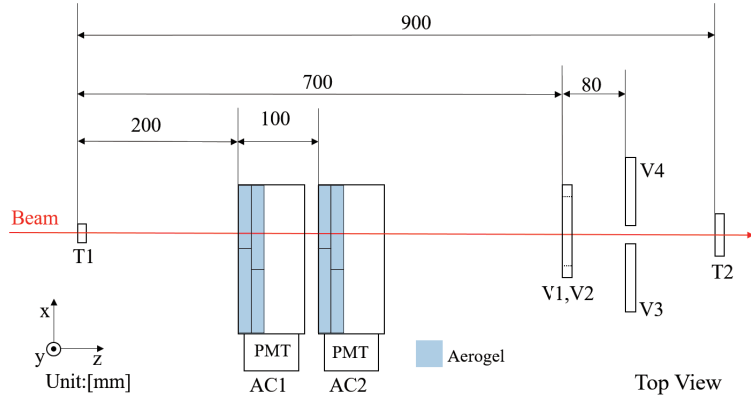


Fig. 6. Detector setup in this test experiment. T1 and T2 are the beam defining counters. V1, V2, V3 and V4 are placed to veto the e^+e^- shower event. AC1 and AC2 are the AC counters with the mirror reflection and diffused reflection, respectively. The aerogel tiles are put with a staggered manner.

parameters, such as reflection type, radiator transparent type and its thickness and so on. Then for the optimal condition, we checked the position and beam direction dependences for the photon yield. The beam rate dependence for the detection efficiency was also measured up to 150 kHz to check the detector performance at the higher singles rate condition.

Fig. 6 show the experimental setup. In order to define the positron beam, we installed two plastic scintillation counters (T1, T2) at the upstream and the downstream of the beam line. AC1 with the mirror reflection and AC2 with the diffused reflection were installed between T1 and T2 counter. In order to veto the e^+e^- shower events, four plastic scintillation counters (V1, V2, V3 and V4) were placed at the downstream of AC2. V3 and V4 were placed apart from the beam center horizontally as shown in Fig. 6. V1 and V2 were placed vertically with the same manner. The experimental trigger was the coincidence between T1 and T2. The four veto counters were used in the offline analysis to requesting no hit on these counters. The charge and time information were digitized with a QDC module (CAEN V792) and a TDC module (CAEN V775), respectively.

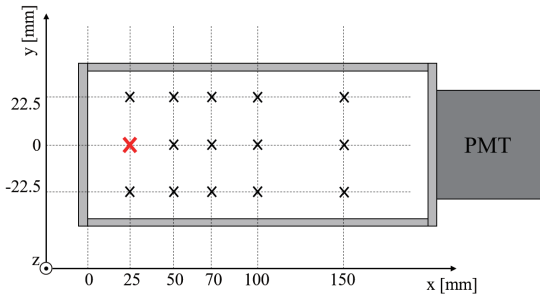


Fig. 7. Coordinate plane at each AC detector. The cross points show the beam position at the study of the position dependence. The red point is the reference point of this study.

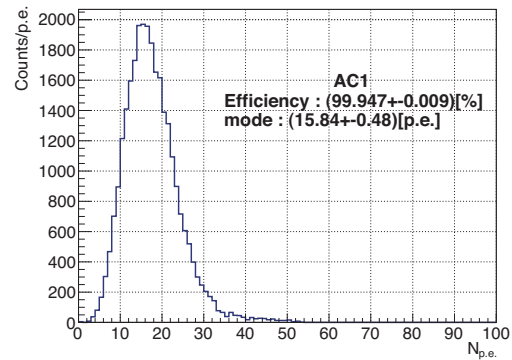


Fig. 8. Obtained photo-electron (p.e.) distribution for AC1 with a clear type radiator of 30 cm thickness.

Fig. 7 shows the coordinate plane at each AC detector. The cross points show the beam position at the study of the position dependence. The red cross point of $(x, y) = (25, 0)$ is the reference point of the study. For other studies such as the radiator thickness study, beam was irradiated to this reference point. Fig. 8 shows the obtained photo-electron (p.e.) distribution for AC1 with a clear type radiator of 30 cm thickness. The p.e. number was derived by using the coefficient from ADC to p.e. which is evaluated from the LED system. In the following analysis, we used the most probable value of p.e. distribution and the efficiency as the criteria of the performance check. The efficiency was defined as

$$efficiency = \frac{N_{AC}}{N_{Beam}}. \quad (1)$$

N_{Beam} was the number of event samples where T1 and T2 counters had correct timing in TDC spectra and four veto counters (V1, V2, V3 and V4) had no hit. N_{AC} was the number of hit of AC where we requested the p.e. number should be larger than the software threshold of 3 p.e., because the hardware threshold was rather low value of ~ 0.5 p.e. and the accidental hit due to the dark current could be triggered.

3.3.1 Radiator thickness dependence

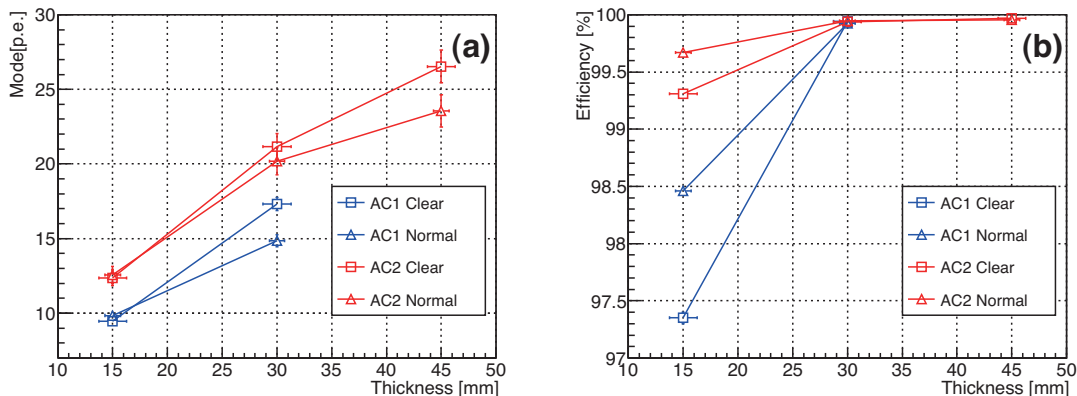


Fig.9. Radiator thickness dependence for the p.e. yield (a) and efficiency (b). The blue and red points show the results for AC1 (mirror reflection) and AC2 (diffused reflection), respectively. The square and triangle show the clear and normal transparency types, respectively.

At first, we checked the radiator thickness dependence for the most probable value of the p.e. number and the efficiency. The beam position was the reference position in Fig. 7 and the beam rate was 1.5 kHz. Fig. 9 (a) shows the radiator thickness dependence for the p.e. yield for all combinations of the transparent type (Clear and Normal) and the reflection method (mirror reflection : AC1 and diffused reflection : AC2). When we compared the reflection method, larger p.e. yield was obtained for the diffused reflection type (AC2). The p.e. yield increased with the radiator thickness but the p.e. number was not linear with the thickness and saturated at the larger thickness due to absorption in the radiator. However, the clear type kept much better linearity with the thickness thanks to the better transmittance. The most important point was that the sufficient p.e. yield more than 20 p.e. could be obtained even for

the normal transparent type with 30 mm thickness. Fig. 9 (b) shows the radiator thickness dependence for the efficiency. By using the radiator thickness more than 30 mm, the efficiency of 99.9% was obtained for all combinations. From these results, we concluded that the aerogel radiator with the normal transparent type was the best candidate considering the extraction rate at the production process.

3.3.2 Position dependence

Table 1. Summary of the basic operation conditions for AC1 and AC2.

	AC1	AC2
Reflection type	Mirror reflection	Diffused reflection
Aerogel type	Clear type	Normal type
Aerogel thickness	30 mm	30 mm
PMT operation voltage	1.8 kV	1.8 kV
ADC value (Charge) for 1 p.e.	74.8 ch (7.5 pC)	38.4 ch (3.8 pC)
Discriminator threshold	20 mV	20 mV

From here, we studied the other dependencies such as the position dependence and so on. These points depend not only the reflection method but also the transparency type of the radiator. However, because there was no large difference between two transparency types when the thickness was 30 mm, we installed the clear type radiator and the normal type radiator into the AC1's frame (mirror reflection) and the AC2's frame (diffused reflection), respectively. The basic operation conditions of two AC counters are summarized in Table 1 .

The position dependences of the AC detectors were studied by changing the beam position to totally 15 points as shown by cross points in Fig. 7. Fig. 10 (a) shows the position dependencies of the most probable value of the p.e. yield for AC1 (blue points) and AC2 (red points). In AC2 with the diffused reflection, the p.e. yield increased depending on the distance between PMT and beam position (photon source point), that is, when the distance is short, the p.e. number is large. On the other hand, in AC1 with the mirror reflection, the p.e. number reached the minimum at $x = 100$ mm, where was the cross point between the tilted mirror and the downstream detector frame. In the mirror reflection, the unwanted position dependence could appear and this also caused the loss of the efficiency as shown in Fig. 10 (b). The diffused reflection type was much better to obtain the uniformly high efficiency.

3.3.3 Angular dependence

In the E40 experiment, the charged particle enters the AC counter with some angles up to 30 degrees. The angular dependence was also studied. Fig. 11 shows the results on the angular dependence, where the y position was fixed to be 0 and the x position was changed to 4 points from 25 mm to 100 mm. At each beam position, the detector was placed with the tilt angle from 0 degree to 30 degrees for the beam direction. Because the pass length in the radiator increased with the angle, the Cherenkov radiated photons also increased. In AC2, as expected, the obtained p.e. number increased with the angle for all x positions. On the other hand, in AC1, the angular dependence was different at the x position

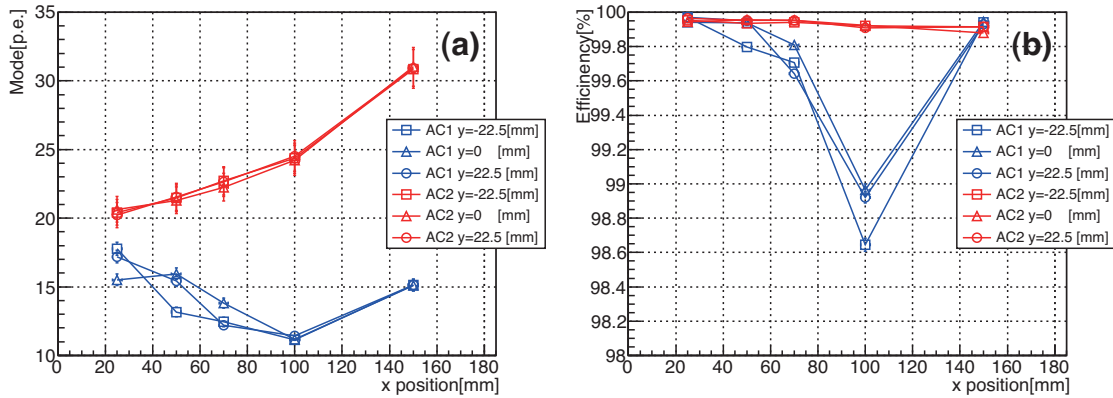


Fig.10. Position dependence for the p.e. yield (a) and efficiency (b). The blue and red points show the results for AC1 (mirror reflection) and AC2 (diffused reflection), respectively. The square, triangle and circle show the results at $y=-22.5$ mm, 0 mm and 22.5 mm, respectively.

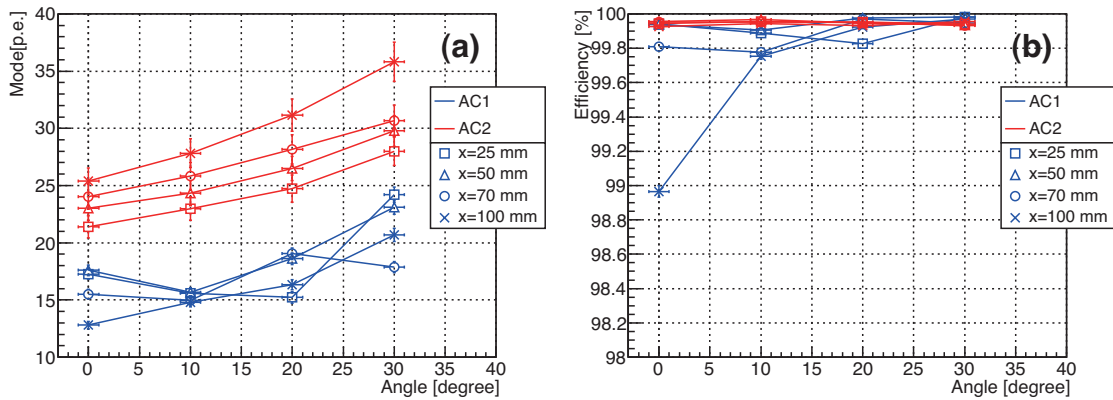


Fig.11. Angular dependence for the p.e. yield (a) and efficiency (b). The blue and red points show the results for AC1 (mirror reflection) and AC2 (diffused reflection), respectively. The square, triangle, circle and cross show the results at $x=25$ mm, 50 mm, 75 mm and 100 mm, respectively.

due to the angular dependence of the photon collection ratio.

3.3.4 Beam rate dependence

In the E40 experiment, high singles rate of ~ 300 kHz is expected for the AC counter. In this test experiment, the beam rate dependence was also studied by increasing the beam intensity up to 150 kHz which was the maximum beam intensity at this experiment. The beam position was the reference point as shown by red cross point in Fig. 7. Fig. 12 shows the pulse height ratio (a) and the efficiency (b) in the standard operation condition where PMT's HV was 1.8 kV for both AC1 and AC2. As can be seen in Fig. 12 (a) where the ratio of the mean p.e. number for the reference value at 1.5 kHz beam intensity is shown, the pulse height decreased with the increase of the beam intensity due to the increase of the dynode current at the last stage in PMT. Because the PMT in AC1 has a larger gain even for the same

operation voltage, the ratio dropped rapidly with the beam intensity. The efficiency also decreased with the beam intensity and could not keep the 99% efficiency even for 80 kHz. In this PMT type, the potential voltage for the final stage of the dynode can not be load from the outside. Therefore, in order to reduce the load current in the dynode, we decreased the operation HV down to 1.3 kV. Fig. 13 (a) shows the ratio of the mean p.e. number for each operation voltage at the beam intensity of 150 kHz. In order to compare with the reference data at HV = 1.8 kV and beam intensity of 1.5 kHz, the mean p.e. number was compared by measuring the ADC value for 1 p.e. for each operation voltage. From this study, the original p.e. yield can be recovered by setting the lower operation voltage around 1.4 kV. The efficiency more than 98% could be kept at high single rate condition of 150 kHz by setting the lower HV value.

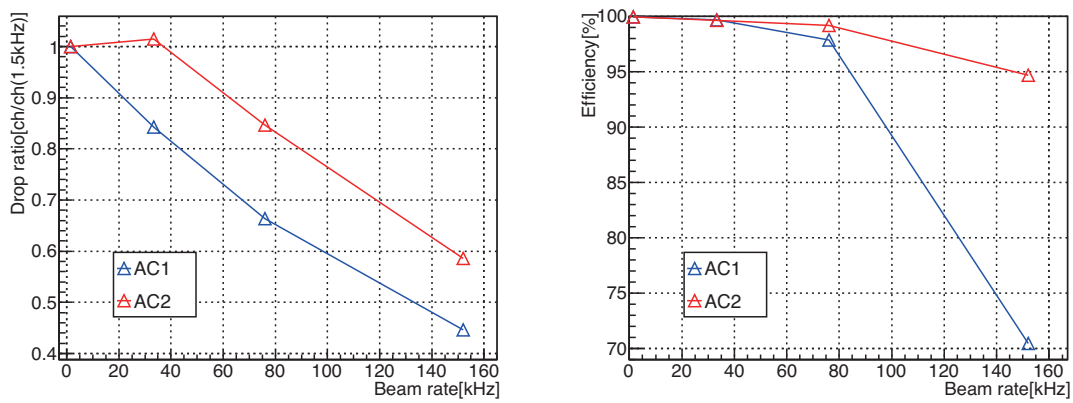


Fig.12. Beam rate dependence for the pulse height ratio (a) and efficiency (b) at the standard operation condition in Table 1. The blue and red points show the results for AC1 (mirror reflection) and AC2 (diffused reflection), respectively.

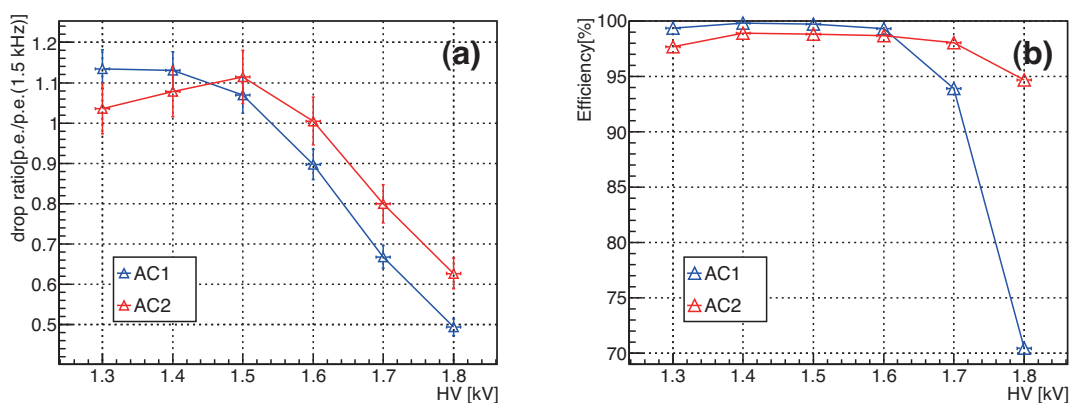


Fig.13. Operation HV dependence for the mean p.e. number's ratio (a) and efficiency (b) at the beam intensity of 150 kHz. The blue and red points show the results for AC1 (mirror reflection) and AC2 (diffused reflection), respectively.

3.3.5 summary and discussion in the test experiment

From this test experiment, we could obtain three important results. The first result was that the aerogel radiator of $n = 1.10$ emitted a large number of Cherenkov radiated photons and the sufficient p.e. number of ~ 20 could be obtained even for the normal transparency type. We decided to use the aerogel radiator with the normal transparent type for the actual AC counter by considering the extraction rate at the production process. The second result was that the diffused reflection was superior for all study points, that is, the p.e. yield, the position dependence and the angular dependence. Finally, PMTs should be operated at the low HV value to prevent from dropping the gain at the high dynode current condition. In the lower HV operation, the pulse height becomes smaller. To compensate the lower gain in PMT, the PMT signal is again amplified with the electric circuit in the actual AC counter.

3.3.6 Optimization of the parameters in the Geant4 simulation

The optical simulation in Geant4 is the one of the most powerful tools to estimate the performance of the optical detector such as the Cherenkov detector. However, there are some parameters to be determined to get a realistic simulation result. As shown in Fig. 2, we performed the Geant4 simulation before the test experiment. In this simulation, there were many uncertainties in these parameters. Here, we adjusted these parameters such as the absorption length in the aerogel radiator by comparing the simulation result with the experimental result. It might be worth describing how to determine these parameters to apply the simulation to other detectors.

- Parameters for PMT

The quantum efficiency of the photo cathode was measured by Hamamatsu Photonics and the values were used in the simulation.

The response function for 1 p.e. in the fine-mesh is not straight forward because some portion of the photo-electron does not hit the mesh-type dynode and move to next dynode stage without any amplification. The response of the fine-mesh PMT was studied in the past research [4] and we also followed the simulation method. Fig. 14 shows the flow chart of this simulation. The probability that the photo-electron does not hit the single dynode mesh is obtained to be 40% from the reference [4]. When the photo-electron does not hit the dynode, the gain is one. On the other hand, when the photo-electron hits the dynode, it could be absorbed in the dynode with some probabilities depending on the hit position on the dynode mesh. If the photo-electron hit near the center of the wire of the mesh, it could be easily absorbed. This absorption probability was set to be 10% from the reference. When the photo-electron is not absorbed, the amplification factor is obeyed by the Poisson distribution with the mean value of M which should be determined by minimizing the difference between the simulation result and the experimental result. The number of the dynode stage of the PMT was 19 and the simulation should be performed for all 19 dynode stages. However, it is already studied from the reference that a reasonable simulation result can be obtained by continuing for 6 dynode stages. In our simulation, we also performed for 6 dynode stages. Fig. 15 shows the QDC spectrum for small photon input from LED and reproduced simulation result. The amplification factor M was obtained to be 3.5 by minimizing the

reduced χ^2 value between these two histograms. The simulated spectrum could be reproduced well with the minimum reduced χ^2 of 2.

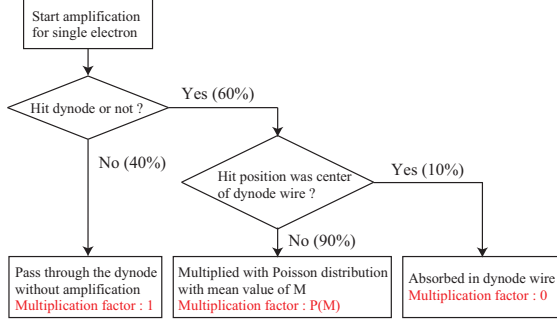


Fig.14. Flow chart in the simulation to estimate the response function for 1 p.e. in the fine-mesh PMT.

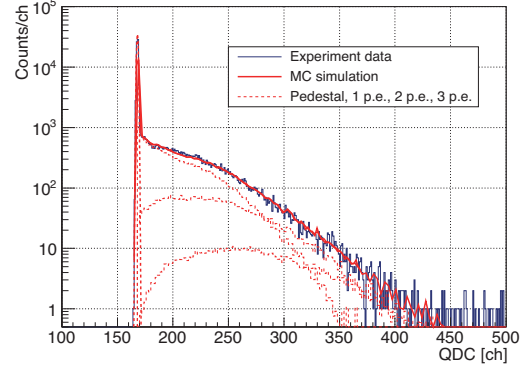


Fig.15. Comparison between the QCD spectrum for small photon input from LED and reproduced simulation result.

- Parameters for the aerogel radiator

The parameters related to the aerogel radiator are refractive index, scattering length and absorption length.

The refractive index, in general, has a wavelength dependence as studied in other references [5] [6]. In our study, we used one pole model to take into account the wavelength dependence. In this model, the refractive index $n(\lambda)$, where λ is the wavelength of incident photon, is represented by the following equation,

$$n(\lambda)^2 - 1 = \frac{a_0 \lambda^2}{\lambda^2 - \lambda_0^2}. \quad (2)$$

The parameter a_0 is the coefficient proportional to the density and λ_0 is a constant value and is set to 90 nm from the reference. In our aerogel radiator, the refractive index was measured to be 1.10 for a wavelength of 405 nm. Therefore the a_0 value can be obtained. In our simulation, this wavelength dependence was taken into account for the refractive index.

The scattering length (L_{scat}) can be calculated from the measured transmittance (T) with the following equation,

$$L_{scat} = -\frac{t}{\ln T}, \quad (3)$$

where t is the thickness of the radiator when transmittance T is measured. Strictly speaking, the transmittance is determined by both two effects of scattering and absorption. However, in case of aerogel, the absorption length is much longer than the scattering length and its effect for transmittance is negligibly small. Fig. 16 shows the measured scattering length for our aerogel radiator. We used this information in the simulation.

The absorption length is the most difficult parameter to estimate. We also estimated the absorption length from the test results. In this simulation, we assumed that the absorption length has the same

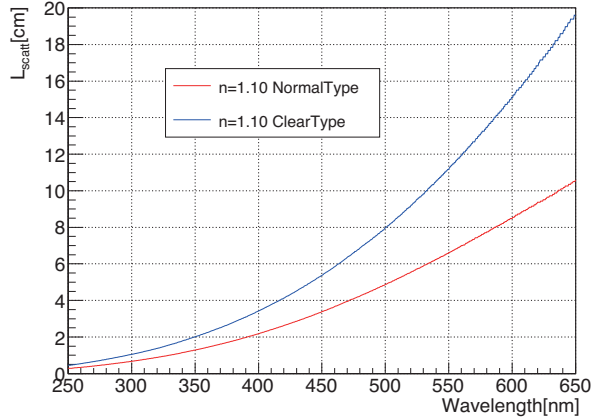


Fig.16. Measured scattering lengths of our aerogel radiators for the normal type (red) and the clear type (blue).

wavelength dependence with the scattering length and the absorption length $L_{abs}(\lambda)$ is represented by the following relation,

$$L_{abs}(\lambda) = Abs \times L_{scat}(\lambda). \quad (4)$$

The coefficient Abs should be derived with inductive approach by reproducing the p.e. distribution data with the simulation result. As will be mentioned later, the Abs value was obtained to be 102.5 by searching for the minimum reduced χ^2 value between the experimental data and the simulation.

- Comparison with the experimental data and the simulation

By taking into all points discussed above, the Geant4 simulation for the prototype detectors was performed again. Fig. 17 shows the comparison between the experimental data of AC2, where the aerogel radiator was the normal type with 30 cm thickness and the reflection type was the diffused reflection, and its simulation result. In order to check the reproducibility for other conditions, the data of radiator thickness study were also compared with the simulations as shown in Fig. 18

The simulation could reproduce data rather well, though there was still room to be improved. However, reproducibility with this level is quite satisfactory because this simulation enables us to estimate the p.e. yield with more than 10% precision.

§4. Performance test of the AC actual detector

4.1 Fabrication of the AC counter

Based on the result of the test experiment, we finalized the design of the AC actual detector and started fabrication of the AC counter. The outer size of the detector was already determined from the spatial limitation as shown in Fig. 2. Fig. 19 shows the photos at the fabrication process. The counter was divided into four rooms by 0.3 mm thickness Al plates and the 3 sheets of Teflon with 80 μm thickness were pasted on the inner surface of the each room. The normal transparency type aerogel radiator with refractive index $n = 1.10$ was used. Two tiles of the aerogel radiator of 15 mm thickness were

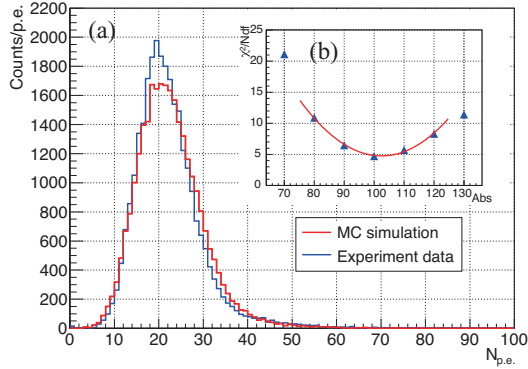


Fig.17. (a) Comparison between the experimental data (blue) of AC2 where the aerogel radiator was the normal type with 30 cm thickness and the reflection type was the diffused reflection, and its simulation result (red). (b) Estimation of the best Abs value by searching for the minimum reduced χ^2 value.

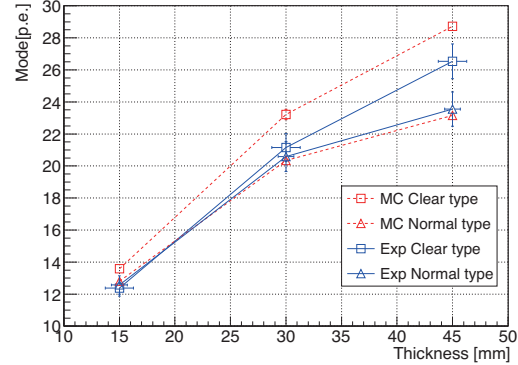


Fig.18. Comparison between data (red) and simulation (blue) for different radiation thicknesses. The square and triangle represent results for the clear and normal types, respectively. The estimated p.e. yield was consistent with data within 10% precision.

mounted and one tile was put on the other tile with the staggered manner in order to reduce ineffective region caused by the gap between the neighbor plate. The aerogel radiators were supported by the cotton strings as shown by red arrows in Fig. 19 which were attached to the detector frame through the hole. Some of the cotton strings were exchanged to the optical fiber for the calibration by guiding lights from LED. The fibers had some cracks on the surface and the light in the fiber can easily escape from the optical trap in the fiber to provide photons to PMTs. Totally 12 PMTs were mounted upside and downside of the detector.

Fig. 20 shows the expected p.e. yield for the AC counter from the Geant4 simulation which was tuned with the test experiment. In all rooms, the sufficient p.e. number of ~ 20 is expected. In actual operation, it is the most important that this performance should be kept at the high singles rate condition. To check these points, we again performed a test experiment at the same beam line in ELPH in November 2016.

4.2 Performance test experiment with a positron beam (2)

We performed a test experiment for the AC actual detector using a positron beam in the GeV- γ test beam line at ELPH for three days in November 2016. The purpose of the experiment is to evaluate the performance of the AC counter at high single rate condition in addition to check the general study topics such as position dependence. By changing the operation condition such as the single p.e. gain of PMTs and the threshold of the discriminator, the operation condition was optimized. The experimental setup was almost the same with the previous experiment in Fig. 6. The prototype detectors (AC1, 2) were replaced by the AC actual counter. Fig. 21 shows the beam points to check the position dependence where

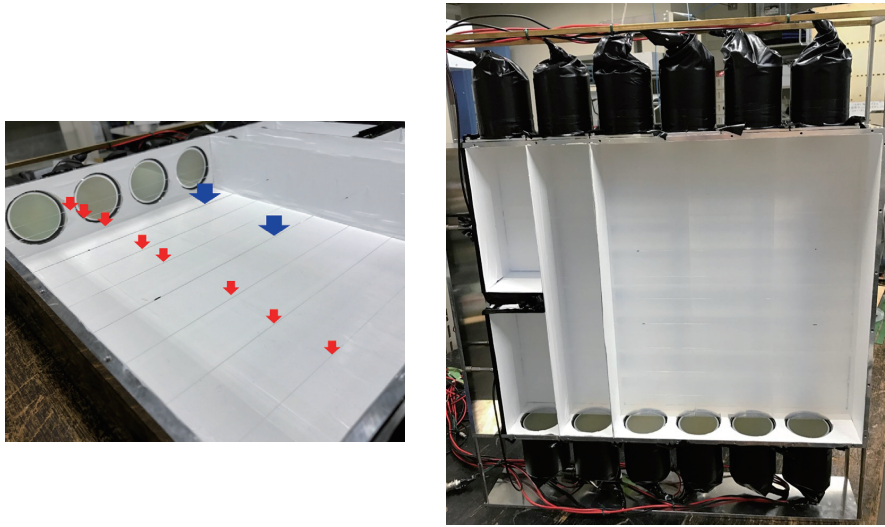


Fig.19. Photographs at the fabrication process of the actual AC detector. The cotton strings shown as red arrows is used to support the aerogel radiators. The blue arrows show the optical fiber for the calibration by guiding lights from LED.

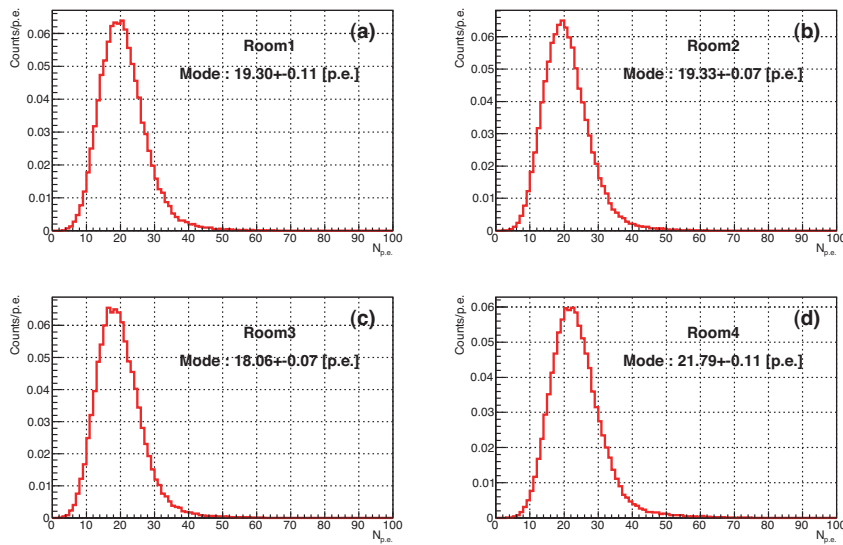


Fig.20. The expected p.e. yield for the AC counter from the Geant4 simulation which was tuned with the test experimental data.

the red cross points show the reference positions for each room. In this experiment, the mean beam rate was increased up to ~ 600 kHz. However the extracted beam in one spill had the time dependence as shown in Fig. 22 where the logic signal from PMT1U was input to the universal FPGA module (HUL module) and the instantaneous beam rate for every triggered timing was calculated from the increases of the counters of the logic signal and clocks for time measurement between the two triggered events. In the analysis, the instantaneous beam rate was taken into account.

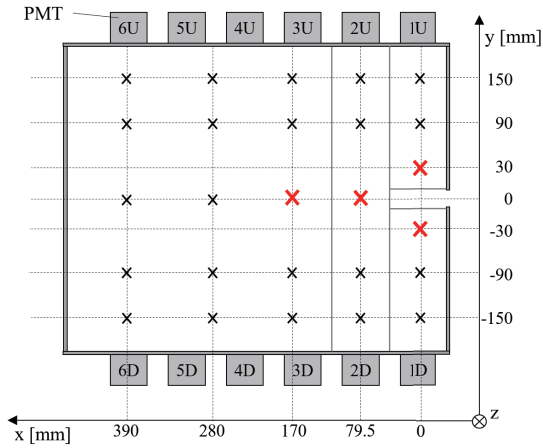


Fig.21. Beam position at the test experiment to check the position dependence. The red cross points show the reference positions for each room.

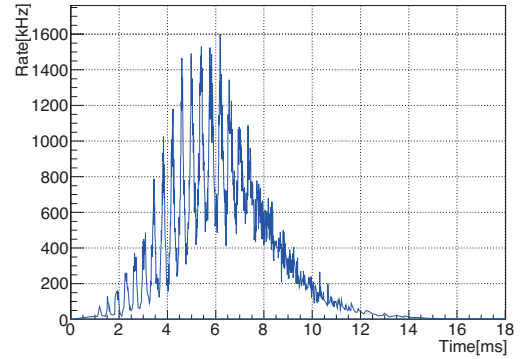


Fig.22. Instantaneous beam rate in one spill.

4.2.1 The photo-electron yield

Fig. 23 shows the typical p.e. yield for the room4 segment. The left 8 histograms show the p.e. yield for each PMT and the p.e. yields were added in software and the right figure was obtained. The obtained p.e. yield was almost consistent with the simulation shown in Fig. 20.

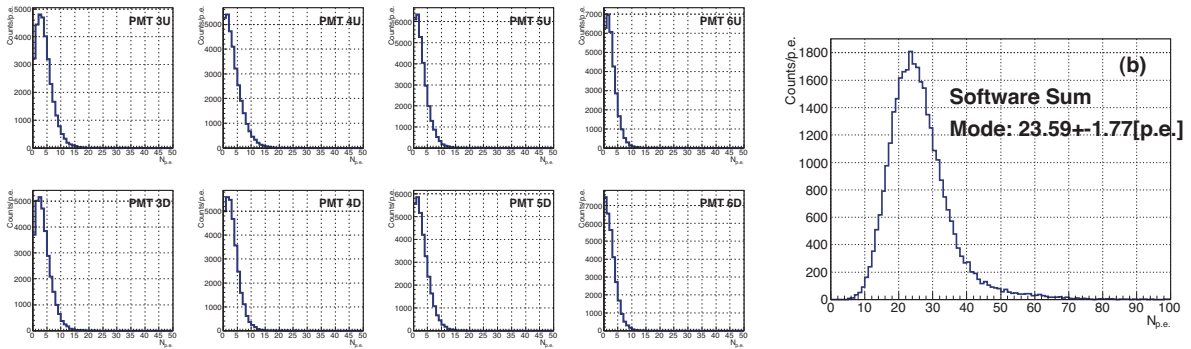


Fig.23. Typical p.e. yield for the room4 segment. The left 8 histograms show the p.e. yield for each PMT and the right histogram shows these summation.

4.2.2 The high rate study

We checked the performance at the high singles rate condition. As shown in Fig. 22, there was a time dependence in its instantaneous beam rate. In the analysis, each triggered event was categorized into three instantaneous beam rates of "100 kHz" from 0 to 200 kHz, "300 kHz" from 200 to 400 kHz and "600 kHz" from 400 to 800 kHz. As for the PMT gain, we prepared three different operation points corresponding to 20, 40 and 60 QDC channels for single p.e. pulse charge. Here, the PMT signals are connected to the amplifier with 10 times gain to operate in the lower operation voltage. Therefore the

present gain was different from that at the previous test experiment for the prototype detector. The beam positions were set to the reference position as shown by the red cross point in Fig. 21. Fig. 24 shows the beam rate dependence of the pulse height for each single p.e. gain. The most probable value of the p.e. distribution at each beam rate was normalized with that at 100 kHz beam rate. Due to the AC coupling of the PMT output, the baseline of the signal shifted upside with the increase of the beam intensity. In Fig. 24 the effect of the pedestal shift was corrected. In the gain of 20, no gain drop was found. On the other hand, in the gain of 40 and 60, the gain was reduced down to 90%. However, the gain drop of this level was acceptable. Fig. 25 and 26 shows the efficiencies for each room at the mean beam rates of 300 kHz and 600 kHz, respectively. Here, the horizontal axis shows the discriminator threshold applied in the hard level and the hard level threshold was converted to p.e. value in software. The room4 kept the most high efficiency because the p.e. yield was the largest. In the mean rate of 300 kHz, which is the expected singles rate in E40, the efficiencies more than 98% could be obtained for all room segments by setting the threshold less than 6 p.e. value. At 600 kHz, the efficiencies became lower a little bit. Even in this rate, by setting threshold around 4 p.e., 97% efficiency could be obtained.

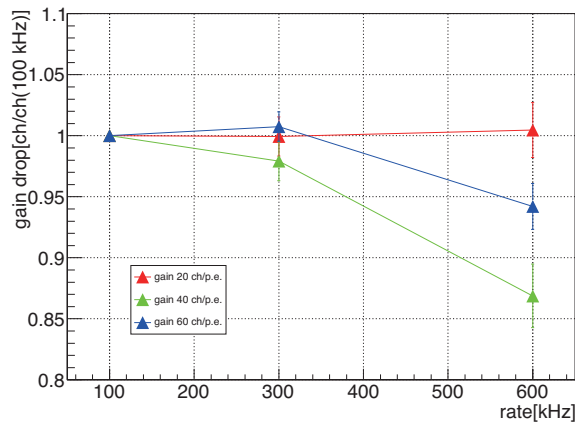


Fig.24. Beam rate dependence of the pulse height for three p.e. gains. The red, green blue points show 20, 40 and 60 p.e., respectively. The error mainly comes from the uncertainty of the baseline shift.

4.2.3 The position dependence

Next, the position dependence of the performance was evaluated. The studied points were shown in Fig. 21 and the beam rate was set to about 30 kHz. The PMT gain was 40 ch for single p.e. charge. Fig. 27 (a) shows the most probable value of the p.e. distribution for each point. As expected from the prototype detector, the p.e. yield increased when the beam position became near the PMTs. Fig. 27 (b) shows the efficiencies and the efficiencies more than 99% were obtained for all positions in this beam rate.

Finally we check the effect that the charged particles passed through the neighbor rooms such as room1 and room3. In case of room1 and room3, the beam position was set at the partition of the Al plate and the detector was placed with a tilt angle of three degrees, which corresponded the angle from the

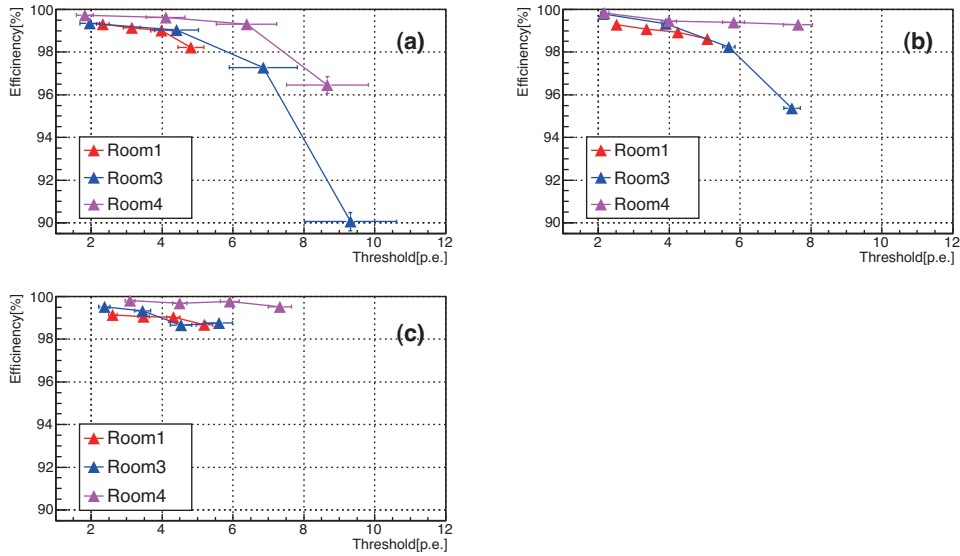


Fig.25. Efficiencies for each room at the mean beam rate of 300 kHz for p.e. gains of 20 (a) , 40 (b) and 60 (c).

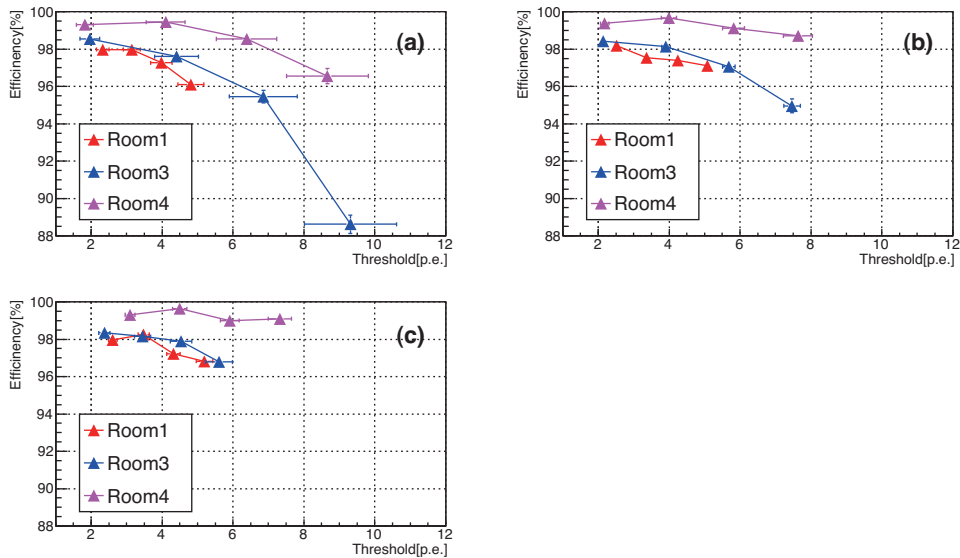


Fig.26. Efficiencies for each room at the mean beam rate of 600 kHz for p.e. gains of 20 (a) , 40 (b) and 60 (c).

target position in the E40 setup. In case of room3 and room4, the tilt angle was set to be 8 degrees. Fig. 28 shows the summed p.e. distribution for neighbor rooms. In these positions, the p.e. yield decreased especially at the partition of room1 and room3. Due to the aluminum partition, the net pass length in the aerogel radiator decreased and the p.e. yield also reduced. At the partition of room3 and room4, because the particle had the larger tilt angle, the effect of this partition reduced and the much better p.e. distribution could be obtained. In order to measure the efficiency, the signals were linearly added by using the Linear FIFO and the output signal was discriminated. Fig. 29 shows the threshold

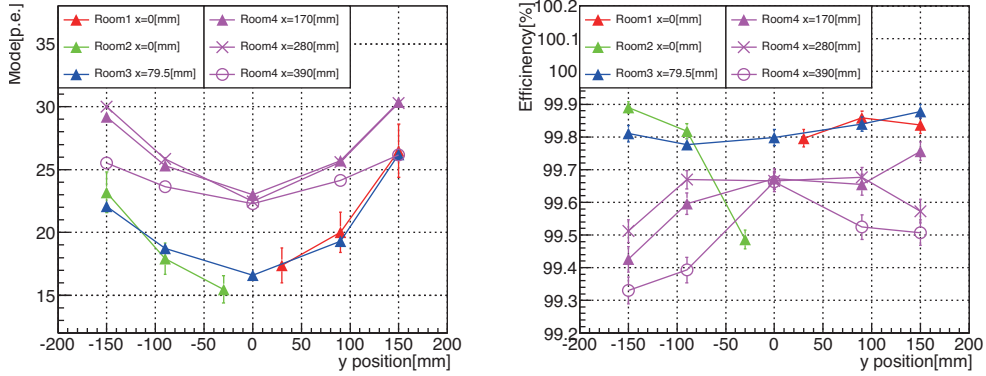


Fig.27. Position dependence for the p.e. yield (a) and efficiency (b) at the beam rate of 30 kHz.

dependence of the efficiency at these partition positions. As a reference, the efficiencies at the normal position for each room were also overwritten. At the partition of room3 and room4, rather high efficiency of 97% could be obtained. On the other hand, the partition position at room1 and room3 resulted in lower efficiency around 93%. However, when we performed the simulation taking into account this effect for the E40 detector configuration where the charged particles were generated from the target with the realistic incident angle, the total efficiency was obtained to be 98%. Therefore this partition effect was not a serious problem.

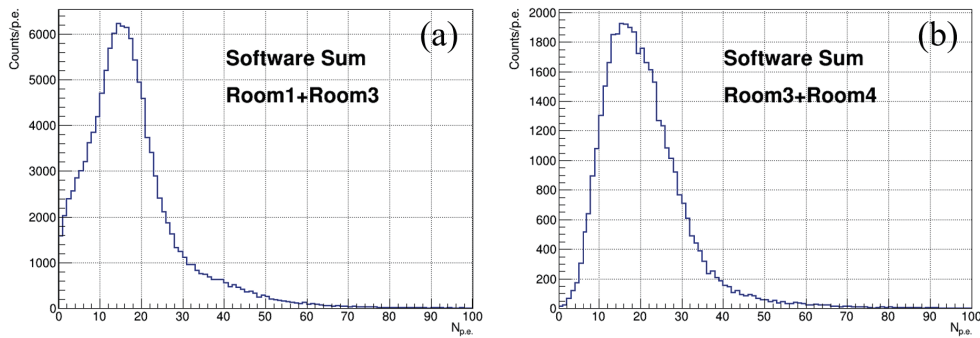


Fig.28. Summed p.e. distribution for neighbor rooms when the beam passes through the partition area. The beam positions were at the border between room1 and room3 (a) and at the border between room3 and room4 (b).

4.2.4 Summary of the test experiment

The AC counter using a normal transparency type aerogel radiator with the refractive index of 1.10 was studied by using a positron beam. We adopted the defused reflection method with a Teflon sheet. As expected from the simulation, the AC counter showed the enough performance such as the p.e. yield and position dependence. The most probable p.e. numbers were larger than 15 p.e. for all positions and the efficiencies were more than 99% at the beam rate of 30 kHz. At the higher beam rate up to 600 kHz, there were still gain drop in the PMTs. However, the gain drop was well suppressed by operating the

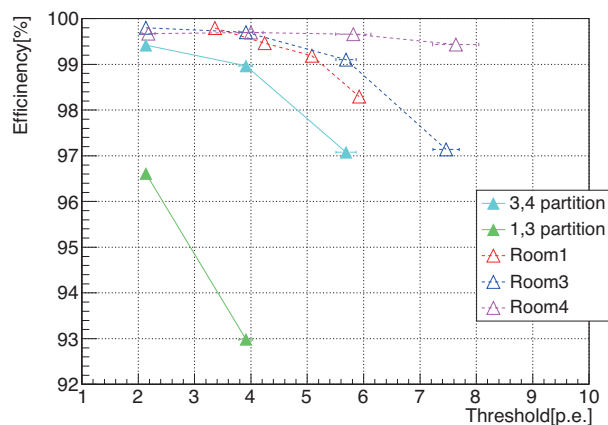


Fig.29. Threshold dependence of the efficiency at the border positions. The efficiencies at the normal position for each room were also overwritten as a reference.

PMTs at lower HV value and by keeping the pulse height with the additional electrical amplifier. The efficiency was obtained to be more than 97% at the high rate condition. The AC counter had internal four rooms which were separated by the aluminum partition to reduce the singles rate for each PMT. Because the partition made an ineffective area, the efficiency decreased to 93% when the particle passed through around the partition region. However, the effect was negligible at the E40 experimental setup. We concluded that the AC counter satisfied the requirements to keep more than 97% efficiency at the actual single rate condition.

§5. Summary

We developed an Aerogel Cherenkov Counter (AC) with the index of 1.10 for the Σp scattering experiment at J-PARC which was used to veto π particles of momentum range up to 1.4 GeV/c. The size of AC was 480 (H) \times 400 (V) \times 80 (T) mm³ which was determined from a geometrical condition of a magnetic spectrometer (KURAMA spectrometer). In order to obtain detection efficiency more than 97%, we adopted the aerogel radiator with index of 1.10 which was rather high index as an aerogel and totally 12 fine-mesh PMTs were used to collect enough photons. The other requirement was that this AC should keep the efficiency under the high single rate condition up to 300 kHz which was the expected value in the Σp scattering experiment. We asked Chiba university group to make the aerogel radiators of $n = 1.10$. They accumulated a skill to make a very transparent type of the aerogel radiator. At first we fabricated the prototype detectors to compare the transparent type of the aerogels and the reflection method, that is, the mirror reflection or the diffused reflection. From the test experiment using a positron beam, as for the reflection method, the diffused reflection was superior at the all study points. As for the transparency, the clear type showed the larger p.e. yield especially when the thickness of the radiator increased. However, the normal type also showed the sufficient p.e. yield of 20 with 30 mm thickness. Therefore we selected to use the normal type radiator considering the difficulty at the production process of the clear type.

One of the important points in this work is that the realistic optical simulation using Geant4 was constructed. One of the most uncertain parameters in the simulation was the absorption length in the aerogel radiator. By minimizing the difference between the simulation and the experimental p.e. yield, the absorption length can be estimated to be the 100 times longer value than the scattering length that can be measured. By using this value, the optical simulation could reproduce the experimental results such as the radiator's thickness dependence for the p.e. yield within a 10% accuracy.

The AC actual counter using the normal transparency type aerogel radiator with the refractive index of 1.10 was fabricated and its performance was evaluated again using the positron beam at ELPH. We adopted the defused reflection method with a Teflon sheet. As expected from the simulation, the AC counter showed the enough performance such as the p.e. yield and position dependence. The most probable p.e. numbers were larger than 15 p.e. for all positions and the efficiencies were more than 99% at the beam rate of 30 kHz. At the higher beam rate up to 600 kHz, there were still gain drop in the PMTs. However, the gain drop was well suppressed by operating the PMTs at lower HV value and by keeping the pulse height with the additional electrical amplifier. The efficiency was obtained to be more than 97% at the high rate condition. We concluded that the AC counter satisfied the requirements to keep more than 97% efficiency at the actual single rate condition.

Acknowledgment

We would like to express our thanks to the staffs of ELPH for their support to provide beam with the excellent condition during the beam time. This work was supported by JSPS KAKENHI Grant Number 23684011 and 15H05442.

References

- [1] M. Tabata *et al.*: Nucl. Instr. Meth. **A668** (2012) 64.
- [2] M. Tabata *et al.*: Nucl. Instr. Meth. **A795** (2015) 206.
- [3] K. Tanabe : Master's thesis, Tohoku university (2015).
- [4] R. Enomoto *et al.*: Nucl. Instr. Meth. **A332** (1993) 129.
- [5] M.F. Villoro *et al.*: Nucl. Instr. Meth. **A480** (1993) 456.
- [6] T. Bellunato *et al.*: Eur. Phys. J. **C 52** (2007) 759.

(ELPH Experiment : #2868)

Performance Evaluation of Silicon-Tungsten Electromagnetic Calorimeter Detector (ALICE FoCal) and High Timing Resolution MRPC-TOF for High Energy Heavy Ion Experiment

R. Aoyama⁷, T. Chujo⁷, T. Hachiya^{4,5,6}, M. Hatakeyama⁷, Y. Hoshi⁷,
T. Ichisawa⁷, M. Inaba⁸, H. Kato⁷, Y. Kawamura⁷, D. Kawana⁷, Y. Miake⁷,
T. Nonaka⁷, K. Ozawa³, S. Sakai⁷, H. Sako², T. Sakamoto⁴, M. Shimomura⁴,
T. Sugitate¹, T. Suzuki⁷, K. Tadokoro⁷, M. Takamura⁷, and S. Takasu¹

¹*Hiroshima University, Kagamiyama, Higashi-Hiroshima 739-8526, Japan*

²*Advanced Science Research Center, Japan Atomic Energy Agency, 2-4 Shirakata Shirane,
Tokai-mura, Naka-gun, Ibaraki-ken 319*

³*KEK, High Energy Accelerator Research Organization, Tsukuba, Ibaraki 305-0801, Japan*

⁴*Nara Women's University, Kita-uoya Nishi-machi Nara 630-8506, Japan*

⁵*RIKEN Nishina Center for Accelerator-Based Science, Wako, Saitama 351-0198, Japan*

⁶*RIKEN BNL Research Center, Brookhaven National Laboratory, Upton, New York 11973-5000,
USA*

⁷*University of Tsukuba, Tsukuba, Ibaraki, 305-8571, Japan*

⁸*Tsukuba University of Technology, Tsukuba, 305-8520, Japan*

In the ALICE experiment at the Large Hadron Collider (LHC) at CERN, there is an upgrade plan to construct a Forward Calorimeter (FoCal) intended for the measurement of direct photons at forward rapidity ($3.5 < \eta < 5.3$). In 2017, we made a new prototype of the electromagnetic part of FoCal detector, including the new silicon sensors and new design of the flexible readout board to fix the design of mini-FoCal detector, which is planned to be produced and tested in 2018. We conducted the test beam experiment by using positron beams at Research Center for Electron Photon Science (ELPH). We measured the signal of minimum ionizing particles (MIP) in this new prototype, and observed the gain variation for MIPs depending on the position of silicon sensor. At the same time, we also conducted the beam test for the prototype of Multi-gap Resistive Plate Chamber (MRPC) as a time-of-flight detector. This R&D of MRPC is aiming for a good timing resolution better than 80 ps for the future use of J-PARC experiments. At this time, based on the Electromagnetic field simulation, we developed a new prototype, in which the rigid ground is in place with the modification of readout pad shape. It is optimized for the impedance matching and transmittance for the wide band signal including more than 1 GHz frequency. We report improvements of the new prototype.

§1. Forward Calorimeter

1.1 Introduction

In the LHC-ALICE, there is an upgrade plan to construct a Forward Calorimeter (FoCal). The full FoCal detector installation during the long shutdown 3 (LS3) in 2024 is under the discussion. The FoCal consists of an electromagnetic calorimeter (FoCal-E) and a hadron calorimeter (FoCal-H). FoCal-E consists of low granularity layer (LGL) for the measurement of the photon energy, and high granularity layer (HGL) for the identification of decay photons and direct-gammas. FoCal-E is a sampling-type calorimeter using tungsten as the particle absorption layer and silicon as the detector layer. The silicon used for LGL of FoCal-E is composed of 64 PADs of about $1\text{cm} \times 1\text{cm}$ with the segmentation of 8×8 . On the surface of silicon, a flexible substrate with circuit for readout is attached, and the tungsten layer is attached on the back side. The silicon PAD sensor we used in this test beam is shown in Fig. 1.

We use APV25 hybrid board (Fig. 2), Scalable Readout System (SRS) and mmDAQ for the readout. APV25 is an analog pipeline ASIC developed for readout of silicon strip detector for the CMS experiment. SRS refers to a system that collects the data from ADC boards and then converts the analog data from APV 25 to the digital (12 bits). The FEC board for SRS system processes data and slow control via DAQ PC. The DAQ software called “mmDAQ” is used in this test beam. Since 2014, we have been working on the LGL detector, and at this time, we used the new silicon photo diode from HAMAMATSU ($500\ \mu\text{m}$ thickness), and a new flexible print circuit board with wire bonding. No analog signal summing for multiple silicon layers is used.

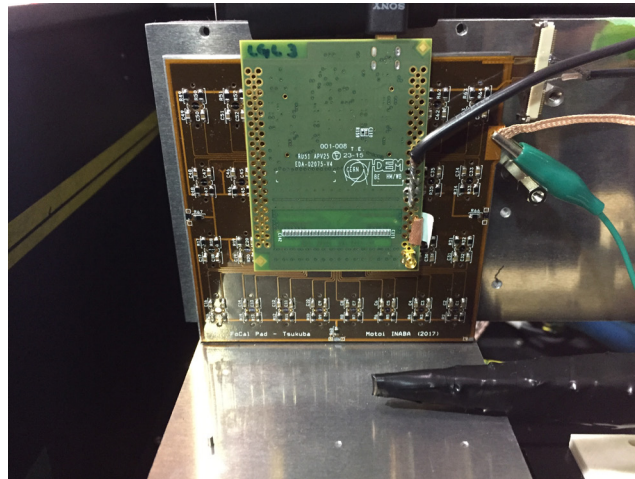


Fig.1. Silicon PADs with flexible board.

1.2 Setup

We placed the silicon sensor for FoCal in the dark box for the light shield. The inside of the dark box is shown in Fig. 3. In this box, there are a detector, a remotely controllable moving stage, a scintillation counter for trigger. To define the beam spot, we use two $10\text{cm} \times 10\text{cm}$ scintillation counters and a $4\text{mm} \times 4\text{mm}$ scintillation counter. These three counter’s coincidence signals were used as beam

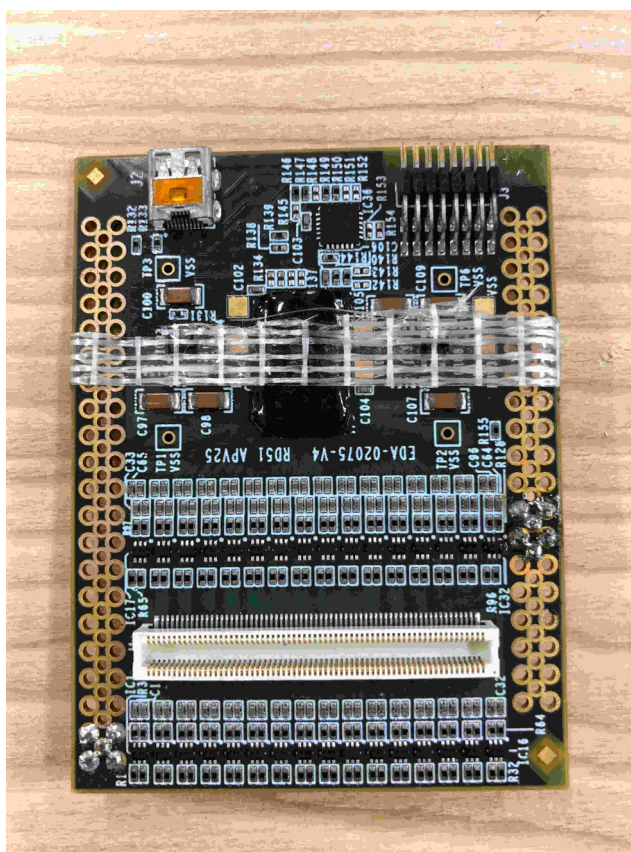


Fig.2. APV25 hybrid board (CERN RD51).

triggers. And the detector is fixed on the stage, and it can be moved in horizontally and vertically with respect to the beam axis. This moving stage is used for the position scan measurements. Also for the measurements of an electromagnetic shower, we placed several tungsten plates in front of the detector.

1.3 Analysis

1.3.1 Observation of Electromagnetic Shower

To enhance the shower signals, the tungsten plates were placed in front of the detector. The purpose of this experiment is the measurement of MIP signals for all silicon pad sensor, so that the whole area of the detector should be exposed by electromagnetic showers. In this measurements, we successfully observed MIP signals and separated from the noise signal as shown in Fig. 4. The most right peak is about twice as much compared to the middle peak, so that it indicates the signals of 2 MIP signals. This charge distribution is made by accumulating the singles for all PADs. The right panel shown in Fig.4 is the simulation result by Geant4. The data agrees well with the simulation.

1.3.2 MIP Signal on All 8×8 Channels

One of the objectives of this beam test is to detect MIP signal in all silicon PADs and establish the gain calibration method for the individual pad. Fig. 5 shows the ADC value of MIP measured at each PAD. There is one dead channel out of 64 PADs, but for other 63 PADs, ADC value of 1 MIP can be



Fig.3. Setup in the dark box for FoCal.

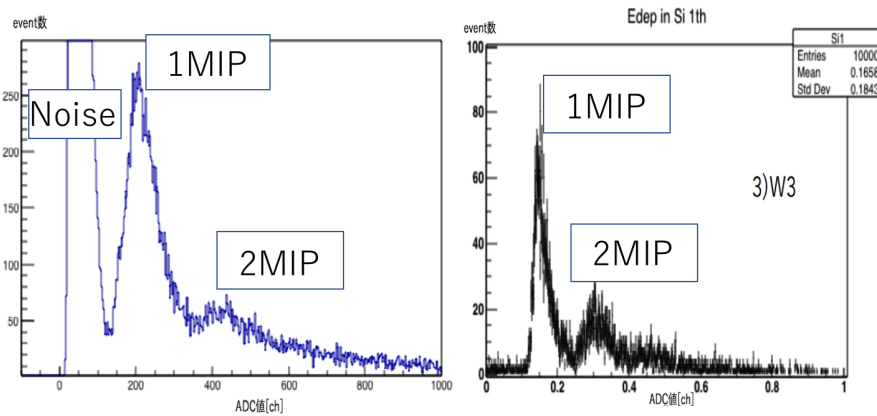


Fig.4. Electromagnetic shower on data (left) and simulation (right) for the single silicon sensors. The horizontal axis is the ADC value and the vertical axis is the number of counts.

clearly seen. As shown in Fig. 5, there is a trend that the ADC value is higher in the vicinity of the center and it gets lower as going outward.

One possibility of the ADC gain variation depending on the silicon location is the silicon wafer, because of the nearly round shape and low gain on the edge, and high gain around the center. It is important to consider this gain variation in the calibration step, for the energy measurement of photons as a calorimeter. We are planing to use the high intensity laser system to inject the infrared laser to silicon, and calibrate the gain for pad by pad. Further detail of this measurements are summarized in [2].

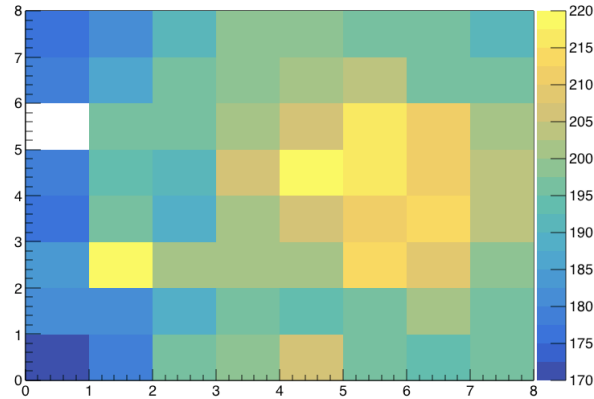


Fig.5. Position dependence of the MIP signal strength for all PAD sensors. The each square represents the geometrical position of silicon sensor used in this test.

§2. Multi-gap Resistive Plate Chamber

Multi-gap Resistive Plate Chamber (MRPC) is a Time of Flight(TOF) detector. MRPC is a gas chamber, and the signal is formed by the electron avalanche in the gas. Among many kinds of TOF detector, MRPC is attractive because it can achieve good timing resolution at low cost which would allow to make a large area TOF. For this reason, the MRPC technology is proposed to use the future experiments at J-PARC.

2.1 Modification based on Electromagnetic field simulation

The electromagnetic field simulation is a useful tool to optimize the detector design and obtain a better timing resolution. For this MRPC prototype, the simulation has done by Sony Global Manufacturing & Operations Corporation. The rigid ground is needed for the simulation, but usual MRPC does not have such a ground in its structure as shown in Fig. 6. We first installed a rigid ground to MRPC and modified some structure based on electromagnetic simulation. Fig .7 shows the new structure MRPC tested at the experiment at ELPH.

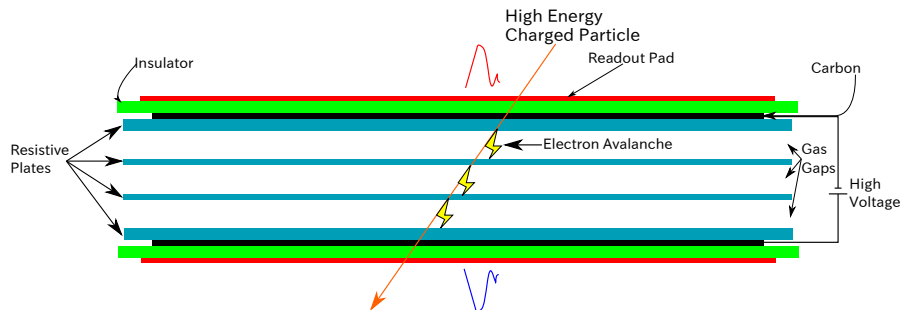


Fig.6. Structure of conventional MRPCs.

This new type MRPC is expected to achieve the following goals.

- Cu ground surrounding the chamber to reduce the noise coming from outside.

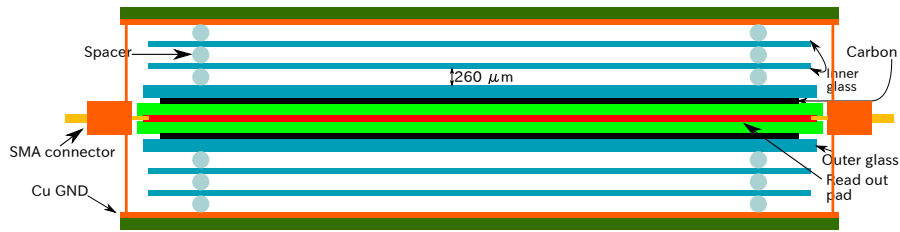


Fig.7. Structure of new type MRPC.

- Better impedance matching at readout pad, and better S/N.
- Enable to use the single-end preamplifier for readout.

We expect a better performance, especially in noise tolerance and property for the high frequency signals by installing rigid ground and by use of the single-end readout.

2.2 Experiment and Analysis

2.2.1 Setup

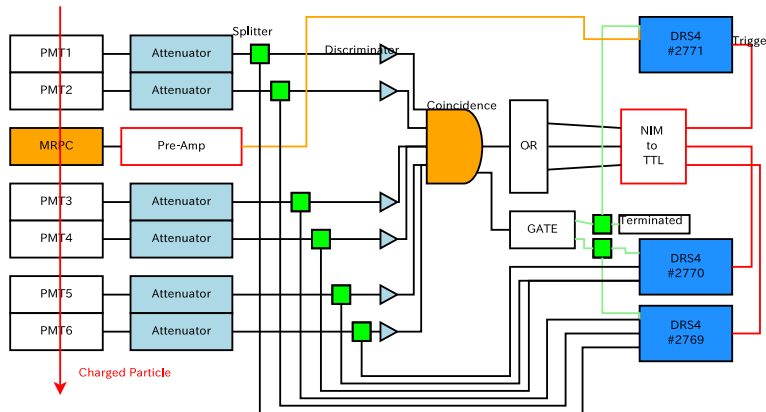


Fig.8. Data taking diagram

The detail of the analysis is described in [3]. Fig. 8 shows the diagram for data taking. We used coincidence of PMT signals from No.1 to No.6 for start timing and beam trigger. MRPC generates stop timing. The distribution of stop timing means the timing resolution of our MRPC. MRPC is placed in the gas box filled with R-134a and SF₆. The gas volume ratio is R-134a : SF₆ = 100 : 5 and SF₆ is a quencher gas. We have two PMTs for each scintillation counter as shown in Fig. 9.

2.2.2 Data analysis and results

The signal shape and parameter definition is as described in Fig. 10. Data points are fitted by Sigmoid function defined as Eq. 1, and extracted the parameters as shown below. In this test, we succeeded to read signals by the single end signal readout. Fig. 11 shows the TOF distribution of this new MRPC prototype. We achieved 213.9 ± 6.6 ps timing resolution. This is better than the value from the previous study by about 50 ps [1]. It leads to a simple readout design, and has a potential to improve the tim-

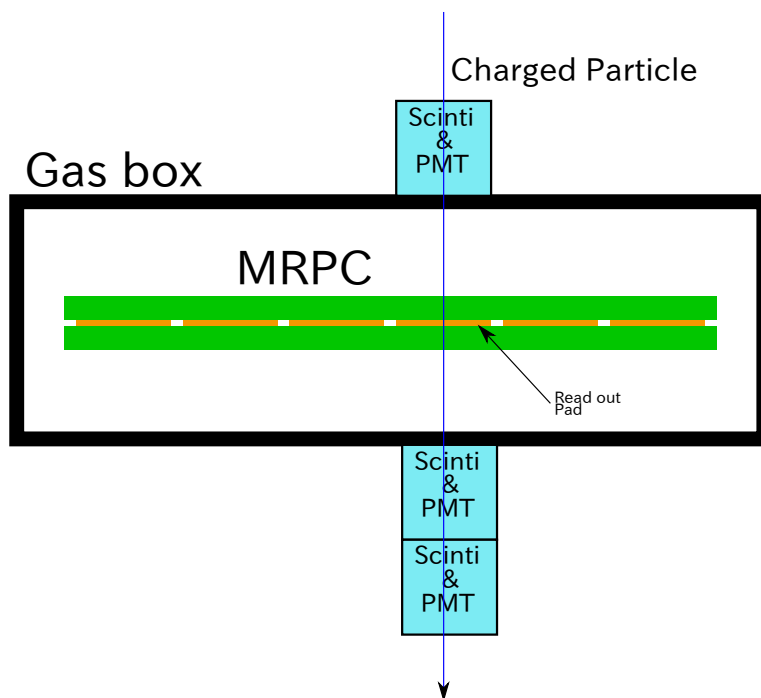


Fig.9. Setup around gas box

ing resolution by reading out the signal for high frequency band width, adopting the GHz preamplifier, which is available in the market.

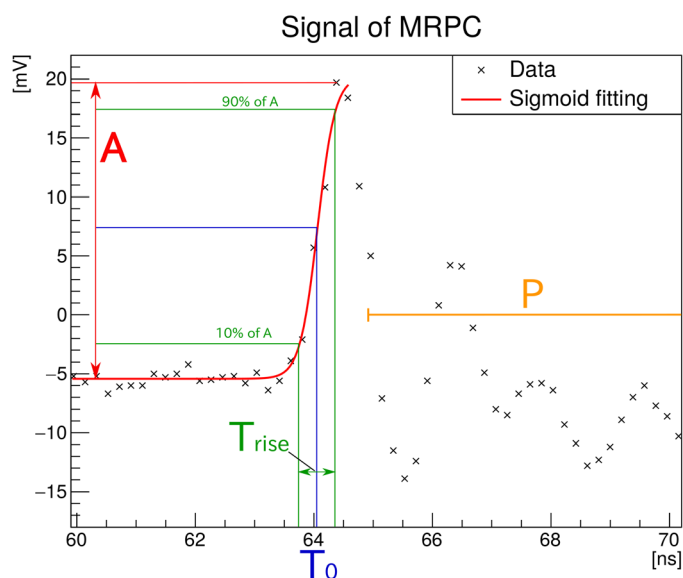


Fig.10. Signal shape and parameter definition. Horizontal axis is the time, and the vertical axis is the pulse height.

$$f(t) = a + \frac{d}{1 + \exp\left(\frac{b-t}{c}\right)} \quad (1)$$

1. A : amplitude of signal.

2. P : pedestal, an integral of post peak.
3. T_0 : stop timing. T_0 is defined as timing the signal reaches half of its amplitude.
4. T_{rise} : time length the signal takes to rise 10% to 90% of its amplitude.

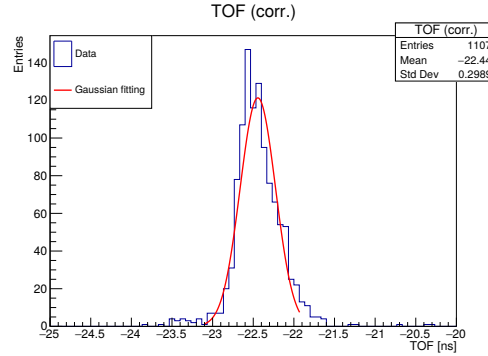


Fig.11. TOF distribution of new type MRPC

Acknowledgment

We would like to thank all its scientists, engineers and technicians at ELPH for their strong support for our experiment, and ELPH accelerator teams for the outstanding performance of the GeV gamma facility. This work was supported by JSPS KAKENHI Grant Numbers JP17H01122, JP15K13475, and JP26220707.

References

- [1] T. Ichisawa, "Multi-gap Resistive Plate Chamber R&D for the large area TOF for the future J-PARC experiment", (Bachelor thesis in FY 2016, Univ. of Tsukuba, Physics, in Japanese)
- [2] K. Tadokoro, "Performance evaluation of Front End Electronics with APV25 hybrid for LHC-ALICE FoCal", (Bachelor thesis in FY 2017, Univ. of Tsukuba, Physics, in Japanese)
- [3] M. Takamura, "R&D of Multi-gap Resistive Plate Chamber (MRPC) detector; readout pad shape for the high frequency signal readout and S/N improvement", (Bachelor thesis in FY 2017, Univ. of Tsukuba, Physics, in Japanese)

(ELPH Experiment : #2870)

Development of high-rate detectors by using MPPC for the charmed baryon spectroscopy experiment at J-PARC

K. Shirotori¹, T. Akaishi², H. Asano³, R. Honda⁴, T. Ishikawa⁵, Y. Ma³,
H. Noumi¹, A. Sakaguchi², H. Sako⁶, T. N. Takahashi¹,
and for the J-PARC E50 collaboration

¹*Research Center for Nuclear Physics (RCNP), 10-1 Mihogaoka, Ibaraki, Osaka, 567-0047, Japan*

²*Department of Physics, Osaka University, Toyonaka 560-0043, Japan*

³*RIKEN, 2-1 Hirosawa, Wako, Saitama 351-0198, Japan*

⁴*Department of Physics, Tohoku University, Sendai 980-8578, Japan*

⁵*Research Center for Electron Photon Science (ELPH), Tohoku University, Sendai, 982-0826,
Japan*

⁶*Advanced Science Research Center (ASRC), Japan Atomic Energy Agency (JAEA), Tokai,
Ibaraki 319-1195, Japan*

Fine segmented detectors for the high-rate beam measurement by using MPPC (Multi-Pixel Photon Counter) are being developed for the charmed baryon spectroscopy experiment at J-PARC. For confirming the performances of the detector elements with MPPC, test measurements of the timing counter with a plastic scintillator and an acrylic Čerenkov radiator, and the scintillation fiber counter were performed. We performed two experiments, for the first test of detector elements in November 2016 and the high-rate beam test in October 2017. In the first test experiment, by using the combination of the plastic scintillator of $3\text{ mm} \times 3\text{ mm} \times 150\text{ mm}$ and 3-mm squared which is installed on the fast signal shaping amplifier, the time resolution of $\sim 70\text{ ps(rms)}$ by the means of the Time-Of-Flight measurement was obtained. The counters with the $\phi 1.0\text{-mm}$ and $\phi 0.5\text{-mm}$ scintillation fiber of 500-mm and 300-mm length had a time resolution of $\sim 650\text{ ps(FWHM)}$ and $\sim 1050\text{ ps(FWHM)}$, respectively. In the high-rate beam test experiment, we evaluated performances of the plastic scintillation and Čerenkov timing counters. Both counters were irradiated by the high-rate beam of the counting rates of 3–5 MHz. The plastic scintillation and Čerenkov timing counters showed time resolution of $\sim 70\text{ ps(rms)}$ and $\sim 50\text{ ps(rms)}$ in the high-rate condition, respectively. Although the baseline change by pile-up effects and performances of the readout module made the time resolution worse than that of the low-rate condition, it was found that both counter satisfied the experimental requirements.

§1. Outline of the J-PARC E50 experiment

Investigation of the heavy quark baryon is a key way to understand a degree of freedom to describe the hadron structure. The diquark correlation which is expected to be a degree of freedom of hadrons can be studied from the spectroscopy of charmed baryons. An experiment to observe and investigate the charmed baryons (J-PARC E50 [1]) was proposed at the J-PARC high-momentum beam line. The

experiment via the $\pi^- p \rightarrow Y_c^{*+} D^{*-}$ reaction at 20 GeV/c using the missing mass technique will be performed for the systematic measurement of the excitation energy, the production rates and the decay products of charmed baryons. From the systematic study of charmed baryons, the diquark correlation which is expectedly an essential degree of freedom to describe the hadron structure can be revealed.

In the E50 experiment, the high-rate beam with a counting rate of 6.0×10^6 per beam extraction cycle (2.0 seconds) is planned to be used due to a small production cross section of the charmed baryon production. Therefore, the development of the high-rate detectors is one of the essential parts for constructing the spectrometer system.

1.1 Time zero counter

It is necessary to measure the 30 MHz beam for determining the beam timing as the reference start timing by using a fine-segmented timing counter (Time zero counter: T0). T0 is required to have good time resolution of less than 100 ps(rms), while the its timing signal should be stable and fast response for determining the start timing of many experimental apparatus in the high-counting rate condition. For satisfying the requirements, the combination of a fine segmented plastic scintillator or an acrylic Čerenkov radiator with MPPC can be a solution for T0. The maximum counting rate of the central segment is expected to be ~ 3 MHz when the horizontal segment of the 3-mm size is connected to the 3-mm squared MPPC. MPPC has good intrinsic time resolution of ~ 200 ps(rms) for the one photoelectron detection [2] so that the time resolution of the counter is determined by the light yield and signal response of the connected plastic scintillator and Čerenkov radiator. For confirming the performances of T0, the test measurements with the combination of the plastic scintillator or Čerenkov radiator with MPPC were performed.

1.2 Scintillation fiber tracker

For measuring the beam tracks, it is necessary for tracking detectors to be satisfied under the operation by assuming the beam with size of 100 mm(horizontal) \times 100 mm(vertical) and expecting total counting rate of 30 MHz. This beam intensity is over the limit of the wire chamber operation so that a high-rate counters such as a scintillation fiber tracker are needed to handle the high-intensity beam. The beam of 100 mm(H) \times 100 mm(V) is measured by the fiber tracker with a multi-layer configuration. The counting rate per 1-mm segment is expected to 0.3–1 MHz from the total intensity of 30 MHz. In this condition, the time resolution of the fiber tracker for measuring the timing information with a narrow timing gate is essential to suppress the accidental hits. It is required to have a resolution of 1 ns(rms) for selecting time gate in the tracking analysis. For confirming the time resolution of the scintillation fiber counter, the test measurements with the combination of the scintillation fiber and MPPC were performed.

§2. First test of detector elements in November 2016

The performances of the detector elements were confirmed by using the low-counting rate beam and the minimum ionization particle conditions. The experiment was performed as a parasite experiment with the detector test for the J-PARC E40 experiment (Spokesperson: K. Miwa).

2.1 Test detector elements

For the test T0 counter, the fast timing plastic scintillator(EJ-228) and MPPC(S13360-3025PE) were used. EJ-228 has both fast rise and decay time of 0.5 ns and 1.4 ns, respectively. The size of scintillator was 3 mm(W) \times 3 mm(T) \times 150 mm(L). In the measurement, 3-mm squared MPPC with 25- μ m pixels which has the fast rising time of 0.6 ns was used. MPPCs were attached to the both edge of the plastic scintillator. The number of detected photoelectrons by using this combination was \sim 100 p.e. from the measurement by using the ^{90}Sr source. Three test T0 counters were used in order to measure Time-Of-Flight.

For the fiber counter, the multi-cladding scintillation fiber(SCFS-78M) and MPPC(S13360-3025PE) were used. The diameters of fibers of ϕ 1.0 mm and ϕ 0.5 mm were used. The length of fibers were 500 mm and 300 mm for the ϕ 1.0-mm and ϕ 0.5-mm fiber, respectively. In this measurement, 3-mm squared MPPC with 25- μ m pixels was used. MPPCs were attached to the both edge of the scintillation fiber. The number of detected photoelectrons by using this combination was \sim 15 p.e. from the measurement by using the ^{90}Sr source.

For the MPPC signal readout, a shaping amplifier which has a fast operational amplifier(AD8000) was used. The detail of the MPPC amplifier is shown in Ref. [3]. The output signal from MPPC is shaped to be the narrow signal with the time width of less than 10 ns.

For the Time-Of-Flight measurement, the reference counters were also used. The counters consisted of the fast timing plastic scintillator(EJ-228) and a metal packaged photomultiplier(R9880U). The size of the plastic scintillator was 3 mm(W) \times 3 mm(T) \times 30 mm(L) and they were staged in parallel for covering the 6-mm region. PMTs were attached to the both edge of the plastic scintillator.

2.2 Experimental conditions

The experiment was performed in the test beam line in the GeV- γ building of the Research Center for Electron Photon Science(ELPH). The positron beam energy was 600 MeV. The experiment was performed as a parasite experiment so that the beam rate was changed during the beam time. Although the beam rates of 1–150 kHz were used in the experiment, the rate dependence of the test counters was negligibly small. The counting rate of each counter was measured to be less than 10 kHz because the size of counter is smaller than that of beam.

All detectors were installed along the beam line. The reference counters were installed at the most upstream and downstream of the experimental setup. The test T0 and scintillation fiber counters were installed between the reference counters. The timing coincident signal from the reference counters was used for the DAQ trigger signal. Timing and charge information from the counters were measured by

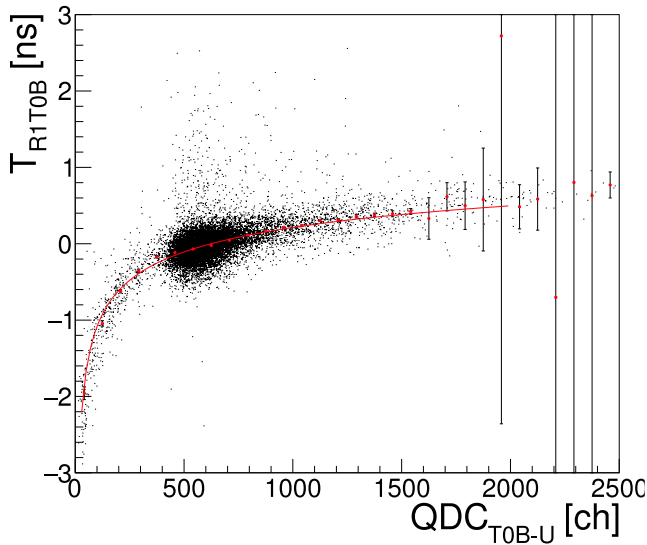


Fig.1. The correlation between TOF of a reference counter and a test T0 counter and ADC before the pulse height correction. The fitting function is shown by the red line.

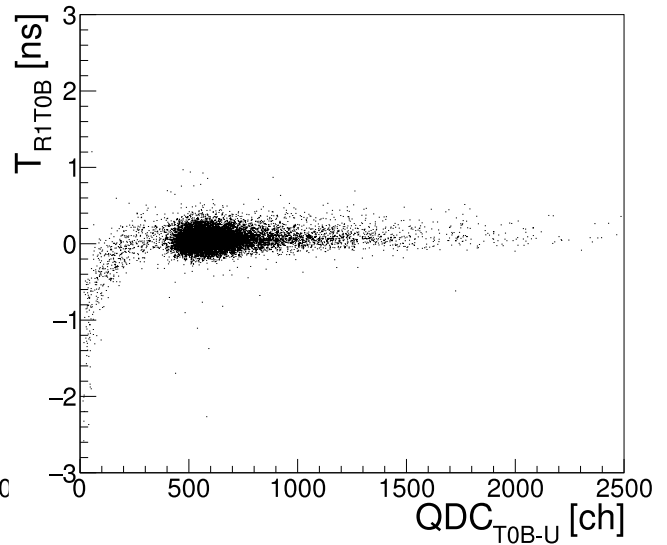


Fig.2. The correlation between TOF of a reference counter and a test T0 counter and ADC after the pulse height correction. It was corrected by using the fitting function.

CAEN TDC(V775) and ADC(V792), respectively.

The dependences of signal threshold, operation voltage of MPPC and beam position were measured. For measuring the signal threshold dependence, the output signals from the counter were discriminated at the 7%, 10% and 15% level of the pulse height of the minimum ionization signal. In order to check dependence of operation voltage of MPPC, the over voltage of MPPC(V_{over}) was changed from 5 V to 13 V by $\Delta V = 2$ V step. For the test T0 counter, the position dependence was checked by changing the beam irradiated positions. by changing height of the counter frame.

2.3 Analysis

The time resolution of each counter was obtained by using the Time-Of-Flight (TOF) method. The signals were measured at the both edge of counters so that the mean time of each counter was used for the TOF measurement. For obtaining the time resolution of the test T0 counter, combinations of both three test T0 counters and reference counters with one of the test T0 counters were used. In the case of the scintillation fiber counters, the combination of the reference counters and one of the fiber counters was used. From the timing information of three combinations of mean times, the intrinsic time resolutions of each counter were obtained.

For measuring TOF, the pulse height dependence of timing was corrected by using the correlation between TOF of two counters and the ADC information. In the correction, two types of correction functions were used. For the correction of the reference counters and counters with MPPC,

$$f(DE) = a + \frac{b}{\sqrt{DE}} + c \ln(DE) + d(DE), \text{ where } DE = ADC - pedestal \quad (1)$$

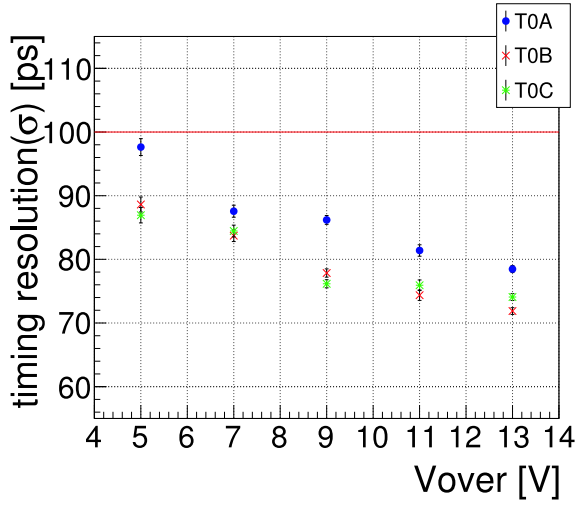


Fig.3. Time resolution of the T0 counters. The horizontal and vertical axis show the time resolution (rms) and over voltage of MPPC, respectively. Blue, red and green points show the time resolution of each counter.

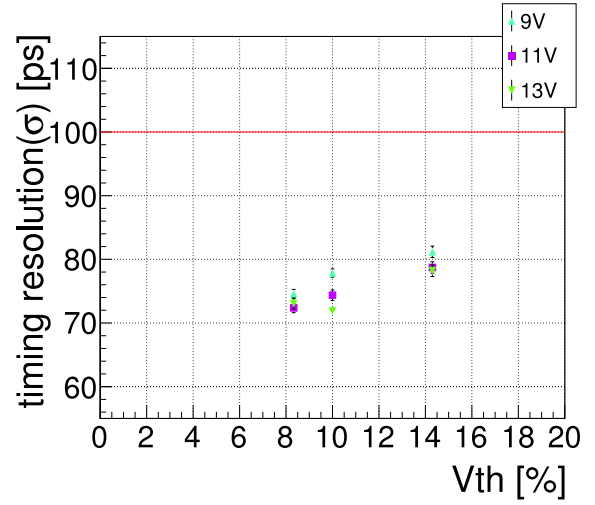


Fig.4. Time resolution of the T0 counters. The horizontal and vertical axis show the time resolution (rms) and signal threshold, respectively. Blue, red and green points show the time resolution of each counter.

and

$$f(DE) = a + \frac{b}{\sqrt{DE}} + c \ln(DE), \text{ where } DE = ADC - pedestal \quad (2)$$

were used, respectively. Figure 1 and Fig. 2 show the correction of the pulse height dependence of the one test T0 counter. Around the energy deposit region by the minimum ionization particle, the correlation was clearly corrected.

The time resolutions of the T0 counters were obtained as a standard deviation of the TOF peak by fitting the Gaussian distribution. On the other hand, the resolutions of the scintillation fiber counters were obtained as full width half maximum the TOF peak. The Time-Of-Flight peak of the scintillation fiber counters had a tail so that the two Gaussian distributions were used for the fitting. For estimating time resolution, we adopted the full width half maximum of the TOF peak.

2.4 Results

2.4.1 T0 counter

Figure 3 shows the time resolution of the T0 counters. The time resolution of 72 ps(rms) was obtained at $V_{over} = 13$ V. From the V_{over} dependence, the time resolution was improved by increasing operation voltage because the photon detection efficiency is increased at the higher V_{over} . The time resolution was improved by changing the signal threshold to be lower values as shown in Fig. 4. Around the 10%-threshold region, there were no drastical improvement of resolution.

By checking the beam irradiated positions, it was found that the difference of time resolution was less than 4 ps so that there was no position dependence along the plastic scintillator as shown in Fig. 5. In the

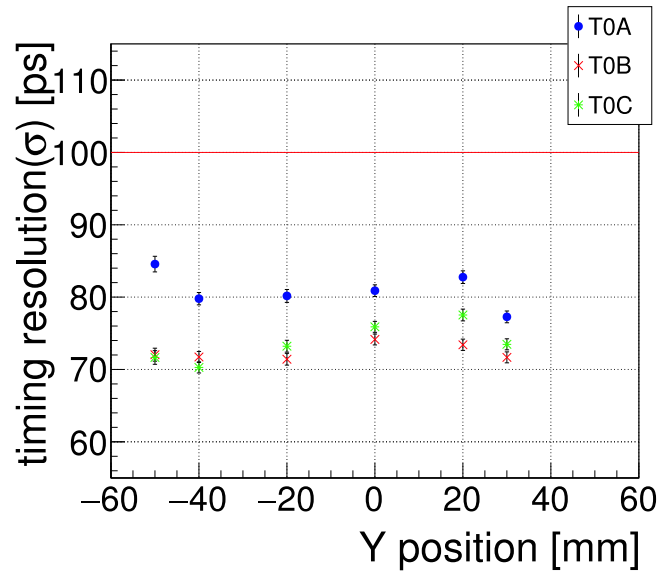


Fig.5. Time resolution of the T0 counters. The horizontal and vertical axis show the time resolution (rms) and signal threshold, respectively. Blue, red and green points show the time resolution of each counter.

spectrometer system for the charmed baryon spectroscopy experiment, the difference of time resolution is negligible small to identify the scattered particle by calculating mass squares with the Time-Of-Flight information. From the results from the time resolution dependence of over voltage of MPPC, signal threshold and beam irradiated position, the requirement of the time resolution of less than 100 ps(rms) was achieved.

2.4.2 Scintillation fiber counter

As shown in Fig. refFig06, the time resolutions of 650 ps(FWHM) and 1050 ps(FWHM) were obtained at $V_{over} = 11$ V for the $\phi 1.0$ -mm and $\phi 0.5$ -mm fibers, respectively. From the V_{over} dependence, the time resolution was improved by increasing operation voltage because the photon detection efficiency is increased at the higher V_{over} . The time resolution was improved by changing the signal threshold to be lower values as show in Fig 7 and Fig 8. In the case of the fiber counter, the fixed values of signal threshold were used. The minimum threshold value corresponded to the 15–20% of the maximum pulse height. Around the 10-mV threshold region, there were $\sim 5\%$ improvement of time resolution. It is confirmed that the time gate of 1 ns can be applied in the tracking analysis to suppress the accidental hits.

2.5 Summary of the first test experiment

By using the combination of the fine segmented plastic scintillator of 3 mm(W) \times 3 mm(T) \times 150 mm(L) and 3-mm squared MPPC which is installed on the fast signal shaping amplifier, it was found for the time resolution of ~ 70 ps(rms) by the means of the Time-Of-Flight measurement. The required time

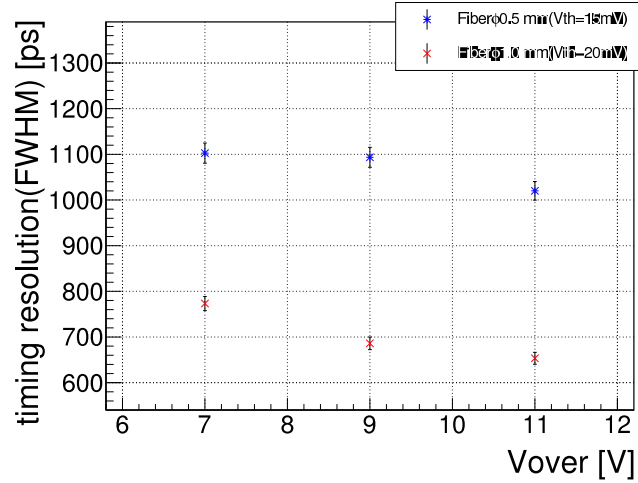


Fig.6. Time resolution of the fiber counters. The horizontal and vertical axis show the time resolution (rms) and over voltage of MPPC, respectively. Red and blue points show the time resolution of counter with the $\phi 1.0$ -mm and $\phi 0.5$ -mm fibers, respectively.

resolution of less than 100 ps(rms) was achieved by taken into account the dependence of over voltage of MPPC, signal threshold and beam irradiated position. The performances of the $\phi 1.0$ -mm and $\phi 0.5$ -mm scintillation fiber counter with a 500-mm and 300-mm length show a time resolution of ~ 650 ps(FWHM) and ~ 1050 ps(FWHM) at $V_{over} = 11$ V, respectively. For suppressing the accidental hits in the tracking analysis, the required time resolution of 1 ns was achieved.

§3. High-rate test of detector elements in October 2017

For the second experiment, the detector elements were irradiated by a high-rate rate beam up to 5 MHz. We evaluated the performances of the time resolution of the test T0 counters by changing beam rates. The preliminary results of the test T0 counters were reported in the second half of the annual reports.

3.1 Test detector elements

The test T0 counters consisted of combinations of a plastic scintillator and an acrylic Čerenkov radiator with MPPC. For the test scintillation counter, a fast timing plastic scintillator(EJ-228) and MPPC(S13360-3050PE) were used. The size of scintillator was 3 mm(W) \times 3 mm(T) \times 150 mm(L). The plastic scintillators were perpendicularly installed to the beam direction and MPPCs were attached to the both edge of the plastic scintillator. For the test Čerenkov counter, an acrylic (PMMA: Polymethyl methacrylate) Čerenkov radiator and MPPC(S13360-3050PE) were used. We used two types of acrylic shapes, called "Bar-type" and "X-type". Bar-type is just acrylic bar with size of 3 mm(W) \times 3 mm(T) \times 150 mm(L) and 1 mm(W) \times 3 mm(T) \times 150 mm(L). The acrylic bar is tilted 48 degrees to the beam axis so that Čerenkov photons reach MPPC placed at an edge of the bar by the shortest path. The number of detected photoelectrons by using this combination was ~ 25 p.e. at the center of radiator from the measurement by using the beam of $\beta \sim 1$. X-type which is a "Cross Shape" acrylic was cut from

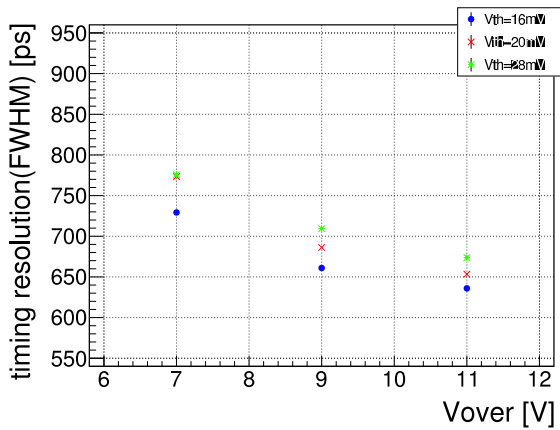


Fig.7. Time resolution of the $\phi 1.0$ -mm fiber counters. The horizontal and vertical axis show the time resolution (rms) and over voltage of MPPC, respectively. Blue, red and green points show the time resolution of each signal threshold value.

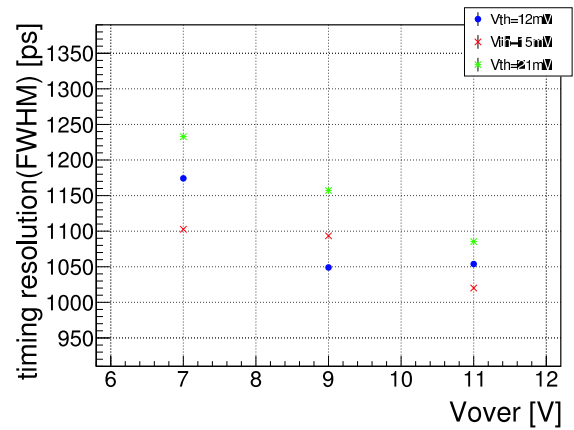


Fig.8. Time resolution of the $\phi 0.5$ -mm fiber counters. The horizontal and vertical axis show the time resolution (rms) and over voltage of MPPC, respectively. Blue, red and green points show the time resolution of each signal threshold value.

an acrylic board having size of 3 mm(W) \times 3 mm(T) \times 150 mm(L) for one side. The opening angle of cross from the beam axis was 48 degrees. MPPCs were attached to the downstream of both edge of the X-type radiator for measuring Čerenkov photons which reach MPPCs by the shortest path. The number of detected photoelectrons by using this combination was ~ 50 p.e. at the center of radiator from the measurement by using the beam of $\beta \sim 1$. For the MPPC signal readout, a shaping amplifier which has a fast operational amplifier(AD8000) was used as described in the Sec. 2. The shaping amplifier was modified to suppress the overshoot after the signal for adding the pole-zero cancellation resistance of 390 Ω on the circuit for 50- μ m pixel MPPC(S13360-3050PE).

For the Time-Of-Flight measurement and making the DAQ trigger signal, two reference counters were also installed at the most upstream and downstream, respectively. The counters consisted of the fast timing plastic scintillator(EJ-228) and a metal packaged photomultiplier(R9880U). The size of the plastic scintillator was 3 mm(W) \times 6 mm(T) \times 30 mm(L). PMTs were attached to the both edge of the plastic scintillator.

In total, 1 plastic scintillation and 3 Čerenkov counters having different shapes were installed. Time resolutions were evaluated from the Time-Of-Flight measurement by using combinations of those counters and reference counters.

3.2 Experimental conditions

The experiment was performed in the second experimental room in the the Research Center for Electron Photon Science(ELPH). Detectors were installed at the downstream of the beam extraction points to the GeV- γ building. For the experiment, the electron and positron beams converted from the extracted γ rays by the 1-mm thick Aluminum cover of the beam pile flange were used. Beam rates were adjusted from the beam current of the accelerator up to 2 MHz/3 mm segment conditions. For obtaining

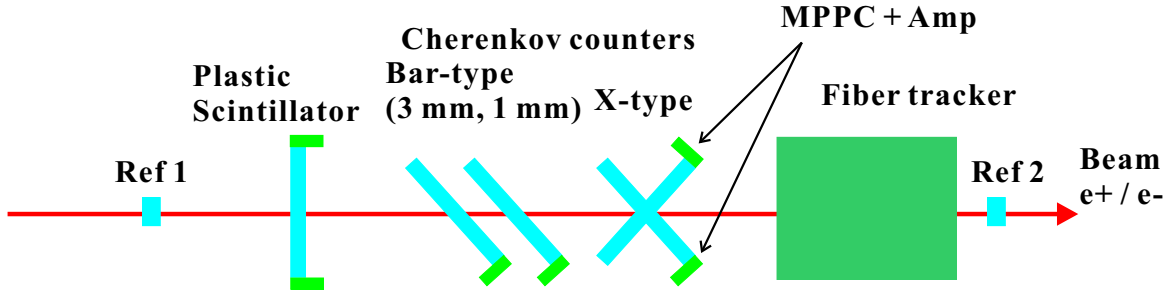


Fig.9. Experimental setup.

more than 3 MHz/3 mm segment conditions, the additional 1-mm thick Aluminum plate was installed on the cover of the beam pile flange, and the beam extraction cycle was changed to be ~ 6 seconds from the usual cycle of 10 seconds. For checking the counting rates of the counters, the visual scaler values in the counting room were roughly measured. In the analysis, the event-by-event scaler values measured by the HUL module [4] were used for determining counting rate of each counter. The hit rate (counts/sec.) of each detector was calculated by running mean in every 200 mseconds to avoid fluctuation caused by dead time of DAQ.

All detectors were installed along the beam line as shown in Fig 9. The reference counters were installed at the most upstream and downstream of the experimental setup. The test T0 counters were installed among the reference counters. The timing coincident signal from the reference counters was used for the DAQ trigger signal. Timing and pulse height information from the counters were measured by the DRS4 module [5] in which a FPGA based High-resolution TDC (HR-TDC) is implemented. The DRS4 module can measure both waveform of input signal and timing signal by discriminator. For obtaining the TOF information, the discriminator signals measured by HR-TDC were used. The waveform information was only used for measuring signal pulse heights for the pulse-height correction and analyzing pile-up effects in the high-rate conditions. The discriminator output signals from DRS4 were used for scalers measured by the HUL module.

For evaluating performances in the high-rate conditions, signal thresholds of 10% level of the pulse height of the minimum ionization signal and 3.5 photoelectrons were used for the scintillation and Čerenkov counters, respectively. The over voltage of MPPC(V_{over}) of 7V was used for the test.

3.3 Analysis

Figure 10 shows the pulse height distribution of the Čerenkov counters. The contribution from the multi-particle hits were small enough. For obtaining the time resolution of the minimum ionization particle conditions and one particle hit condition, of the scintillation and Čerenkov counters, respectively, the higher pulse height events were not used.

The time resolution of each counter was obtained by using the TOF method. In the case of the plastic scintillator and the X-type Čerenkov counters, the signals were measured at the both edge of counters

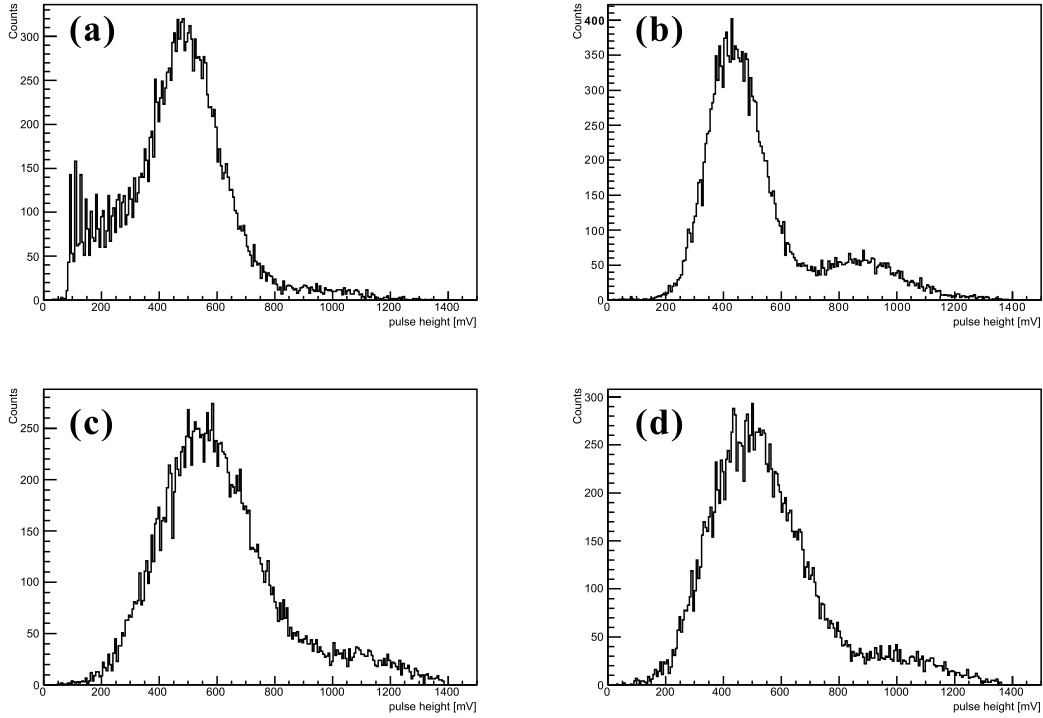


Fig.10. Pulse height distribution of the Čerenkov counters. (a) and (b) show pulse heights of the 1-mm and 3-mm width Bar-type Čerenkov counters. (c) and (d) show pulse heights of top and bottom of the X-type Čerenkov counters, respectively.

so that the mean time of each counter was used for the timing measurement. In the case of the bar-type Čerenkov counters, the signals were measured at one edge of counters. Then, the TOF information was obtained by using the mean times of each counter. From the timing information of three combinations of mean times, the intrinsic time resolutions of each counter were obtained. The combinations between the scintillation counters and reference counters, and between each Čerenkov counter were actually used for the evaluation of the time resolution.

For measuring TOF, the pulse height dependence of timing was corrected by using the correlation between TOF of two counters and the pulse height information. For the correction of the scintillation and Čerenkov counters,

$$f(PH) = a + \frac{b}{\sqrt{PH}} + c \ln(PH), \quad (3)$$

and

$$f(PH) = a + \frac{b}{\sqrt{PH}}, \quad (4)$$

were used, respectively, where "PH" means pulse height measured by the waveform from DRS4.

The event-by-event counting rates of each counter were measured by the HUL scaler. Figure 11 shows the distributions of the event-by-event counting rates of the 3-mm width Bar-type Čerenkov counter. Each distribution shows the counting rate conditions of the average rate of 0.5, 1.5 and 3.0

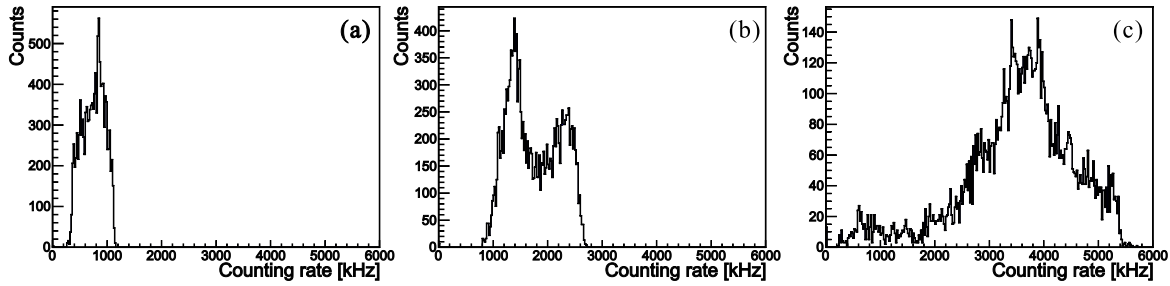


Fig.11. Distributions of the event-by-event counting rate of the 3-mm width Bar-type Čerenkov counter. (a), (b) and (c) show the counting rate conditions of the average rate of 0.5, 1.5 and 3.0 MHz/3-mm segment, respectively.

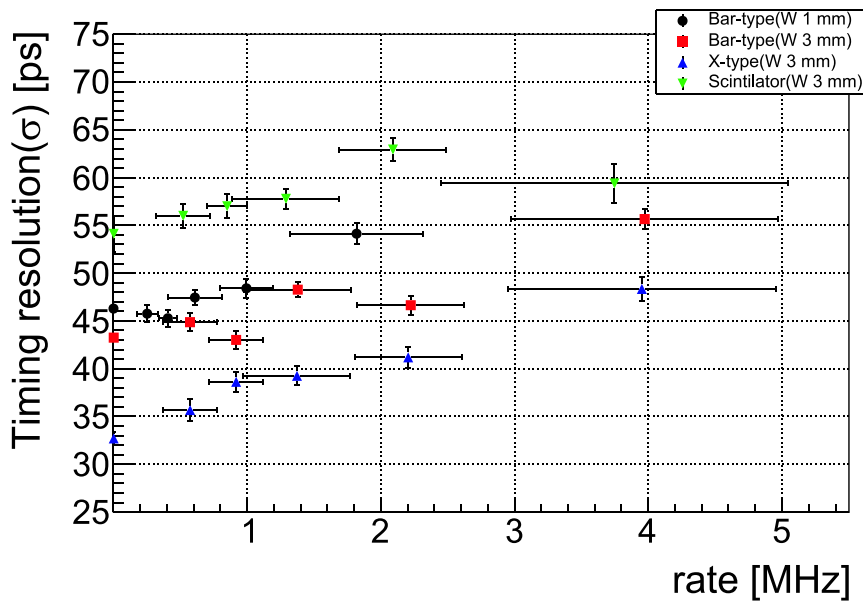


Fig.12. Time resolution by changing counting rate conditions. Horizontal error bars show the range of the counting rate by selecting event-by-event scaler counts.

MHz/3-mm segment. From the distributions of the counting rate of each counter, we selected 5 regions for evaluating the time resolution.

Figure 12 shows the time resolution of each counter by changing the counting rate conditions. Horizontal error bars show the range of the counting rate by selecting event-by-event scaler counts. The result shows that the time resolution of all counters achieved that of less than 70 ps up to 5 MHz. In particular, the X-type Čerenkov counter showed the best time resolution of ~ 50 ps(rms) in the range of 3–5 MHz. In addition, the 1-mm width Bar-type Čerenkov counter showed the same time resolution as of the 3-mm width Bar-type Čerenkov one. It can be explained by the detection of the same number of photon by MPPC without loss by reflection in the PMMA radiator. It means that the total beam rate can be increased when the 1-mm width Čerenkov counters are used. We found that it is possible to use 3 time higher beam in the E50 experiment by using the 1-mm width Čerenkov counters.

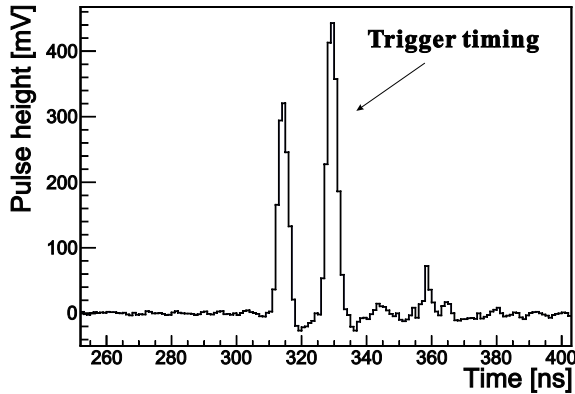


Fig.13. Waveform sample of the 3-mm Bar-type Čerenkov counter at the high-counting rate condition. Signals having events whose timings were 50 ns before the trigger timing was taken as a pile-up event.

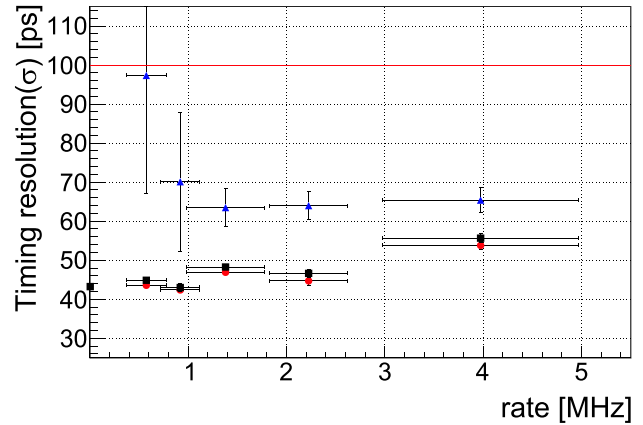


Fig.14. Time resolution of the 3-mm width Bar-type Čerenkov counter by selecting pile-up events. Black, blue and red points show the time resolutions of all events, of pile-up events and without pile-up events, respectively.

The time resolutions became worse by increasing counting rates. Figure 13 shows a waveform sample of the 3-mm Bar-type Čerenkov counter at the high-counting rate condition. From the waveform, the baseline of the trigger timing signal having a pile-up event was affected. Although the signal overshoot had been corrected by implementing the pole-zero cancellation resistance, the ringing pulses after the signal still remained in the overshoot region. For evaluating the effects from the baseline change by the pile-up, signals having events whose timings were 50 ns before the trigger timing was taken as a pile-up event. Figure 14 shows the time resolutions by selecting the pile-up events. By increasing the counting rates, the time resolution became worse. For explaining the dependence of the time resolution in Fig. 14, a base-line shift by pile-up signals causes in part. Response of the amplifier in the DRS4 module may have a rate dependence and affects the time resolution. Even if the time resolution is deteriorated by pile-up, the time resolution (~ 50 ps) better than required on (100 ps) is achieved by using the X-type Čerenkov counter.

3.4 Summary of the second test experiment

The timing counters consist of the combination of a plastic scintillator and an acrylic Čerenkov radiator with MPPC were tested by using the high-counting rate beam by the ELPH facility. By irradiating high-rate beams up to 5 MHz, we found that all counters showed the time resolutions of less than 70 ps(rms). The requirement of the time resolution of less than 100 ps(rms) have been achieved in the high-rate condition even if the time resolution was made worse by pile-up effects and the performances of the DRS4 module. In particular, the Čerenkov counter having "Cross Shape", called X-type, showed the best time resolution of ~ 50 ps(rms) at 3–5 MHz. Therefore, the X-type Čerenkov counter can be the candidate to use the T0 counter for the J-PARC E50 experiment.

Acknowledgment

We would like to acknowledge the outstanding efforts of the staff of the Research Center for Electron Photon Science. We also acknowledge the J-PARC E40 experimental group for accepting to join the test experiment.

References

- [1] H. Noumi *et al.*: J-PARC E50 Proposal (2012).
- [2] Opto-Semiconductor Handbook, Hamamatsu Photonics K.K.
- [3] T. Nishizawa *et al.*, IEEE TNS 61 (2014) 1278.
- [4] R. Honda *et al.*, <http://openit.kek.jp/project/HUL>
- [5] T. N. Tomonori *et al.*, Annual Report 2016 "Development of a FPGA-based high resolution TDC using Xilinx Spartan-6"

(ELPH Experiment : #2876)

Performance of a shower depth measurement method for the KOTO CsI calorimeter

N. Hara¹, K. Kotera^{1*}, T. Mari¹, H. Nanjo¹, H. Nishimiya¹,
Y. Sato¹, N. Shimizu¹, Y. Tajima², T. Yamanaka¹

¹ *Department of Physics, Osaka University, Toyonaka, 560-0043, Japan*

² *Department of Physics, Yamagata University, Yamagata, 990-8560, Japan*

Abstract

We plan to upgrade the J-PARC KOTO CsI calorimeter to distinguish photons and neutrons. Before the upgrade, we tested a prototype detector to confirm that the upgraded calorimeter will have an expected performance at the KOTO experiment.

1 Introduction

The aim of KOTO experiment [1] is to search for a CP-violating neutral kaon decay mode, $K_L \rightarrow \pi^0 \nu \bar{\nu}$. Because the branching ratio predicted by the standard model (SM) is small (3×10^{-11}), the decay mode is sensitive to new physics beyond the SM. The signature of this decay mode has only two photons from a π^0 decay without any other observable particles. Figure 1 shows the KOTO detector. The decay volume shown in the figure is surrounded by a calorimeter [2] and veto counters. The calorimeter measures the energies and hit positions of the two photons, and veto counters detect particles from the background events.

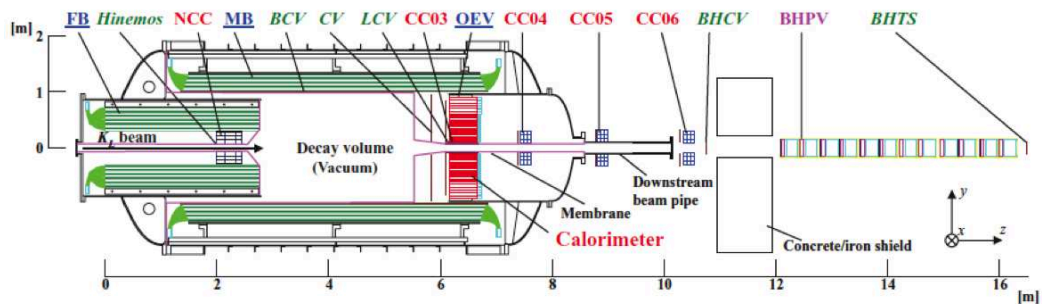


Figure 1: Cut-out view of the KOTO detector assembly. CsI calorimeter is illustrated in red.

The calorimeter is composed of 2716 un-doped CsI crystals stacked inside a 1.9 m diameter cylinder. The central $1.2 \times 1.2 \text{ m}^2$ region is filled with 2240 of $25 \times 25 \times 500 \text{ mm}^3$ crystals (small crystals). The outer region is filled with 476 of $50 \times 50 \times 500 \text{ mm}^3$ crystals (large crystals). Each crystal is read out with a photo-multiplier tube (PMT) attached on its rear surface.

One of the major backgrounds is caused by neutrons directly hitting the calorimeter, making two photon-like clusters. Such events can be rejected if the calorimeter can distinguish between photon clusters and neutron clusters. In addition to rejecting the neutron-induced clusters with the cluster shapes and waveforms, we plan to further reject them by measuring their shower depths. While photons make showers in shallow region, neutrons can make showers at any

*corresponding author: coterra@champ.hep.sci.osaka-u.ac.jp

depths. To measure the shower depths, we will attach silicon photomultipliers (SiPMs) on the front surface of CsI crystals and measure the timing difference between the SiPMs and PMTs.

We have already confirmed that this shower depth measurement method can reduce the neutron background events by more than a factor of 10, even after applying cuts on cluster shapes and waveforms. To confirm the above, we had several bench test, a test beam experiment with neutron and photon mixed beams at the Research Center for Nuclear Physics in Osaka, and a set of simulation studies [3]. After above studies, we have established a method to glue SiPMs on crystals and readout circuits that we will actually use for the KOTO calorimeter. In the experiment reported in this note, we tested these established methods with a small prototype calorimeter to confirm the feasibility of the shower depth measurement, and to measure the timing and energy resolutions under several conditions with the ELPH position beams.

2 Setup

Figure 2 shows a schematic view of the stacked crystals tested at ELPH. It was 3×3 of large crystals surrounding 2×2 of large crystals. As shown in Fig. 3, the detector was placed on a turn table and this table was movable in the horizontal and vertical directions. This setup was placed in a tent with a relativistic humidity of less than 25%. Figure 3 also shows a set of three scintillator counters used to trigger on positrons hitting the CsI crystals in a $10 \times 10 \text{ mm}^2$ area.

On the upstream side of the crystals, we attached SiPMs called Multi-pixel photon counter (MPPC) produced by Hamamatsu K.K. (S13360-6050CS). It has a $6 \times 6 \text{ mm}^2$ sensitive area covered with silicone which is transparent to the ultraviolet (UV) scintillation light (310 nm) from the CsI crystals. One MPPC was used for each small crystal, and four MPPCs were used for each large crystal. The MPPCs were glued on 0.5 mm thick quartz plates which were then glued on the CsI crystals as shown in Fig. 4. This method solves a difficulty to glue the MPPCs with concaved silicone windows on flat crystal surfaces.

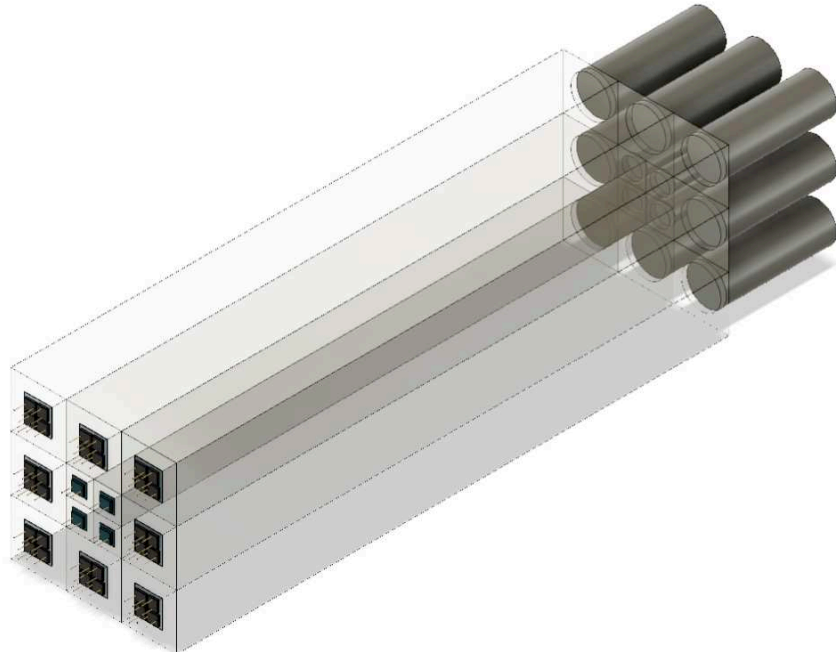


Figure 2: A stack of CsI crystals with MPPCs and PMTs. Each crystal was wrapped with a foil.

The signals from four MPPCs on a single large crystal or four small crystals are merged together to reduce the number of channels and materials of cables in front of the CsI calorimeter in the update design. We had two candidate methods to connect the four MPPCs: (a) the

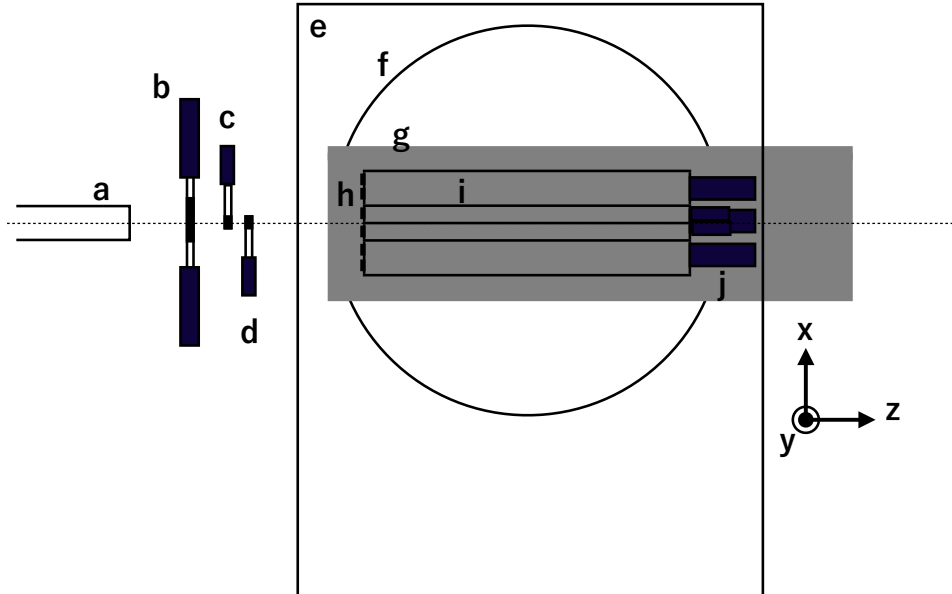


Figure 3: Schematic of beam setup. a: the end of the beam pipe, b: trigger counter to define timing, c and d: trigger counters for defining beam positions ($10.0 \times 10.0 \text{ mm}^2$), e: x-y moving stage, f: turn table, g: detector frame, h: MPPCs, i: CsI crystals, j: PMTs.

MPPC biases are applied in parallel and signals are read out also in parallel (parallel), and (b) the MPPC biases are applied in parallel whereas the high frequency signals are readout in series (hybrid). The latter method was developed for the MEG II upgrade [4]. Figure 5 a) and b) show those two methods. The parallel method has an advantage that the circuit is simple, whereas the pulse becomes wider; the hybrid method makes sharper signals, but the circuit is more complicated. We thus compared the resolutions of timing difference between PMT and MPPCs for the positron showers between those two methods in this study. Moreover, four signals from four of those combined MPPCs were read out together using summing amplifiers as shown in Fig. 5 c) to reduce the number of channels. The signals from the amplifiers were sent to 125 MHz waveform digitizers used for the KOTO detector [5].

To calibrate the timing differences between the MPPC and PMT as a function of the scintillation position, six sets of cosmic trigger counters were located above and below the test detector.

3 Detector configurations

The following detector parameters were changed during the beam time for our studies.

1. The four-MPPC connection methods among “parallel”, “hybrid” and single readout
2. Combinations of CsI crystals for summing amplifiers
3. Beam position, direction, and momentum
4. MPPCs with and without irradiation ¹

These parameters were changed for eight large crystals and four small crystals in several detector configurations for various aims. Figure 6 lists the configurations taken during our three days of run time. In addition to the lists, the beam momentum was scanned in four steps; 200, 400, 600, and 800 MeV/ c for each configuration.

¹The dark current of MPPCs increases proportionally to the irradiation. We prepared MPPCs irradiated with neutrons equivalent to 1.5 times the maximum irradiation estimated for the KOTO running period. The dark current increased by a factor of 100 with the irradiation.

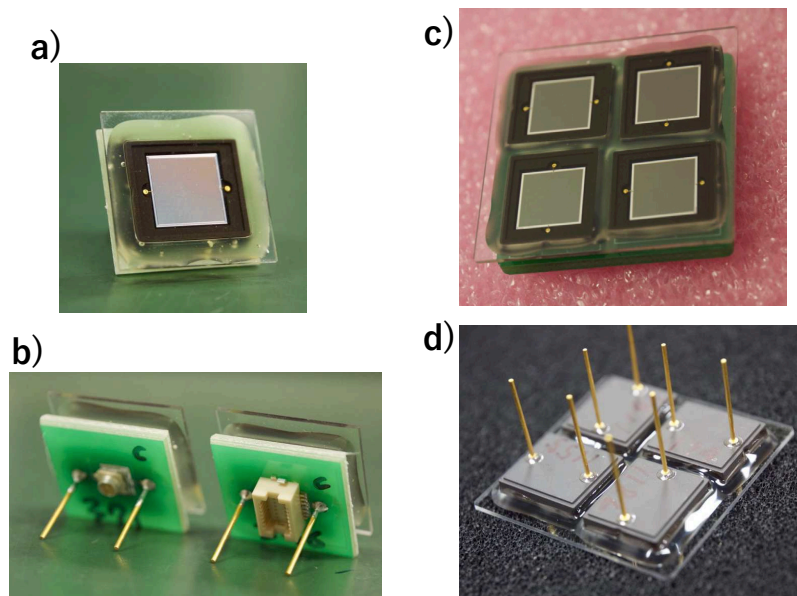


Figure 4: MPPCs glued on quartz plates. a) for small crystal, b) backside view with baseboards for small crystal, c) for large crystal, d) backside view of MPPCs on a crystal without the baseboard to show Alardite around the edges of MPPCs (see text).

4 A preliminary result: Effect of irradiation on MPPCs on the timing resolution

Figure 7 shows the timing resolutions as a function of deposited energy in a crystal. There is no significant difference between the MPPCs with and without the irradiation. We thus concluded that the irradiation during the KOTO running has no effect on the performance of the shower depth measurement method to distinguish neutron showers from photon showers. We also concluded that the MPPC gluing method is feasible, the hybrid connection has better performance than the parallel connection, and the summing amplifier works as expected. The results of other on-going studies will be reported elsewhere.

References

- [1] J. K. Ahn *et al.*, (J-PARC KOTO Collaboration), PTEP, **2017**, 021C01 (2017).
- [2] E. Iwai *et al.*, Nucl. Instrum. Meth. A, **786**, 135 (2015).
- [3] H. Nishimiya, Master thesis, Osaka University (2018) written in Japanese.
- [4] A.M. Baldini *et al.*, Eur. Phys. J. C, **78**: 380 (2018).
M. Ogawa, Master thesis, the University of Tokyo (2016) written in Japanese.
- [5] Y. Sugiyama *et al.*, IEEE Trans. Nucl. Sci., **62**, 1115-1121 (2014).

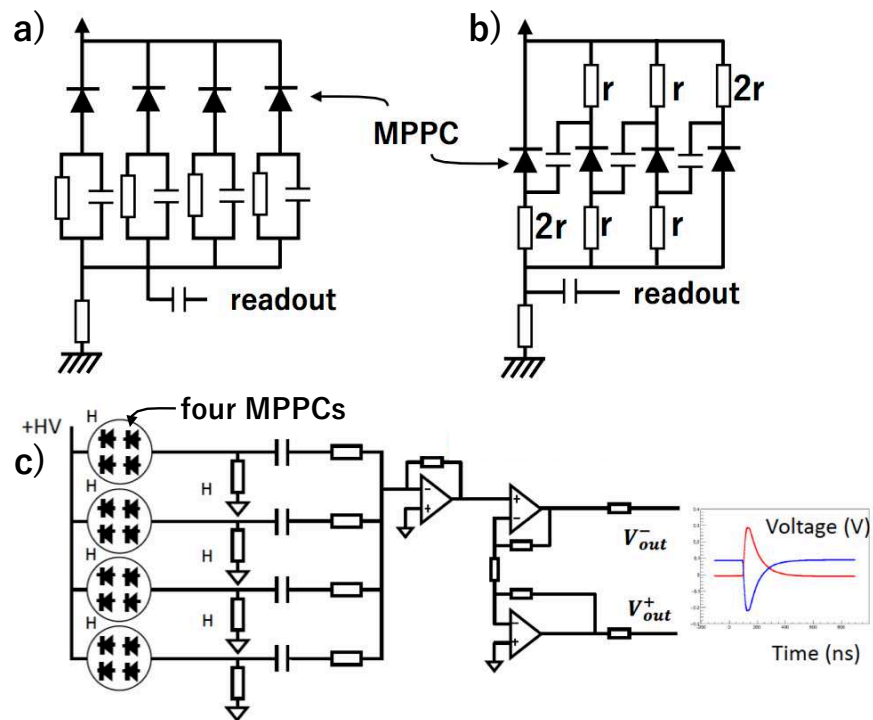


Figure 5: MPPC signal driving circuits. a) parallel connection, b) hybrid connection developed by MEGII collaboration, c) summing amplifier.

Cosmic runs for calibration.		To see performance of seamless crystal (L0 crystal is a seamless crystal (see text))	
to see performance of summed signals: beam hit the large crystal side of center of summed crystals. MPPC=hybrid connection		To see performance of single large crystal.	
to see performance of summed signals: beam hit the small crystal side of center of summed crystals. MPPC=hybrid connection		Cosmic runs for calibration.	
to see performance of the other group of summed signals. MPPC=hybrid connection			

Test 11-0 cosmic run for calibration.		Test 11-4 to see sensitivity to the incident angle, incident angle was scanned: $\phi=20,30,40$ $x=-20, y=50$	
Test 11-1 to see performance of parallel connection (MPPCs on small crystals were connected in parallel).		Test 11-5 dato compare with test 11-1, MPPCs on small crystals were connecte in hybrid.	
Test 11-2 to compare with four-PMMC connected case, small crystals were individually read out.		Test 11-6 to see performance of readout without summing amplifier.	
Test 11-3 to see sensitivity to the incident angle, detector was tilted toward the beam. $\phi=10$ $x=-20, 12.5, 5, y=0$		Test 11-6 to see timing response to high energy beam (-800 MeV), beam was injected from side face: L0=seamless crystal, L7=bonding two crystals.	

Test 12-0 cosmic run for calibration.		Test 12-4 MPPCs were connected in parallel for L6, to see the effect on the large crystal case.	
Test 12-1 L1, L2, L3, and all MPPCs for small crystals were MPPCs irradiated(see text).		Test 12-5 same as the test 12-3, but different injection position.	
Test 12-2 beams were injected from the PMT side.		Test 12-6 to see the effect of MPPCs on the energy resolution of PMT, all MPPCs were removed.	
Test 12-3 to see the effect of irradiation on MPPCs, L1, L2, L3, and all MPPCs for small crystals were MPPCs irradiated(see text).		Test 12-7 same as test 12-6, but different injection position.	

Figure 6: Run configurations and their aims on December 9th, 11th, and 12th data taking. Each color shows crystals that were read out together with a summing amplifier. L0–L7 show ID of large crystals and 0–3 show ID of small crystals. Dots and allows show incidental positions of beams.

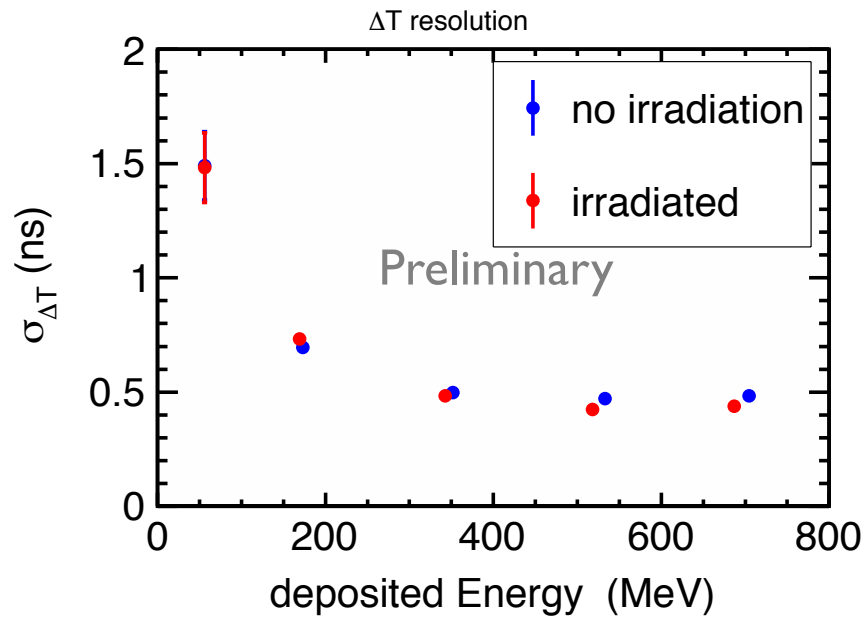


Figure 7: Standard deviation of timing difference between MPPC and PMT as a function of deposited energy. The 60 MeV data were measured with cosmic rays and rest were measured with positrons.

(ELPH Experiment : #2881)

Search for an $\eta'd$ bound state by use of the $\gamma d \rightarrow \eta d$ reaction

H. Fujioka^{1*}, T. Ishikawa², and T. Sekihara³

¹*Department of Physics, Kyoto University, Kyoto 606-8502, Japan*

²*Research Center for Electron Photon Science, Tohoku University, Sendai 982-0826, Japan*

³*Advanced Science Research Center, Japan Atomic Energy Agency, Ibaraki 319-1195, Japan*

Owing to an attractive interaction between an η' meson and a nucleus, the existence of an $\eta'd$ bound state is theoretically predicted. We propose a novel method to investigate this system using the coherent η photoproduction off deuteron, i.e. $\gamma d \rightarrow \eta d$, with the η meson emitted in backward angles. The details are described in a published paper [T. Sekihara, H. Fujioka, and T. Ishikawa: Phys. Rev. C **97** (2018) 045202].

§1. η' meson at finite density

Properties of hadrons is subject to change at finite density, especially as a result of partial restoration of chiral symmetry. For example, the mass of an η' meson, which is approximately $958 \text{ MeV}/c^2$ in vacuum, may be reduced [1–3]. From a theoretical point of view, the mass of an η' meson, the largest among the pseudoscalar meson nonet, is related to the $U_A(1)$ anomaly in QCD. This anomaly effect to push up the η' mass may suppressed at finite density due to partial restoration of chiral symmetry [4]. A mass reduction of an η' meson in a nucleus is equivalent to an attractive interaction between the η' meson and the nucleus, which may lead to the existence of an η' -nucleus bound state, i.e. an η' -mesic nucleus.

Experimental searches for η' -mesic nuclei are being carried out at GSI/FAIR [5], LEPS2 (SPring8) [6], and are planned at BGO-OD (ELSA) [7], with employing missing-mass spectroscopy for (p, d) or (γ, p) reactions on nuclear targets. In general, the sensitivity of finding a peak structure corresponding to an η' -mesic nucleus in a missing-mass spectrum strongly depends on the decay width of the η' -mesic nucleus as well as the signal strength relative to the background level. We propose an alternative method to investigate an η' -mesic nuclei via the s -channel formation [8], in which the background level will be very small and a large decay width is expected not to be troublesome.

§2. $\eta'd$ bound state via coherent η photoproduction off deuteron

If an $\eta'd$ bound state does exist, it may be formed via the $\gamma d \rightarrow [\eta'd]_{\text{bound}} \rightarrow \eta d$ reaction, namely the coherent η photoproduction reaction off deuteron. A detailed description and result of theoretical calculations of the $\eta'd$ bound state and the cross section of $\gamma d \rightarrow \eta d$ are given in Ref. [9].

*Present address: Department of Physics, Tokyo Institute of Technology, Meguro 152-8551, Japan

While the “conventional” coherent process, where a quasi-free η production process ($\gamma N \rightarrow \eta N$) is followed by a recombination of two nucleons into a deuteron, is significant in forward angles with a small momentum transfer, the decay of an $\eta'd$ bound state into ηd will take place isotropically in the center-of-mass frame. As a result, the background η production will be predominantly due to the $[\eta'd]_{\text{bound}}$ formation. Therefore, by looking into the center-of-mass energy dependence of the differential cross section for backward η production, a lineshape of the $\eta'd$ bound state can be obtained.

§3. Feasibility study of a new experiment with FOREST at ELPH

The $\eta'd$ threshold of 2.833 GeV corresponds to the incident photon energy of 1.20 GeV. Therefore, the near-threshold cross section of the $\gamma d \rightarrow \eta d$ reaction can be investigated with a tagged photon beam from the 1.3 GeV electron synchrotron.

While an η meson in the final state can be identified via its 2γ decay with the FOREST spectrometer, the distinction between $\gamma d \rightarrow \eta d$ and $\gamma d \rightarrow \eta pn$ is mandatory; the latter mainly comes from a quasi-free $\gamma N \rightarrow \eta N$ process with a non-negligible differential cross section for backward angles. It calls for a new detector downstream of a liquid deuterium target with the capability of tracking and particle identification. A study with a Monte Carlo simulation is in progress.

Acknowledgment

This work was partly supported by the Grants-in-Aid for Scientific Research from MEXT and JSPS (No. 26400287 and No. 15K17649).

References

- [1] H. Nagahiro and S. Hirenzaki: Phys. Rev. Lett. **94** (2005) 232503; H. Nagahiro, M. Takizawa, and S. Hirenzaki: Phys. Rev. C **74** (2006) 045203.
- [2] S. Sakai and D. Jido: Phys. Rev. C **88** (2013) 064906; Prog. Theor. Exp. Phys. **2017** (2017) 013D01.
- [3] S. D. Bass and A. W. Thomas: Acta Phys. Polon. B **45** (2014) 627.
- [4] D. Jido, H. Nagahiro, and S. Hirenzaki: Phys. Rev. C **85** (2012) 032201(R).
- [5] Y.K. Tanaka *et al.*: Phys. Rev. C **97** (2018) 015202.
- [6] N. Muramatsu: Few-Body Syst. **128** (2013) 997; N. Muramatsu *et al.*: ELPH Annual Report 2015 Vol. 6 (2015) 91.
- [7] V. Metag *et al.*: approved proposal ELSA/03-2012-BGO-OD.
- [8] H. Fujioka *et al.*: Letter of Intent ELPH-2881 (2017).
- [9] T. Sekihara, H. Fujioka, and T. Ishikawa: Phys. Rev. C **97** (2018) 045202.

(ELPH Experiment : #2884)

Development of an Aerogel Cherenkov Counter with Efficient Light Collection

Hiroki Yamada, Nozomu Morita, Kunpei Matsuda, Masahiro Okabe,
Norihito Muramatsu

Research Center for Electron Photon Science, Tohoku University, Sendai 982-0826

We tested the methods to increase the Cherenkov light collection from an aerogel radiator (refractive index = 1.05) to a photomultiplier tube (PMT) through a long air light guide. The test experiment was performed by using a 600 MeV/c positron beam available at Research Center for Electron Photon Science, Tohoku University. The detected light yields at the PMT were compared by changing reflecting material sheets. Several wavelength shifting materials were also coated on the reflecting sheet surface with a solvent to confirm the increase of the light collection. In addition, the dependence of the light collection on the beam injection angle was examined as a basic performance test. These behaviors were confirmed by a Geant4-based Monte Carlo simulation.

エアロジェル・チェレンコフ検出器の集光効率向上を 目指した開発

山田悠樹, 森田希望, 松田薫平, 岡部雅大, 村松憲仁

東北大学電子光理学研究センター 〒982-0826 仙台市太白区三神峯 1-2-1

§ 1. 実験概要

SPring-8 LEPS2 ビームラインのソレノイド実験では、チェレンコフ検出器を置くスペースが非常に限られている。このように既にある設備の制限などによって放射体と光電子増倍管の距離を取らなければならない場合でも高い検出率を得るために、筐体内部の放射体と光電子増倍管の間の部分をエアライトガイドとして用いるというアプローチを試した。またその結果について Geant4 を用いたシミュレーションと比較した。

1.1 内側に張る反射材の工夫

どのような素材がチェレンコフ光の集光を高めるのに最適か、それらの特性について調べた。反射特性による影響やシンチレーションの有無について調べた。

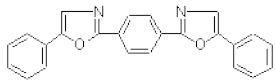
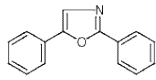
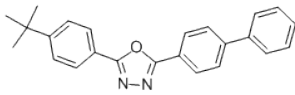
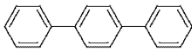
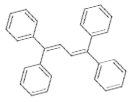
表 1 試験した反射材の種類と特徴

名称	ESR	Teflon(10layer)	Gore-Tex	Tyvek	銀反射シート	アルミシート
素材	ポリエステル系 樹脂	PTTE/ポリテ ラフルオロエチ レン	延伸 PTFE 膜	高密度ポリエ チレン不織布	銀	アルミ
反射率	98.5%	96%	99%	70%	85%	78%
反射特製	鏡面反射	拡散反射	拡散反射	拡散反射	鏡面反射	鏡面反射
シンチレー ション	あり	なし	なし	なし	なし	なし
特徴	380 nm 以下で 反射率が著しく 減衰。	重なるほど、短 波長ほど、優れ た反射率を示 す。	短波長から長 波長まで高い 反射率を保つ が高価。	反射率は低い が、紙状で加 工しやすい。	あまり試されて いない。	反射率は低い が、波長による 影響は小さい。

1.2 波長変換剤

チェレンコフ光は紫外領域の発光強度が大きく、この部分の光電子増倍管の感度がよくない。そこで波長変換剤を反射材上に塗布して用いることで、放出光を可視光領域に変換して集光・検出効率を上げられないか実験した。

表 2 反射材に塗布した波長変換剤の種類と特徴

薬品名	構造	吸収波長 (nm)	発光波長 (nm)
POPOP		308-337	407-454
PPO		248-337	359-391
BPBD		266-337	341-392
pT		248-308	322-364
TPB		128-250	400-460

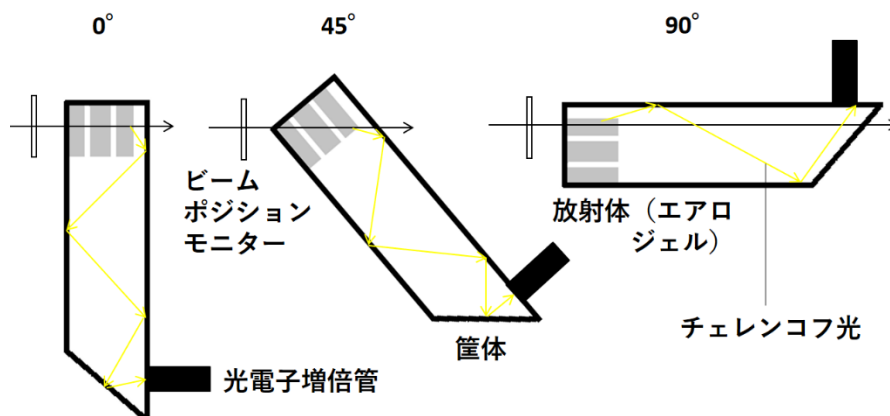


図1 実験セットアップ

§ 2. データ収集

今回の実験は、エアロジェルから出るチェレンコフ光の量の変化を確認するものである。実験では東北大学電子光物理学研究センターの陽電子ビーム（運動量 600 MeV/c）を使用した。図1に示すように、20 mm厚の同じエアロジェル（屈折率 1.05）を3つ重ねて使用し、筐体と垂直（0°）、45°、90°（筐体に付けている光電子増倍管と逆側）からビームを入射した。今回作成したデータ収集系のブロック図は図2の通りである。陽電子ビームによって出たチェレンコフ光であると判断するために、今回の実験で用いた筐体の前にビームポジションモニターを置いた。そこからの信号がある場合のみトリガー信号を作成し、それによるゲート信号に入ったチェレンコフ光の量をADCで測定した。ビームポジションモニターの信号をTDCで測定し、同期した信号を見ているかオフラインで確認した。

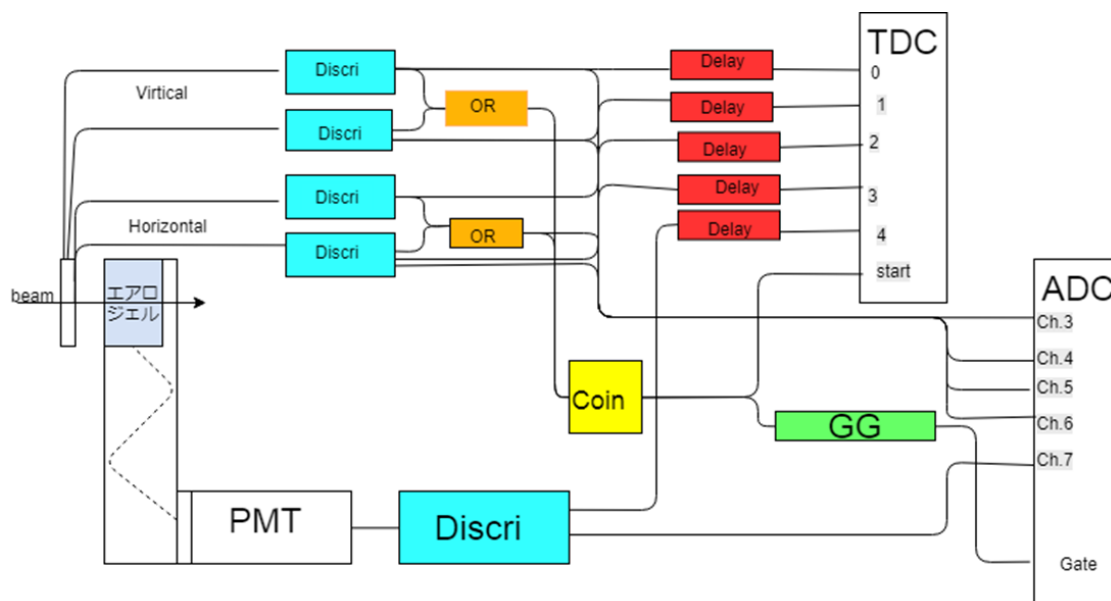


図2 データ収集系のブロック図

§ 3. データ解析

3.1 解析手法

今回の実験は、反射材及び波長変換剤を変化させることで集光効率の改善を試みた。また、集光効率のビーム入射角度による依存性を確認した。

具体的には、以下の光量を比較した。

$$\text{yield} = \text{mean of ADC values} - \text{ADC pedestal}$$

3.2 反射材による違い

結果は図3に示す。図から分かるように yield が最も優れていたのは ESR で 92% だった。また、鏡面反射と拡散反射では有為な差が得られなかったが反射率による依存性は見られ、反射率が上昇するごとに yield は指数関数的に向上している(図4参照)。ただし、Gore-Tex のみは相関から大きく外れた結果を見せた。また、計算によって求めた光電子数と図4の対応関係より、ADC Channel と光電子数の関係式を導いた。

$$\text{光電子数} = 0.083 \times \text{ADC Channel}$$

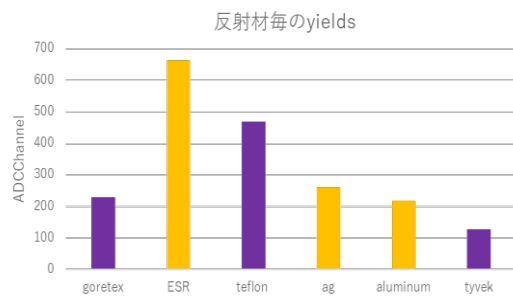


図3 反射材ごとの yield：紫が拡散反射、オレンジが鏡面反射の反射材で、反射率の良い物ほど左に並べた。

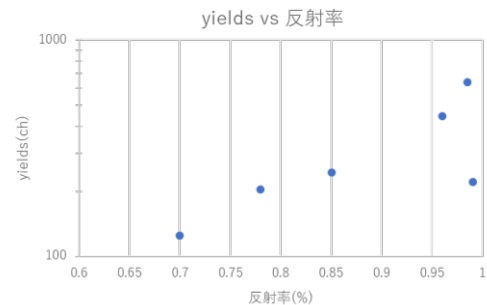


図4 yield vs 反射率

3.3 波長変換剤による違い

結果は図5に示す。全ての波長変換剤で、塗布した筐体が塗布しない筐体に比べて有為な優れた集光効率を見せた。最も向上したのは TPB を塗布した筐体で、yield が 1.2 倍になった。

3.4 角度依存の結果

結果は図6に示す。また、筐体の角度による影響のみを見るため、ビームがエアロジェルを通る厚さによる生成光子数の増減と透過長による影響を考慮して、エアロジェルの厚さを0度のときにそろえる補正をかけた結果も並べてある。

結果から分かるように0度と45度のときはほとんど変わらないが90度のときに yield が 1.6 倍に向上していることが分かる。これは、90度のときに最も反射回数を抑えられているからだと考えられる。



図5 波長変換剤ごとの yield：一番左が何も塗布していない筐体。

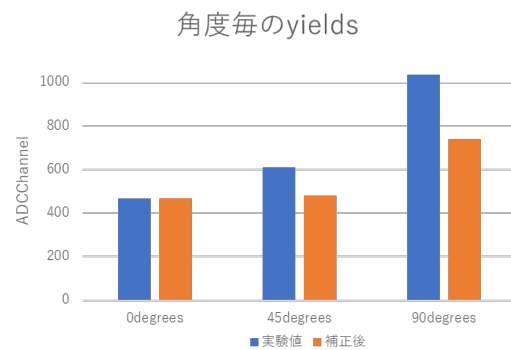


図6 角度ごとの yield

§ 4. モンテカルロ・シミュレーション

Geant4 を用いて、実験での反射材比較と光量の角度依存の結果を、モデル化したシミュレーションで理解できるか確認した。特に、実験では生成光子数を測ることが出来ない点を補う。条件として、反射材の性質(反射率と反射の種類)、筐体とエアロジェル配置、陽電子ビームの方向を指定した。

4.1 角度依存シミュレーション

エアロジェルに対して陽電子ビームが図7左のような方向から入射することを考えた結果、図7右のような結果が得られた。

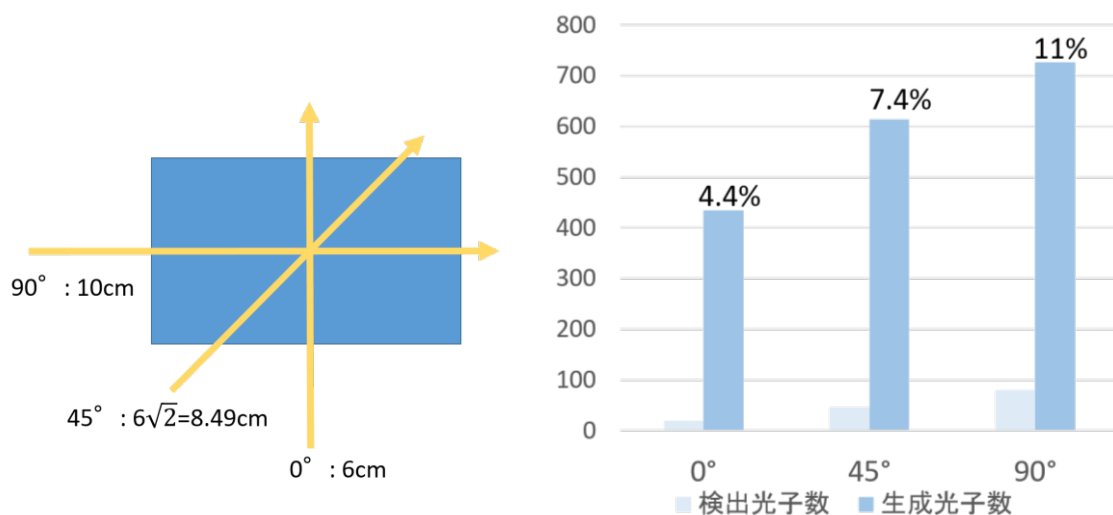


図7 シミュレーションによる光量の入射角度依存性

エアロジェルを陽電子が通過する距離が長いほど多くの光子を放出すると考えられるので、0°、45°、90°に生成光子数が多くなる。角度変化により光路も変化し、反射回数は0°、45°、90°の順に17.1、13.0、13.0回であった。反射回数が少ないほど減衰も少ない。

4.2 反射材比較シミュレーション

各反射材について角度 0° で入射したとき図8のような結果になった。反射率と集光率には相関があることが分かったが、鏡面反射と拡散反射では有意な差は見られなかった。

また、どの反射材でもイベントの検出効率は100%だった。実験では検出できないイベントが多いことから筐体の隙間や反射材のゆがみによる影響が大きいと考えられる。

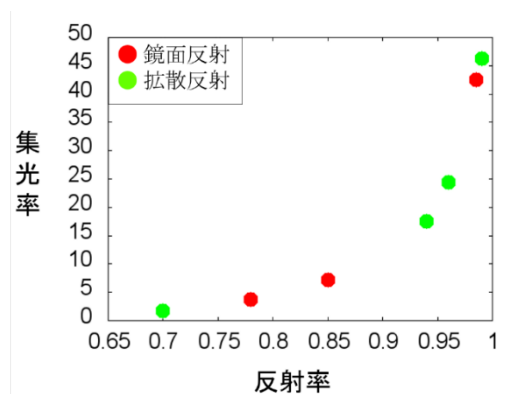


図8 シミュレーションによる反射材の比較

(ELPH Experiment : #2889)

Development of Electro-magnetic Sampling Calorimeter with Active Absorbers

Y. Hasegawa¹, H. Ishihama¹, H. Sato², T. Takeshita¹, R. Terada¹,
Y. Yamashita¹, and Y. Yoshimura¹

¹*Faculty of Science, Shinshu University, Matsumoto, Japan*

²*Institute of Particle and Nuclear Studies, KEK, Tsukuba, Japan*

High performance sampling calorimeter is indispensable for physics measurement at collider experiment and its performance improvement is very important. We made electro-magnetic calorimeter with optical readout from absorber material and tested with positron beam at ELPH at Tohoku University. This calorimeter obtains high performance by acquiring information on the absorption layer using transparent lead glass that can detect Cherenkov light of the absorber with photosensor. In this report, performances of this calorimeter are presented.

§1. Introduction

We are developing full active electro-magnetic calorimeter consisting of active absorption layers and very fine granulated detection layers. The lead glass calorimeter has good energy resolution by energy measurement of electrons and photons, and similarly reads out the absorption layer of lead glass to obtain dramatically higher performance than ordinary sampling calorimeter. In addition, it has a high position resolution of incident photons and electrons due to the high granulated detection layers. Such an sampling electro-magnetic calorimeter could be applied for many experiments which needed both high energy resolution and position / angle resolution. The performances have been verified with the positron beam at ELPH, Tohoku University.

1.1 Electro-magnetic calorimeter and experimental setup

The active absorber EM calorimeter has been introduced in order to improve both energy resolution and position/angle resolution for photons. The calorimeter detector system is shown in figure 1.

This calorimeter consisting of active lead glass absorption layer and very fine granulated detection scintillator layer [1]. The size of one layer of lead glass is $9 \times 9 \times 4 \text{ cm}^3$. It incorporates 9 lead glass blocks of $3 \times 3 \times 4 \text{ cm}^3$ in sizes. For each block aiming at improving the light collection, it is wrapped with a reflector film, and light is not leaked to other blocks. Also, we installed $3 \times 3 \text{ mm}^2$ MPPC [2] for reading Cherenkov light in each block. It is a detector using 27 lead glass blocks in total and 27 MPPCs.

For the scintillator layer, we made $1 \times 1 \text{ cm}^2$ resolution by overlapping strip scintillators in the X and Y directions. In each direction, nine strip scintillators of $18 \times 1 \times 0.3 \text{ cm}^3$ were combined to create a size of $18 \times 9 \text{ cm}^2$. Since they are placed in the X direction and the Y direction, the effective sensitivity

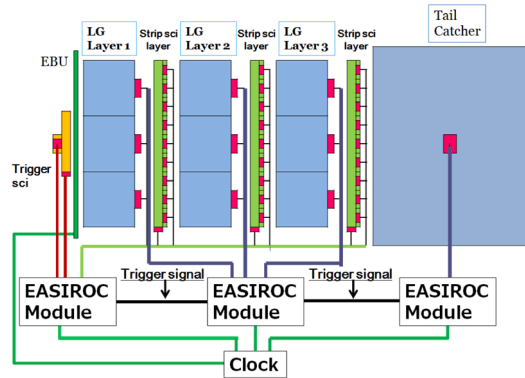


Fig.1. It becomes the DAQ system of this detector. The red line is the output of the trigger detector. The black line is used to divide the trigger signal from the trigger detector. Green line, clock distribution for synchronization of read. Yellow green line read $1 \times 1 \text{ mm}^2$ MPPC of scintillator. Purple line read of MPPC of $3 \times 3 \text{ mm}^2$ of segmented lead glass and $12 \times 12 \text{ mm}^2$ of tail catcher.

region covers the same size as the lead glass absorption layer, $9 \times 9 \text{ cm}^2$. The scintillator is wrapped with a reflector film for each strip in order to improve light yield. Also, because of the uniformity of the scintillator response, the wave length shifted fiber is embedded in the groove. Light reading is performed with one MPPC for each strip, and a total of 54 scintillators and MPPCs of $1 \times 1 \text{ mm}^2$ are used.

Tail Cather is made of a large single lead glass of $12 \text{ cm} \times 25 \text{ cm} \times 12 \text{ cm}$ and uses one MPPC of $12 \times 12 \text{ mm}^2$ to measure the energy at the last detector. At the forefront, we installed the XY trigger and set it to trigger in the $1 \text{ cm} \times 1 \text{ cm}$ area by taking the coincidence each scintillator.

All the signals from MPPCs in total 85 channels are read by three EASIROC modules which had been developed for the MPPC read out through the ether-net [3].

1.2 Results

Here we show some results of the active absorber calorimeter tested at ELPH 2017.

The calibration result of the center channel of layer 2 together with tail catcher is shown in figure 2. Calibration was done by combining with a tail catcher, although calibration was difficult because the back leaked only with lead glass block alone. It is found that the energy dropped by the lead glass block has a good correlation with the ADC count.

Further analysis is going on.

1.3 Conclusion

A sandwich type EM calorimeter has been constructed and tested. A new feature for the detector is using active absorber with segmentation. It became possible to perform calibration of each lead glass block by beam.

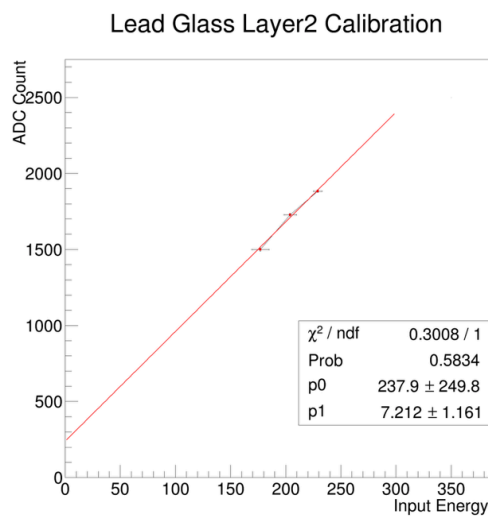


Fig.2. Correspondence between energy and ADC in the center channel of the second layer of lead glass.

Acknowledgment

The authors thank the ELPH accelerator staff for providing the primary electron beam with good quality. They are grateful to M. Miyabe for his technical support in preparation for the measurements.

References

- [1] SF6W lead glass employed at TOPAZ , Kawabata *et al.*: NIM A **270** (1988) 11. *et. al.* NIM A 270(1988) 11.
- [2] MPPC trade mark of Hamamatsu Photonics CO.
- [3] Isamu Nakamura, N.Ishijima, K.Hanagaki, K.Yoshimura, Y.Nakai, K.Ueno, *et al.*:Nuclear Instruments and Methods in Physics Research A **787** (2015) 376-379.

Influence of the Coulomb distortion on the measurement of the proton radius

T. Tamae and T. Suda

Research Center for Electron Photon Science, Tohoku University, Sendai, 982-0826

Influence of the Coulomb distortion on the measurement of the root-mean square (rms) radius of the proton is investigated through a phase-shift calculation. It is shown that the effect is severe even for the lightest nucleus, proton, and disturbs obtaining the rms radius of the proton from Taylor's expansion. However it is found that this difficulty is removed almost completely by the so-called Feshbach correction. In addition, it is confirmed in this study that the cross section has no model dependence in the energy region we are planning to perform the experiment, and depends on only the rms radius.

§1. Introduction

The discrepancy of the proton charge radius measured by electron scattering ($R=0.88$ fm) [1] and muonic hydrogen ($R=0.84$ fm) [2–4] is known as “proton radius puzzle”. In most cases of electron scattering, the experimental data are analyzed in the framework of the plane-wave Born-approximation (PWBA), where no Coulomb distortion is considered. Rosenfelder [5] reanalyzed data measured at Mainz [6–9] and Saskatoon [10] and pointed out that the Coulomb correction increases the proton radius by about (0.008-0.013) fm, the opposite direction of the value from muonic atom. Energies of experiments we are planning to explore is much lower than their energies and the influence from the Coulomb distortion is unknown. In this report we investigate the influence of the Coulomb distortion to our experiment. we treat only the Coulomb scattering, and the magnetic part is separately considered.

§2. Electron Scattering

In the framework of the PWBA, the electron scattering cross section is represented by

$$\frac{d\sigma}{d\Omega} = \sigma_M f_{rec}^{-1} \left[\frac{G_E^2 + \tau G_M^2}{1 + \tau} + 2\tau G_M^2 \tan^2 \frac{\theta}{2} \right] \quad (1)$$

where $\tau = \frac{q^2}{4M^2}$, m being the proton mass. σ_M and f_{rec} are the Mott cross section and a recoil factor, respectively. The information of the structure for the proton is included in the charge and magnetic form factors: G_E , G_M , and in the non-relativistic limit the charge form factor is obtained by the Fourier transformation of the charge distribution $\rho(r)$ as

$$G_E(q) = \int \rho(r) e^{i\vec{r}\cdot\vec{q}} d\vec{r}. \quad (2)$$

As a guide for the following discussion, the charge form factors calculated by the Fourier transformation of the charge density with different proton sizes (rms) are shown in Fig. 1; the difference is a little less than 0.1% at $q^2=0.3 \text{ fm}^{-2}$ for a difference of 0.1 fm of the proton size. At the limit of $q = 0$, the form factor can be Taylor's expansion as

$$G_C = 1 - \frac{1}{6} \langle r^2 \rangle q^2 + \frac{1}{120} \langle r^4 \rangle q^4 - \dots \quad (3)$$

However the cross section is not represented by the simple formula of Eq. (1), if the Coulomb distortion is large.

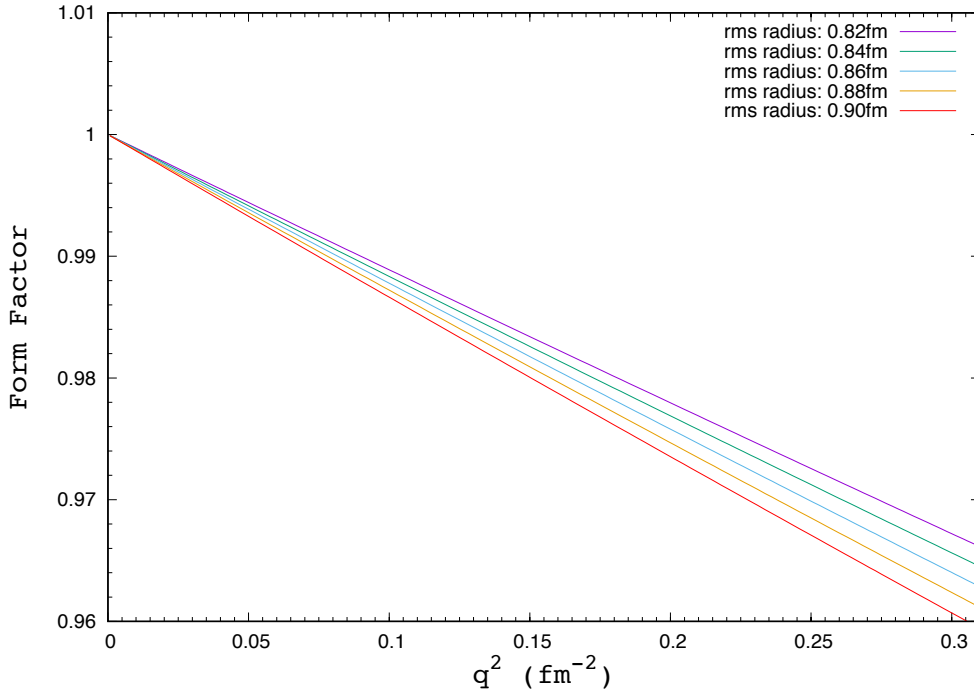


Fig.1. Form factors calculated by the Fourier transformation of the charge density with different rms radius.

§3. Coulomb distortion

In this section, the cross section of the Coulomb scattering including the Coulomb distortion is calculated. Usually the cross section affected by the Coulomb distortion is calculated in the phase-shift analysis [11] using programs such as DREPHA [12] and MEFCAL [13]; they were partly revised, which is described in Appendix. If the effect from the Coulomb distortion is small, the charge form factor defined from the cross section obtained in the phase-shift analysis $(\frac{d\sigma}{d\Omega})_{PSA}$ as

$$|G_C(\vec{q})|_{PSA}^2 = \frac{(\frac{d\sigma}{d\Omega})_{PSA}}{\sigma_M f_{rec}^{-1}} \quad (4)$$

may be in agreement with that from Eq. (2). In this situation, the form factors obtained with different electron energies are expected to scale in the momentum transfer. Figure 2 shows the form factor with the Coulomb distortion calculated using Eq. (4) for rms=0.88 fm; the results calculated by DREPHA and

MEFCAL agree in an order of 10^{-4} in our energy region. It is obvious that the form factors obtained for different electron energies do not scale and the derivative at low momentum transfers changes. It shows that the proton size cannot be derived using a Taylor's expansion of the form factor. It should be noted that the form factor exceeds one at low momentum transfers; it is completely different from the form factor obtained by the Fourier transformation of the charge distribution.

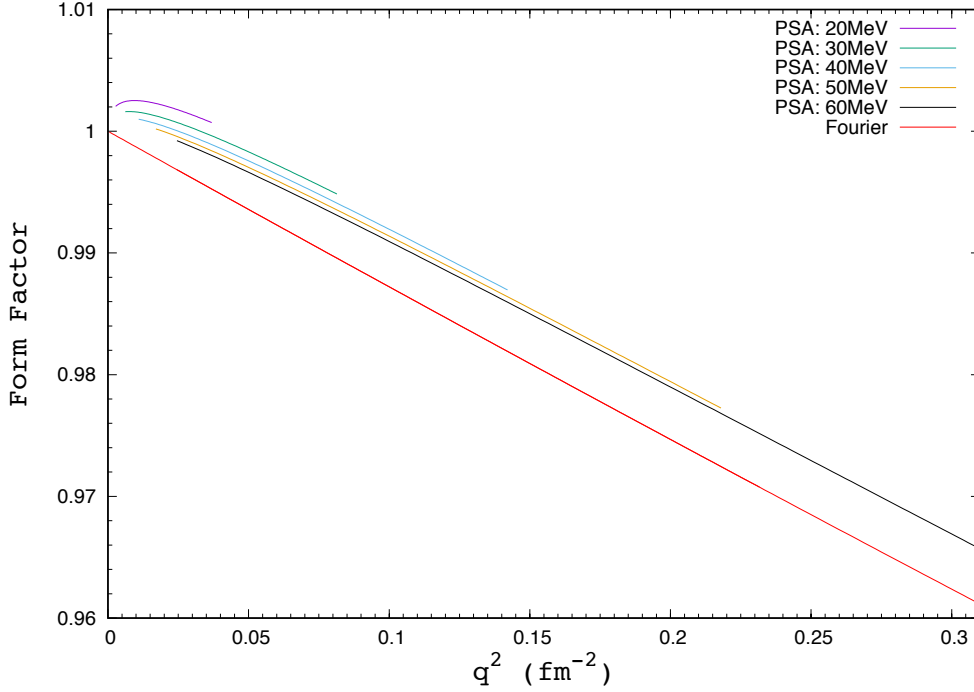


Fig.2. Form factors calculated by the phase-shift analysis (PSA) at $\theta=30^\circ \sim 150^\circ$ and that obtained by the Fourier transformation of the charge density (Fourier) for rms=0.88 fm. The form factors (PSA) calculated with different electron energies do not scale and are different from the result of the Fourier transformation.

§4. Feshbach correction

The Mott cross section is derived from the lowest order Born approximation of the phase shift analysis [14, 15]. Feshbach *et al.* [16, 17] obtained a correction factor from the second-order Born approximation; it is represented as a simple form:

$$f_{Feshbach} = 1 + \frac{Z\alpha\pi (\sin \frac{\theta}{2} - \sin^2 \frac{\theta}{2})}{\cos^2 \frac{\theta}{2}} \quad (5)$$

Equation (4) is rewritten with the Feshbach correction as

$$|G_C(\vec{q})|_{Feshbach}^2 = \frac{\left(\frac{d\sigma}{d\Omega}\right)_{PSA}}{\sigma_M f_{rec}^{-1} f_{Feshbach}}. \quad (6)$$

The form factor calculated using Eq. (6) with a proton size of 0.88 fm is compared to the PWBA in Fig. 3. Results calculated at different electron energies lies on a line, and the difference to the PWBA is small; the rms radius obtained by fitting with a Taylor's series is 0.882 fm. The result shows that the Coulomb distortion can be mostly removed using the Feshbach correction. In order to confirm it

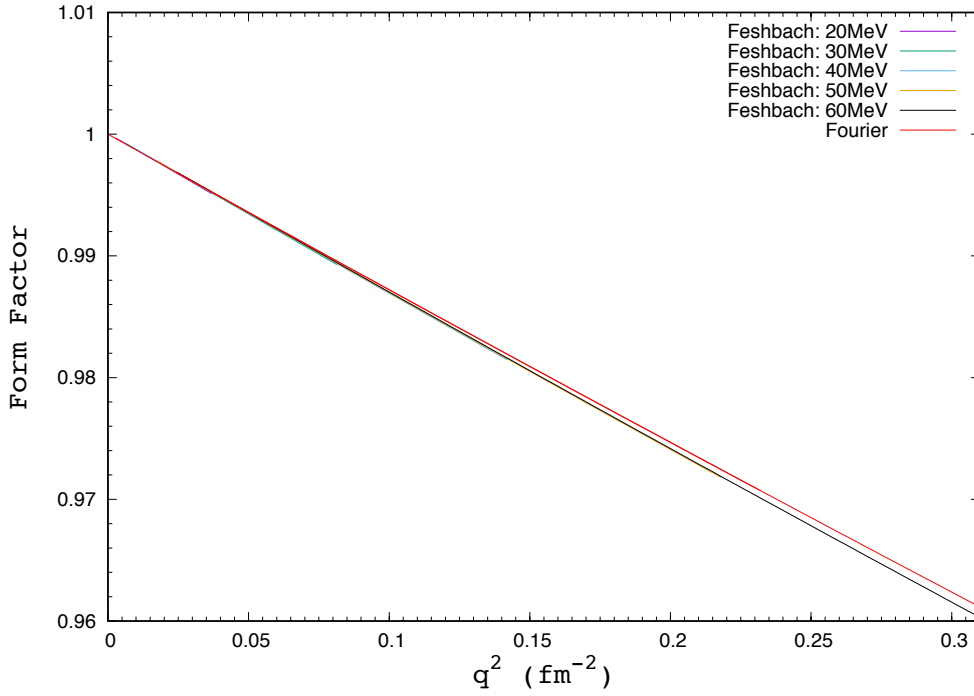


Fig.3. Form factors calculated with the Feshbach correction for rms=0.88 fm. The results for different electron energies align on a lower line close to the line of the Fourier transformation.

numerically, the cross section for the point charge was calculated in the phase-shift calculation. The values of $\sigma_M f_{rec}^{-1} f_{Feshbach}$ agree the results of the phase-shift calculation in the order of 10^{-4} .

§5. Model Dependence

Calculations in the previous section were performed for a dipole form factor (exponential-type charge distribution). Although it is traditionally used for the proton, the charge distribution has a cusp at the origin. Kelly [18] showed the gaussian-like distribution is better to describe experimental data obtained at JLab. The charge distributions of an exponential-type and a gaussian with a same rms radius (0.88 fm) are shown in Fig. 4. The form factors with Feshbach correction calculated using these distributions at an electron energy of 50 MeV are compared in Fig. 5. The difference is very small for low momentum transfers we are planning for experiments, and the cross section is determined by only the rms radius; the difference becomes clearer at higher momentum transfers than 1fm^{-1} as Sick and Trautmann [19] pointed out.

§6. Results

Influence of the Coulomb distortion on the measurement of the proton size were investigated. It was found that the influence was not negligible even for the proton; it is impossible to obtain the proton size by Taylor's expansion of the form factor under a simple PWBA scheme. However, the Feshbach correction reduces the influence dramatically, and we found that the proton size can be obtained with

sufficient accuracy. We compared the form factors for different charge distribution with same rms radius: an exponential-type and a gaussian. Although the charge distributions are much different, the two form

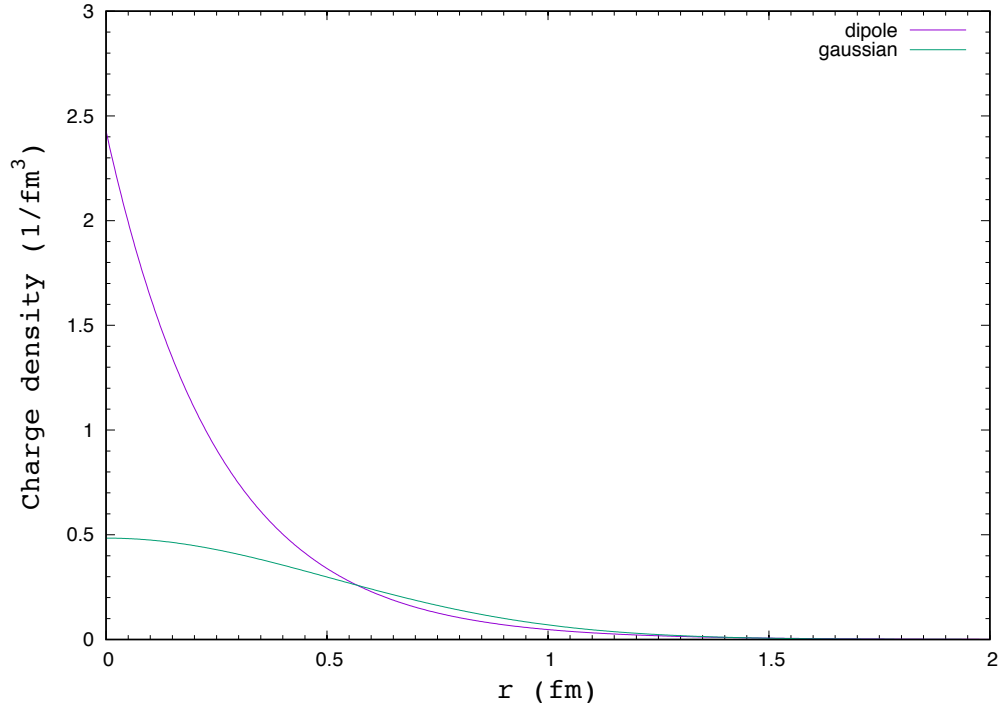


Fig.4. Charge distribution of dipole form factor (exponential) and a gaussian. rms=0.88 fm

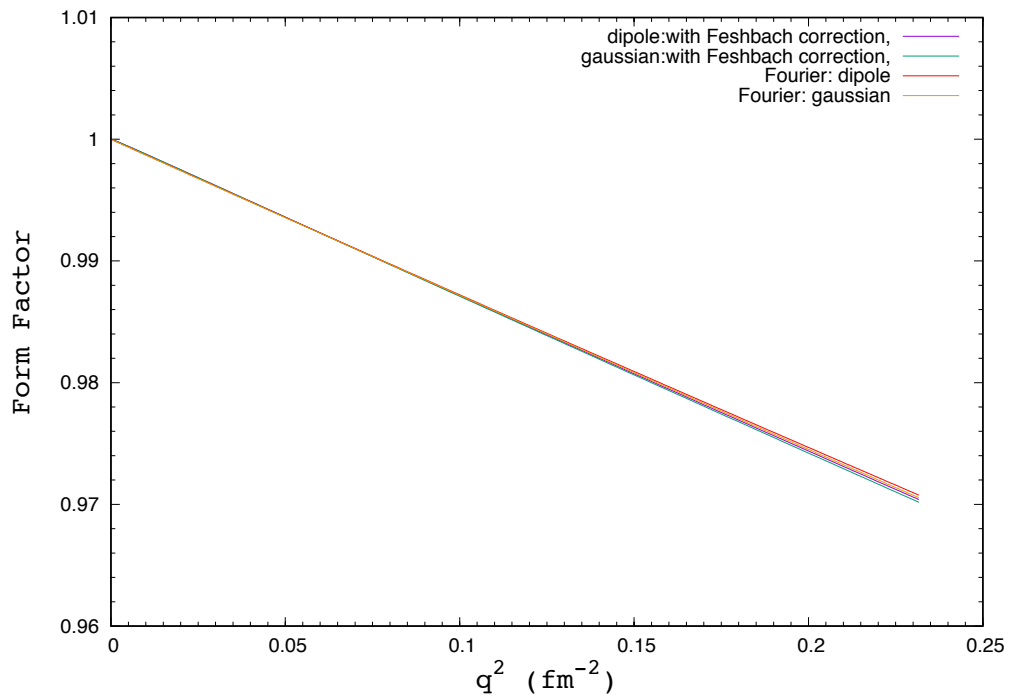


Fig.5. Form factors for different charge distribution with the Feshbach correction: an exponential (dipole form factor) and a gaussian. $E_e=50$ MeV, rms=0.88 fm

factors are hard to be distinguished from each other at $q^2 \leq 0.3 \text{ fm}^{-2}$. As a result, we can conclude that the rms radius of the proton can be obtained without the influence of the Coulomb distortion and difference of the charge distribution. However, It should be noted that the result is true only for the Coulomb part. The contribution of magnetic scattering is not negligible at backward angles: about 70% of the Coulomb part at $E_e = 60 \text{ MeV}$ and $\theta_e = 150^\circ$, for example. In addition, the Feshbach correction does not insure the usability of the Rosenbluth separation. The Rosenbluth separation is useful only in the case where the Feshbach correction can remove the contribution of the Coulomb distortion on magnetic scattering too. If not, the contribution of the magnetic part must be separately subtracted from the measured cross section at first. This problem will be discussed in future.

Appendix

A. Phase-shift Analysis

In this section, the phase-shift calculation of electron scattering is briefly reviewed [11]. The differential cross section of electron scattering is given using a scattering amplitude $f(\theta)$ as follows:

$$\frac{d\sigma}{d\Omega} = |f(\theta)|^2 \left(1 + \tan^2 \frac{1}{2}\theta\right) = |f(\theta)|^2 \sec^2 \frac{1}{2}\theta. \quad (\text{A1})$$

The amplitude is given using Legendre functions and phase-shifts η_j as

$$f(\theta) = \frac{1}{2ik} \sum \exp 2i\eta_j \left(j + \frac{1}{2}\right) \left(P_{j-\frac{1}{2}}(\cos \theta) + P_{j+\frac{1}{2}}(\cos \theta)\right). \quad (\text{A2})$$

However, the amplitude does not converge because of the long-range nature of the Coulomb field. So the amplitude is divided into two parts as

$$f(\theta) = f_c(\theta) + (f(\theta) - f_c(\theta)) \quad (\text{A3})$$

where $f_c(\theta)$ is the Coulomb scattering amplitude, and $f(\theta) - f_c(\theta)$ converges; the treatment of $f_c(\theta)$, which does not converge, is described later. The Dirac equation is written by decomposing into partial waves characterized by the total angular momentum j ,

$$\begin{aligned} \frac{dG_j}{dx} - \frac{j+\frac{1}{2}}{x}G_j + (1-v(x))F_j &= 0, \\ \frac{dF_j}{dx} + \frac{j+\frac{1}{2}}{x}F_j - (1-v(x))G_j &= 0, \end{aligned} \quad (\text{A4})$$

where $x = kr$, $v(x) = V(r)/E$, $k = \frac{E}{\hbar c}$. Individual asymptotic partial waves have the form

$$G_j(x) \sim \sin \left[x + \gamma \ln 2x - \frac{1}{2} \left(j - \frac{1}{2} \right) \pi + \eta_j \right] \quad (\text{A5})$$

where $\gamma = \frac{Ze^2}{\hbar c}$. Wave functions outside the nucleus, which are known as Coulomb functions, are written at a point $x_0 (= kr_0)$ (the ‘‘fitting-on point’’) as two pair of linearly independent functions

$$\begin{aligned} G_j(x_0) &= C_j G_{j,R}(x_0) + D_j G_{j,I}(x_0), \\ F_j(x_0) &= C_j F_{j,R}(x_0) + D_j F_{j,I}(x_0), \end{aligned} \quad (\text{A6})$$

where the subscript $R(I)$ denotes a Coulomb function which is regular (irregular) at the origin. The asymptotic forms of the Coulomb functions are known:

$$\begin{aligned} G_{j,R}(x) &\sim \sin \left[x + \gamma \ln 2x - \frac{1}{2} \left(j - \frac{1}{2} \right) \pi + \eta_j^c \right], \\ G_{j,I}(x) &\sim \sin \left[x + \gamma \ln 2x - \frac{1}{2} \left(j - \frac{1}{2} \right) \pi + \eta_j'^c \right]. \end{aligned} \quad (\text{A7})$$

By comparing Eqs. (A5) and (A7) using Eq. (A6), we obtain

$$\tan(\eta_j - \eta_j^c) = \frac{D_j \sin(\eta_j'^c - \eta_j^c)}{C_j + D_j \cos(\eta_j'^c - \eta_j^c)} = \frac{\sin(\eta_j'^c - \eta_j^c)}{\frac{C_j}{D_j} + \cos(\eta_j'^c - \eta_j^c)}, \quad (\text{A8})$$

where

$$\frac{C_j}{D_j} = \frac{\mathbf{G}_j(x_0)\mathbf{F}_{jI}(x_0) - \mathbf{F}_j(x_0)\mathbf{G}_{jI}(x_0)}{\mathbf{F}_j(x_0)\mathbf{G}_{jR}(x_0) - \mathbf{G}_j\mathbf{F}_{jR}(x_0)}. \quad (\text{A9})$$

The cross section for an extended charge is calculating by inserting η_j obtained here into Eq. (A2), and that for a point charge can be obtained by putting $\eta_j = \eta_j^c$. The Coulomb phase-shifts are calculated by

$$\exp i(\eta_j^c - \eta_j'^c) = \frac{1 - i \tan \pi(j + \frac{1}{2} - \rho_j) \coth \pi \gamma}{|1 - i \tan \pi(j + \frac{1}{2} - \rho_j) \coth \pi \gamma|} \exp \left\{ -i\pi \left(j + \frac{1}{2} - \rho_j \right) \right\}, \quad (\text{A10})$$

$$\exp 2i\eta_j^c = \frac{\rho_j - i\gamma}{j + \frac{1}{2}} \frac{\Gamma(\rho_j - i\gamma)}{\Gamma(\rho_j + i\gamma)} \exp \left\{ i\pi \left(j + \frac{1}{2} - \rho_j \right) \right\}. \quad (\text{A11})$$

where $\rho_j = \sqrt{(j + \frac{1}{2})^2 - \gamma^2}$, $\gamma = \frac{Ze^2}{\hbar c}$. In the case where the nucleus has an extended charge distribution, we solve the Dirac equation and obtain $\frac{C_j}{D_j}$ by Eq. (A9); the procedure is described in Appendix B. As mentioned above the Coulomb scattering amplitude f_c does not converge. Yennie *et al.* multiplied f_c by a function, which vanishes at $\theta=0$, $(1 - \cos \theta)^m$; the new amplitude

$$f_c^{(m)} = (1 - \cos \theta)^m f_c = \frac{1}{2ik} \sum a_l^{(m)} (P_l(\cos \theta)) \quad (\text{A12})$$

rapidly converges and the Legendre polynomials are obtained. The final scattering amplitude is calculated by

$$f(\theta) = \frac{f_c^{(m)}(\theta)}{(1 - \cos \theta)^m} + (f(\theta) - f_c(\theta)); \quad (\text{A13})$$

it converges except the very close angles near $\theta=0$. The choice of $m=3$ is recommended in Yennie's paper, but $m=4$ is used in the original DREPHA program. We found $m=2$ is preferable in order to reduce an oscillation at forward angles.

B. Solving Dirac Equation

We solve the Dirac equation step-by-step from the origin to the fitting-on radius like a Runge-Kutta method, but with higher accuracy [20]. Let $\mathbf{y}_n = \begin{pmatrix} \mathbf{F}_j \\ \mathbf{G}_j \end{pmatrix}_n$ be a radial wave functions at x_n and \mathbf{y}_{n+1} at $x_{n+1} = x_n + h$. The wave functions and the Coulomb potential are expanded into Taylor's series, then

$$\mathbf{y}_{n+1} = \mathbf{y}_n + h\mathbf{y}_n' + h^2 \frac{1}{2!} \mathbf{y}_n'' + h^3 \frac{1}{3!} \mathbf{y}_n''' + h^4 \frac{1}{4!} \mathbf{y}_n^{(4)} + h^5 \frac{1}{5!} \mathbf{y}_n^{(5)} + h^6 \frac{1}{6!} \mathbf{y}_n^{(6)} + h^7 \frac{1}{7!} \mathbf{y}_n^{(7)} + h^8 \frac{1}{8!} \mathbf{y}_n^{(8)} + \dots \quad (\text{B1})$$

By differentiation and multiplication of h on eq. (B1), we get

$$\begin{aligned}
hy_{n+1}' &= hy_n' + h^2y_n'' + h^3\frac{1}{2!}y_n''' + h^4\frac{1}{3!}y_n^{(4)} + h^5\frac{1}{4!}y_n^{(5)} + h^6\frac{1}{5!}y_n^{(6)} \\
&\quad + h^7\frac{1}{6!}y_n^{(7)} + h^8\frac{1}{7!}y_n^{(8)} + \dots \\
h^2y_{n+1}'' &= h^2y_n'' + h^3y_n''' + h^4\frac{1}{2!}y_n^{(4)} + h^5\frac{1}{3!}y_n^{(5)} + h^6\frac{1}{4!}y_n^{(6)} \\
&\quad + h^7\frac{1}{5!}y_n^{(7)} + h^8\frac{1}{6!}y_n^{(8)} + \dots \\
h^3y_{n+1}''' &= h^3y_n''' + h^4y_n^{(4)} + h^5\frac{1}{2!}y_n^{(5)} + h^6\frac{1}{3!}y_n^{(6)} \\
&\quad + h^7\frac{1}{4!}y_n^{(7)} + h^8\frac{1}{5!}y_n^{(8)} + \dots \\
h^4y_{n+1}^{(4)} &= h^4y_n^{(4)} + h^5y_n^{(5)} + h^6\frac{1}{2!}y_n^{(6)} \\
&\quad + h^7\frac{1}{3!}y_n^{(7)} + h^8\frac{1}{4!}y_n^{(8)} + \dots
\end{aligned} \tag{B2}$$

From Eqs. (B1) and (B2) after multiplying appropriate factors a_i , we can make coefficients of h^5 to h^8 in the right side to be zero; the error is an order of h^9 as a result. The coefficients a_i are derived by solving equations

$$\begin{pmatrix} \frac{1}{4!} & \frac{1}{3!} & \frac{1}{2!} & 1 \\ \frac{1}{5!} & \frac{1}{4!} & \frac{1}{3!} & \frac{1}{2!} \\ \frac{1}{6!} & \frac{1}{5!} & \frac{1}{4!} & \frac{1}{3!} \\ \frac{1}{7!} & \frac{1}{6!} & \frac{1}{5!} & \frac{1}{4!} \end{pmatrix} \begin{pmatrix} a_1 \\ a_2 \\ a_3 \\ a_4 \end{pmatrix} = \begin{pmatrix} -\frac{1}{5!} \\ -\frac{1}{6!} \\ -\frac{1}{7!} \\ -\frac{1}{8!} \end{pmatrix}. \tag{B3}$$

The solution is
$$\begin{pmatrix} a_1 \\ a_2 \\ a_3 \\ a_4 \end{pmatrix} = \begin{pmatrix} -\frac{1}{2} \\ \frac{3}{28} \\ -\frac{1}{84} \\ \frac{1}{1680} \end{pmatrix}.$$

Finally we get

$$\begin{aligned}
y_{n+1} - \frac{1}{2}hy_{n+1}' + \frac{3}{28}h^2y_{n+1}'' - \frac{1}{84}h^3y_{n+1}''' + \frac{1}{1680}h^4y_{n+1}^{(4)} \\
= y_n + \frac{1}{2}hy_n' + \frac{3}{28}h^2y_n'' + \frac{1}{84}h^3y_n''' + \frac{1}{1680}h^4y_n^{(4)} + O(h^9),
\end{aligned} \tag{B4}$$

then

$$\begin{aligned}
y_{n+1} &= \left(1 - \frac{1}{2}hA_{n+1} + \frac{3}{28}h^2B_{n+1} - \frac{1}{84}h^3C_{n+1} + \frac{1}{1680}h^4D_{n+1}\right)^{-1} \\
&\quad \left(y_n + \frac{1}{2}hy_n' + \frac{3}{28}h^2y_n'' + \frac{1}{84}h^3y_n''' + \frac{1}{1680}h^4y_n^{(4)} + O(h^9)\right)
\end{aligned} \tag{B5}$$

This equation includes derivatives of y_{n+1} up to fourth order; they can be represented using the Dirac equation;

$$y'_{n+1} = \begin{pmatrix} -\frac{L}{x_{n+1}} & 1 - v_{n+1} \\ -(1 - v_{n+1}) & \frac{L}{x_{n+1}} \end{pmatrix} \begin{pmatrix} F_j \\ G_j \end{pmatrix} \equiv A_{n+1}y_{n+1}, \tag{B6}$$

where

$$x_{n+1} = kr_{n+1}, \quad v_{n+1} = \frac{V_{n+1}}{E}, \quad k = \frac{E}{\hbar c}. \tag{B7}$$

Higher order derivatives are obtained successively, for example,

$$y''_{n+1} \equiv B_{n+1}y_{n+1} = A'_{n+1}y_{n+1} + A_{n+1}y'_{n+1} = (A'_{n+1} + A^2_{n+1})y_{n+1}. \tag{B8}$$

Using obtained matrices, y_{n+1} can be calculated from y_n with Eq. (B5). In DREPHA, a procedure with a lower order of accuracy is used at $x \leq 1$, which is shown in Yennie's paper, and Eq. (B5) at $x > 1$. The procedure using Eq. (B5) through a whole region makes no difference.

B-1. Initial values at the origin

If initial values of the wave function at the origin ($x=0$) is fixed, the wave function can be calculated using Eq. (B5) throughout a whole region. Around the origin, $G(x)$, $F(x)$, and $v(x)$ are expanded into Taylor's series:

$$\begin{aligned} G(x) &= G(0) + G'(0)x + \frac{1}{2!}G''(0)x^2 + \frac{1}{3!}G'''(0)x^3 + \frac{1}{4!}G^{(4)}(0)x^4 + \dots \\ F(x) &= F(0) + F'(0)x + \frac{1}{2!}F''(0)x^2 + \frac{1}{3!}F'''(0)x^3 + \frac{1}{4!}F^{(4)}(0)x^4 + \dots \\ v(x) &= v(0) + v'(0)x + \frac{1}{2!}v''(0)x^2 + \frac{1}{3!}v'''(0)x^3 + \dots \end{aligned} \quad (\text{B9})$$

By using these expressions in the Dirac equation, we obtain

$$\begin{aligned} &G'(0) + G''(0)x + \frac{1}{2!}G'''(0)x^2 + \frac{1}{3!}G^{(4)}(0)x^3 + \dots \\ &\quad -L \left\{ \frac{G(0)}{x} + G'(0) + \frac{1}{2!}G''(0)x + \frac{1}{3!}G'''(0)x^2 + \frac{1}{4!}G^{(4)}(0)x^3 + \dots \right\} \\ &+ \left\{ 1 - v(0) - v'(0)x - \frac{1}{2!}v''(0)x^2 - \frac{1}{3!}v'''(0)x^3 + \dots \right\} \\ &\quad \left\{ F(0) + F'(0)x + \frac{1}{2!}F''(0)x^2 + \frac{1}{3!}F'''(0)x^3 + \frac{1}{4!}F^{(4)}(0)x^4 + \dots \right\} = 0 \end{aligned} \quad (\text{B10})$$

and

$$\begin{aligned} &F'(0) + F''(0)x + \frac{1}{2!}F'''(0)x^2 + \frac{1}{3!}F^{(4)}(0)x^3 + \dots \\ &\quad +L \left\{ \frac{F(0)}{x} + F'(0) + \frac{1}{2!}F''(0)x + \frac{1}{3!}F'''(0)x^2 + \frac{1}{4!}F^{(4)}(0)x^3 + \dots \right\} \\ &+ \left(-1 + v(0) + v'(0)x + \frac{1}{2!}v''(0)x^2 + \frac{1}{3!}v'''(0)x^3 + \dots \right) \\ &\quad \left\{ G(0) + G'(0)x + \frac{1}{2!}G''(0)x^2 + \frac{1}{3!}G'''(0)x^3 + \frac{1}{4!}G^{(4)}(0)x^4 + \dots \right\} = 0 \end{aligned} \quad (\text{B11})$$

Applying an undetermined coefficient method on individual orders of x terms, we can fix the coefficients $G(0), F(0), G'(0), F'(0), \dots$. The first non-zero coefficient is $G^{(L)}(0)$. As the solution is unfixed (arbitrary), we can put it as

$$\frac{1}{L!}G^{(L)}(0)x^L = 1. \quad (\text{B12})$$

Coefficients of higher derivatives can be obtained successively, and finally we can calculate initial values around the origin using

$$\begin{aligned} G(x) &= \frac{1}{L!}G^{(L)}(0)x^L + \frac{1}{(L+1)!}G^{(L+1)}(0)x^{L+1} + \frac{1}{(L+2)!}G^{(L+2)}(0)x^{L+2} \\ &\quad + \frac{1}{(L+3)!}G^{(L+3)}(0)x^{L+3} + \frac{1}{(L+4)!}G^{(L+4)}(0)x^{L+4} \end{aligned} \quad (\text{B13})$$

and

$$\begin{aligned} F(x) &= \frac{1}{(L+1)!}F^{(L+1)}(0)x^{L+1} + \frac{1}{(L+2)!}F^{(L+2)}(0)x^{L+2} \\ &\quad + \frac{1}{(L+3)!}F^{(L+3)}(0)x^{L+3} + \frac{1}{(L+4)!}F^{(L+4)}(0)x^{L+4}. \end{aligned} \quad (\text{B14})$$

It should be noted that the phase-shift is not affected by the choice of $G^{(L)}(0)$ because it is determined from the ratio of G and F .

B-2. Coulomb potential

The Coulomb potential is calculated by the expression

$$-v(x) = \frac{Ze^2}{\hbar c} \frac{1}{x} \left\{ \int_0^x \rho(x')4\pi x'^2 dx' \right\} + \frac{Ze^2}{\hbar c} \int_x^\infty \rho(x')4\pi x' dx' \quad (\text{B15})$$

where the charge density ρ is normalized as

$$\int_0^\infty \rho(x') 4\pi x'^2 dx' = 1. \quad (\text{B16})$$

In the program DREPHA, the value of $v(x)$ and its Taylor's series at the origin is numerically calculated. In MEFCAL, on the contrary, they are calculated directly from Fourier-Bessel parameters of the charge distribution, where the charge distribution is represented as

$$\rho(r) = \sum_i a_i \frac{\sin(i\pi r/R)}{i\pi r/R}, \quad (\text{B17})$$

where R is the cut-off radius. Then,

$$-v(r) = \frac{4Ze^2R^3}{\pi^2\hbar c} \frac{1}{r} \sum_i \frac{a_i}{i^3} \sin(i\pi r/R) + \frac{Z^2e^2}{\hbar c R}. \quad (\text{B18})$$

The potential at the origin and their derivatives, which are used in Eqs. (B10) and (B11), are

$$\begin{aligned} -v(0) &= \frac{Ze^2}{\hbar c} \int_0^R \rho(r') 4\pi r' dr' = \frac{4Ze^2R^3}{\pi^2\hbar c} \left\{ -\frac{\pi}{Rr} \sum_i \frac{a_i}{i^2} \frac{\sin(i\pi r/R)}{i\pi r/R} + \frac{\pi}{R} \frac{1}{r} \sum_i \frac{a_i}{i^2} \cos(i\pi r/R) \right\} \\ &= \frac{8Ze^2R^2}{\pi\hbar c} \sum_{k.\text{odd}} \frac{a_k}{k^2}, \end{aligned} \quad (\text{B19})$$

$$-v'(0) = 0,$$

$$-v''(0) = -\frac{4\pi Ze^2}{\hbar c} \sum_i a_i, \quad (\text{B20})$$

$$-v'''(0) = 0.$$

B-2-1. Exponential-type charge distribution (Dipole form factor)

In the case of the proton, as the dipole form factor is used as a standard form factor, it was added in the programs. The charge distribution is given as

$$\rho(r) = \frac{a^3}{8\pi} \exp(-ar). \quad (\text{B21})$$

As the exponential-type distribution has a cusp at the origin, its Fourier-Bessel expansion does not converge. Instead the potential and its Taylor's series at the origin can be obtained analytically as

$$-v(r) = -\frac{Ze^2}{\hbar c} \left\{ \frac{1}{r} \{ \exp(-ar) - 1 \} + \frac{a}{2} \exp(-ar) \right\} \quad (\text{B22})$$

$$-v(0) = \frac{Ze^2a}{2\hbar c},$$

$$-v'(0) = 0,$$

$$-v''(0) = -\frac{Ze^2a^3}{6\hbar c}, \quad (\text{B23})$$

$$-v'''(0) = \frac{Ze^2a^4}{4\hbar c}.$$

These formulae were added in MEFCAL.

Acknowledgments

We would like to thank Professors J. Friedrich, L. Lapikás, and H. Blok for their useful discussions. This work was supported by Grants-in-Aid for Scientific Reserch (JP16H06340).

References

- [1] for example, J.C. Bernauer *et al.*, Phys. Rev. C 90 (2014) 015206 and its references.
- [2] R. Pohl *et al.*, Nature 466 (2010) 213.
- [3] R. Pohl *et al.*, Science 353 (2016) 669.
- [4] C. Peset and A. Pineda, Eur. Phys. J. A51 (2015) 156.
- [5] R. Rosenfelder, Phys. Lett. 27 (2000) 381.
- [6] G.G. Simon *et al.*, Nucl. Phys. A 333 (1980) 38.
- [7] G.G. Simon *et al.*, Nucl. Phys. A 364 (1981) 285.
- [8] F. Borkowski *et al.*, Nucl. Phys. A 222 (1974) 269.
- [9] F. Borkowski *et al.*, Nucl. Phys. B 93 (1975) 461.
- [10] J.J. Murphy, Y.M. Shin and D.M. Skopik, Phys. Rev. C 9 (1974) 2125.
- [11] D.R. Yennie, D.G. Ravenhall, and R.N. Wilson, Phys. Rev. 95 (1954) 500.
- [12] B. Dreher, DREPHA: a phase-shift calculation code for electron scattering developed at Mainz, communicated by J. Friedrich.
- [13] MEFCAL: a phase-shift calculation code for electron scattering written in NIKHEF, communicated by L. Lapikás and H. Blok.
- [14] N.F. Mott, Roy. Soc. A124 (1929) 425.
- [15] N.F. Mott and H.S.W. Massey, The Theory of Atomic Collisions 2nd edi, Oxford, p80.
- [16] W.A. McKinley Jr. and H.Feshbach, Phys. Rev. 74 (1948) 1759.
- [17] H. Feshbach, Phys. Rev. 88 (1952) 295.
- [18] J.J. Kelly, Phys. Rev. C66 (2002) 065203.
- [19] I. Sick and D. Trautmann, Phys. Rev. C95 (2017) 012501(R).
- [20] W.E. Milne, Numerical Solution of Differential Equations (Dover Publications, Inc., New York) (1953) .

Light meson photoproduction off the proton at the SPring-8 BGOegg experiment

Norihito Muramatsu¹, Jung Keun Ahn¹³, Wen-Chen Chang⁴, Jia-Ye Chen⁵,
 Schin Daté³, Toshiyuki Gogami², Hiroto Hamano², Toshikazu Hashimoto⁶,
 Qing Hua He¹, Kenneth Hicks⁷, Toshihiko Hiraiwa², Yuki Honda¹,
 Tomoaki Hotta², Yosuke Inoue¹, Takatsugu Ishikawa¹, Igal Jaegle⁸,
 Ja Min Jo¹³, Yuuto Kasamatsu², Hitoshi Katsuragawa², Satoshi Kido¹,
 Yuki Yoshi Kon², Shinichi Masumoto⁹, Yuji Matsumura¹, Katsumasa Miki¹²,
 Manabu Miyabe¹, Keigo Mizutani⁶, Taiki Nakamura¹², Takashi Nakano²,
 Masayuki Niiyama⁶, Yuki Nozawa⁶, Yuji Ohashi³, Haruo Ohkuma³,
 Hiroaki Ohnishi¹, Takeshi Ohta², Masaya Oka², Kyoichiro Ozawa¹¹,
 Yuta Sada², Mizuki Sasagawa¹, Takuya Shibukawa⁹, Hajime Shimizu¹,
 Rintaro Shirai¹, Ken'ichiro Shiraishi¹, Yorihiro Sugaya²,
 Mizuki Sumihama¹², Shinsuke Suzuki³, Shintaro Tanaka²,
 Atsushi Tokiyasu¹, Natsuki Tomida², Nam Tran², Yusuke Tsuchikawa¹,
 Tadayuki Ueda¹, Hirohito Yamazaki¹, Ryuji Yamazaki¹, Yuka Yanai²,
 Tetsuhiko Yorita², Chihiro Yoshida¹, and Masaru Yosoi²

¹Research Center for Electron Photon Science, Tohoku University, Sendai, Miyagi 982-0826, Japan

²Research Center for Nuclear Physics, Osaka University, Ibaraki, Osaka 567-0047, Japan

³Japan Synchrotron Radiation Research Institute (SPring-8), Sayo, Hyogo 679-5198, Japan

⁴Institute of Physics, Academia Sinica, Taipei 11529, Taiwan

⁵National Synchrotron Radiation Research Center, Hsinchu 30076, Taiwan

⁶Department of Physics, Kyoto University, Kyoto 606-8502, Japan

⁷Department of Physics and Astronomy, Ohio University, Athens, OH 45701, USA

⁸University of Hawaii at Manoa, Honolulu, HI 96822, USA

⁹Department of Physics, University of Tokyo, Tokyo 113-0033, Japan

¹⁰RIKEN Nishina Center, Wako, Saitama 351-0198, Japan

¹¹Institute of Particle and Nuclear Studies, High Energy Accelerator Research Organization (KEK),
 Tsukuba, Ibaraki 305-0801, Japan

¹²Department of Education, Gifu University, Gifu 501-1193, Japan

¹³Department of Physics, Korea University, Seoul 02841, Republic of Korea

The photoproduction of a light meson such as π^0 , η , and ω was studied by using the data collected with a liquid hydrogen (LH₂) target at the SPring-8 BGOegg experiment. The differential cross sections and photon beam asymmetries of these reactions were measured to examine baryon resonances for understanding the hadron structure at the quark level. By using the LEPS2 photon beam (1.3–2.4 GeV), we can explore the center-of-mass (CM) energy range above the third resonance region, where excited states appear with wide widths. The linearly polarized photon beam, available at the SPring-8/LEPS2

beamline, has advantage to decompose those overlapped states by measuring the interfered amplitudes through the photon beam asymmetries.

The photoproduction of η and ω , whose isospin is zero, couples only to nucleon resonances (N^* s) thanks to the isospin conservation in the s-channel. Particularly, the η photoproduction is a good probe for the N^* s including $s\bar{s}$ content. On the other hand, the π^0 meson is photoproduced via both N^* s and Δ^* s. Nevertheless, the contributing baryon resonances are being understood well because this reaction has been intensively investigated with high statistics at many experiments. The analysis of the π^0 photoproduction at the BGOegg experiment mainly aims the confirmation of the luminosity estimation and the analysis methods for other reaction modes. For all of the above photoproduction processes, the photon beam asymmetries in the energy region greater than $E_\gamma \sim 2$ GeV are very scarce and desired as new experimental information. The BGOegg experiment has obtained such new data as described below.

The individual light mesons were detected at the BGOegg electromagnetic calorimeter to reconstruct the invariant mass. The π^0 and η mesons were identified in the 2γ decay mode, while the ω meson was detected via $\omega \rightarrow \pi^0\gamma \rightarrow 3\gamma$ decays. The BGOegg calorimeter is the “egg”-shaped assembly of 1,320 BGO crystals, covering the polar angle range from 24° to 144° . The proton recoiled in the meson photoproduction was detected at the planar drift chamber (DC) or the BGOegg calorimeter with the charge identification by the inner plastic scintillators (IPS). The DC was installed at the forward acceptance hole of the BGOegg calorimeter, corresponding to the polar angles less than 21° . The experimental data was collected in the latter half of FY2014 (the 2014B cycle) by irradiating a few MHz photon beam onto the 54 mm-thick LH₂ target at the SPring-8 LEPS2 beamline. The energy and intensity of the photon beam were measured at the tagging counter for the recoil electrons from backward Compton scattering. The integrated photon beam counts have reached 3.6×10^{12} in 2014B.

The signal event sample was selected based on the kinematic fit with the constraints by the 4-momentum conservation and the π^0 and η masses. The ω mass was not used for a restricting condition because of its natural width, but the π^0 mass among the decay products was constrained to the PDG value. After requiring the χ^2 probability of the kinematic fit to be greater than 1% or 2%, the remaining sample entries for the π^0 , η , and ω photoproduction become $\sim 650K$, $\sim 56K$, and $\sim 75K$ events, respectively. Background contamination is negligibly small for the π^0 and η photoproduction, while the $\gamma p \rightarrow \pi^0\pi^0 p$ events with a missing γ is broadly distributed under the signal peak in the $\pi^0\gamma$ invariant mass distribution for the ω photoproduction. The ω signal counts were finally estimated to be $\sim 37K$ events by fitting a Voigt function with a background template shape generated by a Monte Carlo (MC) simulation.

The differential cross sections $d\sigma/d\Omega$ were measured in the photon energy bins of each several tens MeV and the meson polar angle bins ($\cos\theta$ at the CM frame) of each 0.1. The photoproduction yields at the individual kinematical bins were divided by the acceptance factors evaluated using the GEANT4-based MC simulations and by the luminosities calculated from the LH₂ target thickness and the number of tagging counter triggers with the 150 m beamline transmission of about 77%. Figures 1 and 2 show the measured differential cross sections for the π^0 photoproduction. The preliminary result

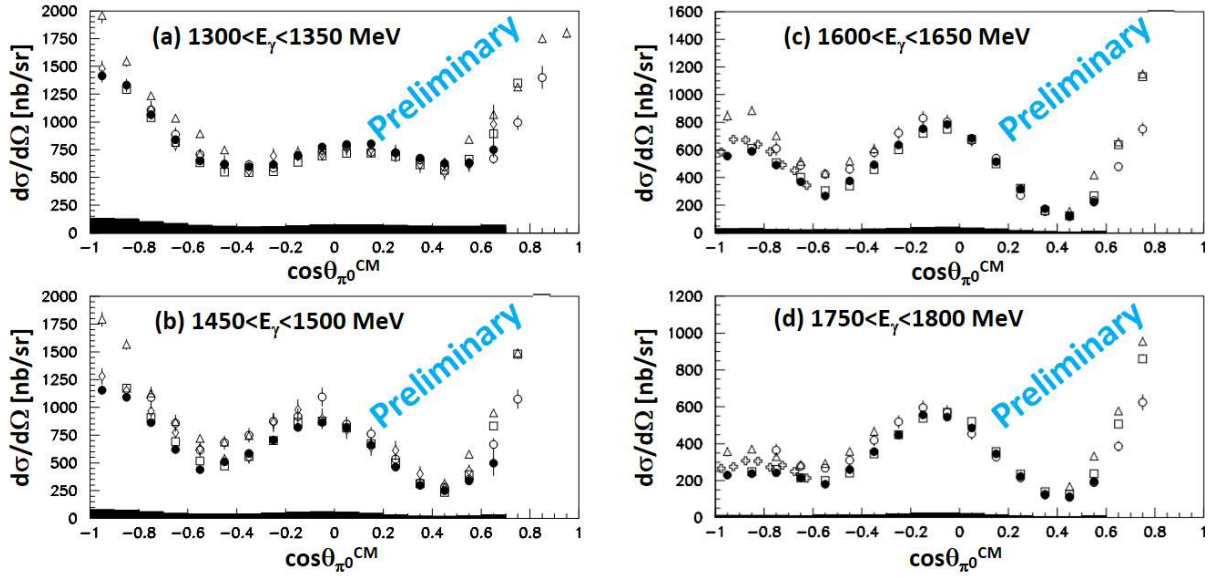


Fig.1. Differential cross section for the π^0 photoproduction at $E_\gamma < 1.9$ GeV. The BGOegg result is shown by the closed circles, while the squares, open circles, triangles, diamonds, and crosses indicate the measurements by CLAS [1], CBELSA 2005 [2], CBELSA 2011 [3], GRAAL [4], and LEPS [5]. The histogram represents the systematic errors of the BGOegg measurement.

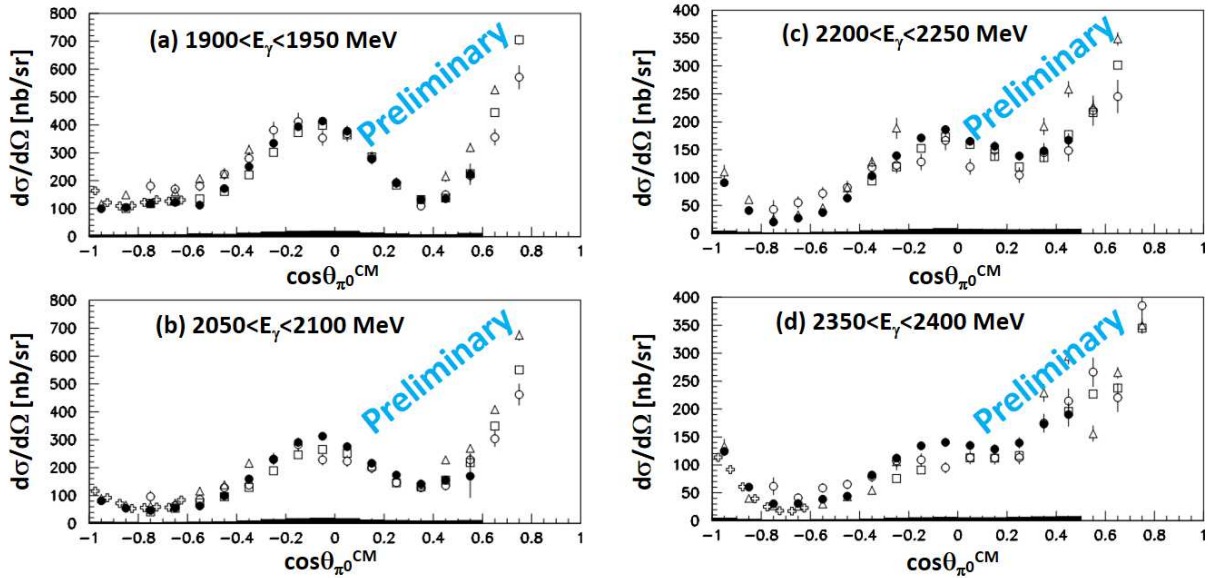


Fig.2. Differential cross section for the π^0 photoproduction at $E_\gamma \geq 1.9$ GeV. The meanings of the markers and the histogram are the same as those in Fig. 1.

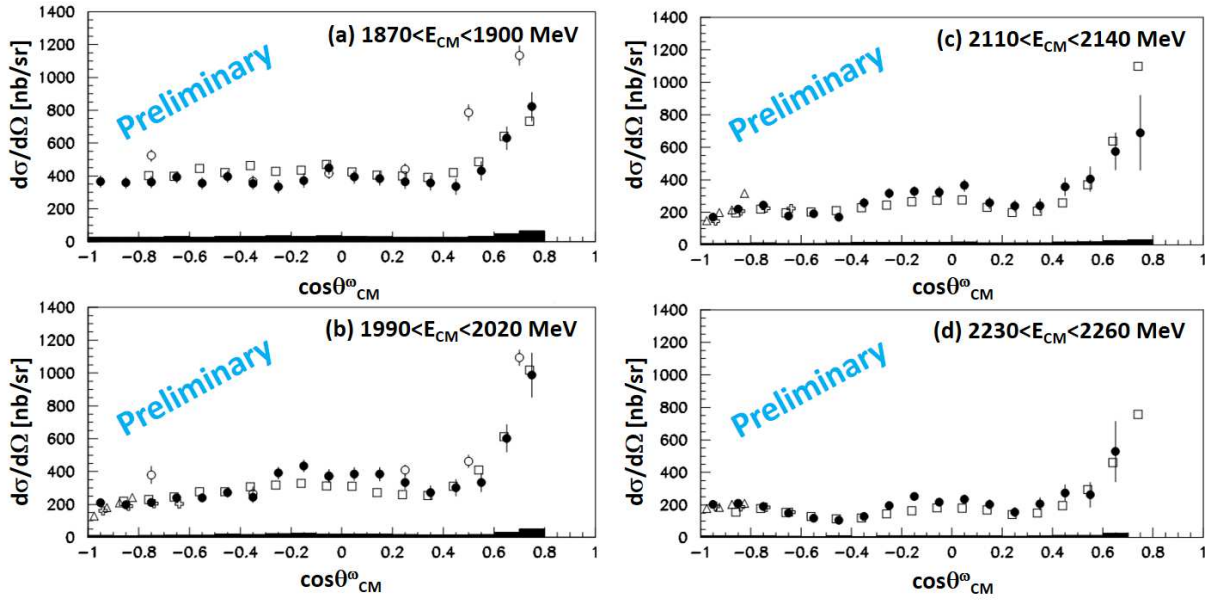


Fig.3. Differential cross section for the ω photoproduction. The BGOegg result is shown by the closed circles, while the squares, open circles, crosses, and triangles indicate the measurements by CLAS [9], CBELSA [10], LEPS [11], and LEPS-TPC [12]. The histogram represents the systematic errors of the BGOegg measurement.

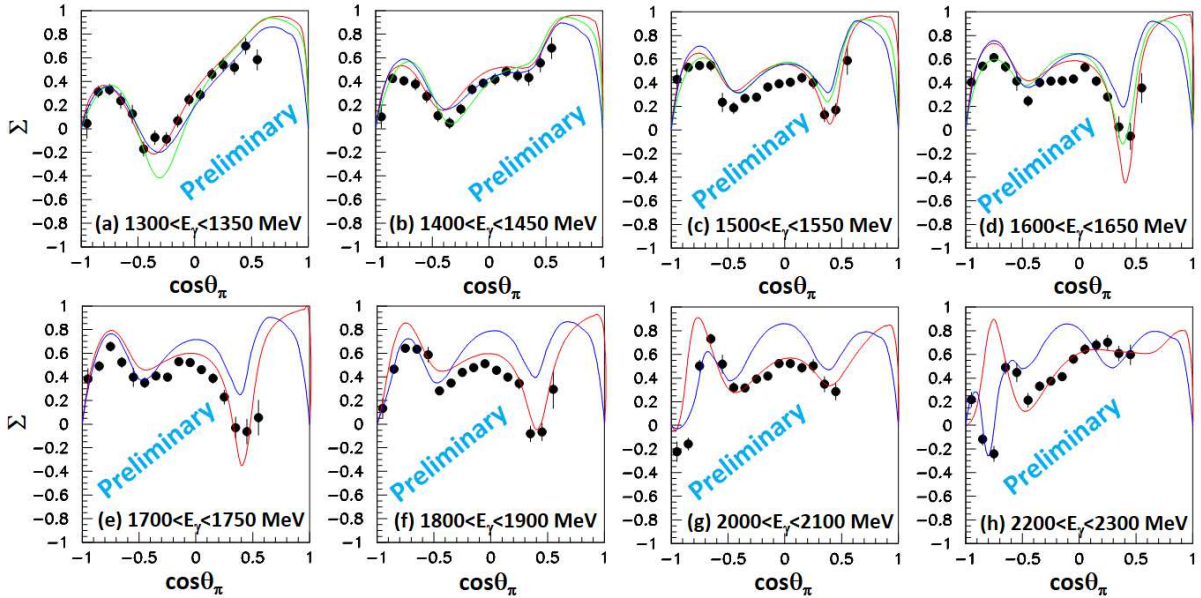


Fig.4. Photon beam asymmetry Σ for the π^0 photoproduction. The BGOegg result (closed circles) is compared with the existing PWA model calculations. The red, blue, and green curves are obtained by the Bonn-Gatchina [6], SAID [7], and ANL-Osaka [8] models, respectively.

of the BGOegg measurement is consistent with the CLAS, GRAAL, and LEPS results, while there are discrepancies from the CBELSA results at low energies and backward angles. The differential cross sections for the ω photoproduction are also measured as shown in Fig. 3, indicating the values close to other experimental results.

The photon beam asymmetry Σ was measured as the yield modulation depending on the azimuthal angle difference between the reaction plane and the photon beam polarization vector. Figures 4 and 5 show the BGOegg results of beam asymmetry measurements for the π^0 and ω photoproduction, respectively. Solid lines indicate the theoretical model calculations by partial wave analyses (PWA). The PWA model calculations generally reproduce the measured beam asymmetries at the lower energies because they are fitted to the existing experimental data. However, the consistencies become worse at the highest energy bins, where the beam asymmetry data is lacking. The new measurements by the BGOegg experiment must provide strong constraints on the decomposition possibilities of N^* s and Δ^* s. New fits by the PWA models are now in progress.

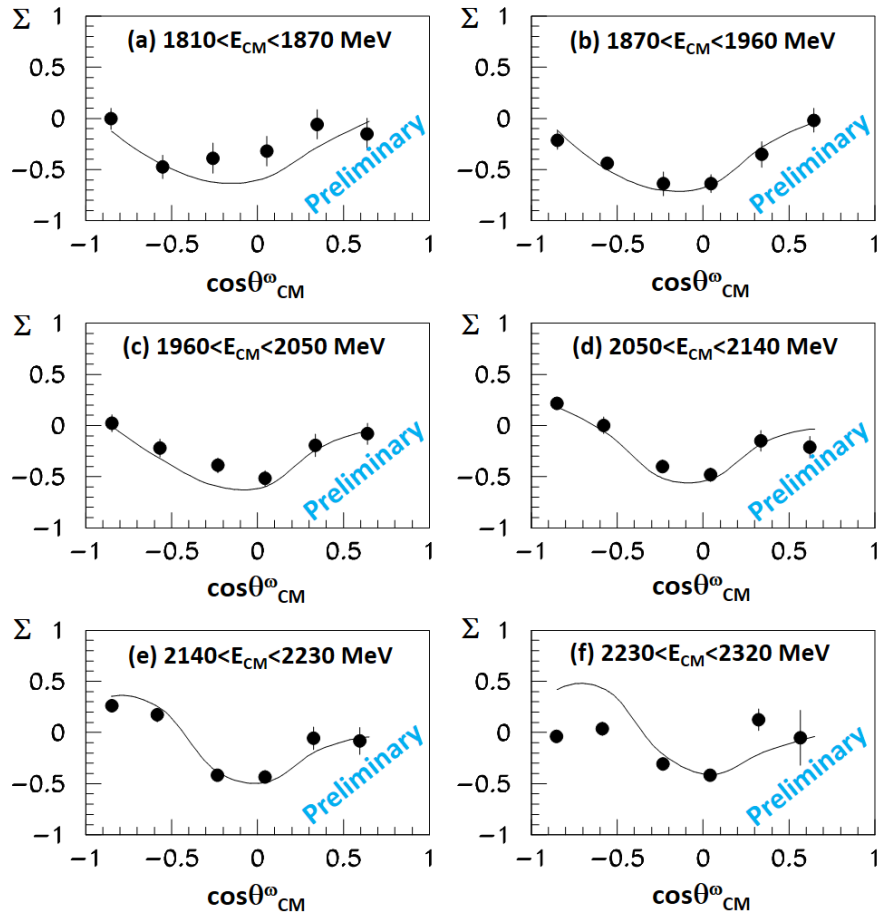


Fig.5. Photon beam asymmetry Σ for the ω photoproduction. The BGOegg result (closed circles) is compared with the existing PWA model calculation by Bonn-Gatchina group (solid lines) [13].

References

- [1] M. Dugger *et al.*, Phys. Rev. C **76**, 025211 (2007).
- [2] O. Bartholomy *et al.*, Phys. Rev. Lett. **94**, 012003 (2005).
- [3] V. Crede *et al.*, Phys. Rev. C **84**, 055203 (2011).
- [4] O. Bartalini *et al.*, Euro. Phys. J. **A26**, 399 (2005).
- [5] M. Sumihama *et al.*, Phys. Lett. B **657**, 32 (2007).
- [6] https://pwa.hiskp.uni-bonn.de/BG2014.02_obs_int.htm.
- [7] http://gwdac.phys.gwu.edu/analysis/pr_analysis.html.
- [8] T. Sato, Private communication.
- [9] M. Williams *et al.*, Phys. Rev. C **80**, 065208 (2009).
- [10] F. Dietz *et al.*, Euro. Phys. J. **A51**, 6 (2015).
- [11] M. Sumihama *et al.*, Phys. Rev. C **80**, 052201R (2009).
- [12] Y. Morino *et al.*, Prog. Theor. Exp. Phys. **2015**, 013D01.
- [13] A. Sarantsev and V. Nikonov, Private communication; P. Roy *et al.*, Phys. Rev. C **97**, 055202 (2018).

A trial to measure a spectral function of η' mesons

H. Shimizu¹, Y. Matsumura¹, J. K. Ahn², W. C. Chang³, J. Y. Chen⁴, S. Daté⁵,
 T. Gogami⁶, H. Hamano⁶, T. Hashimoto⁷, Q. He⁸, T. Hiraiwa⁶, Y. Honda¹,
 T. Hotta⁶, T. Ishikawa¹, J. M. Jo², Y. Kasamatsu⁶, H. Katsuragawa⁶, Y. Kon⁶,
 S. Masumoto⁹, K. Miki¹⁰, M. Miyabe¹, K. Mizutani⁷, N. Muramatsu¹,
 T. Nakamura¹⁰, T. Nakano⁶, M. Niiyama⁷, Y. Nozawa⁷, Y. Ohashi⁵,
 H. Ohnishi¹, T. Ohta⁶, M. Oka⁶, K. Ozawa¹¹, C. Rangacharyulu¹², Y. Sada⁶,
 T. Shibukawa⁹, R. Shirai¹, Y. Sugaya⁶, M. Sumihama¹⁰, S. Suzuki⁵,
 S. Tanaka⁶, Y. Taniguchi¹, A. Tokiyasu¹, N. Tomida⁶, N. Tran⁶,
 Y. Tsuchikawa¹³, T. Ueda¹, H. Yamazaki¹¹, R. Yamazaki¹, T. Yorita⁶,
 C. Yoshida¹, and M. Yosoi⁶

¹*Research Center for Electron Photon Science, Tohoku University, Sendai, 982-0826*

²*Department of Physics, Korea University, Seoul 02841*

³*Institute of Physics, Academia Sinica, Taipei 11529*

⁴*National Synchrotron Radiation Research Center, Hsinchu 30076*

⁵*Japan Synchrotron Radiation Research Institute (SPring-8), Hyogo 679-5198*

⁶*Research Center for Nuclear Physics, Osaka University, Osaka 567-0047*

⁷*Department of Physics, Kyoto University, Kyoto 606-8502*

⁸*Department of Nuclear Science & Engineering, Nanjing University, Nanjing 210016*

⁹*Department of Physics, University of Tokyo, Tokyo 113-0033*

¹⁰*Department of Education, Gifu University, Gifu 501-1193*

¹¹*Institute of Particle and Nuclear Studies, KEK, Tsukuba 305-0801*

¹²*Department of Physics, University of Saskatchewan, Saskatoon S7N 5E2*

¹³*Department of Physics, Nagoya University, Nagoya 464-8602*

An attempt has been made at SPring-8/LEPS2 to measure the spectral function of η' mesons propagating in the nuclear medium, where chiral symmetry in flavor space is expected to be partially restored. The spectral function of η' may provide essential information on how spontaneous symmetry breaking takes place in connection with axial $U(1)$ anomaly and whether an η' -nucleus bound state exists or not. For this purpose, an electromagnetic calorimeter, BGOegg, is employed to detect $\eta' \rightarrow \gamma\gamma$ decay inside a nucleus with a small but detectable probability. The $\eta' \rightarrow \pi^0\pi^0\eta$ decay process may provide another possibility to find a visible effect of chiral symmetry restoration in the nucleus. BGOegg consisting of 1320 BGO crystals exhibits an excellent calorimeter performance both in the energy and mass resolutions.

§1. Introduction

Incorporating quantum electro-weak dynamics and quantum chromodynamics (QCD), the standard model describes nature very well. However, Two big questions remain unsolved in the QCD sector, on

the confinement of quarks and mass generation of hadrons, which have to be solved in the framework of the standard model. These questions arise from the non-perturbative regime of QCD, which is still not well-understood because of a complicated situation brought about by the gauge boson gluon, which carries color charges by itself.

In such a hard environment surrounding non-perturbative QCD, Nambu formulated a low energy chiral effective theory [1] known as the Nambu–Jona-Lasinio (NJL) model that includes no gluon fields, following his pioneering work on spontaneous symmetry breaking. The NJL model that respects chiral symmetry in quark flavor space, originally in iso-spin space for the nucleon doublet, well explains how the hadron mass is generated. It is now widely accepted way of understanding that chiral symmetry is one of the most fundamental properties of QCD and is spontaneously broken in our real world due to $\langle \bar{q}q \rangle \neq 0$, the non-zero vacuum expectation value of quark-antiquark condensate. The $\langle \bar{q}q \rangle$ value is thought to mainly determine the hadron mass. Surprisingly, the $\langle \bar{q}q \rangle$ value accounts for about 99% of the mass of ordinary matter surrounding us, according to many effective theories based on the Nambu theory. (The contribution of Higgs fields to the mass generation of ordinary matter is merely the order of 1%.) However, no clear experimental evidence has been found for this scenario, which has to be proved experimentally in the framework of the standard model.

§2. Chiral symmetry and axial $U(1)$ anomaly

Under $SU(3)$ symmetry for three quark flavors,

$$= \begin{pmatrix} q_1 \\ q_2 \\ q_3 \end{pmatrix} = \begin{pmatrix} u \\ d \\ s \end{pmatrix}, \quad m = \begin{pmatrix} m_1 & 0 & 0 \\ 0 & m_2 & 0 \\ 0 & 0 & m_3 \end{pmatrix} \quad (m_1 \simeq m_2 \simeq m_3), \quad (1)$$

the $q\bar{q}$ meson multiplets are classified into a singlet and an octet, $3 \otimes \bar{3} = 1 \oplus 8$, originally taking place alternatively. But there exists the flavor $SU(3)$ symmetry-breaking interaction, which mixes the singlet and octet states having the same quantum numbers $I = Y = 0$. It is, therefore, convenient to regard the meson multiplet as a nonet belonging to an irreducible representation of a $U(3)$ group. In the low-lying pseudoscalar meson multiplet, $\eta(548)$ and $\eta'(958)$ are the mixtures of the singlet η_0 and the octet η_8 with η' mostly made up of η_0 . The η' meson as a member of the nonet, however, cannot be associated with $U(3)$ symmetry since the η' mass is considerably higher than the masses of the other members, K 's, η , and π 's. This is the axial $U(1)$ problem relating to the singlet η_0 .

The simplest classical QCD Lagrangian for three quark flavors is given by

$$\mathcal{L}_{QCD} = \bar{\psi}(i\gamma^\mu D_\mu - m)\psi - \frac{1}{4}F_{\mu\nu}^a F^{a\mu\nu}, \quad (2)$$

describing a physical system of free quarks ψ and gluons A_μ^a included in the field strength tensors $F_{\mu\nu}^a$. This Lagrangian originally satisfies $U(3)_L \otimes U(3)_R$ chiral symmetry, which decomposes into smaller symmetry groups as

$$U(3)_L \otimes U(3)_R \simeq U(1)_V \otimes U(1)_A \otimes SU(3)_L \otimes SU(3)_R \quad (3)$$

$$SU(3)_L \otimes SU(3)_R \simeq SU(3)_V \otimes SU(3)_A. \quad (4)$$

All Noether currents corresponding to the individual symmetries are conserved for classical fields in the chiral limit. But when we come to quantum fields, the singlet axial current, $\bar{\psi}\gamma^\mu\gamma_5\psi$, caused by the axial $U(1)$ symmetry ($U(1)_A$ symmetry) is not conserved any more since the divergence of this current is now given by

$$\partial_\mu(\bar{\psi}\gamma^\mu\gamma_5\psi) = 2im_j\bar{q}_j\gamma_5q_j + 2N_F\frac{1}{8\pi}\frac{g^2}{4\pi}F_{\mu\nu}^a\tilde{F}^{a\mu\nu} \neq 0, \quad (5)$$

where $\tilde{F}^{a\mu\nu}$ is the dual tensor of $F^{a\mu\nu}$. The first term on the right-hand side vanishes in the chiral limit, while the second term is a non-zero quantity known as the charge density operator that originates from the quantum effect of gluon fields. The other currents remain conserved even for the quantum fields. Thus the topological charge density operator gives rise to the axial $U(1)$ anomaly.

The QCD Lagrangian (2) has now $U(1)_V \otimes SU(3)_L \otimes SU(3)_R$ symmetry in the chiral limit with broken axial $U(1)$ symmetry. Then $SU(3)_L \otimes SU(3)_R$ chiral symmetry is spontaneously broken. To get the effect of the axial $U(1)$ anomaly into effective theories based on the NJL model, which keep possessing axial $U(1)$ symmetry, the Kobayashi-Maskawa-'t Hooft (KMT) six-quark interaction [2] is introduced to break axial $U(1)$ symmetry. An extended NJL model importing the KMT interaction predicts a large in-medium mass reduction of the η' meson by about 150 MeV at the normal nuclear density [3]. According to the prediction for three quark flavors, the η' mass goes down and gets degenerate with the η mass when the nuclear density goes up if a density-independent coupling constant is employed for the KMT term. Consequently a bound state of the η' and a nucleus might come about, depending on the strength of the η' -nucleus potential, which shows an attractive force due to the in-medium η' mass reduction. Although no exact predictions are given for the real and imaginary parts of the η' -nucleus optical potential, the logic described here might lead to an idea of axial $U(1)$ symmetry restoration driven by chiral restoration.

A simple question arises here. Does chiral symmetry restoration really affect axial $U(1)$ symmetry? The axial $U(1)$ anomaly originates from the quantization of gluon fields. And the KMT term is introduced into effective theories just to break down axial $U(1)$ symmetry. The relation between the topological charge of gluon fields and the KMT term is not straight forward. However, we may give an answer to the question from the point of view of "symmetry arguments [4]." The QCD Lagrangian for three quark flavors has $SU(3)_L \otimes SU(3)_R$ chiral symmetry, which is basically equivalent to $SU(3)_V \otimes SU(3)_A$ symmetry and is, therefore, invariant under octet axial transformations generated by the octet axial charges Q_5^b corresponding to the $SU(3)_A$ symmetry. Then octet scalars S^a in the $q\bar{q}$ meson states transform as

$$\theta_5^b[iQ_5^b, S^a] = -d^{abc}\theta_5^b P^c - \frac{2}{3}\theta_5^a P_0, \quad (6)$$

being mixed with octet P^c and singlet P_0 pseudoscalars, where θ_5^b are transformation parameters and d^{abc} denote the d-coefficients of anticommutation relations of $SU(3)$ generators. As a consequence, when the spontaneously broken chiral symmetry is restored, the octet S^a scalars, the singlet $\eta_0 = P_0$ and octet $\eta_8 \in P^c$ pseudoscalars must get degenerate in mass, irrespective of axial $U(1)$ anomaly. This consequence, however, does not necessarily mean axial $U(1)$ symmetry restoration [4]. The $\sigma(500)$ and $f_0(980)$ would be mixtures of the singlet S_0 and an octet S^a scalar. The remaining octet scalars are three

$a_0(980)'s$ and four $\kappa(800)'s$ [5] that are not well established.

§3. $\eta' \rightarrow \gamma\gamma$ decay in the nuclear medium

We try to search for the effect of η' mass going down in the nuclear medium by measuring the spectral function defined as the imaginary part of the η' propagator in a nucleus. An appropriate decay process taking place in the nucleus should be selected at first in this study to avoid undesirable distortion effects from the residual nucleus. We focus on the $\eta' \rightarrow \gamma\gamma$ process, which includes no strong interacting particles in the final state and therefore may also be able to provide information on an η' -nucleus bound state if it exists. The natural width of the η' meson is about 197 keV, which is too narrow, in general, for whatever experiments detecting η' decay in a nucleus, unless η' is bounded. Assuming η' mesons having a momentum of 400 MeV/c in free space, for example, we may observe the $\gamma\gamma$ decay events about 400 fm away from the η' created points with the branching ratio of 2.2% since

$$\beta\gamma\tau_0 \simeq 0.4 \frac{197 \text{ MeV} \cdot \text{fm}}{197 \text{ keV}} = 400 \text{ fm}, \quad (7)$$

where τ_0 is the lifetime of the η' meson. The natural width of the η' meson Γ_0 is given by the sum of all the partial decay widths in free space,

$$\Gamma_0(\eta') = \Gamma_{\gamma\gamma} + \Gamma_1 + \Gamma_2 + \cdots + \Gamma_{\pi\pi\eta} = 197 \text{ keV}, \quad (8)$$

almost determined by the main decay channels, $\eta' \rightarrow \pi\pi\eta$ (65%) and $\eta' \rightarrow \pi^+\pi^-\gamma$ (29%). Each partial width is determined by the invariant amplitude describing the decay process and the phase space volume in the final state, being experimentally obtainable by measuring the total width and the branching ratio to the process under consideration. The partial width of $\gamma\gamma$ decay $\Gamma_{\gamma\gamma}$ is then found to be 4.3 keV corresponding to the known branching ratio of 2.2% to the $\gamma\gamma$ channel.

Using a nuclear target, we would have a hard time, therefore, finding the events decaying into $\gamma\gamma$ inside the nucleus. But the decay events occurring within the nucleus are not absolutely undetectable. The CBELSA/TAPS Collaboration recently provides the most relevant experimental result on the η' -nucleus potential [6], the real part of which is found to be $-(37 \pm 10_{stat} \pm 10_{syst})$ MeV, showing an attractive force. The obtained potential also shows a small imaginary part of $-(10 \pm 2.5)$ MeV, which corresponds to the in-medium width of η' to be about 20 MeV at the normal nuclear density. Taking this value for the total width Γ_A of η' in the nuclear medium, we can estimate the rate of $\gamma\gamma$ decay inside to outside the nucleus. We define here a decay length, L_0 , corresponding to the total decay width $\Gamma_0 = 1/\tau_0$ in free space for a fixed $\beta\gamma \approx 0.4$ of η' ,

$$L_0 = \beta\gamma\tau_0 \simeq 400 \text{ fm} \quad \text{for } \Gamma_0 \simeq 200 \text{ keV}, \quad (9)$$

having another decay length, L_A , corresponding to the total width $\Gamma_A = 1/\tau_A$ in the nucleus,

$$L_A = \beta\gamma\tau_A \simeq 4 \text{ fm} \quad \text{for } \Gamma_A \simeq 20 \text{ MeV}, \quad (10)$$

where τ_A denotes the lifetime of η' in the nucleus. The fraction $R_{\gamma\gamma}(x < r)$ of $\eta' \rightarrow \gamma\gamma$ decay inside the nucleus can be written by

$$R_{\gamma\gamma}(x < r) = \frac{\Gamma_{\gamma\gamma}}{\Gamma_A} \left(1 - \exp\left(-\frac{r}{L_A}\right) \right), \quad (11)$$

where r is the average distance from a η' created point to the boundary in the nucleus. The fraction $R_{\gamma\gamma}(r < x)$ of $\gamma\gamma$ decay outside is then given by

$$R_{\gamma\gamma}(r < x) = \frac{\Gamma_{\gamma\gamma}}{\Gamma_0} \exp\left(-\frac{r}{L_A}\right). \quad (12)$$

Thus the rate of $\gamma\gamma$ decay inside to outside the nucleus is obtained as

$$\frac{R_{\gamma\gamma}(x < r)}{R_{\gamma\gamma}(r < x)} = \frac{\Gamma_0}{\Gamma_A} \left[\exp\left(\frac{r}{L_A}\right) - 1 \right], \quad (13)$$

which is independent of $\Gamma_{\gamma\gamma}$. Provided that an average propagation length r of η' through the nucleus is taken to be 2.7 fm, which is the same length of the carbon radius, and the total width Γ_A of η' in the nucleus to be 20 MeV, we have the rate

$$\frac{R_{\gamma\gamma}(x < r)}{R_{\gamma\gamma}(all)} \simeq 1\% \quad (14)$$

for η' having a relative momentum of 400 MeV/c in the residual nucleus. This effect may be observed in the spectral function of $\eta' \rightarrow \gamma\gamma$ events. The rate is expected to go up if we use a heavier nucleus with a larger radius. In comparison, the similar estimation yields the rate of 6.8×10^{-3} for the case that the total width of η' is unchanged in the nucleus.

Here is another decay process to be investigated to search for chiral restoration phenomena in addition to the $\gamma\gamma$ decay channel. If the η' mass decreases by about 100 MeV in the nuclear medium, $\eta' \rightarrow \pi^0\pi^0\eta$ decay is strongly suppressed since the available momentum space becomes very limited for this channel. This means the partial width of $\eta' \rightarrow \pi^0\pi^0\eta$ decay goes down and accordingly diminishes the branching ratio to this channel. Thus we expect to have

$$\Gamma'_{\pi\pi\eta} \ll \Gamma_{\pi\pi\eta}, \quad (15)$$

where $\Gamma'_{\pi\pi\eta}$ and $\Gamma_{\pi\pi\eta}$ denote the partial decay widths in the nuclear medium and in free space, respectively. It does not matter to have strongly interacting hadrons in the final state in the measurement of the branching ratio in this case. We measure the branching ratio to the $\pi^0\pi^0\eta$ channel using a nuclear target and a liquid hydrogen target to compare the results. Just the change of the branching ratio provides information on partial restoration of chiral symmetry, irrespective of distortion effects taking place on the final-state hadrons in the nuclear medium.

It is useful to have better information on the fundamental properties of the η' meson in free space in the study of η' in the nuclear medium. Precise measurements have recently been made at COSY for the total width of η' [7] and the η' -nucleon scattering length [8], which may yield information on η' scattering processes in the nuclear medium.

§4. BGOegg Experiments at SPring-8/LEPS2

A series of experiments has been conducted at the LEPS2 beamline [9] in SPring-8 to find the effect of partial restoration of chiral symmetry in the nuclear medium. A 2.4 GeV laser-electron-photon beam is utilized with a typical intensity of 10^6 tagged photons/s. The common experimental layout for these experiments is illustrated in Fig. 1. An electromagnetic calorimeter, BGOegg, was installed as the main

detector assembly equipped with a cylindrical drift chamber (CDC) and an inner scintillator hodoscope. Forward-going charged particles can be detected with a time-of-flight (TOF) hodoscope made of resistive

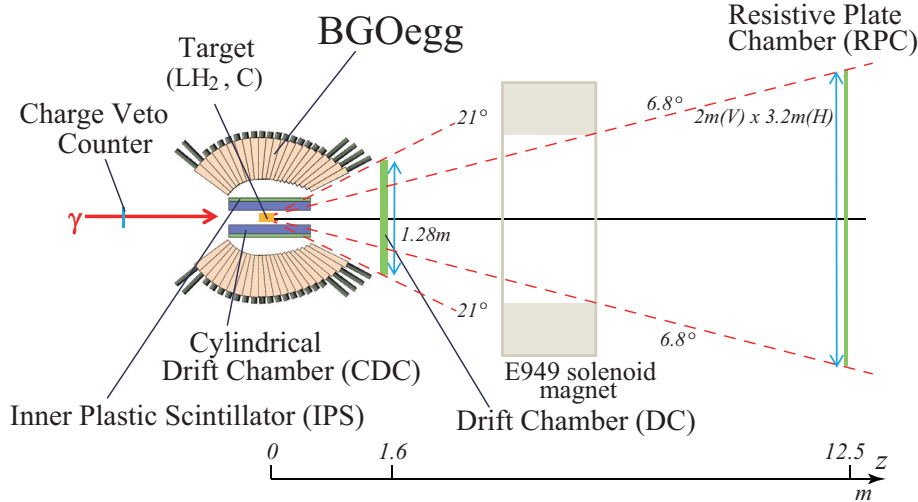


Fig.1. Plan view of the common experimental setup for BGOegg experiments.

plate chambers (RPC) placed 12.5 m downstream of the target. The TOF resolution is found to be 80 ps, which corresponds to the energy resolution of ~ 20 MeV for 2 GeV/c protons. A big solenoid magnet shown in Fig. 1 is not used in the current BGOegg experiments.

The BGOegg calorimeter is an egg-shaped assembly of 1320 BGO crystals covering polar angles from 24° to 144° with a good segmentation of $\sim 6^\circ$ both in the polar and azimuthal directions. Each crystal has a sufficient thickness of 220 mm corresponding to 20 radiation lengths. BGOegg has a self-supporting structure, like a Roman arch bridge, to hold the whole crystals of $\sim 2t$ in weight, having no insensitive area in between adjacent crystals. Consequently, BGOegg provides one of the world's best energy resolutions of 1.3% for 1 GeV photons. This resolution is not the maximum instantaneous value but is obtainable everywhere in BGOegg, except for the edge regions because of extra electromagnetic shower leakage at the boundary.

4.1 The $\eta' \rightarrow \gamma\gamma$ channel

The energy calibration of BGOegg is one of the most important jobs [10] in the BGOegg experiments. By employing a huge number of $\pi^0 \rightarrow \gamma\gamma$ events obtained in the experiments, the calibration was made so as to get the π^0 mass to be the same as the PDG value. We achieved a very beautiful calibration so far as shown in Fig. 2 for a carbon target with a thickness of 20 mm. This is a kind of overall calibration with no particular momentum-selection for $\gamma\gamma$ pairs. Nevertheless, the η and η' peaks are observed just on the right places as depicted in Fig. 2. In this calibration we have 548.6 ± 0.1 MeV (PDG: 547.86 MeV) and 959 ± 1 MeV (PDG: 957.78 MeV) for the η and η' masses, respectively. The overall $\gamma\gamma$ mass resolutions are preliminarily found to be 5.8, 12.9, and 19 MeV for π^0 , η , and η' , respectively. Thus BGOegg exhibits the excellent $\gamma\gamma$ mass resolutions ever made in meson photoproduction experiments in the world. The

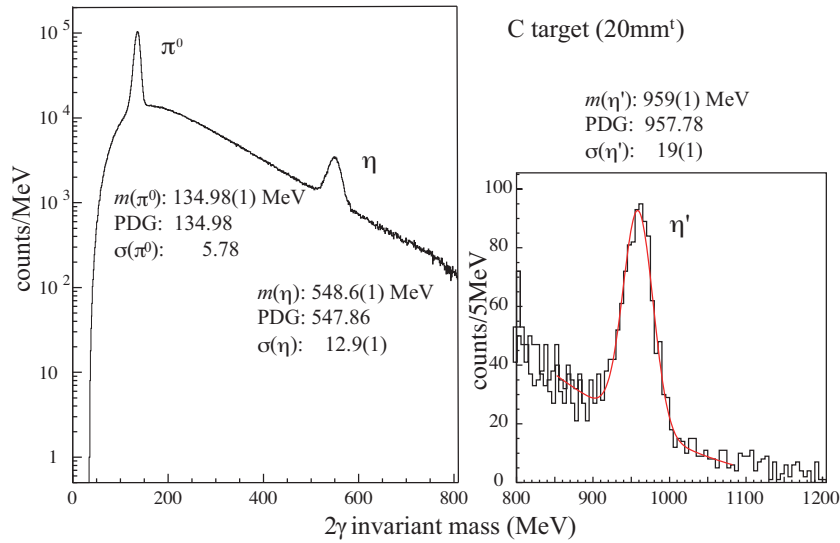


Fig.2. Preliminary results of $\gamma\gamma$ invariant mass spectra obtained in energy calibration of the BGOegg calorimeter. Several times of iteration have been made in the calibration so that the π^0 mass becomes what it should be.

obtained mass resolutions depend on the target thickness because of no vertex information for $\gamma\gamma$ events. We have no way to know the exact vertex point of each event on the macroscopic target, if outgoing particles are all neutral. We assumed all the events were generated at the center of the target. It is expected, therefore, to have better $\gamma\gamma$ mass resolutions with a thinner target.

4.2 The $\eta' \rightarrow \pi^0\pi^0\eta$ channel

The BGOegg calorimeter is one of the most suitable detectors for the measurement of the $\eta' \rightarrow \pi^0\pi^0\eta$ process, being able to detect $\pi^0\pi^0\eta$ events by measuring 6 γ 's with a good mass-resolution. A

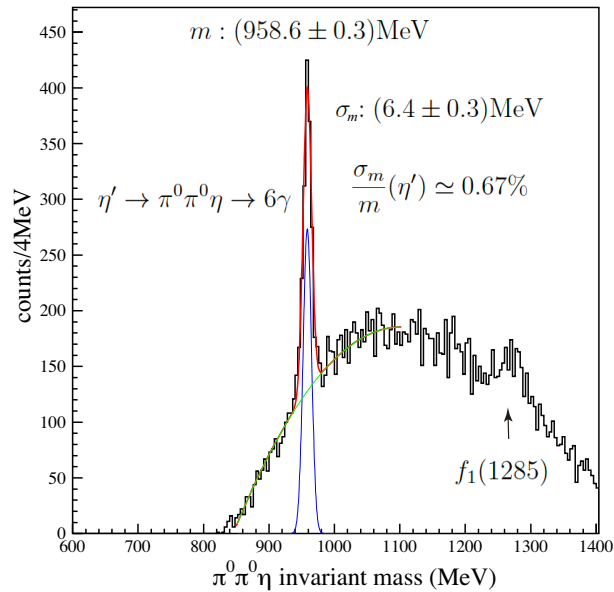


Fig.3. A $\pi^0\pi^0\eta$ invariant mass spectrum obtained in the $\gamma C \rightarrow \pi^0\pi^0\eta X$ reaction.

conceivable change of the decay partial width may be detectable by comparing the branching ratio of

the $\pi^0\pi^0\eta$ channel measured using a nuclear target with that using a hydrogen target. This might be one of the most promising studies to find chiral restoration phenomena. We reconstruct $\pi^0\pi^0\eta$ events from a bunch of three 2γ events of $\eta' \rightarrow \pi^0\pi^0\eta \rightarrow 6\gamma$. By employing a kinematical fit to π^0 and η masses, a $\pi^0\pi^0\eta$ invariant-mass spectrum is obtained for a carbon target. As shown in Fig. 3, the η' peak is observed at 958.6 ± 0.3 MeV with a fairly good mass-resolution of $\sigma_m/m(\eta') \simeq 0.67\%$ ($\sigma_m = 6.4 \pm 0.3$ MeV), which is probably the world best resolution obtained for $\pi^0\pi^0\eta$ invariant mass. The $\pi^0\pi^0\eta$ invariant mass spectrum reveals a clear peak corresponding to the iso-scalar axial vector meson $f_1(1285)$, the main decay channel of which is known to be $f_1 \rightarrow \pi^0\pi^0\eta$.

§5. Summary

The η' meson is a good candidate being able to provide information on the relation between chiral symmetry restoration and axial $U(1)$ anomaly in the nuclear medium. A small but detectable change including the effect of a bound state of η' is expected to come about in the spectral function of η' obtained through the $\eta' \rightarrow \gamma\gamma$ decay process. The experimental data are accumulated for two years with a carbon and a liquid hydrogen target. The energy calibration has been made successfully, yielding overall $\gamma\gamma$ invariant mass resolutions of 5.8 MeV, 12.9 MeV, and 19MeV for π^0 , η , and η' mesons, respectively, for a 20 mm thick carbon target. An excellent $\pi^0\pi^0\eta$ mass resolution of $\sigma_m = 6.4 \pm 0.3$ MeV is obtained at η' mass so far. The data analysis is underway, following a heavy work imposed by ourselves to calibrate 1320 BGO crystals mounted on the electromagnetic calorimeter BGOegg.

Acknowledgment

This work was supported in part by MEXT (Grant No. 19002003), and by JSPS (No. 24244022).

References

- [1] Y. Nambu and G. Jona-Lasinio: Phys. Rev. **122** (1961) 345; **124** (1961) 246.
- [2] M. Kobayashi and T. Maskawa, Prog. Theor. Phys. **44** (1970) 1422;
M. Kobayashi, H. Kondo and T. Maskawa, Prog. Theor. Phys. **45** (1971) 1955;
G. 't Hooft, Phys. Rev. Lett. **37** (1976) 8; Phys. Rev. **D14** (1976) 3432.
- [3] H. Nagahiro, M. Takizawa, S. Hirenzaki, Phys. Rev. **C74** (2006) 045203;
H. Nagahiro *et al.*, Phys. Rev. **C87** (20013) 045201.
- [4] D. Jido, H. Nagahiro, S. Hirenzaki, Phys. Rev. **C85** (2012) 032201(R).
- [5] S.H. Hwang *et al.*, Phys. Rev. Lett. **108** (2012) 092001.
- [6] M. Nanova *et al.*, Phys. Lett. **B727** (2013) 417; Phys. Lett. **B710** (2012) 600.
- [7] E. Czerwiński *et al.*, Phys. Rev. Lett. **105** (2010) 122001.
- [8] E. Czerwiński *et al.*, Phys. Rev. Lett. **113** (2014) 062004.
- [9] H. Shimizu, N. Muramatsu, Nuclear Physics News (2017) **27**:1, 19.
- [10] Y. Matsumura *et al.*, ELPH Annual Report (2014) 95.

(ELPH Experiment : #2775, #2839)

光量子放射化分析のための光核反応収率の測定

大浦泰嗣¹, 寺岬仁志², 山口優貴², 原司², 金子純也², 黒岩憲明², 遠藤勇²,
三浦義隆¹

¹ 首都大学東京大学院理工学研究科分子物質化学専攻 (192-0397 東京都八王子市南大沢 1-1)

² 首都大学東京都市教養学部理工学系化学コース (192-0397 東京都八王子市南大沢 1-1)

Radiochemical measurement of photonuclear reaction yields for photon activation analysis

Yasuji Oura¹, Hitoshi terasaki², Yuki Yamaguchi², Tsukasa Hara²,
Jyunya Kaneko², Noriaki Kuroiwa², Isamu Endo², and Yoshitaka Miura¹

¹ *Department of Chemistry, Tokyo Metropolitan University, Hachioji, 192-0397*

² *Department of Chemistry, Tokyo Metropolitan University, Hachioji, 192-0397*

Relative reaction yields of (γ, n) reaction induced by bremsstrahlung of maximum end-point energy (E_0) of 20 MeV, 25 MeV, and 30 MeV were measured for the target nuclides with mass number from 12 to 204. Relative yields were systematically increased with an increase of target mass number (A_t), that is, a good linear correlation was obtained in double logarithmic plot. Yields for (γ, n) reactions producing isomers, however, were smaller than the systematic yield. Relative yields for $E_0 = 25$ MeV and 30 MeV are almost consistent. At $A_t \geq 80$, however, relative yields for $E_0 = 20$ MeV were slightly higher than those for $E_0 = 30$ MeV. And relative yield of ^{12}C for $E_0 = 20$ MeV was about 10 times lower than one for $E_0 = 25$ MeV or 30 MeV. Using our relative reaction yields, elemental contents can be determined by a single comparator method without standard samples used for a comparison method.

§ 1. はじめに

機器放射化分析法は、高感度な非破壊多元素同時分析法の一つで、核反応により安定核種を放射性核種に変換し、これから放出される γ 線を測定して定量を行なう。原子炉中性子による核反応、主として(n, γ)反応により生じた放射性核種を利用する中性子放射化分析法(NAA)が、多くの分野で広く利用されている。一方、光量子放射化分析法(PAA)は、電子加速器で発生させた制動放射線による(γ, n)反応を利用する放射化分析法で、NAAとは異なる核反応を利用するため、NAAでは困難な元素の定量も行なうことができ、相補的な関係にある。PAAはNAAと同様に非破壊多元素同時分析法であるが、NAAほど利用されていないのが現状である。この理由はいろいろあると思うが、PAAを利用する上で不便な点の一つは、NAAの様にユーザーが利用しやすいまとまった核反応収率データがそろっていないことであろう。単色光子に対する核反応断面積(励起関数)はデータライブラリー(例えば、[1, 2])があるが、制動放射線での照射にはそのまま利用できないし、元素が限られている。また、光核反応の教科書や総説で良く引用される Kato et al.

[3]の反応収率曲線は、収率の単位が $\text{mole}^{-1}\text{R}^{-1}$ であり、利用しづらい。そのため、どれくらいの誘導放射能が生成するかの推定が難しい。Segabade et al. [4]は 1983 年に PAA の教科書を著しているが、この書籍に付属している表がもっともよく整備されている PAA のための反応収率に関するデータの一つであると思われる。この表では、 $^{58}\text{Ni}(\gamma, n)^{57}\text{Ni}$ 反応を基準として、最大エネルギー (E_0) 30 MeV の制動放射線で 1 時間照射したときの誘導放射能比が与えられている。そこで、本研究では、 $E_0 = 30$ MeV での $^{58}\text{Ni}(\gamma, n)^{57}\text{Ni}$ 反応に対する光核反応収率比をもとめ、Segabade et al. の値を確認すると共に、掲載されていない $E_0 = 25$ MeV と 20 MeV の制動放射線を照射した時の核反応収率比も測定した。

放射化分析法での元素の定量は、通常、比較法により行なわれる。すなわち、元素質量既知の試料(比較標準試料と呼ぶ)を未知試料と制動放射線(または中性子)で同時に照射し、式(1)で計数率比から定量を行なう(照射終了直後に減衰補正した計数率は、元素質量に比例する。PAA では、試料をスタック状に並べて照射するので、光子束の補正が必須。)

$$\frac{a_u}{a_s} = \frac{N_u \phi}{N_s \phi_s} = \frac{m_u \phi}{m_s \phi_s} \quad (1)$$

ここで、 a は照射終了直後の計数率、 N は核種数、 ϕ は光子束、 m は定量元素の質量、添え字の u と s はそれぞれ未知試料と比較標準試料を示し、 a_u と a_s は同じ放射性核種の同じエネルギーのガンマ線計数率である。通常、未知試料と比較標準試料に含まれる元素の同位体組成は等しいと仮定できるので、 $N/N_s = m/m_s$ となる。比較法は、あらかじめ定量対象元素を計画し、それらの元素を含む比較標準試料を同時に照射する必要がある。つまり、計画外の元素は、未知試料でそれから生成した放射性核種が検出されても、定量は不可能である。そのため、ある一つの元素の比較標準試料をもちいて、すべての元素を定量することができる単一コンパレータ法が考案されている。その定量の原理を式(2)に示す。

$$\frac{a_x}{a_c} = \frac{N_x \phi_x Y_x (1 - e^{-\lambda_x t}) r_x \epsilon_x}{N_c \phi_c Y_c (1 - e^{-\lambda_c t}) r_c \epsilon_c} \quad (2)$$

ここで、 a は計数率、 N は核種数、 ϕ は光子束、 Y は反応収率、 λ は壊変定数、 t は照射時間、 r はガンマ線放出率、 ϵ は検出器の計数効率、添え字の x と c はそれぞれ定量元素と比較標準元素を示す。既知量 (N_c) の元素 c を未知 (N_x) 試料と一緒に照射すると、 a_x/a_c 、 ϕ_x/ϕ_c と ϵ_x/ϵ_c は、実験で決めることができるので、あらかじめ、すべての元素で Y_x/Y_c を求めておけば、 N_x を定量できる。本研究で測定した反応収率比は、 Y_x/Y_c (c はニッケル) に相当する。NAA では、単一コンパレータ法を汎用化した k_0 標準化法 [5, 6] が開発され、ヨーロッパを中心に広く利用されている。本研究は単一コンパレータ法への適用も視野に入れて、反応収率比の測定を行なった。

本年報では (γ, n) 反応の収率比について報告する。

§ 2. 実験方法

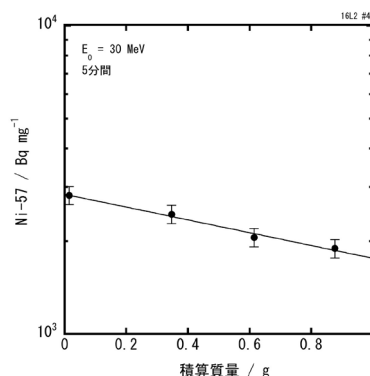
炭素から鉛までの 41 元素を対象とし、それらの単体、酸化物、あるいは塩化物の試薬約 50 mg を Al 箔で包み、直径 10 mm のペレット状の照射試料を作った。5~10 個のこの試薬試料を同じ直径の Ni 箔 (厚さ 0.04 mm) とともにスタック状に石英管に封入し、東北大学電子光物理学研究センターの電子線形加速器にて E_0 が 20 MeV, 25 MeV, ならびに 30 MeV の制動放射線を 5 分間または 10 分間照射した。各元素の試薬試料は石英管内での位置や、同時に照射する試料をかえて、複数回照射した。照射後、適度な時間をおいて、試料をそのまま Ge 半導体検出器で複数回測定した。炭素、フッ素試薬、チタン試薬などの一部の試料

は、粉末試料を取り出し、新しい Al 箔で包み直してから測定を行なった。また、炭素とフッ素試料は、厚さ 1 mm の銅板ではさみ、測定用試料とした。試料は、サム効果が無視できるように、検出器から 10 cm 以上離れた位置において、測定した。

定量した誘導放射能から各標的核種の光核反応収率を $^{58}\text{Ni}(\gamma, n)^{57}\text{Ni}$ 反応収率との収率比として求めた。

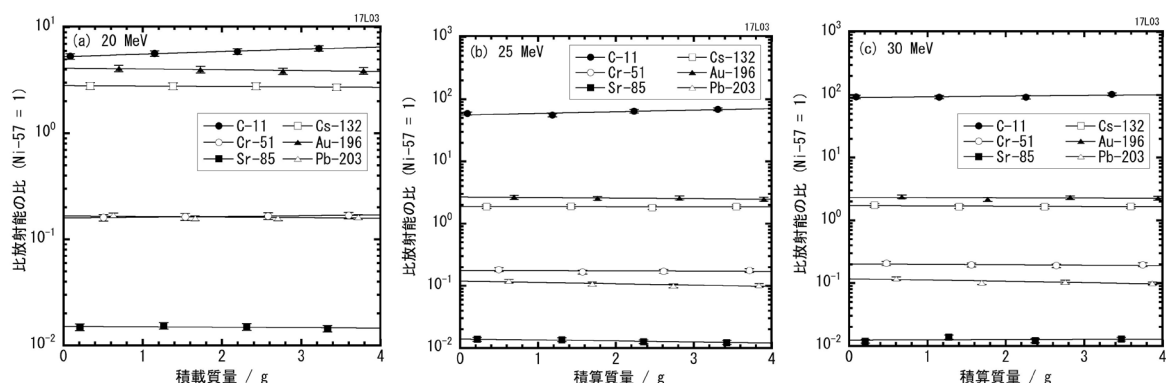
§ 3. 結果と考察

限られた時間で、なるべく多くの元素に対しての反応収率比を得るために、複数の異なる試薬を同時に照射した。複数の試料を同時に制動放射線で照射する際は、ビーム軸にそって試料を並べて照射するため、ビーム上流から下流に向かって、光子束は減少する。そのため、Ni 箔を適当な間隔で並べ、 $^{58}\text{Ni}(\gamma, n)$ 反応で生成した ^{57}Ni の比放射能により、各試料間の光子束を補正する。一例として、第 1 図に $E_0 = 30$ MeV の制動放射線を 5 分間照射したときの石英管内での ^{57}Ni の比放射能の変化を積算質量 [7] に対して示す。正確に反応収率比を得るには、 ^{57}Ni の比放射能の減少率が、各試薬試料中での光核反応生成物の比放射能の減少率と等しい必要がある。そこで、複数個の C 単体, Cr 単体, SrCl_2 , CsCl , Au 箔, PbCl_2 , ならびに Ni 箔を同時に照射し、 (γ, n) 反応で生成した ^{11}C , ^{51}Cr , ^{85}Sr , ^{132}Cs , ^{196}Au , ^{203}Pb , ^{57}Ni の比放射能の変化を調べた。積算質量に対する各比放射能と ^{57}Ni 比放射能との比の変化を第 2 図に示す。ここで ^{57}Ni 比放射能には、積算質量に対する指数関数的変化より各試薬試料の位置へ内挿した値を用いた。いずれの E_0 でも、 $^{11}\text{C}/^{57}\text{Ni}$ は積算質量とともにわずかに増加し、最下流の試料での比放射能の比は、最上流の試料の約 1.1 倍であった。炭素以外の試料では、比放射能の比は積算質量に対してほぼ一定で、 $^{11}\text{C}/^{57}\text{Ni}$ も含めてほとんどの比放射能の比のばらつきは相対標準偏差で数 % であり、最大で 10% ($E_0 = 25$ MeV での $^{11}\text{C}/^{57}\text{Ni}$) であった。



第 1 図 試料スタック内での ^{57}Ni 比放射能の変化。

$^{58}\text{Ni}(\gamma, n)^{57}\text{Ni}$ 反応との反応収率比は、(1) 式から N_x/N_c が既知として得られる。理想的には、対象元素とニッケルとの化合物、あるいは、対象元素とニッケルの混合試料を照射するのが望ましい ($\phi_x/\phi_c = 1$ となる) が、ニッケルとの化合物はほとんど存在しないし、均一な混合試料を正確に調製するのは難しい。そのため、複数枚の既知量のニッケル箔を適当な間隔で試薬試料の間に挟んで照射した。Ni 箔で生成した ^{57}Ni の比放射能は、第 1 図に示すように試料の積算質量に対して、指数関数的に減少する。最小自乗法で得た指数関数より、石英管内での各試薬試料位置における ^{57}Ni 比放射能を計算し、対象核種の比放射能から、反応収率比 Y_x/Y_{Ni} を求めた。この方法 (Ni 箔法と呼ぶ) で得られた反応収率比の確からしさを検討するた



第2図 試料スタック内での比放射能の比の変化。(a) $E_0=20$ MeV. (b) $E_0=25$ MeV. (c) $E_0=30$ MeV.

めに、元素は限られるが、塩化物試薬を照射して、 $^{35}\text{Cl}(\gamma, n)^{34m}\text{Cl}$ 反応を基準とした反応収率比、 Y_x/Y_{Cl} も求めた(塩化物法と呼ぶ)。塩化物試薬を用いることにより、試薬の秤量とフラックス補正の実験的不確かさを排除することができ、より確からしい反応収率比が得られると期待される。 Y_x/Y_{Ni} は、 NiCl_2 試薬を照射して得た $Y_{\text{Ni}}/Y_{\text{Cl}}$ から次式により得た。

$$\frac{Y_x}{Y_{\text{Ni}}} = \frac{Y_x}{Y_{\text{Cl}}} \div \frac{Y_{\text{Ni}}}{Y_{\text{Cl}}} \quad (3)$$

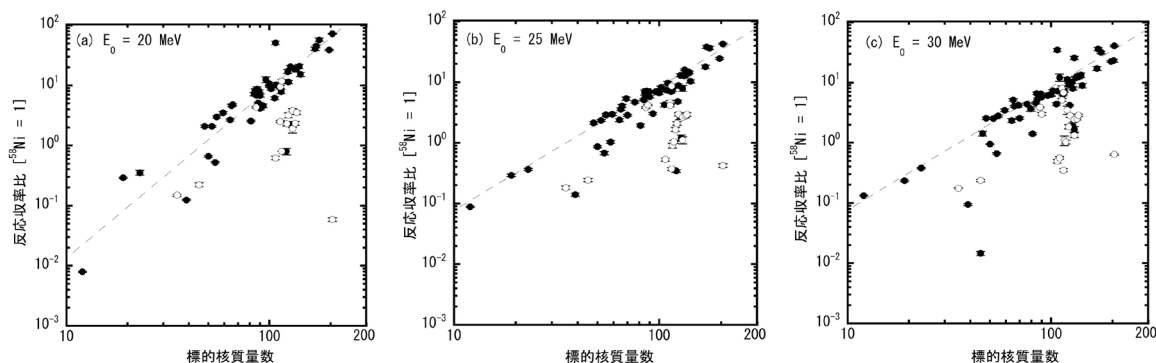
第1表に塩化物法と Ni 箔法のそれぞれで得られた反応収率比を示す。複数の定量値がある場合は、それらの荷重平均を示した。ほとんどの反応で、30 MeV と 25 MeV での照射共に、塩化物法による反応収率比と Ni 箔法による反応収率比の値は不確かさの範囲内で一致しており、値の比は $\pm 10\%$ の範囲内であった。斜体で示した値は、Ni 箔法での値と塩化物法での値の比が $\pm 10\% \sim \pm 20\%$ 異なっており、再検討が必要であるが、本研究で Ni 箔法による得られた反応収率比は十分に確からしいと判断できる。

第1表 異なる方法で定量した反応収率比の比較

標的核種	生成核種	30 MeV		25 MeV	
		塩化物法	Ni 箔法	塩化物法	Ni 箔法
Cl-35	Cl-34m	0.168 ± 0.008	0.175 ± 0.003	0.167 ± 0.007	0.182 ± 0.011
Na-23	Na-22	0.360 ± 0.035	0.379 ± 0.013	0.339 ± 0.03	0.364 ± 0.016
Rb-85	Rb-84	5.99 ± 0.55	<i>6.59 ± 0.34</i>	6.68 ± 0.62	6.80 ± 0.64
Rb-87	Rb-86	6.19 ± 0.57	5.92 ± 0.32	6.95 ± 0.64	7.08 ± 0.67
Sr-88	Sr-87m	4.14 ± 0.89	3.87 ± 0.09	4.7 ± 0.36	<i>4.19 ± 0.11</i>
Sr-86	Sr-85m	3.73 ± 0.81	3.62 ± 0.1	4.47 ± 0.38	<i>3.84 ± 0.13</i>
Sr-86	Sr-85	5.91 ± 1.31	5.41 ± 0.13	6.84 ± 0.64	<i>5.87 ± 0.17</i>
Sr-84	Sr-83	6.33 ± 2.21	<i>4.59 ± 0.16</i>	5.77 ± 0.46	<i>5.10 ± 0.19</i>
Cs-133	Cs-132	11.5 ± 1.1	12.4 ± 0.3	13.1 ± 1.2	<i>16.0 ± 0.5</i>
Ba-132	Ba-131	11.1 ± 1.1	12.0 ± 0.8	12.6 ± 1.2	12.8 ± 1.1
Ba-134	Ba-133m	2.53 ± 0.23	2.49 ± 0.12	2.75 ± 0.23	2.78 ± 0.2
Ba-136	Ba-135m	2.67 ± 0.24	2.86 ± 0.13	2.88 ± 0.24	2.92 ± 0.2
Pb-204	Pb-203	未測定	40.8 ± 1.4	41.3 ± 3.5	42.7 ± 1.2

最大エネルギーが 20, 25, ならびに 30 MeV の制動放射線で照射したときの (γ, n) 反応の反応収率比(複数の測定値の加重平均)を第3図にそれぞれ示す。核異性体などの親核種が存在する場合は、放射平衡

状態での放射能から反応収率を求めた。いずれのエネルギーにおいても、多くの反応収率比は標的核質量数 (A_t) の増加と共に累乗関数的に増加した。○で示した核異性体を生成する反応収率比は、●の基底状態核よりも反応収率比が一般的に小さく、これらは相対的に生成しにくいことがわかった。 E_0 が 25 MeV での反応収率比と 30 MeV での反応収率比は全 A_t 領域で類似した値であるが、20 MeV での値は、 A_t が約 80 より大きい領域では、25 MeV または 30 MeV の値より大きく (最大で約 3 倍)、また、 ^{12}C の値は約 10 倍小さい。原子核での光子による巨大共鳴が生じるエネルギーは A_t が小さいほど高い。 ^{12}C では約 24 MeV [1] であり、 $E_0 = 20$ MeV ではこのエネルギーに達しず、かつ、 $^{12}\text{C}(\gamma, n)^{11}\text{C}$ 反応のしきいエネルギーが 18.7 MeV と高いため、収率が小さくなったと考えられる。第 2 表で本研究で得られた $E_0 = 30$ MeV での反応収率比を文献値 [4, 8] と比較した。Segebade et al. の値は、比較できるように彼らの 1 時間照射時の放射能比の値から反応収率比を計算した値である。それぞれの核反応で本研究での値を含め 3 つの定量値があるが、これらの値が 3 つとも等しい反応は一つもなく、どれか一つが他と異なっている。 ^{89}Y , ^{90}Zr , ^{204}Pb 以外は、本研究での定量値は、2 つの文献値のどちらかと一致した。第 2 表を含めて本研究で定量したすべての反応では、本研究での定量値は Segebade et al. の値よりも小さく、多くは Segebade et al. の値の 1/2 倍から 1 倍の値であった。一部の反応では、100 倍以上、あるいは 1/100 倍以下異なる値もあった。値が一致しない原因は現在のところ不明である。



第 3 図 $^{58}\text{Ni}(\gamma, n)^{57}\text{Ni}$ 反応を基準とした (γ, n) 反応の反応収率比。(a) $E_0=20$ MeV. (b) $E_0=25$ MeV. (c) $E_0=30$ MeV. グラフ内の点線は傾向を表す目安。

§ 4. まとめ

炭素から鉛までの 41 元素で、最大エネルギーが 20 MeV, 25 MeV, 30 MeV の制動放射線を照射したときの (γ, n) 反応の反応収率比を $^{58}\text{Ni}(\gamma, n)^{57}\text{Ni}$ 反応を基準にして求めた。反応収率比は、標的核質量に対して系統的に変化した。今後、 $^{58}\text{Ni}(\gamma, n)^{57}\text{Ni}$ 反応の絶対反応収率を得ることで、絶対収率に変換可能である。本研究で求めた値は Segabade et al. の値よりも全体的に低い値であった。単一コンパレータ法による標準試料の光量子放射化分析を行ない、定量値からどちらの値がより正確か判断するとともに、異なった原因を解明していく予定である。また、 $(\gamma, 2n)$ 反応や (γ, pxn) 反応による生成核種も検出されているので、これらの反応収率比も求め、報告する予定である。

第 2 表 反応収率比の文献値との比較

標的核	生成核	本研究	Masumoto et al. (1978) [8]	Segebade et al. (1983) [4]
C-12	C-11	0.132 ± 0.003	0.12	未測定
Na-23	Na-22	0.379 ± 0.013	0.368	0.51
Ti-46	Ti-45	1.43 ± 0.13	1.54	1.9
Ca-48	Ca-47	2.54 ± 0.14	9.76	2.8
Cr-52	Cr-51	2.53 ± 0.07	2.89	5.2
Mn-55	Mn-54	2.80 ± 0.12	3.56	2.7
Ni-58	Ni-57	1	1	1
Co-59	Co-58	3.47 ± 0.16	3.24	4.5
Cu-65	Cu-64	5.13 ± 0.24	4.96	6.7
Y-89	Y-88	6.46 ± 0.23	8.56	8.1
Zr-90	Zr-89	5.74 ± 0.22	7.18	7.2
Hg-198	Hg-197	未測定	24.6	5.9
Tl-203	Tl-202	23.1 ± 1.3	33.6	28
Pb-204	Pb-203	40.8 ± 1.4	32.9	35

謝 辞

制動放射線照射では、菊永英寿准教授と塚田暁助教をはじめ、電子光理学研究センタースタッフの方々に大変お世話になりました。この場を借りて深く御礼申し上げます。

参 考 文 献

- [1] IAEA-TECDOC-1178 (2000) 72.
- [2] N. Iwamoto *et al.*: JAEA-Conf 2016-004 (2016) 53.
- [3] Kato : J. Radioanal. Chem. (1973) 307.
- [4] C. Segabade *et al.*: "Photon Activation Analysis" de Gryter (1983).
- [5] A. Simonits *et al.*: J. Radioanal. Chem. 24 (1975) 31.
- [6] 米沢, 松江: ぶんせき No.2 (2004) 75.
- [7] 大浦他: 核理研報告 32 (1999) 42.
- [8] K. Masumoto *et al.*: Nucl. Instr. Meth. **157** (1978) 99.

(ELPH Experiment : #2885)

Identification of Elemental Composition and Preparation of Radio-tracer for Recovery of Rare Metals in Household Garbage Incineration Slag by Photon Activation Method.

K. Akiyama^{1,*}, K. Ito¹, S. Kubuki¹, and H. Kikunaga²

¹*Department of Chemistry, Tokyo Metropolitan University, Hachioji, Tokyo 192-0397*

²*Research Center for Electron Photon Science, Tohoku University, Sendai, 982-0826*

Chemical composition of household garbage incineration slag supplied in September, October, and November, 2017 from Tamagawa incineration plant were determined by Photon Activation Analysis under the conditions of maximum electron beam energy of 20 **MeV** with 0.1 **mA** beam current at Research Center for Electron Photon Science (ELPH) of Tohoku University. Amount of determined elements were almost same as each other and almost consistent with the abundance in Earth's crust except for **Ca**, **Cr**, and some undetermined elements. In conclusion, it is necessary to investigate the element composition of incineration slag continuously in the future.

§1. Introduction

Amount of burnable garbage emitted from households is estimated to be about 650 million tons annually in OECD member countries, and also in Japan it is estimated to be about 50 million tons per year [1]. Although these garbage are usually incinerated and then buried as incineration ashes, there are same problems, such as securing the site for the burial disposal, because the emissions of these incineration ashes are enormous. In Tokyo, it is attempted for the improvement of the site problems to reduce of volume by melting and vitrifying of incineration ash and also to reuse these vitrified ash as the roadbed materials, the concrete aggregate, and the agent for the soil improvement. [2]

Kubuki and co-workers reported the chemical composition of vitrified ash of incinerated household garbage (incinerated slag) by induced coupled plasma optical emission spectroscopy (ICP-OES) measurements of their nitric acid solution and also the similarity of their composition with aluminosilicate including iron [3]. It is known that the vitrified solids of aluminosilicate indicate the decomposing ability of organic materials under the light irradiation [4]. If the incinerated slag of similar chemical composition with aluminosilicate indicates the decomposing ability of organic materials, it is possible to use the incinerated slag for the environmental purification, such as water purification, it could be expected as the new effective way to use of incinerated slag. However, incinerated slag contains many impurities, unlike aluminosilicate glass synthesized from the reagents. Since the impurities in incinerated slag include valuable metal elements such as cobalt and manganese, if it is possible to recover these elements

*Correspondence Address: Department of Chemistry, Tokyo Metropolitan University, Hachioji, Tokyo 192-0397

by chemical separation, it will lead to effective use of waste so called "Urban mine" and also to a solution to the universal theme in the contemporary society.

In this study, we aim to recover valuable metal elements from incinerated slag and to develop the recovery method by chemical separation. In this paper, we report the validity of chemical composition in incinerated slag per collecting month quantified by photon activation method.

§2. Experimental

Approximately 100 **mg** of incinerated slag collected in September, October, and November, 2017, were powdered with a handy agate mill. These powdered slag were wrapped in high purity aluminum foil, and then sealed under reduced pressure in a quartz tube for the irradiation with bremsstrahlung. we used JB-1a, whose elemental composition is quantitatively well assigned in National Institute of Advanced Industrial Science and Technology (AIST) Geological Survey of Japan, as the comparative standard for the photon activation analysis. Irradiation with Bremsstrahlung was carried out at Tohoku University, Research Center for Electron Photon Science (ELPH) under the conditions of maximum electron beam energy of 20 **MeV**, 0.1 **mA**. After that, γ ray emitted from samples were measured with a high purity **Ge** semiconductor detector (SEIKO EG&G).

§3. Results and Discussion

Figure 1 shows the γ ray spectra of slag samples collected in September (Slag09), October (Slag10), and November (Slag11), 2017, respectively. These spectra were obtained after about 2 weeks from the end of bombardment. It is presumed that the compositions of elements with high sensitivity in the photon activation are qualitatively very similar because these three spectra are closely similar to each other.

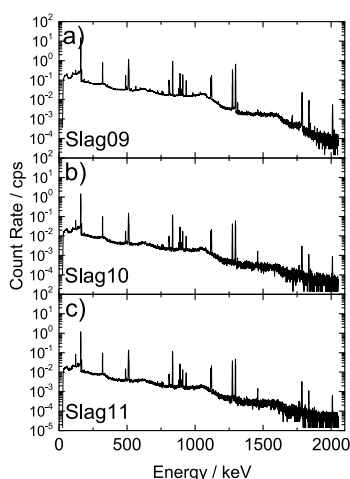


Fig.1. γ ray spectra of a) Slag09, b) Slag10, and c) Slag11 samples.

Table 1 indicates the elemental concentration determined by γ -ray analysis for each slag sample.

Almost all of determined elements in a slag are consistent with each other so that the variation of elemental composition in studied slag samples is found to be little. In addition, it could be seen that the elemental composition of these slags are not so much different from the element abundance in Earth's crust, except for calcium and chromium.

Table 1. Preliminary Concentration of Slag Sample Determined from γ -ray Measurements.

Element	Abundance in Earth's Crust	Slag09	Slag10	Slag11
Ca	5.0%	19.3±2.5%	22.81±0.99%	22.4±1.0%
Fe	6.3%	6.2±0.18%	6.12±0.13%	7.62±0.18%
Al	8.2%	2.73±0.21%	2.96±0.13%	3.17±0.12%
Mg	2.9%	1.869±0.011%	1.96±0.28%	2.10±0.29%
Ti	0.70%	1.68±0.13%	1.62±0.10%	1.511±0.076%
Na	2.3%	1.244±0.032%	2.397±0.036%	2.436±0.032%
Mn	0.11%	0.1924±0.0011%	0.2444±0.0023%	0.2525±0.0022%
Cr	140 ppm	1159±11 ppm	1221±24 ppm	1314±25 ppm
Sr	360 ppm	700±180 ppm		
Zr	130 ppm	127±16 ppm	154±15 ppm	143±17 ppm
Ni	90 ppm	56±34 ppm	78.4±8.4 ppm	128±10 ppm
Rb	60 ppm	45±13 ppm	11.02±0.80 ppm	10.9±1.2 ppm
Co	30 ppm	38.72±0.57 ppm	27.0±2.4 ppm	36.1±1.8 ppm
Nb	17 ppm	18.77±0.87 ppm	22.74±1.2 ppm	25.4±1.5 ppm
Zn	79 ppm	16±11 ppm	32±10 ppm	28.1±9.0 ppm
Y	29 ppm	13.12±0.50 ppm	16.1±1.0 ppm	15.56±0.65 ppm
Sc	26 ppm	5.0±1.0 ppm		
As	2.1 ppm	1.15±0.29 ppm		
Ce	60 ppm	0.34±0.24 ppm	0.419±0.028 ppm	0.474±0.027 ppm
Se	50 ppb	10.5±2.7 ppb		
Au	3.1 ppb	0.44±0.12 ppb		

Table 2 is list of the elements which could not be determined because γ -ray peaks were able to be observed in slag samples but γ -ray peak in JB-1a used for a comparative standard could not be observed because of their low concentration or low sensitivity. It is expected that these elements show sufficiently higher concentrations than the element concentrations in JB1a and the Earth's crust, and it can be considered that these elements should be noted in the study of the recovery of valuable metal elements in the future work. In conclusion, it is necessary to investigate such variation in element composition continuously in the future.

Acknowledgment

We deeply thank to the facility staffs of research center for electron photon science at Tohoku University for supplying the high-quality electron beam. And also we thank to Doctor Kyo Tsukada for helping us in the sample irradiation. This work was partly supported by Tokyo Metropolitan Government (Advanced research program).

Table 2. Undetermined Elements Observed in Slag samples.

Element	Abundance in Earth's Crust	JB-1a Concentration		Observed Sample
Ag	80 ppb	41.0 ppb	<	Slag09
Ba	340 ppm	504 ppm	<	Slag09, Slag10, Slag11
Cs	1.9 ppm	1.31 ppm	<	Slag09
Cu	68 ppm	56.7 ppm	<	Slag09
Nd	33 ppm	26.0 ppm	<	Slag10, Slag11
Pt	3.7 ppb	1.60 ppb	<	Slag09
Sb	0.2 ppm	0.25 ppm	<	Slag09, Slag10, Slag11
Te	1 ppb	NA	<	Slag09, Slag10, Slag11

References

- [1] OECD, "Municipal Waste", in *OECD Factbook 2015-2016: Economic, Environmental and Social Statistics*, OECD Publishing. DOI: 10.1787/factbook-2015-en (2016).
- [2] Waste Report ed. Clean Authority of Tokyo, (2018) vol. 23, p. 7.
- [3] S. Ishikawa, B. Kobzi, K. Sunakawa, S. Nemeth, A. Lengyel, E. Kuzmann, Z. Homonnay, T. Nishida, S. Kubuki, *Pure Appl. Chem.*, **89**, 535 (2017).
- [4] Y. Iida, K. Akiyama, B. Kobzi, K. Sinkó, Z. Homonnay, E. Kuzmann, M. Ristić, S. Krehula, T. Nishida, S. Kubuki, *J. Alloys Compd.*, **645**, 1 (2015).

(ELPH Experiment: #2887)

Radioactive phantom productions for PET and β -ray imaging system

T Fukuchi¹, H. Haba², and H. Kikunaga³¹ *RIKEN Center for Biosystems Dynamics Research, Kobe, 650-0047 Japan*² *RIKEN Nishina Center for Accelerator-Based Science, Wako, 351-0198 Japan*³ *Research Center for Electron Photon Science, Tohoku University, Sendai, 982-0826 Japan*

We have been developing imaging systems for nuclear medicine. In order to test the performance of developing imaging systems, we have produced radioactive phantoms using the photo-dissociation reactions. Produced phantoms were a volumetric $^{44}\text{Ti}/^{44}\text{Sc}$ phantom for a PET imaging and thin ^{22}Na phantoms for a β -ray imaging system. We performed imaging experiments using these phantoms and assessed the basic performance of the developing systems.

§ 1. Introduction

We have been developing the next-generation nuclear medicine imaging systems. One is a multiple-isotope PET (positron emission tomography), and the other is a β -ray imaging system. Both systems are designed to make coincidence with γ -ray using the additional detectors. Therefore, using β -decay nuclide, which promptly emits de-excitation γ -ray emission (so-called positron- γ emitter or β - γ emitter) as a tracer, the γ -ray coincidence enables identification of nuclide or improvement of the imaging qualities.

Figure 1 (a) shows a photograph of our developed PET system. This system is composed of a PET system and additional γ -ray detectors. The PET system consists of pixelized gadolinium orthosilicate (GSO) scintillation detectors and has a ring geometry with 95 mm in inner diameter and 37.5-mm width. The additional detectors are eight bismuth germanium oxide (BGO) scintillation detectors, each of which has size of $50 \times 50 \times 30$ mm³, arranged in two rings mounted on each side of the PET ring [1].

Figure 2 (a) shows a photograph of the developed β -ray imaging system. The system consists of a position sensitive β -ray detector and a large volume γ -ray detector. These detectors were mounted on

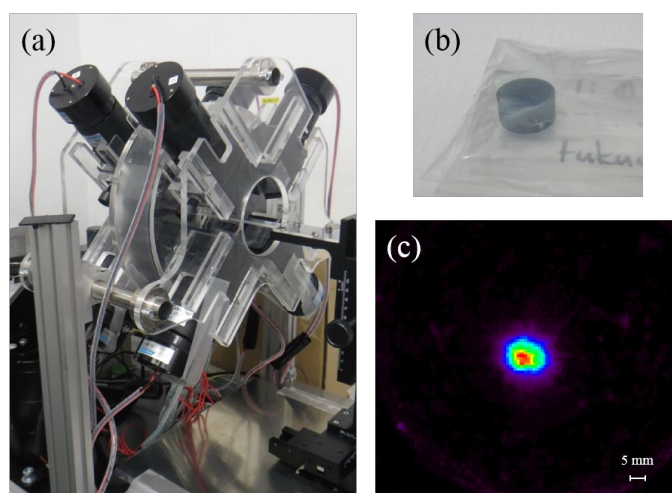


Fig. 1. (a) Our developing PET system with additional γ -ray detectors. (b) Produced $^{44}\text{Ti}/^{44}\text{Sc}$ phantom for PET imaging. (c) An example of reconstructed image of the $^{44}\text{Ti}/^{44}\text{Sc}$ phantom.

the flexible frames and can locate on the arbitrary positional relations. A $35 \times 35 \times 1 \text{ mm}^3$ La-GPS(Ce) scintillator pixelized in 300- μm pitch by a grooving process [2] was employed for the β -ray detection. A bismuth germanium oxide (BGO) scintillator with a size of $50 \times 43 \times 16 \text{ mm}^3$ coupled to a photomultiplier tube was used as a γ -ray detector.

In order to evaluate the performances of our developed systems, it is necessary to perform the phantom imaging experiment, which visualize the already-known radio-tracer distributions.

Therefore, we carried out experiments to produce the ^{44}Ti and ^{22}Na phantoms. Titanium-44 decays to the ^{44}Sc with 59.1 years physical half-life and ^{44}Sc is a positron- γ emitter with a half-life of 3.95 hours. Sodium-22 is also a positron- γ emitter with a half-life of 2.6 years and emits a prompt γ -ray with energy of 1275 keV. Therefore, both nuclides are useful for performance test of our developed systems.

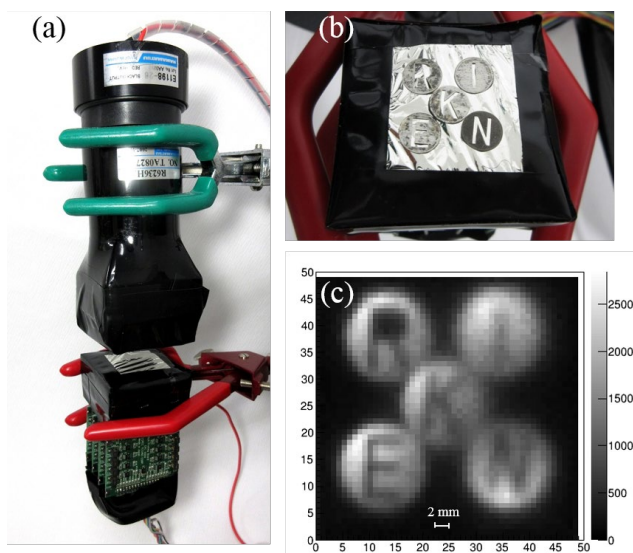


Fig. 2. (a) Our developing β -ray imaging system with additional γ -ray detector. (b) Produced ^{22}Na phantoms and experimental setup. (c) An example of reconstructed image of the ^{22}Na phantoms.

§ 2. Experiments

2.1 $^{44}\text{Ti}/^{44}\text{Sc}$ phantom

Since PET can provide 3-dimensional distribution of a tracer, the phantom should have 3-dimensional distribution for the performance test. Accordingly, we prepared a natural Ti target of a cylindrical shape with 8 mm in diameter and 5-mm thickness (Fig. 1 (b)). A natural existing ratio of ^{46}Ti is 8%, and ^{44}Ti was produced using a photo-dissociation reaction of $^{46}\text{Ti}(\gamma, 2n)^{44}\text{Ti}$. The production experiments were performed at Research Center for Electron Photon Science (ELPH) in Tohoku University. The enclosed target was placed in the back of a platinum converter and cooled with running tap water. The accelerator was operated for 3 hours irradiation at an electron energy of 50 MeV with a mean current around 100 μA .

2.2 ^{22}Na phantoms

Owing to the short flight range of β -ray in a material, the β -ray imaging is restricted to imaging for a 2-dimensional object. Therefore, we prepared the 5 thin disk shape targets for the test of the β -ray imaging system. These targets were made of natural Mg (^{24}Mg isotope ratio: 79%) and has 8 mm in diameters and 0.21-mm thicknesses with alphabetic characters “RIKEN” of 1 mm width mortising. The 3 hours irradiation was performed by the ELPH accelerator in a similar manner with ^{44}Ti production using $^{24}\text{Mg}(\gamma, pn)^{22}\text{Na}$ reaction with electron energy of 50 MeV.

§ 3. Results

3.1 PET imaging

The produced radioactivity in a ^{44}Ti cylindrical phantom was 38 Bq. An imaging experiment for $^{44}\text{Ti}/^{44}\text{Sc}$ cylindrical rod using our developed PET system were performed for 12 hours. From the

reconstructed image of a $^{44}\text{Ti}/^{44}\text{Sc}$ phantom as shown in Fig. 1 (c), we confirmed that our developed PET system has ability to visualize the tracer distribution with low activity by a long hour of measurement. This result indicates our developed system is useful for not only a nuclear medicine but also an activation analysis or non-destructive test in the industrial field.

3.2 Beta-ray imaging

The produced total radioactivity of ^{22}Na phantoms is 3.4 kBq. For these phantoms, a measurement using our developed β -ray imaging system was performed for 10 min. Figure 2 (b) shows photograph of experimental setup. Five phantoms were measured at the same time. From the reconstructed image shown in Fig. 2 (c), the alphabetic characters on phantoms can be easily recognized and we find that our developed β -ray system had about 0.5 mm imaging resolution.

Acknowledgements

The authors thank to the facility staffs of ELPH in Tohoku University for supplying the high-quality electron beam. The authors thank Prof. Yamamoto for the development of the imaging devices. This work was supported by JSPS KAKENHI Grant Number JP15H04770.

References

- [1] T. Fukuchi *et al.*: Medical Physics 44 (6) (2017) 2257.
- [2] S. Yamamoto *et al.*: Journal of Instrumentation 13 (2018) P05028.
- [3] National Nuclear Data Center, Brookhaven National Laboratory. <http://www.nndc.bnl.gov/>.

III. Status Report

Status of Accelerator Facilities in FY2017

Accelerator group

Research Center for Electron Photon Science, Tohoku University, Sendai, 982-0826

The electron accelerator complex: high intensity 60 MeV linac, 90 MeV injector linac and 1.3 GeV BST (booster-storage ring), had been regularly operated for user time in FY 2017 and the total operating time exceeded 2000 hours including the operation of the test accelerator t-ACTS. A large-scale replacement and renovation work in the indoor electrical substation were conducted in the end of FY2017. In the same time, the Experimental Hall No. 1 was also renovated in order to secure the safety in handling the non-sealed RI material, and thus all the machine time was suspended for more than three months. In this report, machine status and some improvements are reported.

§1. Machine operation

1.1 High intensity linac

For the high intensity linac, the operating beam time in FY 2017 reached 240 hours. The electron beam with the energy ranging from 10 to 60 MeV was supplied depending on a requirement of individual machine user. The typical beam current was 120 μA for 50 MeV operation. Although the machine time was performed almost as scheduled, there were some minor troubles in the linac. Those troubles were mainly caused by an aging phenomenon of the machine components, such as the degradation of a signal cable for the current monitor and a breakdown of power supply for NIM crate, etc. A high-voltage control for the electron gun has also trips sometimes due to the failure of the inverter power supply; however the detailed cause is still under investigation. The other minor trouble is so-called “vacuum explosion”, in which the vacuum pressure of beam line suddenly increases and finally results in a suspension of the machine operation because of the trip of ion pumps. Since the deterioration of the ion pumps themselves was presumed, some ion pumps in the downstream part of the accelerating structure were replaced partially.

1.2 Injector linac

The injector linac has stably supplied electron beam with the energy of 90 MeV to BST ring. In these years, however, the thermionic rf gun had a problem that discharges at the cathode cell in the gun have been frequently observed due to deposition of carbon-like matter between the cathode and the cavity wall. Such discharges has begun to occur at around one year after the installation of new cathode. Although the reason for the deposition is still under investigation, currently we have coped with this problem by replacing the cathode once a year. As the other minor troubles, there are failures in cooling

water system which trip the rf modulator. The malfunction of the flow switches is suspected, so that it is planned to replace these suspicious switches.

1.3 BST ring

1.3 GeV BST ring has also well operated to generate high energy gamma rays via bremsstrahlung from internal target wire inserted to the electron beam orbit. Generated gamma rays are not only utilized to the experiment for quark/hadron physics, but also supplied to the test beam line for testing of detectors used in high energy experiments. There were two major troubles in FY2017; one was a breakdown of movable tuner installed in an rf cavity and the other one was a trouble in a power supply of a bump magnet. For both troubles it took more than half a day to restart the user time. Some other minor troubles in BST operation have also occurred and those sources are mainly recognized to be an aged deterioration similar to the high intensity linac. Especially, the aging phenomenon in the klystron power supply for the rf cavity is serious, and thus a project to replace the old klystron to a new rf source based on the solid-state amplifiers is under consideration.

§2. Facility improvements

2.1 Replacement and renovation work in indoor electrical substation

So far, updates of aged electric facilities have been carried out over the past three times. Starting with the renewal of the gas circuit breaker of the extra-high voltage substation in FY2007, in FY2009 the transformers of the substation and an emergency power generator in the indoor substation were renewed, and in FY2013 and FY2014, control panel and some transformers in the indoor substation were updated. Then all remained transformers and low voltage switchboard in the indoor substation were finally updated at the end of FY2017. Also, as a countermeasure against rain leakage due to the aging of buildings, roofs and exterior walls were also refurbished. It took more than three months to complete these replacement and renovation works. Figure 1 shows the inside of the indoor substation before and after the update. Transformers and switchboards, where dangerous high voltage terminals were exposed, were replaced by safe and compact modular equipment. Moreover, in addition to updating the old transformers which had somewhat of losses, the connection of the load equipment was also adjusted so that the load during operation is balanced. Due to this update, the maximum power consumption during accelerator operation is also slightly reduced.

2.2 Renovation of the Experimental Hall No.1

For RI production and research on nuclear and radiochemistry, the electron beam from the high intensity linac is transported to the Experimental Hall No. 1 and then irradiated to various targets arranged in the irradiation apparatus placed just before the beam dump. In response to the new guidance of the Nuclear Regulatory Agency on the handling of unsealed RI sources (limited use under the encapsulated condition) an extensive renovation was carried out at the end of FY2017 in conjunction with renovation of the indoor electrical substation. The main contents of this work are floor and wall



Fig.1. Transformers and switchboards in the indoor substation before (upper picture) and after the replacement (lower). The renovation of the indoor substation was also performed.

treatment to prevent infiltration of the radioactive material, and renovation of the drainage route. In the renovation of the floor surface, concrete was filled in all the piping pits provided on the floor, and the floor surface was also ground and smoothed. After that, painting and coating treatment with 2 mm thickness was applied using epoxy resin with radiation resistance capability. The wall surface was also treated using the same epoxy resin type material with 0.2mm thickness. The inside of the Experimental Hall before and after renovation work is shown in Fig. 2.

§3. Construction plan of new beam line

In the coming shut down period, it is planned to construct a new beam line to conduct an experiment for electron scattering with extremely low energy transfer, which is aiming to solve the “Proton Radius Puzzle” [1, 2]. This experiment requires high quality electron beam with very small energy spread of less than 0.1 % and variable beam energy of about 20 to 60 MeV. The new beam line and a spectrometer for the experiment will be placed in the Experimental Hall No. 1, and share the beam from the high intensity linac with the present RI beam line. At present, a lattice modification of the transport line from the linac, installation of additional beam monitor and beam slit, etc. are under preparation in advance of the construction of the new beam line.



Fig.2. Renovation of wall and floor in the Exp. Hall No.1. Upper picture shows an end part of the beam line in the experimental hall before the renovation. Lower picture shows the reconstructed shield blocks after the renovation.

References

- [1] Randolph Pohl *et al.*, Nature vol. 466, 213 (2010)
- [2] Aldo Antognini *et al.*, Science vol. 339, 417 (2013)

User Support Office Report in FY2017

M. Miyabe¹ and The user support office¹

¹*Research Center for Electron Photon Science, Tohoku University, Sendai, 982-0826, Japan*

The User Support Office coordinate across the users and our facility for management of the beam-time. In 2017 financial year, we had provided the electron, photon and positron beam without apparent problems except for Photon beamline I. From Jan to Mar 2018, we couldn't provide any user beam-time because of the repairing work of electric room.

§1. Introduction

ELPH has three accelerators for Joint Usage/Research. Our facility could provide several beams with following three beam lines,

- 70 MeV electron linear accelerator (linac) at the first irradiation lab (For Radiochemistry)
- Tagged photon beam from 1.3 GeV electron synchrotron called BST ring with 90 MeV injector at the second irradiation lab (For Hadron Physics, **Photon beamline I**)
- Tagged photon beam at the GeV- γ irradiation room (For Hadron Physics, **Photon beamline II**)

In addition, positron/electron beam line for testing detectors is located at the GeV- γ irradiation room. The 70 MeV electron linear accelerator was utilized for the Radiochemistry experiments by photo-nuclear reactions. It could produce radio active source with its high intensity. Both tagged photon beam line was used for Hadron physics experiments. NKS2 and FOREST/BLC experiment have been held in recent years.

§2. Beamtime operated

The total radiation time was 239 hours for the RI linac operation and 1658 hours for the BST operation, and it was 1898 hours in total. The beam provided time (user beamtime) was 1629 hours for the BST operations. Table 1 summarizes the radiation times, and user beam times in fiscal.

Many experiments for testing detectors were made by positron beam line. Positron beam was produced by bremsstrahlung photon beams from the synchrotron. Total 35 shift experiments are performed using this positron beam in this financial year.

A Next generation FOREST experiments (FOREST/BLC) was started by GeV- γ group in ELPH. New bending magnet was installed on the downstream of FOREST detectors and it covers the most forward angle. These new experimental setup enable the zero degree proton detection for the $\gamma d \rightarrow p\eta n$ reaction at $E_\gamma \sim 0.9$ GeV. This reaction gives the zero relative momentum between the η and n . This situation will enable to determine the ηn scattering length. In this financial year, New spectrometers were

installed in the downstream of BLC magnet, and the pilot experiment of FOREST/BLC was performed.

In Photon beam line I, The photon beam was recovered after the repairs for the radiator driving system, NKS2 experiment will carry out in next financial year.

one experiment was carried out for the undergraduate students. this experiment (#2884: N. Muramatsu, ELPH, Tohoku University) is for the education of the undergraduate students in ELPH.

Table 1. Radiation times, and user beamtimes in financial year 2017. They are given by the sum of the times that the beam is coming to the beamline, and that the beam is provided to the users.

Month	RI Linuac	BST Ring	
	radiation (h)	radiation (h)	user (h)
April	2	253	256
May	16	238	234
Jun	29	222	229
July	8	12	13
August	0	0	0
September	14	2	0
October	69	84	81
November	27	626	592
December	74	222	218
January	0	0	0
February	0	0	0
March	0	0	0
Sum	239	1658	1629

§3. ELPH workshops and ELPH seminars

In this fiscal year, ELPH supported four ELPH workshops. The first one is hadron physics (C020: H. Kanda, Kyoto University), the second one is hadron physics (C019: T. Ishikawa, ELPH Tohoku University), the thirds is SNP school 2017 (C017: S. N. Nakamura, Tohoku University), the fourth one is accelerator physics (C018: H. Zen, Kyoto University).

17 ELPH seminars were held in this fiscal year. Seminars title and talker are listed below.

- Shuo Wang, Shandong University, China JinPing underground Laboratory for Nuclear Astrophysics”
- T. Ishikawa, ELPH, ” η photoproduction on the deuteron at $E_\gamma < 1.2$ GeV”
- Y. Tsuchikawa, Nagoya University, ”Experimental study for the “neutron anomaly” via neutral kaon photoproduction at ELPH”
- KIM, Hyun-Chul, Inha University, ”Structure of the $N^*(1685)$ resonance”
- N. Tsukamoto, Tohoku University, ”陽子形状因子の解析と電荷半径及びその不定性”
- T. Iijima, KMI Nagoya University ”Heavy Flavor Hadron Physics at SuperKEKB/Belle II”
- M. Kando, QST, ”高強度レーザーを用いた電子加速の研究の進展と高強度場科学”
- K. Ishida Riken ”ミュオン水素原子の超微細構造エネルギー測定による陽子 Zemach 半径決定”
- H. Sakai KEK ”EURO-XFEL の建設に携わって (DESY 1 年間滞在中の EURO-XFEL の超伝導空洞の量産化試験と XFEL 発振に至るまで) ”

- T. Ohtsuki, Sophia University, "深層学習を用いたランダム電子系の量子相転移の研究"
- G. Mitsuka, Riken "200GeV pp/pA 衝突における前方中性子の横偏極単スピン非対称と ultra-peripheral collision を用いた解釈"
- H. Tanida, JAEA " Λ_c 崩壊と $Kp \rightarrow \Lambda\eta$ 反応における新しい Λ 共鳴の可能性"
- H. Nohmi, RCNP, "重いクォークを含むバリオンの分光研究 : J-PARC の実験からわかること"
- Steven Karataglidis, University Johannesburg, "Exploring exotic nuclei within the MCAS framework"
- Carlo Barbieri, University Surrey, "Self-Consistent Green's Function Studies of Medium Mass Isotopes"
- S. Narita, Iwate University "凝縮系核科学の概要と最近の状況"
- Carlos Bertulani, Texas A&M, "Electromagnetic Probes of Exotic Nuclei"
- Oleg Denisov, INFN-Torino and CERN, "Future QCD facility at SPS (CERN) extracted beams"

Radiation Safety Report 2017

Radiation Safety Office

放射線安全管理室より、2017年度(平成29年4月～平成30年3月)の報告を以下の通り行う。

§ 1. 許認可申請

- H29年4月3日 放射線取扱主任者 選任 石川貴嗣
(H25年6月1日 選任 菊永英寿(正)、武藤俊哉)
- H29年7月11日 定期検査・定期確認(H29年7月25日 合格・適合)
- H29年8月9日 変更承認申請
- H29年10月4日 承認
(変更の内容)
1. 非密封同位元素使用施設の変更(作業室, 汚染検査室の追加)
 2. 非密封同位元素使用核種および数量の変更
 3. 下限数量以下の非密封放射性同位元素の管理区域外使用の核種の追加
 4. 70 MeV 電子線形加速装置のビームライン変更(3.5 m 延長)
 5. 50 MeV 電子線形加速装置の使用時間の変更
 6. インターロック動作の変更
 7. 放射化物保管容器の変更
 8. 使用施設の変更(作業室, 汚染検査室の材質の変更)
 9. 排水経路の変更(使用施設, クライストロン室入口の流しの追加)

§ 2. 個人管理

2.1 放射線業務従事者登録

209人(東北大 68人 学外 77人 研究者以外 64人)

2.2 個人被ばく管理

1年間の個人被ばく線量 5 mSv 以下 209人

2.3 教育訓練

定期講習

平成 29 年 7 月 19 日 登録前教育 10 人 再教育 69 人

特別講演の内容:

青森県エネルギー総合対策局量子科学センター開設準備室 一戸 浩二 氏
「青森県量子科学センターの概要」

不定期の講習

再教育 19 回 28 人

登録前教育(新規教育) 24 回 103 人

§ 3. 自主点検

年 2 回実施 平成 29 年 9 月 29 日、平成 30 年 3 月 14 日

§ 4. 放射性同位元素製造記録

2017 年度に本加速器施設で製造され、共同研究に使用された放射性同位元素は次の通りである。

核種	数量 (kBq)
Au-196	1,700
C-11	12,700
Ce-139	10
Co-56	500
Co-57	1,107
Co-58	800
Co-60	300
Cr-51	100
Cs-132	200
Cs-136	2,000
Cu-64	110,000
Cu-67	4,000
F-18	5,000
I-126	500
K-42	6,400
K-43	42,000

Mn-54	4
Mo-99	2,694,700
Na-22	300
Ni-57	6,700
Pm-143	300
Rb-84	2
Rb-86	500
Sb-124	500
Sc-46	5,200
Sr-85	6
Ta-182	500
Ti-44	1
V-48	300
Y-88	40
Zn-65	4,100
Zr-95	2
全 32 核種	計 2,900,472 kBq

IV. List of Publication

List of Publication (論文リスト) (2017)

Papers Published in Refereed Journals

Demonstration of Coherent Radiation Generation up to 3THz from Femtosecond Electron Pulses

H. Hama, T. Abe, S. Kashiwagi, F. Hinode, T. Muto, H. Saito, K. Nanbu, K. Takahashi,
I. Nagasawa, K. Kanomata, H Saito, and Y. Saito

Int J Opt Photonics Eng, 2:004 (2017).

Study of Cherenkov Radiation from Thin Silica Aerogel

K. Nanbu, S. Kashiwagi, F. Hinode, T. Muto, I. Nagasawa, K. Takahashi, K. Kanomata,
H. Saito, T. Abe, Y. Saito and H. Hama

Int J Opt Photonics Eng, 3:007 (2017).

Construction and commissioning of the compact energy-recovery linac at KEK

Mitsuo Akemoto, Dai Arakawa, Seiji Asaoka, Enrico Cenni, Masato Egi, Kazuhiro Enami,
Kuninori Endo, Shigeki Fukuda, Takaaki Furuya, Kaiichi Haga, Ryoichi Hajima,
Kazufumi Hara, Kentaro Harada, Tohru Honda, Yosuke Honda, Teruya Honma,
Kenji Hosoyama, Eiji Kako, Hiroaki Katagiri, Hiroshi Kawata, Yukinori Kobayashi,
Yuuji Kojima, Yoshinari Kondou, Olga Tanaka, Tatsuya Kume, Masao Kuriki,
Hiroshi Matsumura, Hideki Matsushita, Shinichiro Michizono, Takako Miura,
Tsukasa Miyajima, Shinya Nagahashi, Ryoji Nagai, Hirotaka Nakai, Hiromitsu Nakajima,
Norio Nakamura, Kota Nakanishi, Kazuyuki Nigorikawa, Nobuyuki Nishimori,
Takashi Nogami, Shuichi Noguchi, Takashi Obina, Feng Qiu, Hidenori Sagehashi,
Hiroshi Sakai, Shogo Sakanaka, Shinichi Sasaki, Kotaro Satoh, Masaru Sawamura,
Miho Shimada, Kenji Shinoe, Toshio Shishido, Mikito Tadano, Takeshi Takahashi, Ryota Takai,
Tateru Takenaka, Yasunori Tanimoto, Takashi Uchiyama, Akira Ueda, Kensei Umemori,
Ken Watanabe, Masahiro Yamamoto

Nuclear Instruments and Methods in Physics Research Section A: Accelerators, Spectrometers,
Detectors and Associated Equipment, 877 (2018), 197-219.

核理研から電子光センター、50年の歩み

日出富士雄、濱 広幸

加速器、Vol. 14, No. 2 (2017) 74 – 80

ILCの多角的活用

岩下芳久、山本樹、河村成肇、牧村俊助、野村大輔、下村浩一郎、山崎高幸、柏木茂、

兵頭俊夫、三島賢二、早川岳人、嶋達志
 加速器、Vol. 14, No.4 (2017) 236-242.

Prospects for Electron Scattering on Unstable, Exotic Nuclei (Review paper)

T. Suda and H. Simon

Progress of Particle and Nuclear Physics, 96 (2017) 1-31.

First Elastic Electron Scattering from ^{132}Xe at the SCRIT Facility

K. Tsukada, A. Enokizono, T. Ohnishi, K. Adachi, T. Fujita, M. Hara, M. Hori, T. Hori,
 S. Ichikawa, K. Kurita, K. Matsuda, T. Suda, T. Tamae, M. Togasaki, M. Wakasugi,
 M. Watanabe, and K. Yamada

Phys. Rev. Lett. 118 (2017) 262501.

陽子電荷半径パズル

須田利美

パリティ 33 (2018) 57-59.

極低運動量領域での電子・陽子弾性散乱による陽子荷電半径の精密決定

須田利美、塚田暁

原子核研究 61(2017) 87-98.

Use of different surface covering materials to enhance removal of radiocaesium in plants and upper soil from orchards in Fukushima prefecture.

M. Sato, H. Akai, Y. Saito, T. Takase, H. Kikunaga, N. Sekiya, T. Ohtsuki, and K. Yamaguchi
 Journal of Environmental Radioactivity (in press).

Neutral Kaon Spectrometer 2

M. Kaneta, B. Beckford, T. Fujii, Y. Fujii, K. Futatsukawa, Y.C. Han, O. Hashimoto, K. Hirose,
 T. Ishikawa, H. Kanda, C. Kimura, K. Maeda, S.N. Nakamura, K. Suzuki, K. Tsukada,
 F. Yamamoto, H. Yamazaki

Nucl. Instrum. Meth. A886 (2018) 88-103

Beam helicity asymmetries in $K^+\Lambda$ electroproduction off the proton at low Q^2

P. Achenbach, C. Ayerbe Gayoso, R. Böhm, O. Borodina, D. Bosnar, V. Bozkurt, P. Bydžovský,
 L. Debenjak, M.O. Distler, A. Esser, I. Frišćić, Y. Fujii, T. Gogami, M. Gómez Rodríguez,
 O. Hashimoto, S. Hirose, H. Kanda, M. Kaneta, E. Kim, A. Margaryan, H. Merkel, U. Müller,
 S. Nagao, S.N. Nakamura, J. Pochodzalla, C. Rappold, J. Reinhold, T.R. Saito,
 A. Sanchez Lorente, S. Sánchez Majos, B.S. Schlimme, M. Schoth, F. Schulz, C. Sfienti,
 S. Širca, D. Skoupil, L. Tang, M. Thiel, K. Tsukada

Eur. Phys. J. A53 (2017) no,10, 198

Spectroscopy of pionic atoms in $^{122}\text{Sn}(d,^3\text{He})$ reaction and angular dependence of the formation cross sections

T. Nishi, K. Itahashi, G.P.A. Berg, H. Fujioka, N. Fukuda, N. Fukunishi, H. Geissel, R.S. Hayano, S. Hirezaki, K. Ichikawa, N. Ikeno, N. Inabe, S. Itoh, M. Iwasaki, D. Kameda, S. Kawase, T. Kubo, K. Kusaka, H. Matsubara, S. Michimasa, K. Miki, G. Mishima, H. Miya, H. Nagahiro, M. Nakamura, S. Noji, K. Okochi, S. Ota, N. Sakamoto, K. Suzuki, H. Takeda, Y.K. Tanaka, K. Todoroki, K. Tsukada, T. Uesaka, Y.N. Watanabe, H. Weick, H. Yamakami, K. Yoshida

Phys. Rev. Lett. Accepted

Oxygen-15 labeled CO₂, O₂, and CO PET in small animals: evaluation using a 3D-mode microPET scanner and impact of reconstruction algorithms

Genki Horitsugi, Tadashi Watabe, Yasukazu Kanai, Hayato Ikeda, Hiroki Kato, Sadahiro Naka, Mana Ishibashi, Keiko Matsunaga, Kayako Isohashi, Eku Shimosegawa, Jun Hatazawa
EJNMMI Research 7, (2017) 91.

First demonstration of multi-color 3-D in vivo imaging using ultra-compact Compton camera

Aya Kishimoto, Jun Kataoka, Takanori Taya, Leo Tagawa, Saku Mochizuki, Shinji Ohsuka, Yuto Nagao, Keisuke Kurita, Mitsutaka Yamaguchi, Naoki Kawachi, Keiko Matsunaga, Hayato Ikeda, Eku Shimosegawa, and Jun Hatazawa
Scientific Reports 7 (2017) 2110.

Practical calculation method to estimate the absolute boron concentration in tissues using ¹⁸F-FBPA PET

Tadashi Watabe; Kohei Hanaoka; Sadahiro Naka; Yasukazu Kanai; Hayato Ikeda; Masanao Aoki; Eku Shimosegawa; Mitsunori Kirihata; Jun Hatazawa
Annals of Nuclear Medicine 31 (2017) 481–485.

Charge-to-time converting leading-edge discriminator for plastic-scintillator signals.

T. Ishikawa, Y. Takeda, Y. Honda, Y. Inoue, H. Kanda, S. Kido, Y. Matsumura, M. Miyabe, I. Nagasawa, H. Shimizu, T. Takeda, A.O. Tokiyasu, Y. Tsuchikawa, H. Yamazaki
Nuclear Instruments and Methods in Physics Research Section A, 875(2017) 193-200

First measurement of coherent double neutral-pion photoproduction on the deuteron at incident energies below 0.9 GeV.

T. Ishikawa, H. Fujimura, H. Fukasawa, R. Hashimoto, Q. He, Y. Honda, T. Iwata, S. Kaida, H. Kanda, J. Kasagi, A. Kawano, S. Kuwasaki, K. Maeda, S. Masumoto, M. Miyabe, F. Miyahara, K. Mochizuki, N. Muramatsu, A. Nakamura, K. Nawa, S. Ogushi, Y. Okada, K. Okamura, Y. Onodera, K. Ozawa, Y. Sakamoto, M. Sato, H. Shimizu, H. Sugai, K. Suzuki, Y. Tajima, Y. Taniguchi, Y. Tsuchikawa, H. Yamazaki, R. Yamazaki, and H.Y. Yoshida
Physics Letters B, 772(2017) 398-402.

First Determination of the Level Structure of an sd-Shell Hypernucleus, ¹⁹_ΛF

S.B. Yang et al.,
Phys. Rev. Lett. 120 (2018) 132505(1-5)

Reopening of Research Activities on Strangeness Nuclear Physics at J-PARC

Kazuhiro Tanaka, Hirokazu Tamura,

Nucl. Phys. News 27 (2017) 21-27.

Missing-mass spectroscopy with the ${}^6\text{Li}(\pi^-, \text{K}^+)\text{X}$ reaction to search for ${}^6_\Lambda\text{H}$

R. Honda et al..

Phys. Rev. C96 (2017) 014005(1-23) (Editors' Suggestion).

Identification of regions responsible for the function of the plant K^+ channels KAT1 and AKT2 in *Saccharomyces cerevisiae* and *Xenopus laevis* oocytes

Saito, S., Hoshi, N., Zulkifli, L., Widyastutib, S, Goshima, S., Dreyer, I. and Uozumi,

N. Channels, 510-516, 11 (6) (2017)

Dimerization of GTR1 regulates their plasmamembrane localization.

Ishimaru, Y., Washiyama, K. Oikawa, T. Hamamoto, S. Uozumi, N. and Ueda, M.

Plant Signal. Behav. e1334749, 12, (6) (2017)

Probing native metal ion association sites through quenching of fluorophores in the nucleotide binding domains of the ABC transporter MsbA.

Tatsumi, D., Nanatani, K., Koike, Y., Kamagata, K., Takahashi, S., Konno, A., Furuta, T.,

Sakurai, M. and Uozumi, N.

Biochem. J. 474, 1993-2007 (2017)

Kup-mediated Cs^+ uptake and Kdp-driven K^+ uptake coordinate to promote cell growth during excess Cs^+ conditions in *Escherichia coli*

Tanudjaja, Ellen, Hoshi, N., Su, Y-S., Hamamoto, S. and Uozumi, N.

Sci. Rep. 7, 2122 (2017)

GTR1 is a jasmonic acid and jasmonoyl-l-isoleucine transporter in *Arabidopsis thaliana*.

Ishimaru, Y., Oikawa, T., Suzuki, T., Takeishi, S., Matsuura, H., Takahashi, K., Hamamoto, S.,

Uozumi, N., Shimizu, T., Seo, M., Ohta, H., and Ueda, M.

Biosci. Biotech. Biochem. 81, 249-255 (2017)

Gene expression analyses of the small intestine of pigs in the ex-evacuation zone of the Fukushima Daiichi Nuclear Power Plant

Motoko Morimoto, Ayaka Kato, Jin Kobayashi, Kei Okuda, Yoshikazu Kuwahara,

Yasushi Kino, Yasuyuki Abe, Tsutomu Sekine, Tomokazu Fukuda, Emiko Isogai, Manabu

Fukumoto

BMC Veterinary Research, 13 (2017) 337.

Bound and resonance states of positronic copper atoms.

Takuma Yamashita, Muhammad Umair, Yasushi Kino

Journal of Physics B: Atomic, Molecular and Optical Physics 50 (2017) 205002.

Fusion hindrance for the positive Q-value system ${}^{12}\text{C}+{}^{30}\text{Si}$

G. Montagnoli, A.M. Stefanini, C.L. Jiang, K. Hagino, F. Galtarossa, G. Colucci, S. Bottoni, C. Brogini, A. Cacioli, P. Colovic, L. Corradi, S. Courtin, R. Depalo, E. Fioretto, G. Fruet, A. Gal, A. Goasdu, M. Heine, S.P. Hu, M. Kaur, T. Mijatovic, M. Mazzocco, D. Montanari, F. Scarlassara, E. Strano, S. Szilner, and G.X. Zhang,
Phys. Rev. C, in press.

Determination of fusion barrier distributions from quasielastic scattering crosssections towards superheavy nuclei synthesis

T. Tanaka, Y. Narikiyo, K. Morita, K. Fujita, D. Kaji, K. Morimoto, S. Yamaki, Y. Wakabayashi, K. Tanaka, M. Takeyama, A. Yoneda, H. Haba, Y. Komori, S. Yanou, B.J.-P. Gall, Z. Asfari, H. Faure, H. Hasebe, M. Huang, J. Kanaya, M. Murakami, A. Yoshida, T. Yamaguchi, F. Tokanai, T. Yoshida, S. Yamamoto, Y. Yamano, K. Watanabe, S. Ishizawa, M. Asai, R. Aono, S. Goto, K. Katori, and K. Hagino,
J. Phys. Soc. Jpn. 87 (2018) 014201/1-9.

Role of deformation in odd-even staggering in reaction cross sections for $^{30,31,32}\text{Ne}$ and $^{36,37,38}\text{Mg}$ isotopes

Y. Urata, K. Hagino, and H. Sagawa,
Phys. Rev. C96 (2017) 064311/1-6.

Transition from vibrational to rotational characters in low-lying states of hypernuclei

H. Mei, K. Hagino, J.M. Yao, and T. Motoba,
Phys. Rev. C96 (2017) 014308/1-9.

Applicability of the Wong formula for fusion cross sections from light to heavy systems

N. W. Lwin, N. N. Htike, and K. Hagino,
Phys. Rev. C95 (2017) 064601/1-4.

New and efficient method for solving the eigenvalue problem for the two-center shell model with finite depth potentials

K. Hagino and T. Ichikawa,
Phys. Rev. C95 (2017) 054620/1-7.

Quantum tunneling with friction

M. Tokieda and K. Hagino,
Phys. Rev. C95 (2017) 054604/1-9.

書評 量子散乱理論への招待 ; フェムトの世界を見る物理

萩野浩一
日本物理学会誌 73(2018) 118-119.

ϕ photoproduction on the proton at $E_\gamma=1.5\text{-}2.9$ GeV

K. Mizutani, M. Niiyama, T. Nakano, M. Yosoi, Y. Nozawa, D.S. Ahn, J. K. Ahn, W.C. Chang, J. Y. Chen, S. Daté, W. Gohn, H. Hamano, T. Hashimoto, K. Hicks, T. Hiraiwa, T. Hotta, S.H. Hwang, T. Ishikawa, K. Joo, W.S. Jung, Y. Kato, H. Katsuragawa, M H. Kim, S.H. Kim,

H. Kohri, Y. Kon, H. S. Lee, Y. Maeda, Y. Matsumura, T. Mibe, M. Miyabe, Y. Morino, N. Muramatsu, Y. Nakatsugawa, H. Noumi, Y. Ohashi, T. Ohta, M. Oka, J.B. Park, J.D. Parker, C. Rangacharyulu, S. Y. Ryu, Y. Sada, T. Sawada, T. Shibukawa, S. H. Shiu, Y. Sugaya, M. Sumihama, S. Tanaka, A.O. Tokiyasu, N. Tomida, H. N. Tran, T. Tsunemi, M. Uchida, M. Ungaro, and Y. Yanai (LEPS Collaboration)

Physical Review C 96 (2017) 062201(R).

Differential cross section and photon-beam asymmetry for the $\gamma p \rightarrow \pi^+ n$ reaction at forward π^+ angles at $E_\gamma=1.5-2.95$ GeV

H. Kohri, S. Y. Wang, S.H. Shiu, W.C. Chang, Y. Yanai, D.S. Ahn, J.K. Ahn, J.Y. Chen, S. Daté, H. Ejiri, H. Fujimura, M. Fujiwara, S. Fukui, W. Gohn, K. Hicks, A. Hosaka, T. Hotta, S.H. Hwang, K. Imai, T. Ishikawa, K. Joo, Y. Kato, S.H. Kim, Y. Kon, H.S. Lee, Y. Maeda, T. Mibe, M. Miyabe, Y. Morino, N. Muramatsu, T. Nakano, Y. Nakatsugawa, M. Niiyama, H. Noumi, Y. Ohashi, T. Ohta, M. Oka, J. D. Parker, C. Rangacharyulu, S.Y. Ryu, T. Sawada, H. Shimizu, Y. Sugaya, M. Sumihama, T. Tsunemi, M. Uchida, M. Ungaro, and M. Yosoi (LEPSCollaboration)

Physical Review C 97 (2018) 015205.

Photoproduction of Λ and Σ^0 hyperons with linearly polarized photons at $E_\gamma=1.5-3.0$ GeV

S.H. Shiu, H. Kohri, W.C. Chang, D.S. Ahn, J.K. Ahn, J.Y. Chen, S. Daté, H. Ejiri, H. Fujimura, M. Fujiwara, S. Fukui, W. Gohn, K. Hicks, T. Hotta, S.H. Hwang, K. Imai, T. Ishikawa, K. Joo, Y. Kato, Y. Kon, H.S. Lee, Y. Maeda, T. Mibe, M. Miyabe, K. Mizutani, Y. Morino, N. Muramatsu, T. Nakano, Y. Nakatsugawa, M. Niiyama, H. Noumi, Y. Ohashi, T. Ohta, M. Oka, J.D. Parker, C. Rangacharyulu, S.Y. Ryu, T. Sawada, H. Shimizu, Y. Sugaya, M. Sumihama, T. Tsunemi, M. Uchida, M. Ungaro, and M. Yosoi (LEPS Collaboration)

Physical Review C 97 (2018) 015208.

A study of event mixing for two-pion Bose-Einstein correlations in the $\gamma p \rightarrow \pi^0 \pi^0 p$ reaction

Q. He, J. Ai, T. Ishikawa, T. Li, L. Ma, J. Ma, M. Miyabe, N. Muramatsu, H. Shimizu, Y. Tsuchikawa, Y. Xiang, H. Yamazaki, Y. Zhang

Progress of Theoretical and Experimental Physics 2017-3 (2017) 033D02.

Low-energy eta-nucleon interaction studied with eta photoproduction off the deuteron

S.X. Nakamura, H. Kamano, T. Ishikawa

Physical Review C 96, 042201 (R) (2017).

ダークマターの正体に迫る

協力 森山茂栄／小川 泉／時安敦史／鳥居祥二／浅井祥仁

執筆 福田伊佐央（編集部）

Newton 10月号 解説記事

Design and performance of the spin asymmetries of the nucleon experiment

J.D.Maxwell et al. (SANE collaboration), (SNN 80 of 105),
Nucl. Inst. and Meth. A 885 (2018) 145-159.

Virtual Institute for Quark Nuclear Physics at SPring-8/LEPS2

H. Shimizu and N. Muramatsu,
Nuclear Physics News 27:1 (2017) 19-22.

Replication Experiments at Tohoku University on Anomalous Heat Generation Using Nickel-Based Binary Nanocomposites and Hydrogen Isotope Gas

Y. Iwamura, T. Itoh, J. Kasagi, A. Kitamura, A. Takahashi and K. Takahashi
J. Condensed Matter Nucl. Sci. 24 (2017) 191–201.

Anomalous Excess Heat Generated by the Interaction between Nano-structured Pd/Ni surface and D₂/H₂ gas

T. Itoh, Y. Iwamura, J. Kasagi and H. Shishido
J. Condensed Matter Nucl. Sci. 24 (2017) 179–190.

Collaborative Examination on Anomalous Heat Effect Using Nickel-based Binary Nanocomposites Supported by Zirconia

A. Kitamura, A. Takahashi, K. Takahashi, R. Seto, Y. Matsuda, Y. Iwamura, T. Itoh, J. Kasagi, M. Nakamura, M. Uchimura, H. Takahashi, T. Hioki, T. Motohiro, Y. Furuyama and M. Kishida
J. Condensed Matter Nucl. Sci. 24 (2017) 202–213.

【クローズアップ】凝縮系核反応の現状と今後の発展

岩村康弘
パリティ, Vol32, No.05, p.44-49, 2017.

Papers Published in International Conference Proceedings

Observation of Coherent Undulator Radiation in THz Region

S. Kashiwagi, H. Saito, F. Hinode, K. Kanomata, S. Miura, T. Muto, I. Nagasawa, N. Nishimori, K. Nanbu, Y. Saito, K. Takahashi and H. Hama
Infrared Physics and Tech. (in press).

Numerical Study of Cherenkov Radiation from Thin Silica Aerogel

H. Hama, K. Nanbu, H. Saito, Y. Saito
Proc. 38th Int. Free Electron Laser Conf., Santa Fe, NM, 471 – 473 (2017).

Measurement of Pionic ¹²¹Sn atoms at the RI beam factory

Kenta Itahashi, Georg P.A. Berg, Hiroyuki Fujioka, Hans Geissel, Ryugo S. Hayano, Satoru Hirenzaki, Natsumi Ikeno, Naohito Inabe, Satoshi Itoh, Daisuke Kameda, Toshiyuki Kubo, Hiroaki Matsubara, Shinichiro Michimasa, Kenjiro Miki, Hiroyuki Miya,

Masaki Nakamura, Takahiro Nishi, Shumpei Noji, Shinsuke Ota, Ken Suzuki, Hiroyuki Takeda, Koichi Todoroki, Kyo Tsukada, Tomohiro Uesaka, Helmut Weick, Koichi Yoshida

Proceedings, 4th International Conference on Exotic Atoms and Related Topics (EXA 2011) :
Vienna, Austria, September 5-9, 2011

Spectroscopic Study of Hyperon Resonance Below KbarN Threshold via the $d(K^-,n)$ Reaction

K. Inoue, S. Ajimura, G. Beer, H. Bhang, M. Bragadireanu, P. Buehler, L. Busso, M. Cargnelli, S. Choi, C. Curceanu, S. Enomoto, D. Faso, H. Fujioka, Y. Fujiwara, T. Fukuda, C. Guaraldo, T. Hashimoto, R. S. Hayano, T. Hiraiwa, M. Iio, M. Iliescu, Y. Ishiguro, T. Ishikawa, S. Ishimoto, T. Ishiwatari, K. Itahashi, M. Iwai, M. Iwasaki, Y. Kato, S. Kawasaki, P. Kienle, H. Kou, Y. Ma, J. Marton, Y. Matsuda, Y. Mizoi, O. Morra, T. Nagae, H. Noumi, H. Ohnishi, S. Okada, H. Outa, K. Piscicchia, M. Poli Lener, A. Romero Vidal, Y. Sada, A. Sakaguchi, F. Sakuma, M. Sato, A. Scorde, M. Sekimoto, H. Shi, K. Shirotori, D. Sirghi, F. Sirghi, K. Suzuki, S. Suzuki, T. Suzuki, K. Tanida, H. Tatsuno, M. Tokuda, D. Tomono, A. Toyoda, K. Tsukada, O. Vazquez Doce, E. Widmann, B. K. Wuenschek, T. Yamaga, T. Yamazaki, H. Yim, Q. Zhang, and J. Zmeskal

JPS Conf.Proc. 17 (2017) 072003

High-Resolution Decay-Pion Spectroscopy of ${}^4_{\Lambda}$ H Hypernuclei

P. Achenbach, F. Schulz, S. Nagao, S. Aulenbacher, J. Beričić, S. Bleser, R. Böhm, D. Bosnar, L. Correa, M. O. Distler, A. Esser, H. Fonvieille, I. Friščić, Y. Fujii, M. Fujita, T. Gogami, H. Kanda, M. Kaneta, S. Kegel, Y. Kohl, W. Kusaka, A. Margaryan, H. Merkel, M. Mihovilović, U. Müller, S. N. Nakamura, J. Pochodzalla, A. Sanchez Lorente, B. S. Schlimme, M. Schoth, C. Sfienti, S. Širca, M. Steinen, Y. Takahashi, L. Tang, M. Thiel, K. Tsukada, A. Tyukin, and A. Weber

JPS Conf. Proc. 17, 011001 (2017).

The Recent Results of Strangeness Photoproduction in the Threshold Region at ELPH-Tohoku

Hiroki Kanda, Brian Beckford, Petr Bydžovský, Takeji Fujibayashi, Takao Fujii, Yu Fujii, Kenta Futatsukawa, Toshiyuki Gogami, Yun-Cheng Han, Osamu Hashimoto, Kentaro Hirose, Kenji Hosomi, Ryotaro Honda, Alan Iguchi, Takatsugu Ishikawa, Masashi Kaneta, Yusuke Kaneko, Yuma Kasai, Taito Kawasaki, Chigusa Kimura, Shogo Kiyokawa, Takeshi Koike, Kazushige Maeda, Nayuta Maruyama, Masao Matsubara, Koji Miwa, Yohei Miyagi, Sho Nagao, Satoshi N. Nakamura, Takashi Nishizawa, Akira Okuyama, Miloslav Sotona, Tadaaki Tamae, Hirokazu Tamura, Kyo Tsukada, Nobu Terada, Mifuyu Ukai, Tie-Shan Wang, Fumiya Yamamoto, Takeshi O. Yamamoto, and Hirohito Yamazaki

JPS Conf. Proc. 17 (2017) 062006(1-4)

The Performance Of The Scrit Detectors For Electron-RI Scattering Experiment

Akitomo Enokizono, Kousuke Adachi, Takahiro Fujita, Masahiro Hara, Mitsuki Hori, Toshitada Hori, Sin'ichi Ichikawa, Keita Kasama, Kazuyoshi Kurita, Kazuki Namba, Tatsuya Ohnishi, Shin-Nosuke Sasamura, Toshimi Suda, Tadaaki Tamae, Kyo Tsukada, Mamoru Togasaki, Nobuaki Uchida, Masanori Wakasugi, Shou Wang, Masamitsu Watanabe, Kouhei Yamada

Proceedings, 26th International Nuclear Physics Conference (INPC2016) :Adelaide, Australia, September 11-16, 2016

The Scrit Electron Scattering Facility At Riken RI Beam Factory

Tetsuya Ohnishi, Masahiro Hara, Toshitada Hori, Shinichi Ichikawa, Masamitsu Watanabe, Masanori Wakasugi, Kosuke Adachi, Akitomo Enokizono, Takahiro Fujita, Mitsuki Hori, Shinnosuke Sasamura, Mamoru Togasaki, Nobuaki Uchida, Kouhei Yamada, Kazuyoshi Kurita, Keita Kasama, Kazuki Namba, Kyo Tsukada, Tadaaki Tamae, Toshimi Suda, Shuo Wang, Takashi Kikuchi

Proceedings, 26th International Nuclear Physics Conference (INPC2016) : Adelaide, Australia, September 11-16, 2016

First Result from Scrit Electron Scattering Facility : Charge Density Distribution Of ^{132}Xe

Kyo Tsukada, Keita Kasama, Kazuki Namba, Toshimi Suda, Tadaaki Tamae, Masahiro Hara, Shinnichi Ichikawa, Tetsuya Ohnishi, Masanori Wakasugi, Masamitsu Watanabe, Kousuke Adachi, Akitomo Enokizono, Toshihiro Fujita, Mitsuki Hori, Kazuyoshi Kurita, Shinnosuke Sasamura, Mamoru Togasaki, Nobuaki Uchida, Kouhei Yamada

Proceedings, 26th International Nuclear Physics Conference (INPC2016) : Adelaide, Australia, September 11-16, 2016

Low-energy Scattering Parameters Between the eta Meson and Nucleon from eta Photoproduction on the Deuteron

T. Ishikawa, K. Aoki, H. Fujioka, Y. Honda, T. Hotta, Y. Inoue, K. Itahashi, H. Kanda, H. Kawai, K. Maeda, Y. Matsumura, M. Miyabe, S. Miyata, N. Muramatsu, T. Nishi, H. Ohnishi, K. Ozawa, H. Shimizu, R. Shirai, M. Tabata, A.O. Tokiyasu, Y. Tsuchikawa, and H. Yamazaki

ACTA PHYSICA POLONICA B, 48(2017) 1801-1806.

Search For A Ξ Bound State In The $^{12}\text{C}(\text{K}^-, \text{K}^+)\text{X}$ Reaction At 1.8 GeV/c in J-PARC

Tomofumi Nagae et al..

PoS INPC2016 (2017) 038-44

Spectroscopy of Nuclei with Multi-Strangeness by Using New S-2S Spectrometer at J-PARC

Toshiyuki Gogami et al..

JPS Conf. Proc. 18 (2017) 011031(1-6)

The First Gamma-ray Spectroscopic Study of sd-shell Hypernucleus, $^{19}_{\Lambda}\text{F}$

S.B. Yang et al..

JPS Conf. Proc. 17 (2017) 012004(1-4)

High Statistics Σp Scattering Experiment Using High Intensity Pion Beams at J-PARC

K. Miwa et al..

JPS Conf. Proc. 17 (2017) 041002(1-6)

Search for Excited State of Σ Hypernucleus in the J-PARC E13 Experiment

M. Nakagawa et al..

JPS Conf. Proc. 17 (2017) 012009(1-4)

Gamma-ray Spectroscopy of Hypernuclei — Recent Results and Prospect at J-PARC —

H. Tamura et al.,

JPS Conf. Proc. 17 (2017) 011004(1-11)

Time course change of radiocesium concentration in wild mushrooms collected in Miyagi prefecture, Japan from 2011 to 2014

A. Irisawa, Y. Kino,

Proceedings of the 4th International Conference on Environmental Radioactivity

ENVIRA2017, (2017) 29-32.

A coupled rearrangement channel analysis of positronium antihydride

Takuma Yamashita, Yasushi Kino, Emiko Hiyama, Svante Jonsell, Piotr Froelich,

Journal of Physics, Conference Series, 875 (2017) 052031

Degradation of electron-irradiated polyethylene studied by positron annihilation lifetime spectroscopy

Karin Onodera, Toshitaka Oka, Yasushi Kino, Tsutomu Sekine,

Journal of Physics: Conference Series, 791 (2017) 012026

Uptake of Radioactive Cesium by Intestinal and Probiotic Bacteria

K. Saito, K. Kuroda, T. Sekine, M. Fukumoto, Y. Kino, T. Fukuda, H. Yamashiro, H. Shinoda,

H. Isogai, J. Kobayashi, J. Nishimura, Y. Abe, N. Nishida, M. Kouno, E. Isogai,

Journal of Integrated Field Science, 14 (2017) 111.

Evolving theoretical descriptions of heavy-ion fusion: from phenomenological to microscopic approaches

K. Hagino

EPJ Web of Conf. 163 (2017) 00022/1-6.

Three-body model for nuclei near and beyond drip line

H. Sagawa and K. Hagino,

Acta Phys. Polon. Supp. 10 (2017) 211-224.

Description of multi-nucleon transfer and fusion reactions with the coupled-channel method

G. Scamps, D. Bourgin, F. Haas, K. Hagino, and S. Courtin,

PoS INPC2016 (2017) 213/1-7.

Beyond-mean-field approach to low-lying spectra of Λ hypernuclei

K. Hagino, H. Mei, J.M. Yao, and T. Motoba,

JPS Conf. Proc. 17 (2017) 012007/1-4.

Kaonic-Atom X-ray Spectroscopy with Superconducting Microcalorimeters

T. Hashimoto, M. Bazzi, D.A. Bennett, C. Berucci, D. Bosnar, C. Curceanu, W.B. Doriese, J.W. Fowler, H. Fujioka, C. Guaraldo, F. Parnefjord Gustafsson, R.S. Hayano, J.P. Hays-Wehle, G.C. Hilton, T. Hiraiwa, M. Iio, M. Iliescu, S. Ishimoto, K. Itahashi, M. Iwasaki, Y. Ma, H. Noumi, G.C. O'Neil, H. Ohnishi, S. Okada, H. Outa, K. Piscicchia, C.D. Reintsema, Y. Sada, F. Sakuma, M. Sato, D.R. Schmidt, A. Scordo, M. Sekimoto, H. Shi, D. Sirghi, F. Sirghi, K. Suzuki, D.S. Swetz, K. Tanida, H. Tatsuno, M. Tokuda, J. Uhlig, J.N. Ullom, S. Yamada, T. Yamazaki, and J. Zmeskal

JPS Conf. Proc. 17, 072001 (2017)

Probing Strong Interaction with Kaonic Atoms – from DAΦNE to J-PARC

J. Zmeskal, M. Sato, M. Bazzi, G. Beer, C. Berucci, D. Bosnar, M. Bragadireanu, P. Buehler, M. Cargnelli, A. Clozza, C. Curceanu, A. D'uffizi, L. Fabbietti, C. Fiorini, F. Ghio, R. Golser, C. Guaraldo, T. Hashimoto, R.S. Hayano, M. Iliescu, K. Itahashi, M. Iwasaki, P. Levi Sandri, J. Marton, P. Moskal, H. Ohnishi, S. Okada, H. Outa, D. Pietreanu, K. Piscicchia, . Poli Lener, A. Romero Vidal, F. Sakuma, E. Sbardella, A. Scordo, H. Shi, D. Sirghi, F. Sirghi, K. Suzuki, I. Tucakovic, O. Vazquez Doce, E. Widmann

JPS Conf.Proc. 17 (2017) 071001

Spectroscopic Experiment of $\Lambda(1405)$ via the In-flight $d(K^-, n)$ Reaction at J-PARC K1.8BR

S. Kawasaki, S. Ajimura, G. Beer, H. Bhang, M. Bragadireanu, P. Buehler, L. Busso, M. Cargnelli, S. Choi, C. Curceanu, S. Enomoto, D. Faso, H. Fujioka, Y. Fujiwara, T. Fukuda, C. Guaraldo, T. Hashimoto, R. Hayano, T. Hiraiwa, M. Iio, M. Iliescu, K. Inoue, T. Ishikawa, S. Ishimoto, K. Itahashi, M. Iwai, M. Iwasaki, P. Kienlep, H. Kou, Y. Ma, J. Marton, Y. Matsuda, H. Mizoi, O. Morra, T. Nagae, H. Noumi, H. Ohnishi, S. Okada, H. Outa, D. Pietreanu, Y. Sada, A. Sakaguchi, F. Sakuma, M. Sato, M. Sekimoto, H. Shi, K. Shirotori, D. Sirghi, F. Sirghi, K. Suzuki, S. Suzuki, T. Suzuki, K. Tanida, H. Tatsuno, M. Tokuda, M. Tomono, A. Toyoda, K. Tsukada, E. Widmann, T. Yamaga, K. Yoshida, T. Yamazaki, H. Yim, Q. Zhang, J. Zmeskal

JPS Conf.Proc. 13 (2017) 020018

Study of non-strange dibaryon resonances via coherent double neutral-pion photoproduction on the deuteron

Takatsugu Ishikawa, Hisako Fujimura, Ryo Hashimoto, Qinghua He, Shun Kaida, Manabu Miyabe, Norihito Muramatsu, Hajime Shimizu, Koutaku Suzuki, Yusuke Tschikawa, Hirohito Yamazaki, Shin'ichi Masumoto, Hiroki Kanda, Kazushige Maeda, Kyoichiro Ozawa.

PoS(Hadron2017)065 (2018).

Low-energy scattering parameters between the eta meson and nucleon from eta photoproduction on the deuteron

T. Ishikawa, K. Aoki, H. Fujioka, Y. Honda, T. Hotta, Y. Inoue, K. Itahashi, H. Kanda, H. Kawai, K. Maeda, Y. Matsumura, M. Miyabe, S. Miyata, N. Muramatsu, T. Nishi, H. Ohnishi, K. Ozawa, H. Shimizu, R. Shirai, M. Tabata, A.O. Tokiyasu, Y. Tsuchikawa, H. Yamazaki

Acta Physica Polonica B48, 1801 (2017).

Study of $\Sigma\pi$ Invariant Mass Spectrum in the $d(\gamma, K^+)X$ Reaction

Atsushi Tokiyasu for the LEPS collaboration

JPS Conf.Proc. 17 (2017) 082002

ηn Scattering Length from the $\gamma d \rightarrow p \eta n$ Reaction at $E_\gamma \sim 0.9$ GeV

Takatsugu Ishikawa, Hiroyuki Fujioka, Yuki Honda, Tomoaki Hotta, Yosuke Inoue, Kenta Itahashi, Hiroki Kanda, Hideyuki Kawai, Kazushige Maeda, Manabu Miyabe, Seiya Miyata, Yuji Matsumura, Norihito Muramatsu, Hiroaki Ohnishi, Kyoichiro Ozawa, Mizuki Sasagawa, Hajime Shimizu, Ken'ichiro Shiraishi, Makoto Tabata, Atsushi O Tokiyasu, Yusuke Tsuchikawa

JPS Conf.Proc. 13 (2017) 020031

Study of the $d(\gamma, K^+)\Sigma\pi N$ Reaction at LEPS

Atsushi Tokiyasu for the LEPS collaboration

JPS Conf.Proc. 13 (2017) 020017

Spectroscopic Study of Λ Hypernuclei with Electron Beams at Jefferson Lab

Satoshi N. Nakamura, Toshiyuki Gogami and Liguang Tang,

JPS Conf. Proc. 17, 011002 (2017).

Study of Λ -n Interaction via FSI in $\gamma+d$ Reaction

Masashi Kaneta for the NKS2 collaboration

JPS Conference Proceedings 17 (2017) 062002-1 - 062002-4

Photoproduction of η' mesons at SPring-8/LEPS2

H. Shimizu

Acta Phys. Pol. B48 (2017) 1819-1824.

Anomalous Excess Heat Generated by the Interaction between Nano-structured Pd/Ni surface and D_2 gas

T. Itoh, Y. Iwamura, J. Kasagi and H. Shisido

Proceedings of ICCF20, 2-7 Oct 2016, Sendai, Japan, p.60-70

Observation of ^{141}Pr by ^{40}Ar Scattering (RBS) on Cs Implanted Pd/CaO multilayer foil with D_2 Gas Permeation

J. Kasagi, R. Tajima, Y. Honda, T. Itoh, Y. Iwamura, H. Kikunaga, and S. Tsuruga

Proceedings of the 20th International Conference on Condensed Matter Nuclear Science, pp.160-165.

Invited Talk and Oral Presentations at International Conferences

SLiT-J, a project of high brilliant compact 3 GeV light source in Japan (Invited oral presentation)

Hiroyuki Hama

Diamond light source, Oxford, UK, Nov. 16, 2017.

SLiT-J, a project of high brilliant compact 3 GeV light source in Japan (Invited oral presentation)

Hiroyuki Hama

ALBA light source, Barcelona, Spain, Nov. 14, 2017.

Smith-Purcell FEL (Oral presentation)

Hiroyuki Hama

National Electronics and Computer Technology Center, Khlong Luang, Pathum Thani, Thailand, Dec. 26, 2017.

ELPH present status (Oral presentation)

Hiroyuki Hama

Scandinova Systems, Uppsala, Sweden, Mar. 12, 2018.

Observation of coherent undulator radiation in THz region (Oral presentation)

S. Kashiwagi, H. Saito, F. Hinode, K. Kanomata, S. Miura, T. Muto, I. Nagasawa, N. Nishimori, K. Nanbu, Y. Saito, K. Takahashi and H. Hama.

The 9th International Workshop on Infrared Microscopy and Spectroscopy with Accelerator Based Sources, WIRMS 2017 25-28 September, 2017 Worcester College, Oxford UK

Coherent Undulator Radiation from Extremely Short Electron Bunches (Basic course) (Lecture)

Radioactive Isotope Production via Photo Nuclear Reaction using High Power Electron Linac (Application) (Lecture)

Shigeru Kashiwagi

日本インド加速器スクール (International School on Electron Accelerators, Free Electron Laser and Application of electron beam/THz Radiation 2018), Inter University Accelerator Centre (IUAC), New Delhi, India, 03-06 March 2018

Bunch length measurement system for ultra-short electron bunch using Cherenkov radiation (Oral presentation)

Fujio Hinode

3rd International workshop on CSR and free electron lasers from ultra-short bunch electron beam, Hefei, China, 3/13-14, 2018

Overview of SLiT-J Proposal – a high brilliant compact 3GeV light source project – (Oral presentation)

Nobuyuki Nishimori

Meeting on TPS and SLiT-J Projects, NSRRC Hsinchu, Taiwan, Feb. 14, 2017.

Commission results of the compact ERL high voltage DC gun (Invited oral presentation)

Nobuyuki Nishimori

The 59th ICFA Advanced Beam Dynamics Workshop on Energy Recovery Linacs, CERN Geneva, Switzerland, Jun. 21, 2017.

Development of a multialkali photocathode DC gun for high current operation (Oral presentation)

Nobuyuki Nishimori

The 59th ICFA Advanced Beam Dynamics Workshop on Energy Recovery Linacs, CERN Geneva, Switzerland, Jun. 22, 2017.

Development of a multialkali photocathode DC gun for a Smith-Purcell THz FEL (Oral presentation)

Nobuyuki Nishimori

2nd International workshop on CSR and free electron lasers from ultra short bunch electron beam, ELPH Sendai, Japan, Sep. 20, 2017.

A Study of Generation of Variable Polarized THz Superradiance Using a Crossed Undulator (Oral presentation)

Hirotooshi Saito

2nd International workshop on CSR and free electron lasers from ultra short bunch electron beam (ELPH, Tohoku University), 20 September 2017.

Sub-picosecond bunch length measurement using Cherenkov radiation from a thin silica-aerogel (Oral presentation)

Yuki Saito

2nd International workshop on CSR and free electron lasers from ultra short bunch electron beam (ELPH, Tohoku University), 20 September 2017.

Study on Generation of Variable Polarized Coherent THz Radiation Using a Crossed Undulator (Oral presentation)

Hirotooshi Saito

International workshop on CSR and FELs from ultra-short bunch electron beams (NSRL, Hefei), 13 March 2018.

Electron Scattering Activities in Japan (Oral presentation)

T. Suda

RAON シンポジウム、Daejon、Korea 2017年3月7日

Electron scattering for neutron-rich exotic nuclei (Invited oral presentation)

T. Suda

ECT*研究会 “Walk on the neutron-rich side”, Trento, Italy, 2017年4月13日

Probing two-nucleon system in nuclei and electron scattering off exotic nuclei (Invited oral presentation)

T. Suda

QFS workshop、ヨーク大学、イギリス 2017年7月24日

The SCRIT Electron Scattering Facility (Invited oral presentation)

T. Suda

ISPUN 国際シンポジウム、ハーロン、ベトナム、2017年9月25日—10月1日

Proton Charge Radius by electron scattering under the lowest-ever momentum transfer (Invited oral presentation)

T. Suda

FPU 国際会議、名古屋大学、名古屋市、2018年1月8—9日

Proton Radius Measurement in ELPH (Invited oral presentation)

T. Suda

International Symposium on Nucleon Structure, 山形大学、山形、2018年3月8日

RI production at ELPH (Invited oral presentation)

H. Kikunaga

The 7th Yamada Workshop on RI Science Evolution 2018 (RISE18), Osaka, 3/16-17, 2018

First result from SCRIT electron scattering facility with ^{132}Xe target (Invited oral presentation)

K. Tsukada

The 10th International Conference on Nuclear Physics at Storage Rings、

金沢2017年11月13日—18日

Proton radius puzzle at ELPH (Oral presentation)

Y. Honda

The 15th g-2/EDM collaboration meeting, Kyushu University, 2017年12月11-14

Hadrons in medium (Invited oral presentation)

H. Tamura

The 21st Particle and Nuclei International Conference (PANIC2017), 2017.9.1~9.5, Beijing, China.

Experimental studies of high density baryonic matter with and without strangeness (Invited oral presentation)

H. Tamura

XVII International Conference on Hadron Spectroscopy and Structure (Hadron2017), 2017. 9. 25~9.29, Salamanca, Spain.

Prospect for Hypernuclear Studies at J-PARC K1.1 Beam Line (Prospect on $S = -1$ Hypernuclei) (Invited oral presentation)

H. Tamura

“Advances and open problems in low-energy nuclear and hadronic STRAngeness physics” workshop 2017.10.23-10.27, Trento, Italy.

Hypernuclear physics with kaon (and pion) beams (Invited oral presentation)

H. Tamura

The 2nd EMMI workshop: Anti-matter, hyper-matter, and exotica production at the LHC, 2017.11.6~10, Torino, Italy.

Nuclear Physics with Strangeness (Invited oral presentation)

H. Tamura

56th International Winter Meeting on Nuclear Physics, 2018.1.22 ~ 1.26, Bormio, Italy.

Properties and behavior of baryons in a nucleus studied from precise gamma-spectroscopy and weak decays of Λ hypernuclei

H. Tamura

International Workshop on the Project for the Extended hadron Experimental Facility at J-PARC 2018.3.26~28, KEK Tokai Campus, Tokai, Japan.

Nuclear reaction in atomic collision under a screening effect from negatively charged massive particle (Invited oral presentation)

Y.Kino,

13th International Conference of Computational Methods in Science and Engineering, April 21-25, 2017, Thessaloniki, Greece.

Time course change of radiocesium concentration in wild mushrooms collected in Miyagi prefecture, Japan from 2011 to 2014 (Oral presentation)

Y. Kino,

Proceedings of the 4th International Conference on Environmental Radioactivity ENVIRA2017, May29-June 2, 2017.

Nuclear reaction in muon atomic collision (Oral presentation)

Yasushi Kino,

The 30th International Conference on Photonic, Electronic and Atomic Collisions (ICPEAC XXX), Cairns, Australia, 2017/7/26-8/1.

Fusion barrier distributions for superheavy elements (Invited oral presentation)

K. Hagino.

International Symposium on Physics of Unstable Nuclei 2017 (ISPUN17), Halong City, Vietnam, September 25-30, 2017.

Three-body approach to unbound nuclei (Invited oral presentation)

K. Hagino

IIRC Symposium on Perspectives of the physics of nuclear structure, Tokyo, Japan, November 1-4, 2017.

Capture barrier distributions and superheavy elements (Invited Oral Presentation)

K. Hagino

International Symposium on RI beam physics in the 21st century: 10th anniversary of RIBF,
December 4-5, 2017.

Heavy-ion fusion reactions and superheavy elements (Invited oral presentation)

K. Hagino

YITP school on “Recent Progress of Nuclear Structure and Reaction Physics”, Yukawa
Institute for Theoretical Physics, Kyoto University, December 18-22, 2017.

Search for ϕ meson bound states (Invited oral presentation)

H. Ohnishi

XVII INTERNATIONAL CONFERENCE ON HADRON SPECTROSCOPY AND
STRUCTURE (2017), Salamanca, Spain, September 25th-29th 2017.

Non-strange dibaryons from photoproduction experiments at ELPH (Invited oral presentation)

T. Ishikawa

2017 JAEA/ASRC Reimei Workshop: Hadronic Resonances and Dense Nuclear Matter,
Ibaraki Quantum Beam Research Center (IQBRC), Tokai, Japan, December 11-13, 2017.

Study of non-strange dibaryon resonances via coherent double neutral-pion photoproduction on the
deuteron (Oral presentation)

T. Ishikawa

XVII International Conference on Hadron Spectroscopy and Structure, Salamanca, Spain,
September 25-29, 2017.

Low-energy scattering parameters between the eta meson and nucleon from eta photoproduction on the
deuteron (Invited oral presentation)

T. Ishikawa

2nd Jagiellonian Symposium of Fundamental and Applied Subatomic Physics, Collegium
Maius, Jagiellonian University Kraków, Poland, 4-9 June, 2017.

Study of Hypernuclei with Electron Beams (Invited oral presentation)

S. Nakamura

Gordon Research Conference, Nuclear Chemistry, New London NH USA, 8-23 June 2017.

Results from the hypernuclear physics experiment at JLab and future perspectives (Invited oral
presentation)

S. Nakamura

XVII International Conference on Hadron Spectroscopy and Structure (HADRON2017),
Salamanca, Spain, 25th-29th Sep 2017.

An experimental approach to the hypertriton puzzle with hypernuclear (electro-)photo production (Oral
presentation)

S. Nagao and S.N. Nakamura

Advances and open problems in low-energy nuclear and hadronic STRAnge physics (ASTRA), ECT*, Trento Italy, 23-27 Oct. 2017.

Electro-photo production of Λ hypernuclei and perspectives (Invited oral presentation)

S. Nakamura

2nd EMMI Workshop, Anti-matter, hyper-matter and exotica production at LHC, Turin Italy, 6-10 Nov. 2017

Photoproduction of η' mesons at SPring-8/LEPS2 (Invited oral presentation)

H. Shimizu

2nd Jagiellonian Symposium, Krakow, June 4-10, 2017.

Anomalous Heat Generation Experiments Using Metal Nanocomposites and Hydrogen Isotope Gas (Oral presentation)

Y. Iwamura

12th International Workshop on Anomalies in Hydrogen Loaded Metals, Costigliole d'Asti (AT), Italy. 5-9 June 2017.

Anomalous Excess Heat Generation by the Interaction between Nano-structured Pd/Ni surface and D_2/H_2 gas (Oral presentation)

Y. Iwamura

12th International Workshop on Anomalies in Hydrogen Loaded Metals, Costigliole d'Asti (AT), Italy. 5-9 June 2017.

Recent Progress on Transmutation Experiments induced by D_2 gas permeation (Oral presentation)

T.Itoh, J. Kasagi, Y.Iwamura, S.Tsuruga

12th International Workshop on Anomalies in Hydrogen Loaded Metals, Asti, Italy, 5-9 June 2017

学位論文（電子光理学研究センター所属）

修士論文 「光生成反応による中間子核子間相互作用の決定精度の評価」

笹川 瑞貴, 平成 29 年度, 東北大学

修士論文 「低屈折率シリカエアロゲル薄膜からのチェレンコフ光を用いたサブピコ秒バンチ長計測」

齊藤 悠樹, 平成 29 年度, 東北大学

修士論文 「光生成による核子共鳴探索実験のための光子ビーム形状測定」

白井 凜太郎, 平成 29 年度, 東北大学

学位論文（他機関所属）

修士論文 「 $\gamma d \rightarrow d\pi^+\pi^-$ 反応によるダイバリオンの探索」

室井 佑太, 平成 29 年度, 東北大学

修士論文 「 Λ ハイパー核電磁分光実験のためのセプタム磁石の設計 — Λ NN 相互作用のアイソスピン依存性の解明に向けて—」

相田 元気, 平成 29 年度, 東北大学

修士論文 「 Λ_n 終状態相互作用研究に向けた Multi-gaps Resistive Plate Chamber の開発」

竹内 大貴, 平成 29 年度, 東北大学

修士論文 「シロイヌナズナの Na 輸送体 AtHKT1 の機能解析」

竹林 昂亮, 平成 29 年度, 東北大学

V. Members of Committees

Steering Committee

2017

Hiroyuki HAMA*	ELPH
Toshimi SUDA	ELPH
Hiroaki OHNISHI	ELPH
Fujio HINODE	ELPH
Shigeru KASHIWAGI	ELPH
Norihito MURAMATSU	ELPH
Hidetoshi KIKUNAGA	ELPH
Hirokazu TAMURA	Graduate School of Science
Satoshi NAKAMURA	Graduate School of Science
Kouichi HAGINO	Graduate School of Science
Fuminori MISAIZU	Graduate School of Science
Yasushi KINO	Graduate School of Science
Nobuyuki UOZUMI	Graduate School of Engineering
Atsuki TERAOKA	Graduate School of Engineering
Masaki FUJITA	Institute for Materials Research
Yuji TAKAKUWA	Institute of Multidisciplinary Research for Advanced Materials
Takeo EJIMA	Institute of Multidisciplinary Research for Advanced Materials
Nobuyuki NISHIMORI	Institute of Multidisciplinary Research for Advanced Materials
Keiichi EDAMATSU	Research Institute of Electrical Communication
Masatoshi ITOH	Cyclotron and Radioisotope Center
Kenji TSUDA	Frontier Research Institute for Interdisciplinary Sciences

* Chairperson

General Advisory Committee

2017

Hiroyuki HAMA*	ELPH, Tohoku University
Toshimi SUDA	ELPH, Tohoku University
Hiroaki OHNISHI	ELPH, Tohoku University
Hidetoshi KIKUNAGA	ELPH, Tohoku University
Hirokazu TAMURA	Graduate School of Science, Tohoku University
Yasushi KINO	Graduate School of Science, Tohoku University
Masatoshi ITOH	CYRIC, Tohoku University
Kenji TSUDA	Frontier Research Institute for Interdisciplinary Sciences, Tohoku University
Tomohiro UESAKA	RIKEN Nishina Center
Daisuke JIDO	Graduate School of Science and Engineering, Tokyo Metropolitan University
Takashi NAKANO	RCNP, Osaka University
Tomohumi NAGAE	Graduate School of Science, Kyoto University
Ryukou KATO	Accelerator Laboratory, KEK
Hideaki OHGAKI	IAE, Kyoto University
Akihiko YOKOYAMA	College of Science and Engineering, Kanazawa University
Yasuji OURA	Graduate School of Science and Engineering, Tokyo Metropolitan University

* Chairperson

Program Advisory Committee

2017

Toshimi SUDA	ELPH, Tohoku University
Hiroaki OHNISHI	ELPH, Tohoku University
Shigeru KASHIWAGI	ELPH, Tohoku University
Hidetoshi KIKUNAGA	ELPH, Tohoku University
Satoshi NAKAMURA*	Graduate School of Science, Tohoku University
Asao YAMAMURA	Institute for Materials Research, Tohoku University
Kiyoshi TANIDA	ASRC, Japan Atomic Energy Agency
Megumi NARUKI	Graduate School of Science, Kyoto University
Masaru YOSOI	RCNP, Osaka University
Yoshihiko SHOJI	LASTI, University of Hyogo
Yasuji OURA	Graduate School of Science and Engineering, Tokyo Metropolitan University
Koichi TAKAMIYA	Research Reactor Institute, Kyoto University

* Chairperson

VI. Approved Experiments

平成 29 度前期採択課題一覧

課題番号	課 題 名	申込責任者
2868	高エネルギー重イオン実験用 Si-W 電磁カロリメータ検出器 (ALICE FoCal)および高時間分解能 MRPC-TOF の性能評価	中條 達也
2869	放射性バナジウム V-48 を用いたバナジウム・レドックスフロー電池の隔膜の研究	白崎 謙次
2870	チャームバリオン分光実験(J-PARC E50)用シンチレーションファイバー検出器およびタイミング検出器のテスト実験	白鳥 昂太郎
2871	MPPC を用いた BGO 結晶カロリメータの開発	村松 憲仁
2872	Position Sensitive Scintillation Counter (PSSC)を用いたビーム形状診断装置の開発	時安 敦史
2873	BM4 ビームラインにおける実光子標識化装置の改善	金田 雅司
2874	$\gamma d \rightarrow K^+ \Lambda n$ 反応での終状態相互作用を用いた Λn 相互作用測定実験で用いる MRPC の性能評価	金田 雅司
2875	光子ビームを用いたハイパー核生成実験のための新 TOF 検出器の性能評価	永尾 翔
2876	J-PARC KOTO 実験における undoped CsI 結晶両読みの性能評価	南條 創

平成 29 度後期採択課題一覧

課題番号	課 題 名	申込責任者
2877	ガンマ線と中性子の分別能力を高めた GAGG 電磁カロリメータの性能評価	外川 学
2878	ハイパー核寿命測定に向けた大立体角検出器の性能評価	永尾 翔
2879	MPPC を用いたビーム位置検出器の開発と電子・陽電子ビーム形状の測定	宮部 学
2880	Multi-gap Resistive Plate Chamber のプレアンプ評価	金田 雅司
2881	$\gamma d \rightarrow \eta d$ 反応を用いた ηd 束縛状態の探索	藤岡 宏之
2882	FOREST 超前方荷電粒子検出で拓く物理	石川 貴嗣
2883	新光子標識化装置 TaggerIIs の性能評価	田島 靖久
2884	エアロジェル・チェレンコフ検出器の基礎研究	村松 憲仁
2885	家庭ごみ焼却スラグに含まれる希少金属元素の回収を目指した光量子放射化法による成分同定およびトレーサー作成	秋山 和彦
2886	光量子放射化法によるプロメチウム (Pm) 内包金属フラウレンの合成を目的とした RI 製造III	秋山 和彦
2887	放射化イメージング分析用装置開発のための RI 製造	福地 知則
2888	光核反応収率の標準化とその利用に関する基礎研究	菊永 英寿
2889	吸収体からの光を利用し高い精度を実現するサンプリング型カロリメータの性能検証	竹下 徹
2890	Multi-gap Resistive Plate Chamber の時間分解能性能評価 (国際共同大学院「宇宙創成物理学」高度実験)	金田 雅司
2891 (随時)	短寿命 RI 供給プラットフォーム主催の RI 利用者研修会に用いる Co トレーサーの製造	池田 隼人

ELPH ANNUAL REPORT 2017

December 2018

Research Center for Electron Photon Science, Tohoku University
1-2-1, Mikamine, Taihaku, Sendai 982-0826, Japan

印刷所 株式会社 東北プリント
仙台市青葉区立町24番24号
TEL 022 (263) 1166(代)

